CELLULOSE NANOMATERIALS: *FROM EXTRACTION TO BIOMEDICAL APPLICATIONS*

by

BRODY ALLEN FROST

B.S., Virginia Polytechnic Institute and State University, 2016

M.S., Virginia Polytechnic Institute and State University, 2017

A DISSERTATION SUBMITTED IN PARTIAL FULFILLMENT OF
THE REQUIREMENTS FOR THE DEGREE OF

DOCTOR OF PHILOSOPHY

in

THE FACULTY OF GRADUATE AND POSTDOCTORAL STUDIES

(Chemical and Biological Engineering)

THE UNIVERSITY OF BRITISH COLUMBIA

(Vancouver)

August 2021

© Brody Allen Frost, 2021

The following individuals certify that they have read, and recommend to the Faculty of Graduate and Postdoctoral Studies for acceptance, the dissertation entitled:

CELLULOSE NANOMATERIALS: *FROM EXTRACTION TO BIOMEDICAL APPLICATIONS*

submitted by Brody A. Frost in partial fulfillment of the requirements for

the degree of Doctor of Philosophy

in Chemical and Biological Engineering

Examining Committee:

Dr. E. Johan Foster, Chemical and Biological Engineering, UBC
Supervisor

Dr. Orlando Rojas, Chemical and Biological Engineering, UBC
Supervisory Committee Member

Dr. Dirk Lange, Jack Bell Research Center, UBC
Supervisory Committee Member

Dr. Scott Renneckar, Forestry and Wood Science, UBC
University Examiner

Dr. Feng Jiang, Forestry and Wood Science, UBC
University Examiner

Abstract

With societal, industrial, and clinical progress continuously reaching greater heights, the crucial need for enhanced materials with versatile properties is ever increasing to help this growth. As such, polymer nanocomposites (PNCs) have been heavily researched, becoming redefined as their own class of materials, focusing on fundamental structure/property relationships, manufacturing techniques, and commercial applications, due to their remarkable properties and application versatility. Through countless nanoparticle and polymer matrix variations, PNCs can be finely-tuned to exhibit a multitude of unique characteristics. Utilizing this concept, the research laid out in the combined chapters of this dissertation sought to produce various PNCs embedded with cellulose nanocrystals/nanofibrils (CNCs/CNFs) and magnetic nanoparticles (MNPs) to obtain uniquely tunable properties to further progress the biomaterials field for biomedical applications. Initially, CNCs were extracted from the otherwise useless agricultural waste product of spent coffee grounds through phosphoric acid hydrolysis, and analyzed using multiple physical and chemical characterization techniques. In particular, a few crucial properties determined were aspect ratio of 12 ± 3, crystallinity of 74.2%, surface charge density of 48.4 ± 6.2 mmol/kg cellulose, and the ability to successfully reinforce PNCs, comparing well to other literature data and common commercial CNCs. Following extraction, CNCs/CNFs, as well as MNPs, were incorporated into various polymer matrices, including poly(ethylene glycol) diacrylate, sodium alginate, gelatin, and polyurethane, among others. Through solution casting and 3D bioprinting fabrication methods, as well as composition manipulation, CNCs/CNFs were able to reach ideal percolating networks within the PNCs for maximum mechanical reinforcement with minimal hindrance of the polymer matrix's natural properties. The various PNC hydrogel scaffolds successfully demonstrated tunability of their nanostructural, mechanical, hydration, and biodegradation properties, utilizing the benefits of manipulated composition, crosslinking density, and nanofiller orientation to increase versatility for tissue engineering constructs. Additionally, MNP incorporation was shown to successfully produce inductive heating responses to promote topographical shape memory effects, while invoking minute thermal dissipation into surrounding environments to reduce thermal shock to seeded biological components. The success of this work makes strides to overcome a few crucial disadvantages of current PNC biomaterial hydrogels, specifically their inability to regenerate biomimetic native tissues during wound healing.

Lay Summary

Polymer nanocomposites (PNCs) are a class of materials combining two components, a polymer matrix and embedded nanoparticles, to produce unique, tunable, and versatile characteristics. With the vast range of characteristics, these PNCs can be applied in multiple scientific and industrial fields, such as aerospace, automotive, electronics, and biomedical. The research performed in this dissertation provides a novel method for the extraction and utilization of cellulose nanomaterials from the otherwise useless agricultural waste product of spent coffee grounds, leading to lower landfill occupation. Additionally, the extracted cellulose nanomaterials, as well as magnetic nanoparticles, were incorporated into various polymer matrices to fabricate unique PNCs for biomedical applications. The fabricated PNCs showed enhanced mechanical properties, tunable cell growth alignment, and remote shape changes through induction heating. The results reported in this dissertation successfully demonstrate the remarkable property manipulation of unique PNCs through incorporation of different nanoparticles into various polymer matrices for biomedical applications.

Preface

This dissertation comprises of original, unpublished, independent work (Chapters 1, 2, and 7) by the author, Frost, B.A., as well as collaborative and published works (Chapters 3, 4, 5, and 6). The collaborative and published works are further detailed below:

Chapter 3 is based on work conducted at Virginia Polytechnic Institute and State University by Brody Frost and Dr. E. Johan Foster, and a version has been published. Frost, B.A., Foster, E.J. Isolation of Thermally Stable Cellulose Nanocrystals from Spent Coffee Grounds via Phosphoric Acid Hydrolysis. *J Renew Mater* **2020**, *8*(2), 187-203.

Chapter 4 is based on work conducted at Virginia Polytechnic Institute and State University by Brody Frost, Bradley P. Sutliff, Patrick Thayer, Dr. Michael J. Bortner, and Dr. E. Johan Foster, and a version has been published. Frost, B.A., Sutliff, B.P., Foster, E.J. et al. Gradient Poly(ethylene glycol) Diacrylate and Cellulose Nanocrystals Tissue Engineering Composite Scaffolds via Extrusion Bioprinting. *Front Bioeng Biotechnol.* **2019**, *7*, 280. The author Frost, B.A. was responsible for all ink and sample fabrication processes, all sample testing and characterization except for the rheology (conducted by Sutliff, B.P.), and writing most of the manuscript.

Chapter 5 includes work conducted at the University of Arkansas by Hayden Carlton, Ricardo Martinez, and Dr. David Huitink, and a version has been published. Frost, B.A., Carlton, H., Foster, E.J. et al. Controlled Shape Memory Effects of Magnetic Polymer Nanocomposites via Induction Heating. *Green Materials*. **2021**, *0*(0), 1-15. The author Frost, B.A. was responsible for all sample fabrication methods, all hydrogel testing and characterization, and writing the majority of the manuscript. The author Carlton, H. was responsible for the induction heating tests and characterization. Additionally, the work within this chapter has led to the production of a U.S. Patent application (63/181,785) for the novel approach towards inductively heated PNC systems for topographical changes.

Chapter 6 includes work conducted at the University of British Columbia by Brody Frost, Victoria French, and Dr. Johan Foster, with collaboration from Dr. Dirk Lange. The author Frost, B.A. received the following certifications required for animal model trials from the Animal Care Committee ethics board: ACUP_CCACFA_Jul2020st12Br18;

ACUP_IWRRM_Oct2020ost12Bro81; ACUP_IWRRR_Nov2020ost12Bro6; ACUP_RSCIPM_Nov2020ost12Bro6; ACUP_RSCIPR_Nov2020ost12Bro6; ACUP_RAR_Dec2020ost12Bro42; ACUP_RSX_Dec2020ost12Bro63.

Table of Contents

List of Tables

List of Figures

List of Abbreviations

2D	Two dimensional
2.5D	Two and a half dimensional
3D	Three dimensional
4D	Four dimensional
AFM	Atomic force microscopy
AM	Additive manufacturing
BCA	Bicinchoninic acid
BSA	Bovine serum albumin
$CaCl_2$	Calcium chloride
CAD	Computer-aided design
CNC	Cellulose nanocrystals
CNF	Cellulose nanofibrils
CNM	Cellulose nanomaterials
Cu-Ni	Copper nickel
diH_2O	Deionized water (18 MΩ)
DLS	Dynamic light scattering
DMA	Dynamic mechanical analysis
DMF	N,N'-dimethylformamide
DMSO	Dimethyl sulfoxide
DSC	Differential scanning calorimetry
ECM	Extracellular matrix
EDS	Energy-dispersive X-ray spectroscopy
FDA	Food and Drug Administration (US)
Fe-Co	Iron cobalt
Fe-Ni	Iron nickel
Fe-Pt	Iron platinum
Fe_3O_4 NP	Iron (III) oxide nanoparticles
FWHM	Full width at half maximum
$\dot{\gamma}$	Shear rate

GTA	Glutaraldehyde
HCl	Hydrochloric acid
h-CNC	Non-functionalized cellulose nanocrystals
H&E	Hematoxylin and eosin
IR	Infrared
K	Flow consistency index
LAP	Lithium phenyl-2,4,6-trimethylbenzoylphosphinate
M-G	Masson-Goldner
MNP	Magnetic nanoparticles
η	Viscosity
n	Flow behavior index
N-11	Polyamide 11 (Nylon-11)
NaCl	Sodium chloride
NaOH	Sodium hydroxide
NIH	National Institute of Health (US)
NP	Nanoparticles
PBS	Phosphated buffer saline
p-CNC	Phosphated cellulose nanocrystals
PEGDA	Poly(ethylene glycol) diacrylate
PLA	Poly($_{D,L}$-lactide)
PLM	Polarized light microscopy
PNC	Polymer nanocomposite
PU	Polyurethane
PVAc	Polyvinyl acetate
SA	Sodium alginate
s-CNC	Sulfated cellulose nanocrystals
SCW	Super/Subcritical water
SEM	Scanning electron microscopy
SLA	Stereolithography
SMP	Shape memory polymer

T_c	Crystallization temperature
$T_{d5\%}$	Onset of 5 wt% thermal degradation
TEM	Transmission electron microscopy
T_g	Glass transition temperature
TGA	Thermogravimetric analysis
THF	Tetrahydrofuran
TiO_2	Titanium dioxide
T_m	Melting temperature
TPU	Thermoplastic polyurethane
UTS	Ultimate tensile strength
UV	Ultraviolet
vol%	Volume percent
v/v	vol% to vol% ratio
wt%	Weight percent
w/w	wt% to wt% ratio
XPS	X-ray photoelectron spectroscopy
XRD	X-ray powder diffraction
ZnO	Zinc oxide

Acknowledgements

This dissertation comprises efforts of several individuals, without whom this work would never have been possible. Above all, I would like to deeply thank my research supervisor, Dr. E. Johan Foster, for his many years of mentoring and advising. Over the last six years of my academic career, transitioning from undergraduate studies to Masters to PhD, Dr. Foster has shown me continuous support, encouragement, patience, guidance, and confidence in my abilities, which I am eternally grateful. Through his masterful expertise as an advisor and freedom to pursue my specific interests, I have strengthened my knowledge and independence in research, to become an expert in biomaterials engineering. Lastly, with infinite gratitude, I would like to show appreciation to Dr. Foster for always being there to push me forward, for understanding when things got tough, and talking me through all of the ups and downs as I pursued my graduate studies.

Additionally, I would like to thank my committee members, Dr. Dirk Lange and Dr. Orlando Rojas, for their insight into my research and dissertation, as well as their assistance throughout my entire transition and academic career at UBC.

I would like to offer my appreciation to my lab group, Foster Advanced Materials Group, as well as my fellow researchers and co-authors, for all of their hard work and assistance over the years. I'm thankful for the opportunity to get to know and spend quality time with so many wonderful peers during my graduate studies, whom have helped me learn, grow, and become a much more diverse researcher.

I would like to thank the University of British Columbia and the Department of Chemical and Biological Engineering for accepting me in my final year of my PhD degree, as well as Kristi Chow for all of the help with the requirements for my specific admission conditions.

Finally, special thanks are owed to my family and my wife for all of their continuous support, encouragement, love, and faith in my abilities over the years, especially when things got tough and I started to struggle.

Chapter 1: Introduction

1.1 Introduction to Nanomaterials and Polymeric Nanocomposites

Polymeric nanocomposites (PNCs) have become increasingly popular in the last few decades due to their remarkable properties and application versatility.[1-2] As such, they have become redefined as their own class of materials, focusing on fundamental structure/property relationships, manufacturing techniques, and commercial applications.[1-2] Through enhanced knowledge of the complex interfacial interactions between nanoparticles and polymer matrices, as well as new nanomaterials being discovered regularly, the breadth of PNCs material class is ever expanding.[1-4] In addition, analysis and understanding of the intercalation process of various fillers and polymer matrices, allows for precise nanoparticle incorporation into PNCs without hindering the natural abilities of the polymer in which they are embedded.[1-3]

Utilizing different types of nanoparticles and polymer matrices, a multitude of uniquely tunable characteristics can be obtained, including mechanical reinforcement,[5-7] electrical conductivity,[8-9] smart materials,[4,10-12] air and water purification,[13-16] among others.[1-2,4,17-18] Furthermore, with the overwhelming advances of new PNC materials regularly, scientific and industrial limitations, as well as the gaps between them, are closing significantly.[10,17-18] For example, a range of industries, such as biomedical, aerospace, electronics, and automotive, are continuously investing large amounts of time and resources to find better alternatives for common commercial applications through innovative material research.[17-18]

Although there are countless nanoparticles used to enhance PNCs,[2,17-18] cellulosic nanomaterials (CNMs) and magnetic nanoparticles (MNPs) are some of the most widely researched due to their unique properties.[19-20] Most polymer systems are mechanically soft in nature and lack certain intrinsic capabilities, such as electrical conductivity, however, overcoming these deficiencies without significantly hindering the natural properties of the polymer itself has been a constant problem.[10,17-18] By using CNMs, including cellulose nanocrystals (CNCs) and cellulose nanofibrils (CNFs), inherently soft polymers can be mechanically reinforced to withstand forces well beyond their natural abilities. The incorporation of CNMs can also promote high degrees of hierarchical nanostructuration within PNCs through controlled orientation of their large aspect ratios.[19] Additionally, MNPs incorporated into certain polymers can produce “smart” PNCs that are not only electrically conductive, but also respond to magnetic fields during induction

heating. Specifically, the ability of polymers to cross between thermal transitions, in which the physical properties can be altered, allows for MNPs to promote shape memory effects through internal thermal fluctuations effects.[20] Utilization of these two unique nanoparticles have led to an influx of innovative PNCs for a variety of research and industrial applications.

1.2 Cellulosic Nanomaterials

As the most abundant natural polymer on earth, cellulose has received a high degree of interest as an impactful sustainable resource.[21] It is mainly found in plant cell walls, as well as a few organisms, and consists of a tightly packed linear structure generating high degrees of crystallinity and great physical strength for structural support.[22-23] Cellulose comprises of unbranched homopolysaccharide glucose molecules with 1-4 β linkages, as well as hydrogen bonding between the C2 and C6 hydroxyl groups, creating the formation of remarkably strong crystalline regions throughout the cellulose chains, shown in **Figure 1**.[22-24]

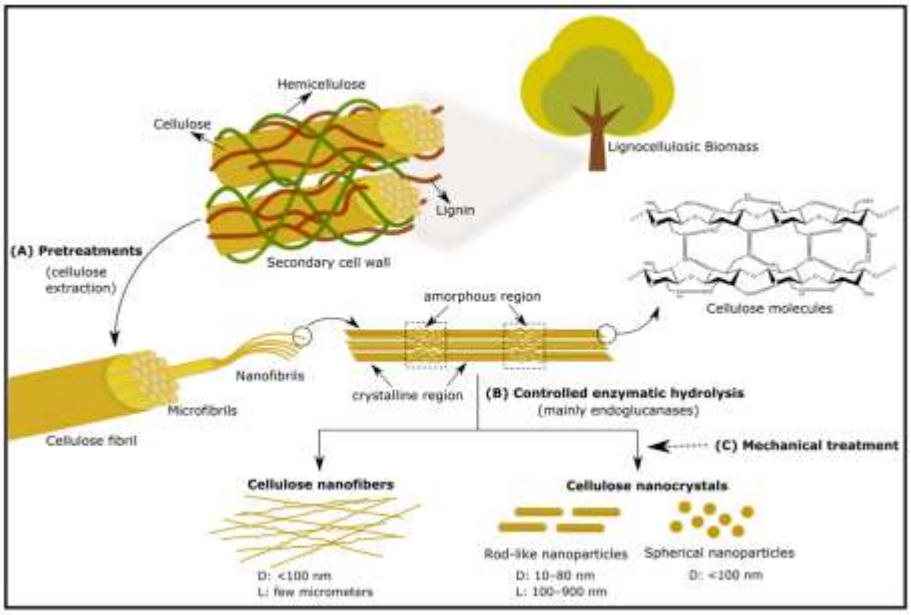

Figure 1.1 General schematic of cellulose nanomaterial extraction from natural and sustainable sources. Through various extraction methods, lignocellulosic biomass can be purified by removing lignin and hemicellulose to produce pure cellulose, and subsequent CNMs.[25] Reprinted with permission through the Creative Commons Attribution license for open access articles: Michelin, M. et al. *Molecules* 2020, *25* (15), 3411.

Although cellulose is a useful resource in and of itself, it can be further broken down into several components for increased applicability.[25] Through various extraction methods, CNMs can be isolated from multiple cellulose sources, characterized, and incorporated into a vast range of

polymer matrices for improved PNC properties.[24-25] Specifically, is the ability of the CNMs to drastically improve the mechanical properties and structural integrity of PNCs, as well as introducing nanostructuration through percolated networks.[20,26] Additionally, through manipulation of the aspect ratio and surface functionalization of the CNMs, specific properties such as thermal resistance, solvent dispersibility, mechanical reinforcement, enhanced barrier properties, and filtration efficiency can be finely-tuned for adaptation into various industries and applications.[20,26]

1.2.1 Sources and Abundance of Cellulose

Cellulose is widely-regarded as the most abundant biopolymer in the world, with roughly 10^{10} to 10^{11} tons synthesized and destroyed annually.[21,25] A multitude of CNM sources, including those from plant biomass,[26-32] agricultural waste products,[33-38] bacteria,[39-42] and tunicates.[43-44]

Plant biomass and agricultural wastes comprise the majority of cellulose sources, specifically trees and stalk-like plants, and is directly related to their physical strength and stiffness through support in the cell walls.[26-38] Cellulose is naturally synthesized and develops functionality, flexibility, and high specific strength through its hierarchical structure within cell walls.[26-28] Plant cell walls are comprised of two-part structures with a common fiber-composite organization, similar to that of animal ECMs and reinforced concrete.[28,32] Within the overall structure, the most important component of the primary cell wall is the fiberglass-like structure of bundled highly-ordered crystalline cellulose microfibrils that develops to enhance structural integrity as the plant cells mature.[27-29] Since no two plant species are the same, the biological components that make up each vary significantly from species to species. For example, softwood and hardwood trees, such as pine, cedar, spruce, oak, and beech, contain roughly 40-50% cellulose, while fibrous plants, such as cotton, hemp, and flax, can contain between 30-75% cellulose, all with varying degrees of polymerization between 10,000-15,000, depending on the species.[25-26,30] Not only does the specific plant species impact the quantity and quality of cellulose produced, but the quality of nutrient composition found in the soil and surrounding environment in which they grow also play a large role.[28,32-33] The organic materials and water content found in the soil, as well as the available sunlight, temperature, and humidity where the plants grow, directly correlate to the content and structuration of the cellulose, ranging from cellulose type I_α, I_β, II, III_I, III_{II}, IV_I, and IV_{II}.[25,28,33] Cellulose I_α and I_β are the two main native allomorphs that create the stable structure throughout

the plants walls, running in parallel and antiparallel chain packing directions, respectively.[25,28,31,33] The next most common allomorph is cellulose II, which is typically formed through industrial alkaline treatment processes needed to purify cellulose sources.[25] Through further ammonia treatment of cellulose I and II, cellulose III_I and III_{II} can be obtained which can be characterized as the more disordered phases of cellulose.[25,28,33] Lastly, cellulose IV_I and IV_{II} are typically prepared through heat treatment of cellulose III_I and III_{II} in glycerol.[25] However, cellulose III_I, III_{II}, IV_I, and IV_{II} can be reverted back to their original allomorphs of cellulose I and II through high temperatures and water-saturated environments.[25,28,31]

Due to the ease of extraction, large amounts of established protocols, and high crystalline cellulose content, wood, cotton, and other fibrous plants have been the main source of cellulose for industrial processes and CNM production, specifically in the pulp, paper, and textile industries.[26,28,30-32] However, agricultural waste and residue are starting to become more widely accepted as new sources of cellulose, with subsequent extraction methods being discovered regularly.[33-38] As landfill occupation continues to increase at alarming rates, large amounts of research are being conducted on methods to reduce disposal of materials that can be either recycled or reused.[34-35] Since roughly 75% of available landfill area is occupied by the nearly $3.7x10^9$ tons agricultural waste products disposed of annually, establishing renewable methods to reduce the quantities of waste is essential.[35-38] Therefore, CNM extraction from otherwise useless agricultural waste and residue has been heavily researched to confront this growing demand.[35,37-38] For example, CNM extraction and isolation studies have been performed on cereals (maize, wheat, etc.),[32,34-35] rice husks,[25,31] soy bean hulls,[34-36] sugarcane bagasse,[25,32,36] and bamboo,[32,37] among many others,[25,31-38] as progression towards mitigating the enormous waste occupation in landfills. As well, similar to the commonly used plant biomass, the variances in sources and agricultural processing lead to variances in cellulose structuration and subsequently isolated CNM properties.[25]

Along with plant biomass and agricultural wastes, cellulose can be produced and extracted from a few organisms, including bacteria and tunicates.[32,39-44] The Gram negative bacteria *Acetobacter xylinum* has been the most extensively researched, among *Gluconacetobacter xylinum*, *Rhizobium*, *Komagataeibacter xylinus*, and *Agrobacterium*, for their high purity (>90 %) cellulose I and II ribbon formations without the extra lignin, hemicellulose, pectin, and other

biological components, demonstrating a few improved characteristics over plant-sourced cellulose.[32,39-42] A few superior properties include largest aspect ratios, higher crystallinity and degree of polymerization, naturally developed ultrafine fiber shapes, non-cytotoxic, and enhanced water-holding capabilities (up to 99 % water).[29,32,39-42] However, the overall production process is very expensive and slow to synthesize, making it more suitable for small research projects and limited in industrial uses.[39-42] As the only known animal source of cellulose, another extensively research organism is the tunicate, which utilizes the relatively pure, high crystalline and aspect ratio cellulose in their "tunic" for protection when approached by predators.[32,43-44] The cellulose in tunicates lend structural and mechanical stability through hydrogen bonding of CNMs within the outer-walls, however, they are able to severe these hydrogen bonds to return to an initial relaxed and flexible state.[43-44] The cellulose extracted from tunicates share characteristics similar to bacterial cellulose, in which purity, aspects ratios, crystallinity, and degree of polymerization are higher than plant-based sources, although not quite at the same level.[32,43-44] However, tunicates are relatively easy to source, lending greater applicability for industrial processing, rather than for specific research purposes, giving them a leg up on other cellulose sources.[43-44]

1.2.2 Extraction Methods of Cellulose Nanomaterials

In addition to cellulose, most commonly used sources comprise of other biopolymer components, which need to be removed during CNM extraction.[25-26] Various extraction methods, such as acid hydrolysis, mechanical milling, subcritical water (SCW), and enzymatic hydrolysis are used to isolate the crystalline regions of cellulose by breaking down the weaker, disordered amorphous regions.[45-58] Each technique has its advantages and disadvantages, lending uniqueness to all of the subsequently produced CNMs with regards to chemical composition, physical properties, and morphology, among other characteristics.[45-58]

1.2.2.1 Chemical Extraction

The most commonly used method of CNM extraction is acid hydrolysis, which utilizes concentrated acids to breakdown the amorphous region of cellulose, resulting in the isolation of the tightly packed crystalline regions, depicted in **Figure 2**.[45-49]

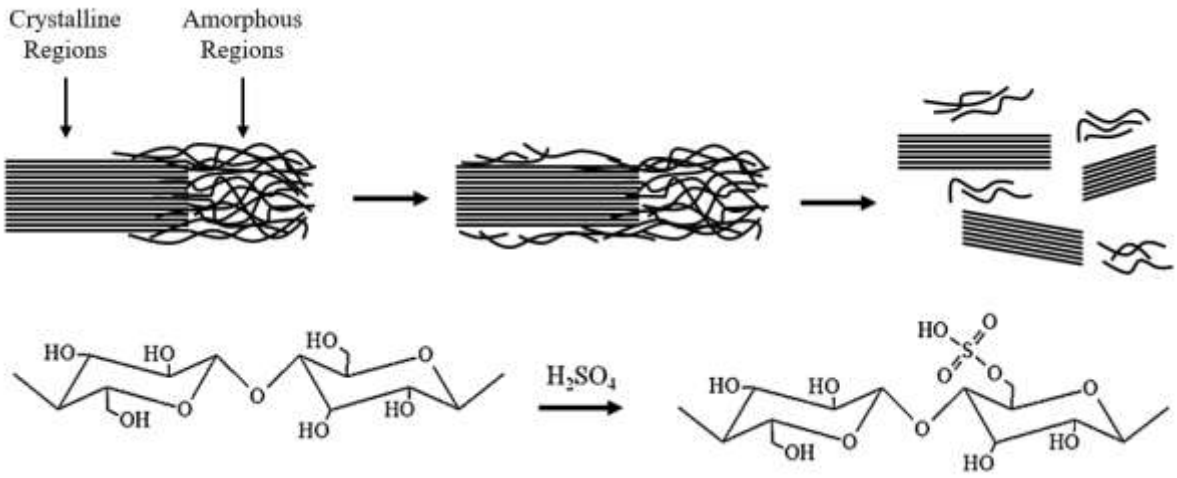

Figure 1.2 General schematic depicting the process of acid hydrolysis, in which the amorphous regions are hydrolyzed to extract isolated crystalline regions (CNMs) with various functional groups. Specifically depicted above is the use of sulfuric acid to produce CNMs esterified with sulfate functional groups.[59]

Since cellulose sources vary depending on species and habitats, as mentioned previously, the structural distribution of crystalline and amorphous cellulosic components vary drastically as well.[47] Therefore, one of the most significant benefits is the manipulation, adaptation, and adoption of various acid hydrolysis procedures for industrial and commercial production, due to ease of use, scalability, and widely established protocols.[45-49] The typical acid hydrolysis procedures include highly-concentrated acid solutions, reacting under strong agitation for 60 to 120 mins at temperatures ranging from 60 to 100 °C to break down cellulose fibers into CNFs and CNCs, depending on the desired nanoscale and crystallinity.[45-46] Sulfuric acid hydrolysis has been the most heavily researched and established, due to its reactive strength and subsequent hydroxyl group esterification by functional sulfate groups.[45-46,59] This particular acid is popular since it is able to strongly isolate CNMs, while requiring lower concentrations to hydrolyze the disordered cellulose regions when compared to its counterparts.[45-48] Along with sulfuric acid, a few other lesser studied acids, including hydrochloric acid, phosphoric acid, and acid mixtures, have been investigated due to the variety of characteristics obtained through each unique process.[45-46] Hydrochloric acid and phosphoric acids have been studied for their ability to produce CNMs with different surface functionalization, further discussed in *Section 1.2.3*. Specifically, hydrochloric acid shows the ability to produce unmodified CNMs, suitable for essential modifications, while phosphoric acid produces CNMs with higher thermal stability and biocompatibility.[46,48-49] Lastly,

other acid combinations, including acetic acid and nitric acid mixtures, have been studied to determine any variations in characteristics.[46] Unlike other acids, in concentration ratios of 10:1 v/v nitric to acetic acid, hydrolysis of the amorphous cellulose regions results in uniquely shaped spherical particles with diameters from 6 to 20 nm with no apparent surface charges.[46] While acid hydrolysis is regarded as the ideal extraction method for CNMs, the overall process leads to large quantities of chemical waste needing to be recycled or disposed, making it less environmentally friendly than more recently developed methods.[45,50-56] For example, after successful acid hydrolysis, the resulting CNM suspension still requires centrifugation to decant the supernatant, multiple day dialysis to reduce the pH, and lyophilization to completely isolate the CNMs.[45-46] Therefore, methods developed to omit these extra post-processing steps have been increasingly researched, including mechanical milling, SCW hydrolysis, and enzymatic hydrolysis.[50-58]

1.2.2.2 Mechanical and High Energy Extraction

As materials science progresses towards a more sustainable and renewable direction, greener and more environmentally friendly methods of processing raw cellulose materials into CNMs are being developed, including mechanical milling[50-52] and SCW hydrolysis.[53-56] Mechanical milling involves aggressive impact velocities, pressures, and shear forces to break apart the disordered amorphous regions through high energy cleaving of the cellulose fibers along the longitudinal axis, subsequently forming CNFs and CNCs.[45,50-52] To accomplish these high energy forces, a few methods have been established, including high energy ball milling, planetary milling, high pressure homogenization, and ultrasonification.[45,50-52] High energy ball milling and planetary milling utilizes stainless steel, titanium, or ceramic balls and high velocity movements to generate enormous impact, cleaving cellulose fibrils through force.[45,50] Although not as effective as traditional isolation methods, it stands as the most simple, time-conserving, and cost-effective "green" extraction method compared to its counterparts.[45,50-52] High pressure homogenization exerts intense pressures and shear forces into a cellulose slurry by passing it into a vessel at high velocities, typically used to cleave cellulose microfibrils into further nanostructured particles.[45,51] Slightly different from the other mechanical methods, ultrasonification uses the process of defibrillating cellulose into CNMs through hydrodynamic forces produced by ultrasound.[52] When submerged, ultrasonic waves create mechanical oscillation within the liquid, resulting in formation, expansion, and implosion of microscopic gas bubbles through ultrasonic energy

absorption.[45,52] Though these methods are effective in isolating CNMs, compared to their acid hydrolysis counterparts, mechanical milling tends to produce CNMs with lower crystallinity and thermal stability, due to the remaining amorphous regions not completely removed.[45,50,52]

Over the last decade, the use of sub/supercritical water as an effective solvent, catalyst, and reactant for hydrolytic conversions and extractions of organic compounds has received increased interest through a number of successful studies.[53-56] SCW hydrolysis is the process of simultaneously heating water between 320 to 350 °C, while pressurizing to 25 MPa in a closed vessel, in order to extract organic materials through higher diffusion, activity, and ionization of water, while reducing the accompanied pyrolysis associated with sub/supercritical temperatures, diagramed in **Figure 3**.[53-56]

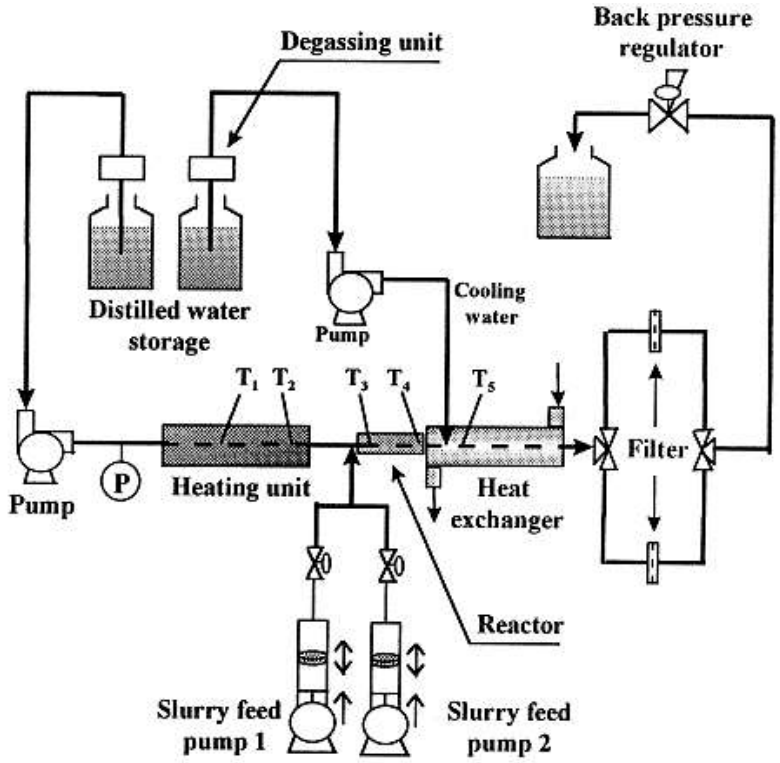

Figure 1.3 Image depicting the a generic SCW reactor setup for organic material extraction, specifically CNM extraction.[53] Reprinted with permission from Elsevier: Sasaki, M. et al. *The Journal of Supercritical Fluids* 1998, *13* (1), 261-268.

Recent literature has shown that CNM extraction using SCW conditions on cellulose slurries leads to lower corrosion, lower and cleaner effluent, and lower cost of reagents, however, the extraction results of CNMs are limited to purified cellulose sources and small scale

reactions.[53,56] Additionally, SCW as a pretreatment has been shown to remove non-cellulosic components to a greater degree than previously established alkali bleaching procedures.[53,56] Unfortunately, SCW hydrolysis requires enormous amounts of energy to promote an ionization level high enough to breakdown the disordered amorphous cellulose regions, currently making it hard to scale to industrial applicability.[53-54]

1.2.2.3 Biological Extraction

Enzymatic hydrolysis is a biological process that uses enzymes, such as laccase and cellulase, for the digestion and modification of cellulose fibers.[45,57-58] It involves the depolymerization of amorphous cellulose, as well as any residual hemicellulose, while reducing the environmental impact from high water demand and chemical waste disposal.[45,57-58] However, the process involves three arduous steps and mild conditions.[57] The first and second steps are relatively quick, hydrolyzing roughly 60 to 70 % of the cellulose, yet completion of hydrolysis during the third step remains incredibly time consuming, leading to long operation times.[45,57] Although the CNMs produced by enzymatic hydrolysis tend to have increased crystallinity, aspect ratios, and thermal stability, due to these significant time demands and overall expense, this process still remains in its infantile stages, employed solely for small research applications.[57-58] Another downside of CNMs produced through enzymatic hydrolysis involves a tendency to show a higher tendency to agglomerate with lower stability in aqueous suspension.[57]

1.2.3 Surface Modification and Functionalization

As previously mentioned, a multitude of different methods can be used to hydrolyze cellulose, creating different surface functionalization on the CNMs with varying chemical and physical properties.[45-49,60-64] The most common functionalization method involves acid hydrolysis through a particularly chosen acid, in which no additional steps are required, therefore, common surface modifications include acetate, sulfate, phosphate, hydroxyl, and carboxyl groups.[60-64] However, additional CNM modification can be made post-processing, including TEMPO, acetate, and succinic anhydride esterification, among others.[60-62] These functional groups not only change the chemical structure of the CNMs, but the physical, morphological, optical, and thermal properties as well, further discussed below in *Section 1.2.4*.[60-64]

1.2.4 Characterization (Physical, Chemical, Thermal, and Optical)

In order to completely characterize the physical, chemical, and optical properties of CNMs, countless equipment and techniques have been employed, including SEM, TEM, AFM, DLS, ssNMR, XRD, DMA, rheology, Raman spectroscopy, EDS, XPS, CHNS-EA, FTIR, conductometric titration, zeta potential, SIMS, TGA, DSC, PLM, UV-vis, and turbidity, among many others, as reviewed by Foster et al.[65-69] Utilizing these characterization techniques along with the vast range of extraction, isolation, and modification methods, CNMs can be thoroughly examined for a range of manipulative properties.[65-69]

Physical, morphological, and mechanical properties of CNMs are typically analyzed through electron microscopy, mechanical testing, and a few spectroscopic techniques, including SEM, TEM, AFM, DLS, ssNMR, XRD, DMA, rheology, and Raman spectroscopy.[65-67] Macroscopic morphological properties can be observed through various imaging techniques, including SEM, TEM, AFM, and DLS. SEM and TEM bombard CNMs with focused beams of accelerated electrons inside of a vacuum, while capturing the various reflected (SEM) and transmitted (TEM) particles to generate highly magnified, nanoscale images.[65] AFM involves running a nano-sized probe across the surface of prepared CNM films, while measuring the reflected movements. Through these precise measurements of amplitude, phase, deflection, and modulus from the force applied to the needle running across the rough surface, particle size and dispersion can be delicately analyzed [65-66] DLS utilizes light scattering techniques in dilute aqueous suspensions to measure time-dependent fluctuations in scattered light intensities and determine the hydrodynamic "apparent particle size".[65] All of these techniques focus on the macroscopic properties of the CNMs, including overall shape, length, width, and aspect ratios.[65] Their structures consist of rod-like shapes ranging from 100 nm – 10 μm in length, 5 nm – 100 nm in width, and aspect ratios of up to 200, depending on the type of CNM (i.e. CNCs, CNFs, MFCs, etc.).[32,45,65]

On the micro and nanoscopic scale, morphology and crystallinity are characterized through ssNMR and XRD, including analysis of atomic structure, micro-/nano-morphology, allomorphs, amorphous contributions, phase structure, bulk crystallinity, crystallite size, and internal structure order.[65-67] SsNMR uses combined techniques of cross-polarization, magic angle spinning, and dipolar decoupling devices to measure the distance between two select labeled heteronuclei, while XRD employs a CuX_{α} X-ray tube, diffracted beam graphite monochromator, and NaI scintillation

detector to measure diffraction patterns and peak intensities of the crystalline cellulose.[65-67] However, compared to XRD, ssNMR shows greater relevancy and resolution, with abilities to measure direct relations between the crystalline indices, the dimensions of the crystals, the presence of relatively large amorphous phases, and indicate crystalline index values for a given system, providing the morphology of the CNMs.[65-67] Crystallinity can range drastically from 40 – 100 %, with various allomorphs (Cellulose I, II, III_I, III_{II}, IV_I, and IV_{II}) and internal structure order, such as helical, triclinic, and monoclinic metastable structuration, depending on the source and extraction method of CNMs.[25,45,65-67]

Lastly, mechanical and viscoelastic properties are commonly characterized through AFM, DMA, rheology, and Raman spectroscopy.[45,65-69] Through these various techniques, crucial properties, such as tensile, bulk, and flexural strengths and moduli, viscoelastic properties of gels, flow behavior, microstructure formation, particle interactions, suspension viscosities, and stiffness of molecular backbone, have been thoroughly studied.[65-68] Due to their remarkably high crystallinity and tightly packed, hydrogen bonded structure, CNMs demonstrate incredible strength to weight ratios, with elastic moduli up to 220 GPa, ultimate tensile strengths up to 10 GPa, and a low density of roughly 1.6 g/cm^3.[32,45,65-67] In comparison, these properties make CNMs stronger and stiffer than Kevlar fibers, and strength to weight ratio around 8 times higher than stainless steel.[45,66-67] However, their high stiffness also leads to exceedingly low flexibility, with elongation to ruptures typically less than 8 %.[32,65-68]

Through the extraction, isolation, and modification methods described above, CNMs can vary significantly with regards to chemical properties and composition. To determine these variances, chemical and elemental analyses, including EDS, XPS, CHNS-EA, FTIR, conductometric titration, zeta potential, and SIMS, have been employed.[65-66,68-69] The chemical structure of CNMs consist of carbon, hydrogen, and oxygen atoms that form glucose molecules, therefore, when additional elements are present through surface modifications, they can be easily detected.[65,68] EDS and XPS utilizes high-energy beams of charged particles or x-rays to irradiate the surface of the material, energizing the core shell electrons enough to escape from their atoms to become photoelectrons.[65-66] Each core shell electron has a specifically defined energy associated with it, therefore, by measuring the energy of the photoelectrons, the chemical compositions of the materials can be analyzed.[65] Additionally, CHNS-EA and SIMS are used to determine major

elemental compositions of organic substances through combustion and ion-sputtering, respectively, followed by filtration and detection of specific elements.[65-66] FTIR, ssNMR, conductometric titration, and zeta potential, on the other hand, are employed to analyze the specific surface functionalization with regards to charge density and chemical bonds.[65,68-69] The surface functionalization and charge density of the CNMs are crucial when determining their colloidal stability in a variety of solvents.[65] The greater the electrostatic repulsion through increased substituent contents (up to 26 mmol/kg cellulose) and associated surface charge densities (up to 330 mmol/kg cellulose), the greater the stability in suspensions.[68-69] As well, the analyzed surface adsorption, covalent bonding, and surface chemistry, are necessary to determine the dispersive properties within various polymer matrices and cellular interactions *in vivo*.[65,68-69]

Although not as significant as the physical and chemical analyses, with regards to complete characterization, as well as industrial applicability, thermal and optical properties also need to be characterized.[65-66,68-70] Thermal properties are analyzed through TGA and DSC to determine degradation temperatures and any thermal transitions, relative to industrial processing techniques.[65] Their high thermal stability typically ranges between 200 – 350 °C with minimal thermal expansion coefficient around 0.01 ppm/K, depending on the crystallinity, size, and surface functionalization/modifications, while demonstrating no apparent thermal transitions.[45,68-69] Lastly, optical properties are analyzed through PLM, UV-vis, and optical microscopy, to determine turbidity and agglomeration in suspensions, visible light transmittance, and CNM network alignment in nanocomposite samples.[65-66,70] PLM shows shear birefringence through polarized lenses for alignment analysis in PNCs, and UV-vis and turbidity for observing absorption and reflection of light over a range of wavelengths (300 nm to 800 nm).[65,70] A few demonstrated properties are high visible light transmittance over 90 %, opalescent appearance when formed into a film, and increased opaqueness with increased suspension concentrations.[45,65,70]

1.3 Cellulose Nanocomposites

CNMs have been well explored in the past few decades, with ever increasing methods of isolation and applications. As such, it has been studied as a renewable substitute for countless raw polymers and as a nanofiller for improved PNC applications, including better colloidal stabilities, mechanical reinforcement,[71-76] enhanced barrier properties,[77-79] energy storage,[80-81] flexible electronics,[80-81] and tunable hydrophilicity/hydrophobicity,[82-83] among many others.[29,45,66] Their

many unique properties allow for usage in a variety of applications, but are most known for their incredible strength to weight ratio for reinforcing nanocomposites, sustainability, and impact on environmentally friendly and biodegradable solutions.[45,71-76] Through bolstering unique properties of PNCs, CNMs have been further employed in multiple industries, including aerospace, automotive, biomedical, electronics, water waste/pollution management, and construction, among countless others.[45,66,71-74]

1.3.1 Mechanical Reinforcement

Due to their natural rod-like shape, high aspect ratios, and incredibly high crystallinity, stiffness, and strength to weight ratio, CNMs have been incorporated into a variety of PNCs for substantial mechanical reinforcement.[45,71-76] However, in order to maximize the reinforcement properties, the polarity of CNMs through high electrostatic repulsion is also significant for ideal dispersion among the polymer matrices. Their enhanced ability to disperse in a multitude of polymers allows for an exfoliated nanocomposite structure, rather than phase separated or intercalated composites, in which an ideal percolation threshold can be achieved.[75-76] Exfoliated structures imply a complete dispersion with almost 100 % filler-matrix interactions, while intercalated and phase separated structures imply a combination of filler-matrix interactions with significant filler-filler interactions, observed in **Figure 4**.[76]

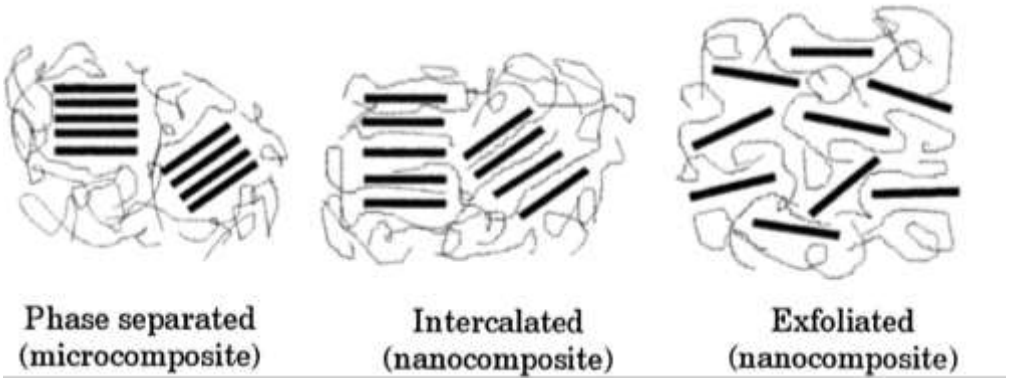

Figure 1.4 Examples of possible dispersion mechanisms of CNMs in polymer matrices, with subsequently formed PNC morphologies.[76] Reprinted with permission from Elsevier: Miao, C. et al. *Current Opinion in Solid State and Materials Science* 2019, *23* (4), 100761.

With increasing filler-filler interactions in the PNCs, a larger quantity of defects typically occur through agglomerations acting as stress concentrators.[76] For example, studies by Meesorn et al.[75] and Miao et al.,[76] have proven the significance of PNC mechanical reinforcement, given the

high electrostatic repulsion, large aspect ratios, and strong hydrogen bonding of the CNMs, allowing for an ideal percolation threshold to be reached with lower filler content, in order to retain the natural elasticity and durability of the polymer matrix, while still promoting greatly enhanced mechanical reinforcement.[73,75-76] Additionally, CNMs have been shown to act as effective nucleating agents, improving crosslinking capacities and densities of curable polymer resins, further bolstering their mechanical reinforcement applicability among a variety of polymer matrices.[73,76]

1.3.2 Enhanced Barrier Properties

Similar to mechanical reinforcement, CNMs incorporated into PNCs utilize large aspects ratios and high electrostatic repulsion to enhance barrier properties for both air and water films and filtration, to improve emissions, packaging shelf life, and fresh water quality, among others.[45,71-73,77-79] The presence of non-permeable CNMs dispersed in an exfoliated structure significantly increases the permeant tortuosity and overall path length, greatly reducing the permeability of gases, specifically water vapor and oxygen, depicted in **Figure 5**.[72-73]

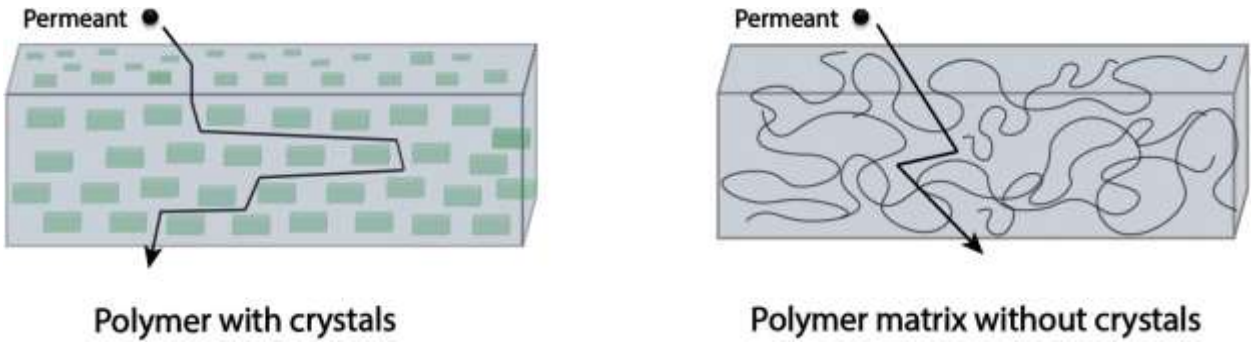

Figure 1.5 Images depicting the presence of non-permeable crystals (CNMs) in a polymer matrix (left**) for increased permeant tortuosity and path length to enhance barrier properties against water vapor and oxygen compared to an amorphous polymer matrix (**right**).[72] Reprinted with permission from Elsevier: Calvino, C. et al. *Progress in Polymer Science* 2020, *103*, 101221.**

Studies performed by Karkhanis et al.[77] and Khan et al.,[79] have shown that CNMs incorporated, even at small quantities (1-5 wt%), can reduce water vapor and oxygen permeability by 30-40 % and 65-75 %, respectively.[77,79] This significant reduction in both water vapor and oxygen permeability has vast applicability for industrial products, such as packaging and coatings. For example, PNC films created using CNMs show decreased deteriorative reactions and microbial growth when used for food packaging, while also promoting flavor entrapment, aroma barrier, and

grease and oil resistance.[77] In addition to enhanced barrier capabilities for water vapor and oxygen, surface modifications of CNMs can benefit filtration membranes through improving specific ion exchange.[78-79] Membranes use a variety of filtration methods, including osmosis, high-efficient ultrafiltration, heavy metal binding, and electrostatic interactions, all of which produce highly pure air and water void of impurities.[78-80] A study by Chakrabarty et al. shows the benefits of PNC films using CNFs modified with hydroxyl groups reacted with polyglycidyl methacrylate to produce cation-exchanging membranes for increased cadmium binding capacity, for water filtration of heavy metals.[78] Another study by Gopakumar et al. shows the ability of CNM membranes to successfully filter heavy metals, microbes, dyes, pesticides, and organic contaminants, through CNMs with hydrophobic functionalities, such as silyl groups.[80]

1.3.3 Other Properties

Along with the most notable abilities of mechanical reinforcement and enhanced barrier properties, energy storage,[74,81-82] flexible electronics,[74,81-82] hydrophilicity/hydrophobicity,[83-84] and cellular adhesion and adsorption,[85-87] have also been researched for further sustainable PNC applications. CNMs have been studied as a promising candidate for flexible energy storage and electronic devices through electrodes on cellulose, such as metal oxides, graphene, carbon nanotubes, metal nanowires, and a few conducting polymers.[74] By utilizing liquid electrolytes in combination with the structural advantage of CNMs, ionic species can traverse between these electrode surfaces at room temperature, leading to applications for Li-ion batteries with high electrical ionic conductivity approaching 10^3 S/cm.[74,81-82] As for flexible electronics, CNMs have shown great potential as a green and renewable advanced electrochemical energy conversion and conservation devices, such as solar cells, piezoelectric materials, and supercapacitors.[81-82] Utilizing CNMs as a reinforcing agent within these devices, attributes including power conversion efficiency and piezoelectric performance, can be significantly enhanced.[81]

Similar to the effects necessary for enhance barrier properties, CNMs with varying surface functionalization and modifications can induce hydrophilicity or hydrophobicity into the PNCs in which they are dispersed.[83-84] With the abundance of hydroxyl groups found on their surface, CNMs demonstrate naturally high degrees of intrinsic hydrophilicity.[83] However, certain industries and applications, such as packaging and electronics, view hydrophilicity as a deterrent, in which moisture causes detrimental effects, thus limiting CNM applicability. Therefore, to

combat these limitations, studies by Panchal et al.[83] and Farnia et al.[84] have shown incorporation of CNMs with different surface functionalization (i.e. fluorinated, sulfated, hydroxylated, carboxylated, etc.) into various polymers, successfully fabricate PNCs with tunable hydrophilicity and hydrophobicity.

Lastly, CNMs have shown the capability of promoting cellular adhesion and adsorption, further discussed in *Section 1.6*.[85-87] Through tunable mechanical reinforcement, inherent hydrophilicity, and various surface modifications, incorporation of CNMs into biocompatible polymer matrices have proven to increase biomimicry of native ECMs.[85-87]

1.4 Magnetic Nanoparticles

Unlike CNMs, MNPs are less complex with regards to sourcing, production, and properties, however, are still equally as useful among PNCs for enhancing applicability and stimuli-responsive behavior.[20,88-91] MNPs are typically produced through grinding bulk materials, however, this method of fabrication technically leads to irregular particle shapes. To combat this challenge, more technical methods to synthesize uniform spherical shapes have been developed, including plasma atomization, wet chemistry, and deposition from gas phases and aerosols.[20,88,90] Although there are a few types of MNPs, including iron-based, nickel-based, and cobalt-based, magnetite nanoparticles (Fe_3O_4 NPs) are the most common due to their ease of use through extensive literature references, as well as remarkable known magnetic capabilities.[20,88-91] In addition, nickel and cobalt are susceptible to oxidation and prove to be toxic, making their applications limited.[88] Through incorporation of these MNPs and subjection to applied magnetic fields, PNCs can exhibit a variety of magnetic effects, including paramagnetism, diamagnetism, ferromagnetism, antiferromagnetism, and ferrimagnetism, depending on the desired application.[20,90] Additionally, MNPs promote high levels of electrical conductivity within otherwise electrically resistant polymers, producing PNCs with the capability of carrying an electrical current through electron transference.[20,88,90-91]

1.5 MNPs for PNC Smart Materials

With the abilities of MNPs to promote stimuli-responsive behaviors in PNCs, a multitude of smart materials, including SMPs, have been researched and fabricated for employment in a variety of applications.[20,88-99] Specifically, are the notable capabilities to promote magnetic, thermal, and electrically conductive properties in otherwise inert polymer matrices through both

direct and indirect stimulation. As well, by exploiting the remarkable surface-to-volume ratios of MNPs, significantly less filler quantity is required to obtain these stimuli-responsive behaviors.[88-99] Through implementation of electrical currents and/or magnetic fields, PNCs embedded with MNPs demonstrate 2.5D and 4D hierarchical manipulation, promoting shape memory effects through thermal responses.[92-94] In order to activate shape memory effects, SMPs need to pass a certain thermal transition temperature (T_g), switching between an externally strained and relaxed state.[92,94,97] This can be achieved using induction heating methods, which involves intense magnetic fields activating MNP's ability to transform electromagnetic energy into heat, and dissipating it into the surrounding environment.[93] With uniform MNP dispersion and specific magnetic field strengths, induction heating has the capability to promote fast and selective site heating, without the need for hot liquids or gaseous mediums, among other direct contact methods.[92-93]

Utilization of these stimuli-responsive PNCs with induction heating capabilities have shown great potential in a variety of fields, including nanotechnology, biochemistry, organic and physical chemistry, and materials science.[97-98] Studies performed by Mohr et al.[92] and Bayerl et al.[97] have employed MNPs into polyurethane, biodegradable multiblock copolymer, high density polyethylene, and polyamide 6, to produce magnetically activated PNCs. Utilizing alternating magnetic fields (f = 258, 430, and 2500 kHz; H = 30 kA/m) on these cold-drawn PNCs, in which residual stresses are captured through cooling under constant strain, drastic shape memory effects can be exploited.[92,97] Additionally, a few other literature reviews of stimuli-responsive polymers by Bayerl et al.,[93] Stuart et al.,[95] and Roy et al.[96] have consolidated the remarkable progress of induction heating methods for shape memory activation, showing the versatility of MNPs use in a multitude of polymer matrices and composite structures (i.e. fibers, fabrics, 3D constructs, etc.). Through careful analysis of MNP morphology and their interactions with the surrounding polymer matrices and magnetic fields, electromagnetic responses can be finely tuned for various degrees of thermal effects and applications.[93,95-96] Specifically, biomedical applications, such as biosensors, drug delivery, diagnostics, tissue engineering scaffolds, "smart" optical systems, and actuating mechanisms for muscle tissue mimicry, are some of the most widely researched with regards to induction heating through MNP incorporation, further detailed in *Section 1.6*.[95-96,108-112]

1.6 CNM and MNP Polymer Nanocomposites for Tissue Engineering Applications

In particular, tissue engineering applications utilizing CNMs and MNPs have been rapidly rising due to their versatility, biocompatibility, and stimuli responsiveness.[32,45,68,85-91,98-112] As previously discussed, CNMs demonstrate a vast range of physical and chemical properties through different extraction methods and surface modifications.[32,45,68] These unique properties allow for the fabrication of bio-based scaffolds for tissue engineering, wound healing, drug delivery, and regenerative medicine approaches, while promoting sustainability and natural biocompatibility.[32,45] A plethora primary literature reviews, including those performed by Hickey et al.,[86] Amalraj et al.,[100] Lin et al.,[101] Dutta et al.,[105] and Joseph et al.,[107] have showed tremendous adaptation of CNMs for biomedical applications. Natural ECMs not only allow for cell attachment, but provides biochemical and biophysical cues for cell and tissue maturation and proliferation as well.[86] Through incorporation with other biocompatible polymer matrices, CNMs have the potential to increase nutrient, cell, protein, and other bioactive adsorption, leading to improved ECM structuration and overall tissue growth.[100-101] Additionally, the biochemistry obtained through various CNM modifications and surrounding environments have significant effects of cell differentiation, morphology, adhesion, maturation, proliferation, and subsequent overall viability.[86-87] For example, CNMs functionalized with negatively charged anionic groups, specifically phosphate groups, have shown an increased ability to promote cellular adhesion, proliferation, and viability.[85,87]

Another key component for tissue biomimicry is the ability to form cohesive 3D scaffold constructs, with controlled hierarchical nanostructuration for enhanced ECM generation.[85,100-107] It is imperative for future regenerative techniques to not only possess an increased rate of wound healing, but also intricate structuration, integration, and aftermath of tissue regeneration for optimal retainment of native physiological functionality.[100-107] With the incorporation of CNM networks into biocompatible PNCs, 3D-oriented nanostructuration can be achieved and utilized as a critical design criteria for the success of future tissue engineering and regenerative medicine techniques.[85,102,104] Exploiting both biomimetic materials and embedded biological components, along with CNM nanostructured CNM networks, cohesive biomaterial composites and tissue interactions and integration can be obtained to better mimic natural tissue ECM.[85,104-106] For example, a study by Espinosa et al.[85] utilizes PLA as an amorphous polymer matrix seeded with

CNMs to produce a multilayer nanocomposite scaffolds mimicking mature articular cartilage. By constructing a three-layer architecture of these scaffolds, the orientation and ECM components of natural articular cartilage were proven successful, resulting in improved and guided morphology, orientation, and phenotypic states of cultured chondrocytes.[85]

Additionally, although not as common, CNMs can be used by themselves to fabricate hydrogels and hydrophilic dressings for a few wound healing and tissue engineering applications, as discovered through research by Wang et al.,[103] Dutta et al.[105] and Ferreira et al.[106] These produced scaffolds demonstrate high levels of hydrophilicity, porosity, structuration, and robust strength to weight ratios, all of which play critical roles as analogues to various tissue ECMs.[103,105-106]

Alongside CNM incorporation for biomedical applications, so can MNPs be employed, specifically for enhanced stimuli-responsive PNCs.[88-91,98-99,108-112] As previously noted, MNPs have the ability to induce indirect stimulation within polymer matrices, resulting in various 4D effects.[92-93,98-99] In addition to inducing thermal manipulations through absorption of electromagnetic energy within PNCs, MNPs also demonstrate excellent chemical stability, non-toxicity, biocompatibility, and high saturation magnetization, further promoting their utilization for biomedical applications of controlled and targeted drug delivery systems, bio-sensors, cell labelling, bio-imaging, contrast agents, photothermal and photoablation therapy, UV radiation protection, cancer and gene therapy, and hyperthermia.[108-112] In particular, literature reviews by Cardoso et al.,[108] Anderson et al.,[109] and McNamara et al.[112] embellish not only the abilities of the typically used Fe_3O_4 NPs, but also bimetallic and alloyed MNPs, including Fe-Co, Fe-Pt, Fe-Ni, Cu-Ni, ZnO, and TiO_2 NPs, further diversifying their exploitation in the biomedical realm. For example, these various forms of MNPs have been shown to be an effective treatment for tumors through targeted hyperthermia, subsequently destroying cancerous cells with temperatures above 42 °C.[112] Overall, literature reviews of MNPs seeded in polymer matrices have been widely researched, however, there are still a few crucial biocompatible questions requiring answers.[108-112]

Chapter 2: Scope and Objectives

As biomedical technology and clinical practices continue to improve through the decades, the need for biomaterials that confront any new arising challenges is essential.[1] Specifically, biomaterial scaffolds for wound healing applications that increase rate of recovery, as well as quality of regenerated tissue.[1-3] The research performed in the dissertation is based on the hypothesis that utilizing 3D biomaterial constructs with unique nanostructuration and stimuli-responsive properties will promote enhanced wound healing through better biomimicry of native tissue. Further described in several stages, is a novel extraction method of CNCs from the renewable agricultural waste source of spent coffee grounds, followed by preparation, fabrication, and characterization of innovative biocompatible PNCs for a multitude biomedical applications. Moreover, each biocompatible PNC scaffold was designed for a unique purpose, including mechanically gradient composite scaffolds for various ECM mimicry for tissue engineering, stimuli-responsive substrates with controlled topographical manipulations via induction heating for mechanical ejection of embedded cells, and nanostructured hydrogel composite scaffolds for enhanced wound healing and regenerated tissue structuration to mitigate scar tissue formation.

Through the thorough literature review defined in Chapter 1, a few methods have been defined to improve these biomedical PNC scaffolds using CNCs and MNPs as nanofillers. Biomaterial resins, such as PEGDA, typically have very low viscosities, limiting their 3D printability to SLA techniques rather than a variety AM techniques.[4] The first method involves the production of viscous bioinks to enhance cell embedment and multi-compositional scaffolds with gradient mechanical properties through extrusion bioprinting.[1-2,4] Along with improving 3D printability of biomaterials through increased viscosities, hierarchical structuration of fabricated PNC scaffolds is necessary to promote enhanced tissue regeneration through better biomimicry of natural ECMs. The second method involves controlled topographical and hierarchical manipulation for 2.5D and 4D capabilities using indirect stimulation, promoting cell/biological component release, drug delivery, bioseparations, and wound healing applications through higher dimensionally structured hydrogel interfaces.[5] Lastly, the third method involves nanostructuration of 3D constructs to better simulate native ECMs for greater wound healing potential by regenerating new healthy tissues with correct orientation, while simultaneously reducing or

mitigating scar tissue formation.[2-3] From this literature review, the following chapters have been researched and produced, further shown in **Figure 2.1**.

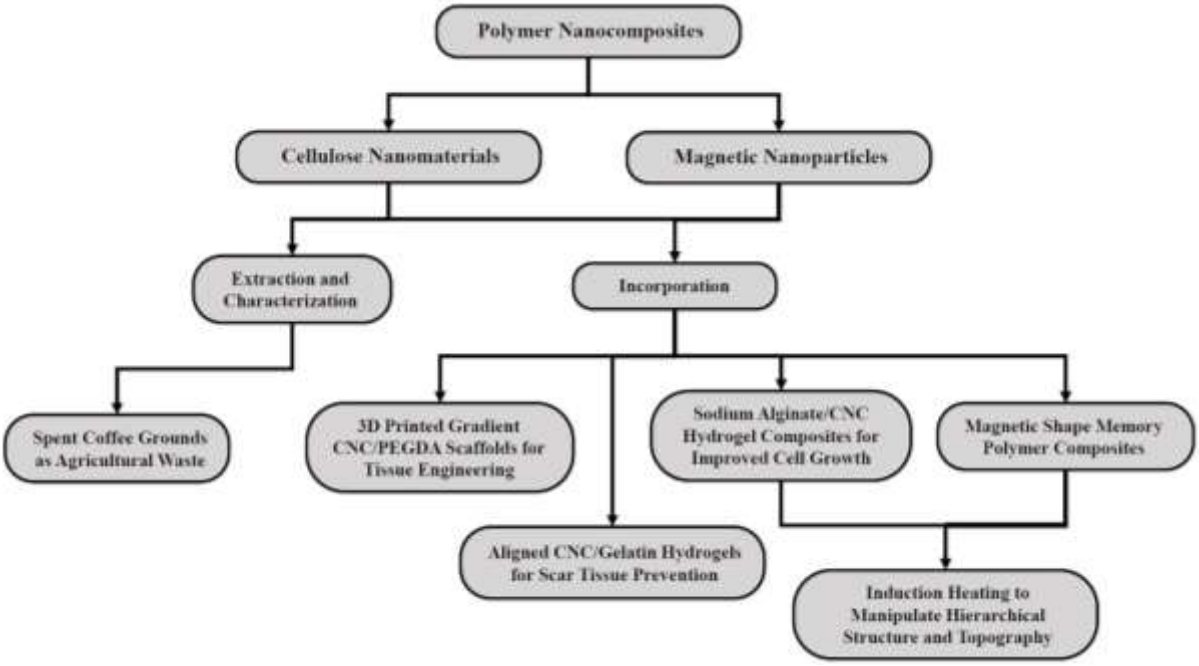

Figure 2.1 Flow diagram depicting the process of research throughout the chapters of this dissertation. Starting from the concept of fabricating novel polymer nanocomposites, the flow of research portrayed in this schematic shows the progressive steps of choosing specific nanomaterials, followed by extraction, characterization, and incorporation, leading to successful applicability for a multitude of biomedical designs.

Chapter 3 focuses on the extraction and isolation of CNCs from spent coffee grounds, otherwise disposed as a massive agricultural waste product. A novel three-step method of bleaching, purification, and phosphoric acid hydrolysis, producing CNCs comprising surface phosphate moieties is described in detail. Ideal hydrolysis parameters were determined from manipulating a previously established procedure by Espinosa et al.,[6] in which bleaching process, temperature, reaction time, and acid concentration were further varied from the cited study. Following extraction, the isolated phosphated CNCs were chemically, physically, and mechanically characterized through established techniques by Foster et al.,[7] and compared to other commercially available and industrial extracted CNCs to determine viability.

Chapter 4 describes a novel preparation method for mechanically gradient hydrogel composite scaffolds for biomedical applications. Bioinks comprised of PEDGA solution and CNC suspension were created and characterized through rheology to determine viscosity and shear

thinning properties. Following rheological characterization, a unique 3D bioprinting technique was employed to establish a protocol of fabricating layer-by-layer scaffolds of varying PEGDA and CNC content. To determine the effect of mechanical reinforcement, single-composition scaffolds were printed and analyzed individually. As well, multi-composition scaffolds were also studied through bioprinting and characterization to show tunability of mechanical gradients for specific ECM stiffness, as well as different tissue characteristics.

In addition to utilizing CNCs as a nanofiller, Chapter 5 reports on the use of MNPs in PNCs to produce specific stimuli-responsive behaviors. Multiple concentrations of MNPs were incorporated into polymer matrices, including TPU, PVAc, and N-11, to fabricate magnetic PNCs. Following fabrication, each PNC substrate was heated past its respective thermal transition temperature, strained to roughly 200% of its original length, and subjected to induction heating via magnetic fields. The shape memory effects induced through induction heating were studied with regards to varying MNP content, inherent polymer crystallinity, thermal transition temperatures, and strength of magnetic fields. Additionally, SA and CNC hydrogel composites were fabricated with varying mechanical and hydration properties to simulate various ECM properties for cell growth, and attached to the PNC substrates. Furthermore, since living cells require incredibly specific conditions to maintain vitality, thermal dissipation and hydration studies were conducted to ensure the cells would endure no thermal shock nor dehydration. Finally, the combined hydrogel and PNC substrate construct was subjected to thermal transition temperatures, inducing internal pressure through a topographical shape change, as a novel method of cellular ejection from embedded positions with minimal damage.

With the heavy focus of biomedical applicability in the present dissertation, Chapter 6 sought to demonstrate the capabilities of CNC/CNF and gelatin composite hydrogel scaffolds to enhance wound healing, specifically within skin tissue. The majority of literature references researching wound healing materials tend to focus on the rate of wound healing, while disregarding the structuration and functionality of the regenerated scar tissue.[8] Utilizing solution casting and previously established 3D bioprinting techniques, the effects of CNC/CNF alignment on the structuration of new cell and tissue growth, while minimizing the generation of fibrous scar tissue, were researched. Additionally, biodegradation properties were finely-tuned between 2 days and 8 weeks to show effects of scaffold degradation rate on new cell and tissue growth. In order to

determine the clinical efficacy of scar tissue prevention during wound healing, and following scaffold fabrication, characterization, and optimization, *in vivo* animal studies were theorized on how the significance of controlled alignment and structuration of complex hydrogel scaffolds would affect inhibition of random tissue orientation during the natural healing processes, reducing undesired scar tissue formation.[9-10]

Chapter 7 concludes and summarizes the research projects performed throughout the dissertation, and lends insight into future work needed to further progress the applicability of these biomedical scaffolds into clinical settings.

Chapter 3: Isolation of Thermally Stable Cellulose Nanocrystals from Spent Coffee Grounds via Phosphoric Acid Hydrolysis

3.1 Introduction

Cellulose is one of the most abundant natural, renewable, and biodegradable polymers on Earth, and can be obtained from various sources including bacteria, forestry, and agricultural wastes (agro-wastes).[1-2] It is mainly found in plant cell walls, lending its physical strength to the structure of the plant due to its strong, tightly packed structure.[1-2] Its linear unbranched homopolysaccharide structure comprising of 1-4 β linked glycosidic bonds, as well as the hydrogen bonding of the C2 and C6 hydroxyl groups between cellulose molecules, allows for the formation of crystalline regions throughout the cellulose chains.[3-4] These crystalline regions can be isolated by multiple techniques, with acid hydrolysis being the most common. This technique utilizes concentrated acids to hydrolyze the amorphous region of cellulose, resulting in the isolation of the crystalline regions.[5-6] The most common and industrial/commercial acid hydrolysis procedure utilizes sulfuric acid due to the ease of use and established protocols, although other acids have been employed as well, such as phosphoric acid and hydrochloric acid.[5,7-8] These isolated crystalline nanomaterials, better known as cellulose nanocrystals (CNCs) and cellulose nanofibrils (CNFs), have been proven to have significant impacts on the field of polymer science.[5-6]

CNCs and CNFs have been well explored in the past few decades, with ever increasing methods of isolation and applications.[5-6] As previously mentioned, multiple different acids can be used to hydrolyze cellulose, which create different functionalizations on the surfaces of CNCs (i.e. sulfate, phosphate, and hydroxyl groups, among others), and lead to varying chemical and physical properties.[8-10] Although their structures are relatively the same, consisting of rod-like shapes ranging from 100 nm-1000 nm in length and 5 nm-20 nm in width, the varying functionalization of the surface change properties such as dispersion in solvents, thermal stability, biocompatibility, and crystallinity or stiffness.[8,11-12] Their many unique properties allow for usage in a variety of applications, but are most known for their incredible strength to weight ratio for reinforcing nanocomposites, sustainability, and impact on environmentally friendly and biodegradable solutions in industry.[5-6,13] The use of CNCs as a reinforcing agent in polymer nanocomposites, has seen a drastic rise in the last few years, leading to many new applications in many different

fields.[14-17] When CNCs are added into a polymer, they have the ability to not only change the mechanically behavior, but also to increase properties such as water absorption in hydrophilic polymers, produce repeatable actuation, and promote particle adsorption and cell growth and viability.[5-6,11-12,18-19] Some applications in particular that have been explored are reinforcement in polyethylene, polyester, and polyurethane nanocomposites for use in automotive, textile, and biomedical industries,[11-12,14,20-22] as well as use in optical,[23] electronic,[24] and stimuli responsive materials,[25-29] and airborne filtration systems.[30] The usefulness of CNCs and CNFs have given rise to a growing market for cellulose nanomaterials, with nearly 10,000 tons being produced per year and used in high-end industrial products as reported by Future Market Inc. (2019).[13]

As previously mentioned, trillions of tons of cellulose are produced globally annually, making it an almost inexhaustible feed source. For example, over six billion cups of coffee are consumed daily, leading to enormous amounts of raw cellulosic material just from spent coffee grounds.[1,4,31-32] However, much of the cellulose is discarded as waste into landfills to eventually biodegrade.[33] One of the biggest impacts on landfill occupation has been from the agro-wastes produced by crop harvesting, food industry waste, and textile industry waste.[33-35] Due to the overwhelming amount of cellulosic materials discarded every year, extracting useful materials from various waste sources could potentially decrease landfill area, while leading to useful applications of the extracted material.[33-34] For example, corn stover,[36-37] rice husks,[38] cotton,[39] and sugarcane bagasse[40] have had extensive research performed on the extraction of cellulose nanomaterials utilizing acid hydrolysis. However, there remains many other cellulose sources that have yet to be studied, such as spent coffee grounds, of which this research will focus.

Although research has been successful with isolating CNCs from coffee husks and coffee silverskins, spent coffee grounds have yet to be researched.[41-42] This report seeks to provide a method of CNC extraction from spent coffee grounds utilizing adaptations of known purifying and hydrolyzing procedures.[8,43] Once extracted, the CNCs are thoroughly characterized by current techniques and compared to literature to determine the viability of spent coffee grounds as a source for isolation of useful CNCs.[9] One of the most important factor of success will be determining the new CNC's ability to mechanical reinforce a polymer. The greater the mechanical reinforcement, the greater the ability to fine tune polymer nanocomposites, which will increase the variety of

potential applications, as mentioned above.[11-12,21,44] If proven successful, this research could provide an alternative way to recycle and reuse an otherwise useless waste material.

3.2 Experimental Methods

3.2.1 Materials

Café Bustello very fine coffee grounds were purchased from Food Lion in Blacksburg, Virginia. All chemicals including toluene, ethanol, 85% v/v phosphoric acid, sodium hydroxide pellets, acetic acid, N,N-dimethylformamide (DMF), dimethyl sulfoxide (DMSO), tetrahydrofuran (THF), and bovine serum albumin (BSA) were purchased from Sigma-Aldrich. McKesson 3% topical hydrogen peroxide was purchased from Amazon.com. Nanovan stain consisting of a suspension of vanadium particles in water was purchased from Nanoprobes. Texin RxT85A thermoplastic polyurethane (PU) was purchased from Covestro. Commercial cellulose nanocrystals (CNCs) were purchased from the University of Maine Nanocellulose Facility.

3.2.2 Purification and Bleaching of Cellulose

Café Bustello coffee grounds were run through a Keurig K series coffee machine to make a normal 8 oz. cup of coffee. It should be noted that the coffee grounds going through the heated water of the Keurig (roughly 90 °C) experienced no thermal decomposition. As well, the initial roasting of the coffee beans to enhance flavor happens between 180-240 °C, therefore the cellulose within coffee grounds underwent no prior thermal decomposition before use.[45] The spent coffee grounds were then left out to dry overnight before starting the cellulose extraction process. The relative composition of the spent coffee grounds after drying and before purification is shown below in **Table 3.1**.[31-32,46]

Table 3.1 Relative chemical composition of spent coffee grounds, adapted from Mussatto et al. and Ballesteros et al.[31-32,46]

Chemical Component	Dry Weight (g/100g)
Cellulose	8-10
Hemicellulose	36-39
Lignin	23
Protein	13-17
Fat	2-3
Acetyl Groups	2

Ashes	1-2
Other (Not Specified)	4-15

The following purification and bleaching procedure was adapted from Marett et al. and Mueller et al.[43,47] Approximately 40 g of dried spent coffee grounds were measured out and purified utilizing a Soxhlet extraction procedure with a 1000 mL mixture of 1/3 ethanol and 2/3 toluene by volume. The solvent mixture was added to a round bottom flask under the extractor and placed into a silicone oil bath at 120 °C to be boiled overnight, ensuring a significant amount of time to remove soluble monomers such as lipids. After roughly 24 h of extraction, the coffee grounds were removed and left to dry overnight.

Following the Soxhlet extraction, a 1 M sodium hydroxide bath was used to remove the soluble hemicellulose. The base wash was created by mixing 120 g of sodium hydroxide pellets with 3000 mL of deionized (DI) water and heating to 70 °C while continuously stirring until all of the pellets were dissolved. The extracted material was added to the solution for 4 h and subsequently separated via vacuum filtration. The resulting material was then washed with DI water until the liquid remained clear, approximately six times. This entire procedure was repeated one more time due to the extensive quantities of hemicellulose.

Immediately following the base washes, the almost-pure cellulose was added to a hydrogen peroxide/acetic acid solution in order to remove the remaining non-cellulosic components including lignin. The wash comprised of 1440 mL of 3% hydrogen peroxide, 60 mL of acetic acid, and 1500 mL of DI water (48 v/v, 2 v/v, and 50 v/v of each component, respectively) and was heated to 60 °C while stirring constantly. The cellulose was added to the wash for 4 h before separation via vacuum filtration. The resulting cellulose was then washed with DI water until the liquid remained clear, approximately four times. Again, this entire procedure was repeated one more time due to the extensive quantities of the remaining non-cellulosic components.

3.2.3 Acid Hydrolysis of Cellulose

The following phosphoric acid hydrolysis procedure was adapted from Espinosa et al.[8] Two grams of the purified cellulose was added to 100 mL of DI water and cooled in an ice bath for 15 min. Phosphoric acid was slowly added dropwise via a dripping funnel, while maintaining a solution temperature of below 20 °C, until a phosphoric acid concentration of 10.7 M was achieved (approximately 292 mL). After the addition of the acid was complete, the solution was

placed in a silicone oil bath preheated to 100 °C and stirred for a predefined time of 2 h. After the completion of the reaction, the solution was immediately moved into an ice bath until room temperature was reached. The phosphorylated CNCs (p-CNCs) were separated from the supernatant by centrifugation at 10000 rpm for 10 min. The separated supernatant was decanted, replaced by an equal amount of DI water, and centrifuged again. This step was repeated until the supernatant remained clear (approximately five times). The p-CNCs dispersion was dialyzed against DI water for 7 days, replacing the water every day, until a neutral pH of 7 was reached. The yield of p-CNCs was approximately 10%, however, it should be noted that the yield was highly dependent on the small content of cellulose residing in the raw spent coffee grounds.[31-32,46] To dry the p-CNCs, the suspension underwent a solvent exchanged into acetone by replacing 2/3 of the aqueous suspension with equal parts of acetone using the previously described sonication and centrifugation techniques. This process was repeated roughly 4 to 5 times to ensure complete exchange. Once the p-CNCs were exchanged into acetone, the suspension was poured into a Teflon petri dish and dried on a hotplate overnight. The subsequently dried p-CNCs were then used in the following characterization techniques, *Sections 3.3.4 – 3.3.11*, and redispersed into respective solvents as needed.

3.2.4 Microscopy

SEM samples were prepped by dispersing p-CNCs in DMF with a concentration of 0.1 mg/mL, and sonicating at 110 W and frequency of 40 kHz with a Branson M2800 ultrasonic bath for 1 h. A droplet of the dispersion was then placed onto a silicon wafer attached to an aluminum SEM stand, and left in a desiccator to dry overnight. Each sample was sputter coated with 5 nm of iridium using a Leica ACE600 Sputter to prevent charge buildup, and imaged using a LEO 1550 field-emission SEM at 5 kV.

TEM samples were prepped by dispersing p-CNCs in DI water with a concentration of 0.01 mg/mL, and sonicating at an amplitude of 40 with a 20 kHz Q55 Qsonica horn sonicator for 10 mins. Next a solution of BSA in DI waster was created at a concentration of 0.2 mg/mL, and mixed with the p-CNC dispersion in a 1:1 ratio. The subsequent mixture was then sonicated further at 110 W and frequency of 40 kHz with a Branson M2800 ultrasonic bath for 1 h. A droplet of the mixture was placed onto a copper TEM grid and left for 1 min to ensure attachment of p-CNCs. A drop of NanoVan stain was then added to the TEM grid for 30 s, before being quickly submerged

in a beaker of DI water to remove any excess materials. The grid was left in a desiccator to dry overnight. Imaging was performed using a JEOL 2100 TEM.

3.2.5 Energy-dispersive X-ray Spectroscopy

EDS samples were prepped similarly to the SEM samples, however instead of dispersing in DMF, the p-CNCs were dispersed in DI water with a concentration of 10 mg/mL. The dispersion was sonicated at 110 W and frequency of 40 kHz with a Branson M2800 ultrasonic bath for 1 h. A drop of the dispersion was placed on a silicon wafer and left in a desiccator to dry overnight. As well, phosphorus has a relatively similar signal as iridium, therefore the samples were sputter coated with 5 nm of gold-palladium. Analysis was performed using a LEO 1550 field-emission SEM at 10 kV.

3.2.6 X-ray Photoelectron Spectroscopy

XPS samples were prepped similarly to the EDS samples, however a concentration of 1.0 mg/mL was used. The dispersion was sonicated at 110 W and frequency of 40 kHz with a Branson M2800 ultrasonic bath for 1 h. A drop of the dispersion was placed on a silicon wafer and left in a desiccator to dry overnight. The samples were not sputter coated prior, and analysis was performed using a PHI Quantera SXM-03.

3.2.7 Conductometric Titration

Conductometric titration was performed following a known protocol by Foster et al. 0.15 g of p-CNCs were dispersed in 300 mL of DI water and sonicated in an ultrasonic bath for 1 h. 5 mL of 0.5 M NaCl solution and 0.02 M HCl solution were added to the dispersion prior to titrating.[9] Titration was carried out by a Metrohm 905 Titrando automatic titrator dosing 0.05 mL of 0.02 NaOH solution per data point using an Metrohm 800 Dosino automatic doser, and measuring conductivity and pH with a Metrohm 856 conductivity module. Due to the addition of the NaCl, a calculated conductivity was used instead of the measured conductivity, following the equation used in Foster et al.[9] The data was plotted and analyzed using Excel, and surface charge density calculated using an adapted protocol and equation by Espinosa et al.[8]

3.2.8 X-ray Powder Diffraction

XRD was performed on dry p-CNCs in powder form using a Panalytical X'Pert powder XRD system. A CuKα radiation source was used at 45 kV and 30 mA, and scattered radiation was

detected in the range of 2θ = 0°-50°. Percent crystallinity was determined using the peak deconvolution method similar to that of Zhang et al.[48]

3.2.9 Thermogravimetric Analysis

TGA was performed on dry p-CNCs in powder form using a TA Instruments TGA Q500 thermal analyzer. 10 mg of p-CNCs were measured into a platinum TGA pan, and heated from 25 °C to 500 °C at a rate of 10 °C/min. The decomposition temperature was determined by the loss of 5 wt% after the residual water had been removed from the sample.

3.2.10 Dispersability and Dynamic Light Scattering

The dried p-CNCs were dispersed in DI water, DMSO, DMF, and THF, decreasing in polarity, with a concentration 10 mg/mL. Each dispersion was sonicated using a 20 kHz Q55 Qsonica horn sonicator at an amplitude of 40 for 10 mins, followed by further sonication in an ultrasonic bath for 1 h. The dispersions were lined up in order of decreasing polarity and imaged immediately after sonication, and 1 h, 1 d, and 10 d post-sonication.

DLS samples were prepped by dispersing p-CNCs into DMF at a concentration of 0.01 mg/mL. The dispersion was sonicated using the same protocol mentioned above for dispersibility studies. The dispersions were then transferred to a quartz cuvette, and analyzed using a Malvern Zetasizer Nano-ZS DLS instrument to determine relative particle size within a suspension.

3.2.11 Mechanical Reinforcement

Three different compositions of composites were fabricated for mechanical reinforcement testing; neat PU, 10 w/w commercial CNCs in PU, and 10 w/w p-CNCs in PU, following an adapted procedure from Frost et al.[21] The CNCs were dispersed in DMF at a concentration of 10 mg/mL using the same sonication protocol discussed in dispersibility testing. The PU was dissolved in DMF at a concentration of 40 mg/mL using a hot plate at 140 °C while stirring at 1000 rpm for 1 h or until all the PU pellets had dissolved. Once the CNC suspensions and PU solution were completely homogenous, they were mixed together in the ratios specified above. The combined mixture was placed in an oil bath at 140 °C while stirring at 750 rpm until enough DMF was evaporated to increase viscosity (to the 'viscosity of molasses'). The viscous mixture was then transferred to a Teflon dish, set on a hot plate at 100 °C, and left overnight to slowly evaporate the DMF. After drying overnight, the samples were put into a vacuum oven at 80 °C and -27 in*Hg for 2 h or until all DMF was removed.

After complete removal of the solvent, each composition was hot pressed using a 3851-0 Carver Press at 140 °C and 3 MPa of pressure for 5 min, using 0.9 mm– 1.0 mm aluminum spacers to ensure uniformity of thickness throughout the film. Each pressed film was cut with a razor blade into five 1.0 cm wide ribbons for tension testing. Tension testing was performed utilizing a TA Q800 Dynamic Mechanical Analyzer (DMA) on five of each composite composition to determine the mechanical reinforcement properties of the composites. Each sample was tested using an isostatic force test with a force ramp rate of 3 N/min at 25 °C until a maximum of 18 N was reached.

3.3 Results and Discussion

3.3.1 Isolation of p-CNCs from Spent Coffee Grounds

Due to the excessive amount of non-cellulosic components in the spent coffee grounds,[31-32,46] the bleaching and purification process was adjusted to obtain a purer form of cellulose, yielding an off-white, slightly tan color. Of the 40.0 g of dried spent coffee grounds, a resulting 4.2 g yield was left after the bleaching and purification process, which correlates well to the previously reported amount of cellulose found in spent coffee grounds.[31-32,46] Following the extensive bleaching and purification process, extraction of p-CNCs from spent coffee grounds utilizing phosphoric acid hydrolysis proved successful. The cellulose was hydrolyzed using the same parameters as the procedure by Espinosa et al., however, an extra 30 min was added to the reaction time in order to fully hydrolyze the cellulose.[8] Phosphoric acid hydrolysis was chosen over the conventional sulfuric acid hydrolysis because of the difference in the resulting physical and chemical properties. Compared to traditional sulfated CNCs (s-CNCs), p-CNCs have a lower surface charge, decreasing dispersibility in many organic solvents, leading to more agglomerations within polymer composite systems. However, they have also been shown to have a higher thermal stability and biocompatibility (better cell growth and viability), which is crucial for multiple polymeric applications.[5,8,11-12] The p-CNCs were successfully characterized, **Table 3.2**, following current analyzing techniques in literature and compared to other fabricated p-CNCs and current industrial CNCs.[8-9,49-50]

Table 3.2 Physical and chemical properties of fabricated p-CNCs compared to fabricated p-CNCs in literature and commercial s-CNCs from UMaine and CelluForce.[5,8,49-50]

	Coffee p-CNCs	p-CNCs (Espinosa)[7]	p-CNCs (Vanderfleet)[8]	UMaine s-CNCs	CelluForce s-CNCs
Substituent content (phosphate and sulfate groups, respectively) (mmol/kg cellulose)[1]	25.8 ± 9.6	3.95 ± 0.8	18.8 ± 3.3	1.06 ± 0.2	8.1 ± 0.05
Charge concentration (mmol/kg cellulose)[2]	48.4 ± 6.2	10.8 ± 2.7	N/A	330 ± 15	255 ± 10
Carbon (%)[1]	58.5 ± 0.39	44.19 ± 0.15	N/A	~77	~77
Oxygen (%)[1]	40.5 ± 0.39	49.5 ± 0.08	N/A	~23	~23
Length (nm)[3]	199 ± 27	316 ± 127	326 ± 70	134 ± 52	183 ± 88
Diameter (nm)[3]	17 ± 4	31 ± 14	N/A	7 ± 2	6 ± 2
Aspect ratio[3]	12 ± 3	11 ± 1.5	N/A	19	31
Apparent crystallinity (%)[4]	74.2	81	95	85	89.9
Onset of thermal decomposition, $T_{d5\%}$ (°C)[5]	310	305	~300	~260	~263
Mechanical reinforcement tensile modulus at 10 wt% CNCs (MPa)[6]	58.6 ± 2.7	N/A	N/A	113.7 ± 9.7	N/A
Mechanical reinforcement yield stress at 10 wt% CNCs (MPa)[6]	2.6 ± 0.1	N/A	N/A	3.6 ± 0.0	N/A

[1] Determined by XPS (*Section 3.3.6*)

[2] Determined by conductometric titration (*Section 3.3.7*)

[3] Determined by TEM (*Section 3.3.4*)

[4] Determined by XRD (*Section 3.3.8)*

[5] Determined by TGA (*Section 3.3.9*)

[6] Determined by DMA (*Section 3.3.11*)

[7] Referenced from Espinosa et al.[8]

[8] Referenced from Vanderfleet et al.[49]

3.3.2 Microscopy: SEM and TEM

Both SEM and TEM were employed to determine whether p-CNCs were successfully obtained, and if so, to characterize the average aspect ratio. SEM imaging was performed first and compared to literature, to establish a preliminary presence of p-CNCs. The SEM images show the distinct rod-like shape of the p-CNCs, however, lack of a more diluted dispersion caused aggregation of the particles while drying. The resulting mat of material, shown in **Figure 3.1**, is assumed to be the aggregated p-CNCs due to its common drying agglomeration, similar results found in literature.[43,51-52]

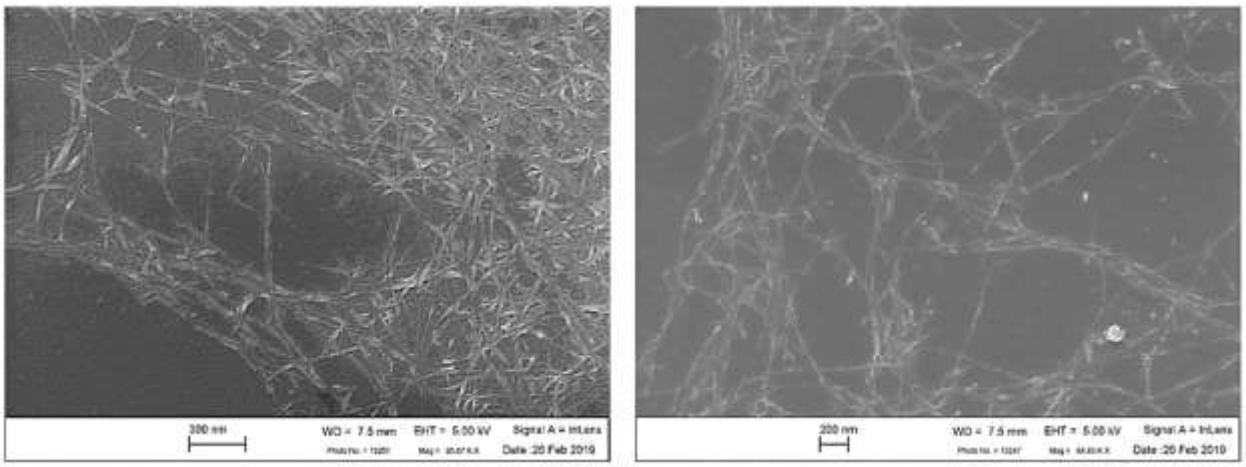

Figure 3.1 Preliminary SEM images of the p-CNCs to establish their existence.

TEM was subsequently conducted to determine the length, width, and aspect ratio of the p-CNCs, shown in **Figure 3.2**, and compared to those found in literature [8,11,49].[8,11,49] It should be noted that although the images in **Figure 3.2** show a darkened region from the agglomeration of BSA protein around the p-CNCs, the measurements were not affected. ImageJ image measurement software was used to measure 15 individual p-CNCs from varying images, resulting in an average length of (199 ± 27) nm, average width of (17 ± 4) nm, and aspect ratio of 12 ± 3. Although the aspect ratio of the p-CNCs resides in the lower range of literature values[5-6] (for

reference, 10 for cotton and 67 for tunicates)[12], there should still be significant amount of mechanical reinforcement when introduced into a polymer matrix, discussed later in *Section 3.4.8*.

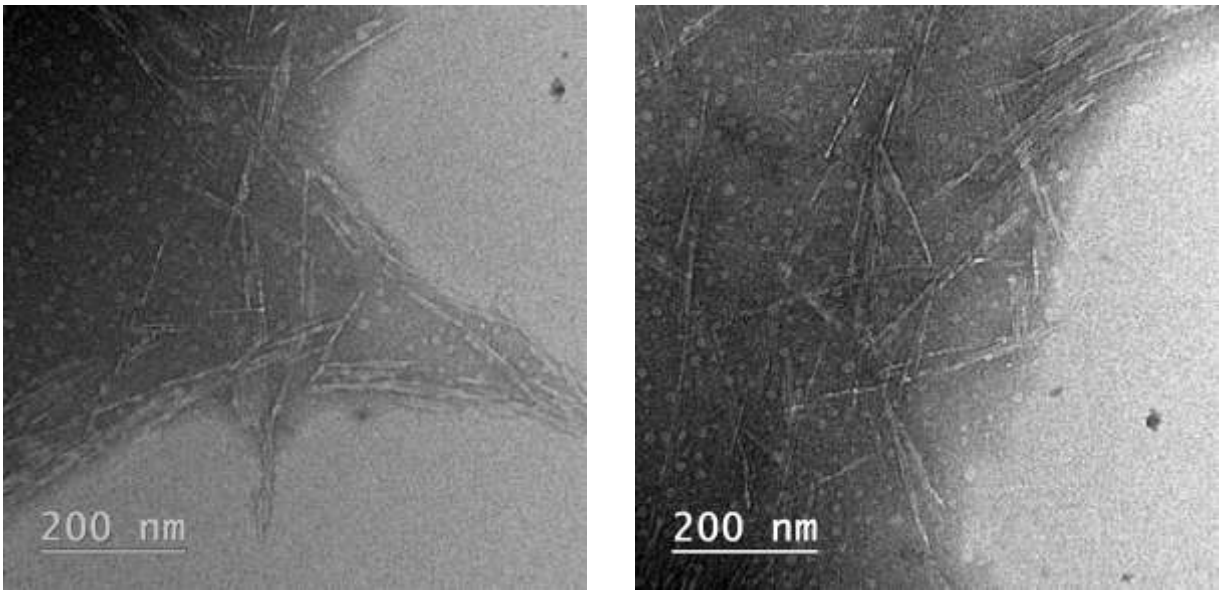

Figure 3.2 TEM images of isolated p-CNCs dispersed in a 1:1 mixture of 0.01 mg/mL p-CNCs in DI water and 0.2 mg/mL BSA solution. The BSA was shown to produce a darker halo around the p-CNCs due to agglomeration of the protein.

3.3.3 Chemical Composition: EDS and XPS

EDS and XPS were conducted for elemental analysis of the p-CNCs, specifically for carbon, oxygen, and phosphate content. The elemental analysis resulted in a carbon content of (58.5 ± 0.39) wt%, and an oxygen content of (40.5 ± 0.39) wt%, which are typical values for cellulose and its derivatives.[8] The phosphate content was shown to be (0.08 ± 0.03) wt%, which was then converted to (25.83 ± 9.6) mmol/kg cellulose for a more accurate comparison to literature values.[8,49] It is typical to see a lower phosphate content for p-CNCs when compared to other functionalized CNCs, specifically the sulfation of s-CNCs, which ranges from 80 mmol/kg cellulose-350 mmol/kg cellulose.[43,49] However, the phosphate content observed for the p-CNCs is much higher than expected when compared to other studies (i.e. 3.95± 0.8 mmol/kg cellulose for Espinosa et al. and 8.2 mmol/kg cellulose-44.5 mmol/kg cellulose from Vanderfleet et al.).[8,49] Spent coffee grounds contain a certain wt% of phosphorus, and although it is assumed that all of the non-cellulosic materials were extracted during the bleaching and purification process, there is

a potential chance for some of the phosphorus to remain, resulting in a higher phosphate content.[31-32,46]

3.3.4 Surface Charge Density: Conductometric Titration

During acid hydrolysis, CNCs often become functionalized with associated groups of the acid being used, for example phosphate groups via phosphoric acid hydrolysis. Conductometric titration was employed to obtain the surface charge density of the functionalized p-CNCs, shown in **Figure 3.3**. With the addition of phosphate substituents attached to the cellulose via ester bond, the surface charge should increase when compared to a blank titration. Utilizing adapted procedures from Foster et al. and Espinosa et al.,[8-9] surface charge density was calculated to be (48.4 ± 6.2) mmol/kg cellulose.

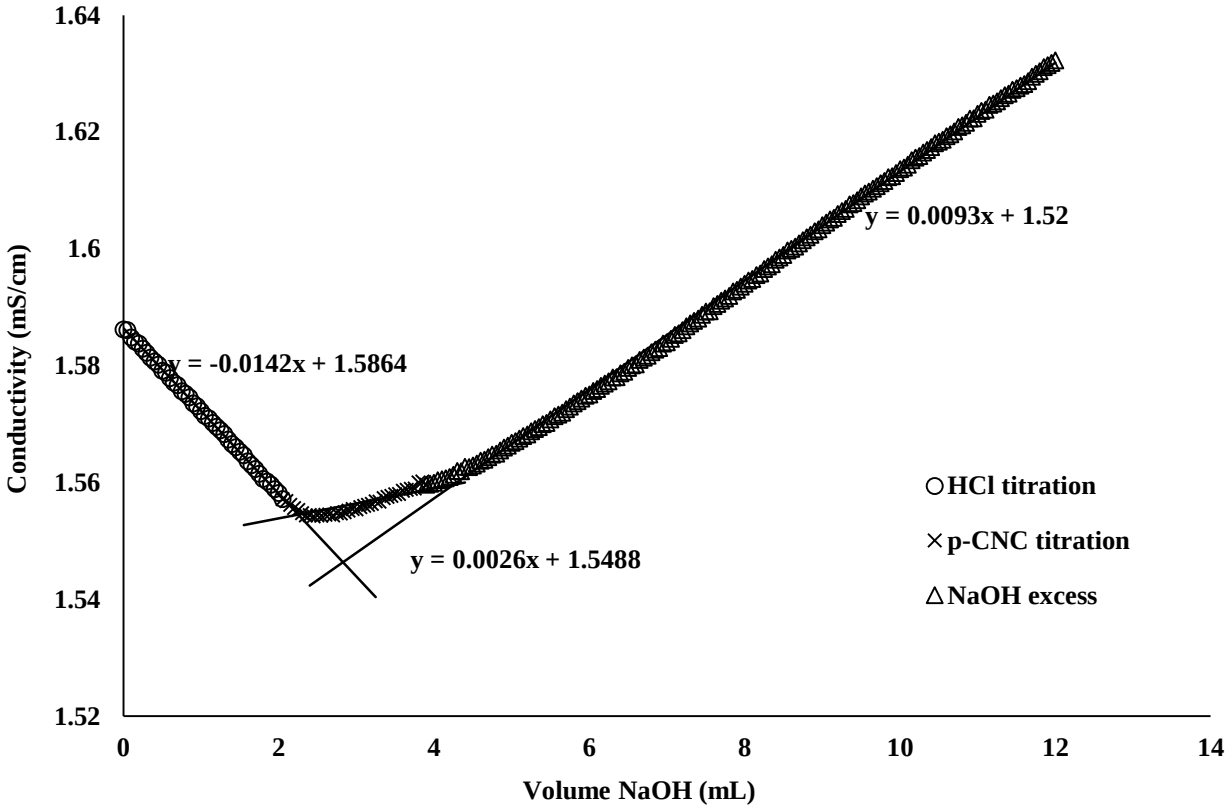

Figure 3.3 Plot of conductometric titration data, showing conductivity versus volume of NaOH added. Each individual region of titration is shown, i.e. HCl titration, p-CNC titration, and excess NaOH. The equations shown were used to calculate the surface charge density of the p-CNCs using an established protocol by Espinosa et al.[8]

Although the surface charge is relatively high for p-CNCs compared to literature (10.8 ± 2.7 mmol/kg cellulose by Espinosa et al.[8]), it correlates to the higher phosphate content of the spent

coffee ground p-CNCs observed by EDS and XPS during elemental analysis.[49] The higher surface charge density will allow for easier dispersion in polar solvents such as water, DMSO, and DMF, however, will inherently lower the onset of thermal degradation, further discussed *Section 3.4.6 and 3.4.7*, respectively.

3.3.5 Crystallinity: XRD

XRD was performed to obtain the apparent crystallinity of the p-CNCs, shown in **Figure 3.4**. The crystalline peaks occur at 2θ values of 16.5°, 20.5°, 22.5°, and 34.5°, which line up with the 110, 012, 200, and 004 planes, respectively, and indicative of cellulose type I.[53] It is common that an additional peak appears at 14.5° lining up with a $1\bar{1}0$ peak, when analyzing CNCs, however no peak occurred for the p-CNCs.[53-54] This could indicate that not all of the amorphous region was hydrolyzed during the extraction process, leading to a slightly lower crystallinity. Under the assumption that the $1\bar{1}0$ and 110 peaks were the same intensity, a peak deconvolution method adapted from Zhang et al. was used to remove the amorphous material regions and calculate an apparent crystallinity of 74.2%.[48] The typical crystallinity of CNCs reported in literature ranges from 64% to 90%, with the majority residing in the mid to upper 70s.[53,55] Crystallinity is crucial for CNCs because the higher the crystallinity, the higher the stiffness they will impart on a polymer matrix during mechanical reinforcement.[5,56] The p-CNCs showed a normal percent crystallinity compared to literature, which is suggested correlate to increased mechanical reinforcement properties. As well, each peak was separated and analyzed using the Scherrer equation with full width at half maximum (FWHM) to determine the size of each crystal plane, following an analysis by Kumar et al. and Das et al.[57-58] The resulting crystallite sizes were 8.6 nm, 5.7 nm, 3.4 nm, and 2.9 nm, for the 110, 012, 200, and 004 planes, respectively.

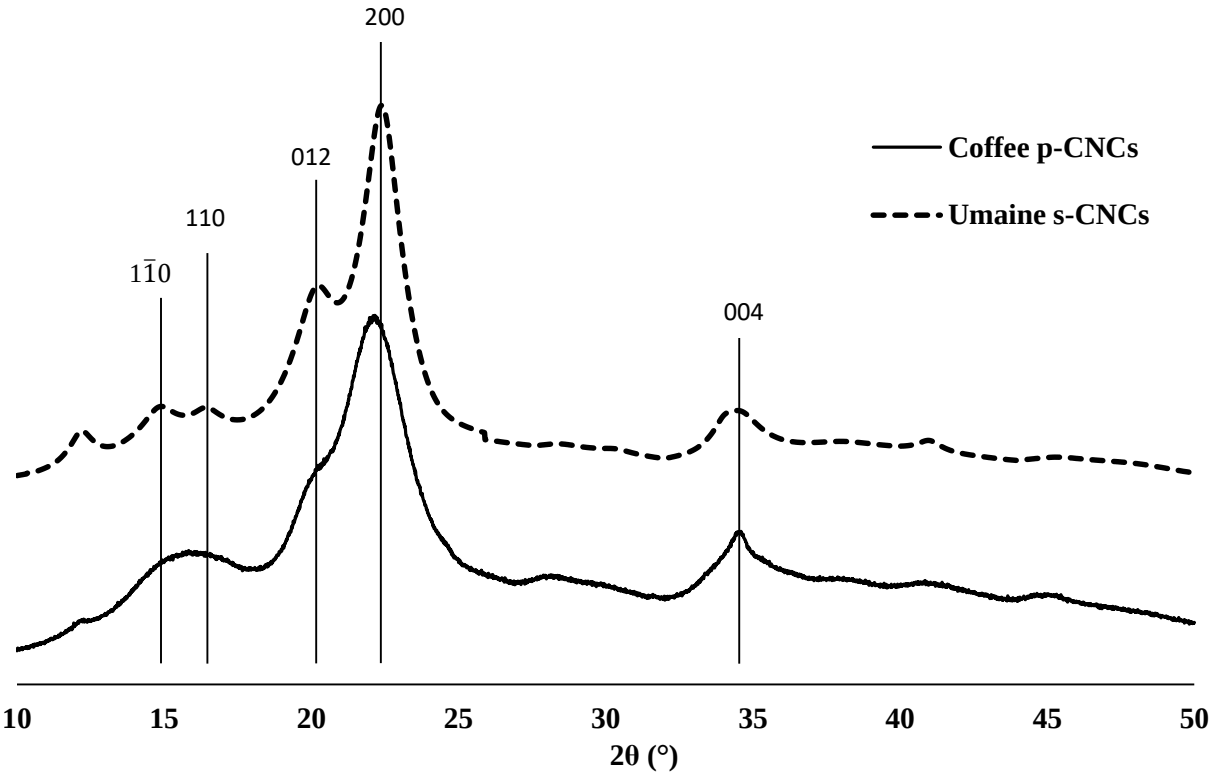

Figure 3.4 XRD spectra showing the crystalline peaks associated with the p-CNCs compared to those of commercial UMaine s-CNCs, with the 110, 012, 200, and 004 planes indicative of cellulose type I. The s-CNCs show an additional peak at the 1$\bar{1}$0 plane which is associated with a higher crystallinity.[55]

3.3.6 Thermal Stability: TGA

P-CNCs have been shown in literature to have an increased onset of thermal degradation when compared to other functionalized CNCs. This is believed to be caused by the instability of higher number of surface charges attributed to different functionalization, such as sulfate or carboxyl groups instead of phosphate groups.[8,49] As surface charge increases or decreases, thermal stability responds oppositely, resulting in changing onsets of thermal degradation, i.e. 285 °C and 330 °C for s-CNCs and unmodified CNCs (h-CNCs), respectively.[8] It should be noted that h-CNCs possess only unmodified hydroxyl groups produced from hydrolysis via hydrochloric acid. TGA of p-CNCs showed an onset of thermal degradation, measured at a loss of 5 wt% after the loss of humidity content ($T_{d5\%}$), of 310 °C, shown in **Figure 3.5**. This correlates well with other reported onsets of p-CNCs ranging from 290 °C-330 °C, sitting in between the higher and lower $T_{d5\%}$ of the s-CNCs and h-CNCs.[8,49,56] It should be noted that the $T_{d5\%}$ of each sample was shifted with respect to the humidity content of roughly 4 wt%, 6 wt%, and 3 wt% for the p-CNCs, s-CNCs, and h-

CNCs, respectively. The difference in humidity content can be attributed to increasing water absorption by the CNCs as surface charge density increases.[5-6] Higher thermal stabilities have proven to be useful for multiple applications, such as casting and melt pressing films, and extrusion processing, without causing degradation or reduction of properties of the CNCs.[14,22,59]

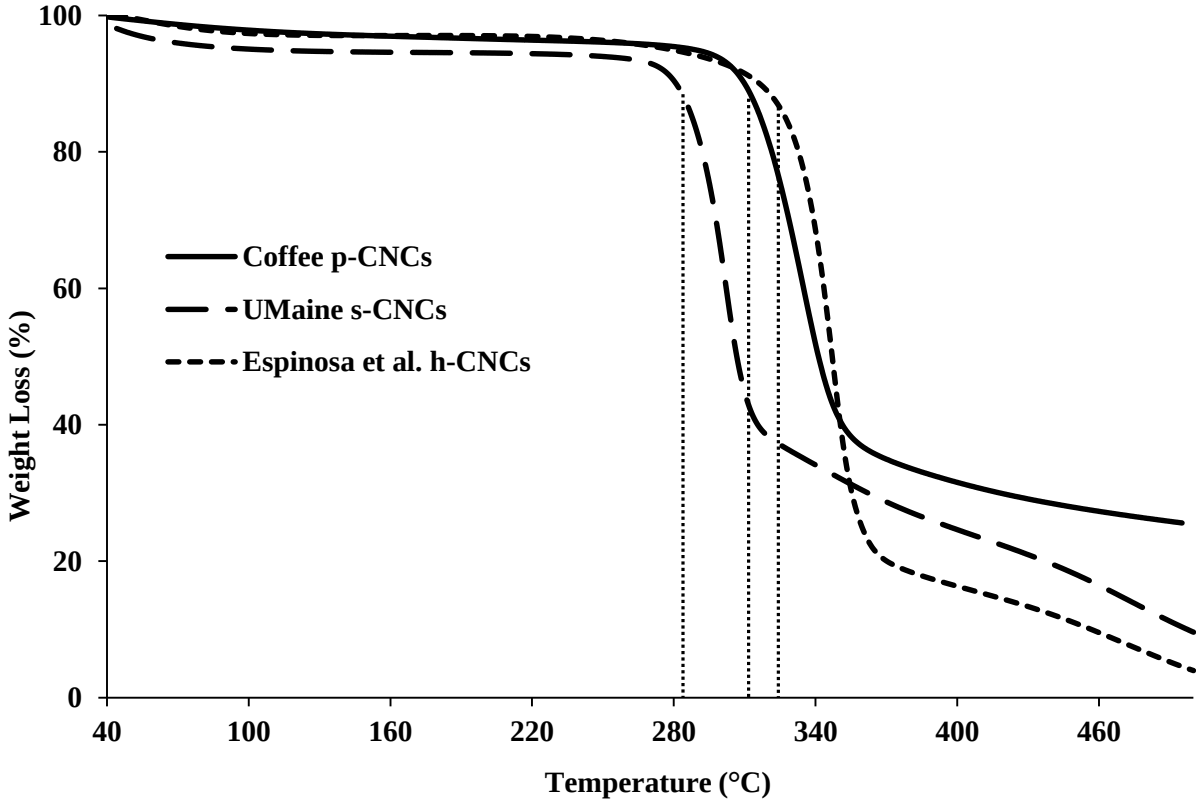

Figure 3.5 TGA plot comparing the thermal degradation of the isolated p-CNCs to commercially available s-CNCs. The vertical dotted lines refer to the onset of thermal degradation at $T_{d5\%}$=310 °C for the p-CNCs and $T_{d5\%}$=285 °C for the s-CNCs. These can also be compared to h-CNCs found in literature with an onset of $T_{d5\%}$=330 °C.[8]

3.3.7 Dispersibility and DLS

After initial sonication in the solvents, the p-CNCs showed good dispersion in water, DMSO, and DMF, while remaining agglomerated in THF. Continuing to monitor the dispersions, the p-CNCs did not show precipitation or agglomeration in either the water, DMSO, or DMF after a full ten days, as shown in **Figure 3.6**. Furthermore, the p-CNCs dispersed in DMSO and DMF continued to improve over time, and showed no signs of precipitates or agglomerations after an extended time of over two months. The higher clarity within the DMSO and DMF suspensions

show ideal dispersions with no precipitates or subsequent refraction of light.[8,43,60-61] Therefore, it should be noted that although birefringence behaviors were not displayed using crossed nicols, the dispersability is still comparable to literature references for both with and without birefringence, in which precipitates can be seen in non-ideal solvents such as THF and partially for water.[8,43,60-63] A key factor of CNCs dispersion has to do with the amount of charge on the surface, and how well they repel each other and accept the solvent. As surface charge increases due to higher phosphate contents or different functionalization (i.e. sulfate groups or carboxyl groups), dispersion in solvents increases since repulsion between CNCs is greater.[5-6]

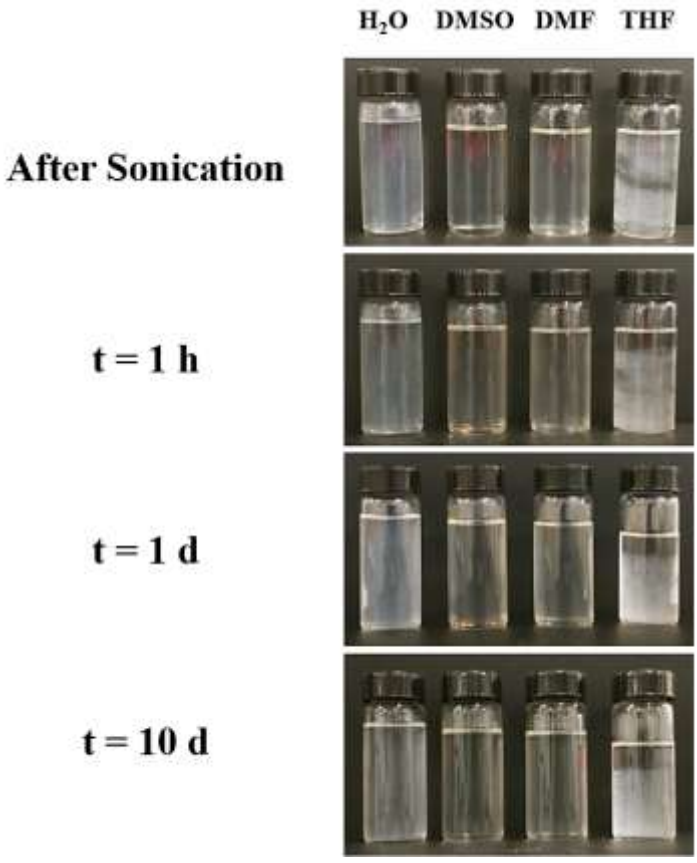

Figure 3.6 Images showing the 10 mg/mL p-CNC dispersions in water, DMSO, DMF, and THF, immediately following sonication, and subsequent times of 1 h, 1 d, and 10 d. The solvents used decrease in polarity from left to right.

Further characterizing dispersibility of the p-CNCs, DLS was used to determine apparent particle size in a diluted DMF dispersion. DMF was chosen as the dispersant of choice due to overwhelming literature regarding CNC dispersion in DMF.[8,21] DLS of the p-CNC suspension showed typical bimodal peaks with an apparent size of 139 nm-562 nm, which resides on the larger

end of literature, with normal sizes ranging from 163 nm-250 nm for Vanderfleet et al. to upwards of 400 nm-500 nm for Shanmugarajah et al.[49,64] The larger size range can be attributed to the difficulty of perfectly redispersing dried p-CNCs into solvents, therefore retaining small aggregates within the suspension is possible and probable. The ability for CNCs to disperse readily in solvents is crucial for integrating them into polymer composites. Uniform dispersion in the polymer matrix creates ideal networks between CNCs and the matrix, allowing for isotropic behaviors while retaining little to no defects from CNC agglomeration.[21]

3.3.8 Mechanical Reinforcement in Composites

The p-CNCs dispersed in the PU matrix showed a significant increase in mechanical properties compared to the neat PU, increasing the tensile modulus from (20.8 ± 0.8) MPa to (58.6 ± 2.7) MPa and increasing yield stress from (1.8 ± 0.1) MPa to (2.6 ± 0.1) MPa, respectively. However, the p-CNC composites showed lower mechanical properties when compared to commercial UMaine s-CNC composites, with a tensile modulus of (113.7 ± 9.7) MPa and yield stress of (3.6 ± 0.0) MPa, shown in **Figure 3.7**. Although there was not as much of an increase in mechanical reinforcement with the p-CNCs as with the s-CNCs, significant reinforcement with regards to the pure polymer shows potential for use in many polymer composite applications. The ability of the p-CNCs to reinforce the polymer matrix is crucial to the variety of applications of which it can be useful, such as strengthening a polymer for automotive industry compared to use in intervertebral disc or cartilage replacement.[11-12,21,44]

To avoid common misconception, it should be noted that although tension testing is typically run using controlled crosshead displacement or strain ramp on an Instron,[65-67] stress versus strains curves, and subsequent tensile moduli, can be determined through controlled force ramps using a DMA.[21,43,68-69] DMA uses an input of force while measuring the resultant strain, leading to an acceptable linear regime for tensile moduli analysis.[21,43,68-69]

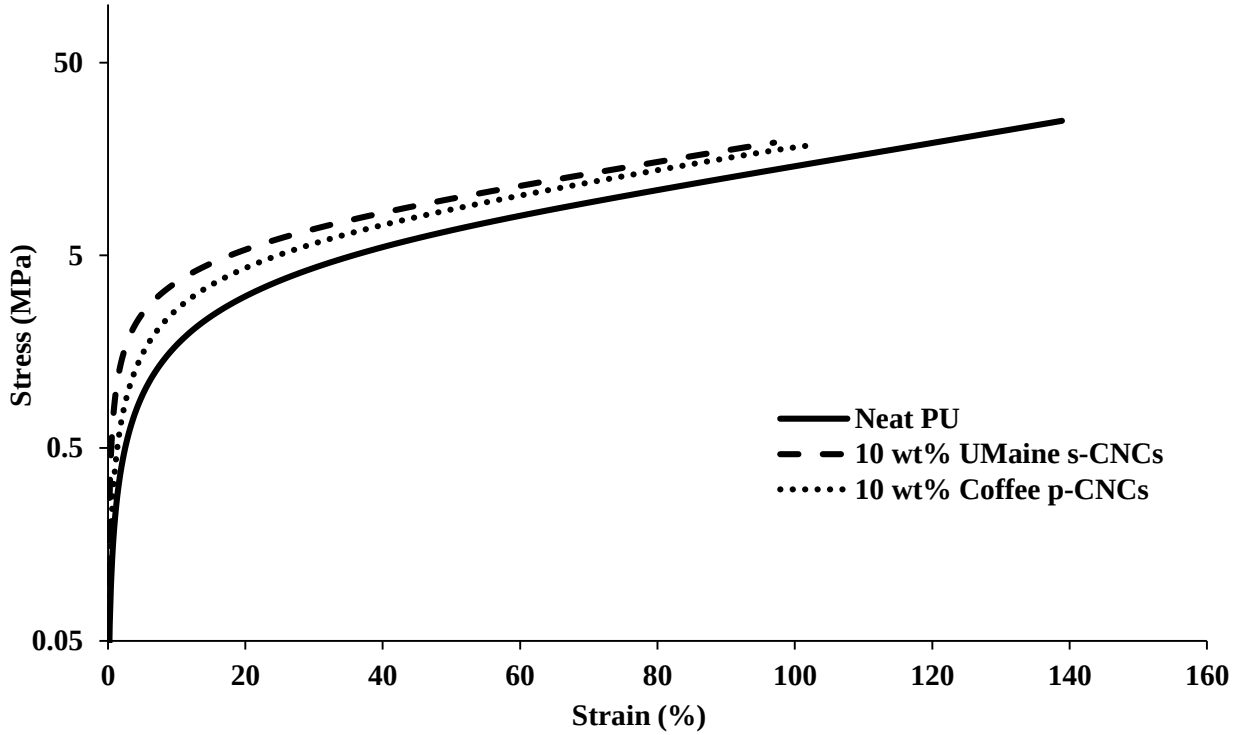

Figure 3.7 Tensile test results obtained with a DMA under controlled force ramp, showing a typical stress versus strain plot of neat PU, 10 wt% commercial UMaine s-CNCs in PU, and 10 wt% isolated p-CNCs in PU, to determine the reinforcement properties of the p-CNCs.

These differences can be caused by many variables, however, the most probable are surface charge density, crystallinity, and aspect ratio. As discussed previously in *Section 3.4.7*, surface charge density has a drastic impact on the ability of CNCs to disperse in a solvent. P-CNCs show a lower dispersibility than commercial s-CNCs in common solvents, which can lead to a less uniform dispersion and more agglomerations within the polymer matrix.[8] A continuous network of CNCs and high number of CNC-polymer interactions are needed to create a mechanically robust composite. These problems can cause defects in the continuous CNC network, reducing the overall mechanical properties from lower CNC-polymer interactions.[8] As alluded in *Section 3.4.5*, crystallinity plays a major role in the reinforcement of a polymer matrix. The higher the crystallinity of the CNCs, the higher the stiffness and strength, which directly correlates to increased reinforcement.[43,52] However, the p-CNCs produced in this study showed an around average crystallinity, therefore is assumed to not have had much impact on the decreased reinforcement. The final notable variable for the lower mechanical reinforcement is the aspect ratio of the p-CNCs compared to the commercial s-CNCs, most likely caused by the source of

cellulose.[11-12] The p-CNC aspect ratio of 12 ± 3, which were derived from spent coffee grounds, is on the lower end of the 10-40 aspect ratio range for the commercial s-CNC derived from wood pulp. As aspect ratio increases, the critical percolation threshold in the polymer composites decreases, resulting in less CNCs needed to create a continuous network and mechanically reinforce the polymer.[12] Therefore, at 10 wt% CNCs in PU, the commercial s-CNCs will have greater stress transfer between the CNCs and polymer matrix due to a larger, stiffer continuous network of CNCs.[11-12,70] However, it has been shown that as long as the aspect ratio is at or above 10, significant reinforcement is achieved in most polymer composite systems, as proven by the p-CNCs in this study.[12]

3.4 Conclusions

This study sought to establish a protocol for the isolation and characterization of p-CNCs from spent coffee grounds as a potential cellulosic waste material. The extraction of p-CNCs from the amorphous cellulose via phosphoric acid hydrolysis was proven successful, and further chemical and physical characterization determined the viability of the p-CNCs' usefulness. The resulting p-CNCs showed an aspect ratio of 12 ± 3, an apparent crystallinity of 74.2%, and a high phosphate content and surface charge density of (25.8 ± 9.6) mmol/kg cellulose and (48.4 ± 6.2) mmol/kg cellulose, respectively. The p-CNCs showed dispersibility in multiple organic solvents, with DMSO and DMF being the best candidates for dispersion. Nanocomposites were made using 10 wt% isolated coffee p-CNCs in PU and 10 wt% commercial UMaine s-CNCs in PU, and compared to determine the mechanical reinforcement ability in p-CNCs in a polymer-based nanocomposite. Although the nanocomposite reinforced with p-CNCs did not exhibit the same mechanical reinforcement as the commercial s-CNCs, there was still a three-fold increase in tensile modulus when compared to the neat PU. The dispersibility and mechanical reinforcement bodes well for the ability of the p-CNCs to be used in many polymer nanocomposite applications, in which fine tuning of p-CNC concentration is needed to achieve the necessary mechanical properties.[11-12,21] As well, the high phosphate content will increase the biocompatibility of the p-CNCs and cell adhesion and growth when introduced into a biocompatible polymer system.[44] The produced p-CNCs from spent coffee grounds compared well to other isolated CNCs from agricultural wastes throughout literature. Although the yield of CNCs was only about 8%-10% of the starting raw material, the nearly limitless source of spent coffee grounds worldwide allows for

potential mass quantities to be produced, regardless of low yield. With this in mind and the promise shown in this study, advancements toward industrial scalability should be further researched to determine the overall economic and environmental benefits of these results. Specifically, by the known sulfuric acid hydrolysis procedure already used in many industrial CNC manufacturers, such as University of Maine and Celluforce.[50]

Chapter 4: Gradient Poly(ethylene glycol) Diacrylate and Cellulose Nanocrystals Tissue Engineering Composite Scaffolds via Extrusion Bioprinting

4.1 Introduction

Additive manufacturing (AM) technology, also known as rapid prototyping, was originally introduced towards the end of the 1980s, and has grown substantially in the last few decades.[1-2] The process involves a "bottom-up" approach by adding materials layer by layer to create three-dimensional parts directly from computer-aided design (CAD) models, rather than the typical subtractive manufacturing approach.[1-3] The major AM processes include directed energy deposition, vat polymerization, powder bed fusion, material jetting and extrusion, sheet lamination, and binder jetting. All of these can be sub-sectioned into many other specific categories based on applications for which they are applied.[3-6] Additionally, AM processes have been expanded to multiple materials ranging from metal alloys, to polymer composites, to ceramics and concrete, lending to the current state of materials development and functionality.[3,5,7-8] With the many recent improvements in AM technology, a variety of industrial applications are now being discovered and commercialized, including applications in aerospace, automotive, architecture, electronics, medicine/biomedical, and even sports.[3,5-6,9] Most notably however, is the rise of biomedical applications, such as bioprinting/biofabrication of tissues, orthopedic implants and prosthetics, and regenerative medicine, among many others.[5-6,9-11] Bioprinting has experienced rapid growth in the last few years, becoming an important aspect in the biomedical field.[10-13] It utilizes multiple aspects of tissue engineering such as biomimicry, autonomous self-assembly, and mini-tissue building blocks through precise layer by layer positioning of compatible bioinks to produce complex 3D functional living tissues.[11-14] These bioinks typically consist of biologically compatible materials, with or without seeded cells, in a resin or ink form that can be cast, printed, or otherwise molded, and subsequently crosslinked by a stimulus to create a biomaterial scaffold.[11-14]

The four main types of bioprinting techniques are laser-assisted bioprinting, inkjet bioprinting, extrusion bioprinting, and stereolithography (SLA), all of which have been heavily studied in the bioprinting field.[13-19] Each of these techniques use unique processes such as thermal, piezoelectric, mechanical, and light energy, to develop complex tissue scaffolds with high

resolution (1-500 µm) and high cell viability (80-98%).[13-19] Although all of these techniques have been used for bioprinting of tissue engineering and regenerative medicine applications, each have their limitations and disadvantages. For example, SLA can only print single photocurable polymer resins with a single cell type, while extrusion bioprinting can print multi-material assemblies with varying cell types.[13,18-19] However, extrusion bioprinting falls short with bioinks needing to possess a certain viscosity in order to hold shape after printing.[13-14,17-18] Therefore, research has been poured into improving these techniques to broaden their capabilities in the bioprinting field,[13-19] with this study focusing on the extrusion bioprinting technique and compatible bioinks.

These printing techniques combined with advancing cell biology and biomaterials have allowed for the progression of tissue engineering and regenerative medicine to applications, such as organ replication and wound repair.[11-14,20-21] Initially, the challenges facing bioprinting were biological in nature, relating to cell viability and long-term functionality after printing (apoptosis).[6,10,14] Thus, bioprinting began as a way to print complex 3D biocompatible and biodegradable scaffolds that could later be seeded with cells and support matrices such as extracellular matrix.[10] Countless research to solve this limitation has since pushed bioprinting techniques past the challenges of integrating cells into bioinks, and towards printing functional tissue scaffolds.[6,11,13-14] However, these advancements have led to even more challenges, with further progression needed for improved reliability and functionality of bioprinting for major medical applications.[6,10-11,13-14,21] For example, the availability of transplantable organs is drastically lower than the demand for organ transplant patients.[20] The demand of organ transplants in the US in 2015 was 121,070 individuals, while only 2,553 were available, leading to an average of 22 people dying from waiting, per day.[21] With efficient and effective bioprinting technologies, this major problem could become much less significant in a society with the ability to artificially replicate functional organs.[20-21] Thus, research focused on improving bioprinting in specific areas such as bioprinter technology, biomaterials, cell sources, vascularization, innervation, maturation, and complex 4D functionalization is crucial to address the medical problems facing society.[11]

Recent research has started to explore the areas of embedded stem cells and gradient scaffolds in pursuit of future tissue replacement.[12,21-26] The nearly limitless ability of stem cells to differentiate into functional cells promises to contribute to the regeneration of mesenchymal tissues such as bone, cartilage, muscle, ligament, tendon, and adipose, and could lead to much

more complex 4D tissue engineering concepts utilizing bioprinting techniques.[12,21-24] A few studies by Tasoglu et al., Irvine et al., and Moore et al., have demonstrated the ability and significance of embedding stem cells into 3D bioprinted scaffolds, which could offer great potential for multiple regenerative medicine applications and further development of regenerative therapies.[12,21-23] With environmental factors playing a major role in stem cell differentiation and growth, gradient (multi-material) scaffolds utilizing different materials and biological components could be of significant importance with regards to complex 4D bioscaffolds for tissue engineering applications.[21-23,25] Gradient scaffolds have been recently researched for tissue engineering applications in a few studies by Bracaglia et al., An et al., Woodfield et al., and Bittner et al., proving the efficacy of bioprinting complex 4D scaffolds.[25-28] However, these studies, among others, focus mainly on porosity gradients for cell integration and growth, rather than utilizing gradients of materials, stiffness, cell types, and biological factors.[25-28] Furthermore, these studies use SLA bioprinting, or other similar techniques, which only focus on a single cell type and material per scaffold instead of broadening the variety of gradients by other bioprinting techniques such as extrusion bioprinting.[11,25-28]

With current trends leading towards gradient scaffold fabrication and stem cell embedment, this paper seeks to further progress the field of bioprinting by fabricating novel poly(ethylene glycol) diacrylate (PEGDA)/cellulose nanocrystal (CNC) bioinks with varying ratios of PEGDA to CNCs, that can be used with a pneumatic extrusion bioprinting method to create single material scaffolds and gradient scaffolds for potential complex 4D tissue engineering applications. PEGDA and CNCs are both biocompatible materials that have been researched extensively for biomedical applications such as tissue engineering and regenerative medicine, however there are still many useful applications that have yet to be explored.[29-36] Most, if not all, of the PEGDA bioscaffolds[29-33] and CNC-reinforced bioscaffolds[33-36] have been fabricated using SLA and direct light curing due to their low viscosity, only allowing for the use of one material in resin form and one type of cell. Extrusion bioprinting has the ability to overcome these limitations by allowing different print heads to carry different compositions and/or materials and imbedded cell types, increasing the available complexity of the printed scaffolds.[11] Different ratios of PEGDA to CNCs will be used to tune the viscosity and resulting mechanical properties of each bioink, in order to allow printability of gradient scaffolds varying in composition, stiffness, and hydration. Cast scaffolds

will also be fabricated to compare the extrusion printing method with conventional casting and curing methods. These bioinks and printed scaffolds will be rheologically and mechanically tested, respectively, to determine the success of CNC reinforcement within the PEGDA matrix, as well as the variation in properties from a single composition scaffold to a gradient composition scaffold. Although it was not within the scope of this study, embedment of stem cells within each composition of PEGDA/CNC bioinks could prove effective in varying differentiation based on the different stiffness and hydration regions of the gradient scaffolds.[12,21-22,24] This ability to incorporate not only stem cells, but also multiple types of cells in varying bioinks using multiple print heads, could be used to increase the availability of tissue engineering applications featuring multi-component tissue replacements, such as ligaments, tendons, and membranes.[11-12,21-22]

4.2 Experimental Methods

4.2.1 Materials

Poly(ethylene glycol) diacrylate (PEGDA, M_n 575) and lithium phenyl-2,4,6-trimethylbenzoylphosphinate (LAP) were purchased from Sigma-Aldrich. Commercial sulfated cellulose nanocrystals (CNCs) in the form of an 11.8 wt% aqueous suspension was purchased from the University of Maine Nanocellulose Facility. The CNCs were extracted from a wood source and characterized with average dimensions of 150-200 nm in length and 5-20 nm in width, sulfur content of 0.94 wt%, and surface charge density of 330 ± 15 mmol/kg cellulose. All printing consumables including UV-resistant amber print cartridges, disposable plastic petri dishes, and 30, 25, and 22 gauge sterile high-precision conical bioprinting nozzles were supplied by CELLINK.

4.2.2 Fabrication of Bioinks

The 11.8 wt% aqueous CNC suspension was diluted to a 10 wt% suspension using DI water for ease of composition calculations (i.e. 11.8 mL of DI water was added to 100 mL of the 11.8 wt% CNC suspension to create a 10 wt% CNC suspension). PEGDA was then added to the 10 wt% CNC suspension to create a 500 mL mixture with ratios of 95/5, 90/10, 80/20, 70/30, and 60/40 w/w PEGDA to CNC mixtures, excluding wt% of the water. To reduce water content and increase viscosity, the mixtures were dried in an IKA RV 10 Auto Pro V-C Rotary Evaporator set at 20 mbar and 32 °C, and rotating at 70 rpm for 1 h. This resulted in gels resembling a thick paste, like that of Elmer's® glue. After rotary evaporation, 0.067 wt% LAP was added to each gel. The resulting gels of each composition were weighed in the wet state, then air-dried in a fume hood

and weighed again to determine the actual composition of the bioinks to be used for printing, shown in **Table 4.1**. All bioinks were transferred into laboratory glass containers and stored in the refrigerator until use.

Table 4.1 Final bioink compositions, including wt% DI water, after 1 h in the rotary evaporator, determined by drying and verified by TGA.

Composition (w/w PEGDA/CNC)	wt% PEGDA	wt% CNC	wt% Water
95/5	71.1	3.7	25.2
90/10	46.8	5.2	47.9
80/20	28.6	7.1	64.3
70/30	27.9	11.9	60.1
60/40	20.0	13.0	66.6

The actual bioink compositions, mentioned in **Table 4.1**, were verified using thermogravimetric analysis (TGA). 10 mg of each bioink was measured into a platinum TGA pan, and heated from 25 to 500 °C at a rate of 10 °C/min using a TA Instruments TGA Q500 thermal analyzer. The bioink compositions were determined based on the weight left after complete water loss, shown in **Figure 4.1**.

4.2.3 Rheology

Rheology measurements were performed on an TA Instruments ARG2 torsional rheometer with a 40 mm plate upper geometry and a Peltier plate lower geometry with a trim gap of 1050 μm and a testing gap of 1000 μm. All measurements were carried out at 25 °C with a solvent trap. Each sample was pre-sheared at 1 s^{-1} for 30 seconds and allowed to equilibrate for 5 minutes. Yield stress measurements were conducted with a stress sweep, applied from 0.01 Pa to 1000.0 Pa with 10 points per decade at a frequency of 1.0 Hz with 10 samples taken per cycle. Steady shear measurements were conducted over the range 0.005 - 100.0 s^{-1} with 10 points per decade with a tolerance of 5% torque for 3 consecutive cycles. A 5 s delay was implemented to avoid rate ramp artifacts, and measured results were averaged over a 30 second time period. Yield stress values were calculated using the Trios onset function. A power-law model (**Eq. 1**) was fit to each set of shear sweep data, where the power-law is traditionally used to model the shear-thinning region of polymeric fluids. In this model η is the viscosity, K is the flow consistency index, $\dot{\gamma}$ is the shear rate, and *n* is the flow behavior index.

$$\eta = K\dot{\gamma}^{n-1} \quad \text{Eq. 1}$$

4.2.4 Casting PEGDA/CNC Scaffolds

Two methods were used for preparing the cast PEGDA/CNC scaffolds: casting and curing in a Teflon petri dish, and injecting and curing in between glass microscope slides. The casting process was made with the intention of determining the curing ability and swelling/drying capabilities of the bioink scaffolds. A 5 mL syringe, without the needle, was used to extract 5 mL of each PEGDA/CNC bioink composition. Each bioink was then extruded into a 60 mm Teflon petri dish and let to sit for 1 h. This allowed ample time for the bioinks to settle and ensure that the surfaces were flat and uniform. It should be noted that the bioinks remained stable over the hour and no settlement of CNCs was observed. UV initiating light from a UVP UVL-21 compact UV lamp with a wavelength of 365 nm at 4 W, 0.16 A, 115 V, and 60 Hz was applied directly to each bioink for 60 s to ensure full curing, following an adapted procedure from Fairbanks et al.[32]

The injection process was made with the intention of making usable cast bioink scaffolds for mechanical testing. Two 76 mm x 51 mm plain glass microscope slides were separated using 1.0 mm thick Teflon sheeting on each end, while the center region remained open. Each end was then clamped with a RV 05.10 balljoint clamp and tightened to ensure no slippage would occur and uniformity throughout the scaffold. As above, a 5 mL syringe, without the needle, was used to extract 5 mL of each PEGDA/CNC bionink composition. Each bioink was then injected in the open center between the two glass slides. Although 5 mL of the bioink was not needed to fill in between the glass slides, all of the material was injected to ensure removal of all air bubbles and potential defects. Once a uniform film was obtained, the bioink was cured using the previously mentioned curing technique, following an adapted procedure from Fairbanks et al.[32] The samples were then removed from the glass slides, and cut into 5.0 mm wide ribbons for future mechanical testing.

Swelling and drying tests were performed on the cast scaffolds to determine shrinking and permanent deformation with environmental changes. Each bioink scaffold that was cast and cured in the Teflon petri dishes was removed and immediately imaged. They were then left to dry for 24 h in a fume hood, and subsequently imaged again. After the drying process, each scaffold was submerged into 100 mL of DI water and left for another 24 h before being imaged again.

4.2.5 Bioprinting PEGDA/CNC Scaffolds

Each bioink composition was loaded into a 3 mL UV-resistant amber print cartridge (CELLINK, Blacksburg, VA), and capped on both the open end and nozzle end to prevent the bioinks from leaking and losing water. All scaffold printing used a three-printhead printer (CELLINK BIO X, Blacksburg, VA).

Preliminary printing using a generic rectangle configuration with a rectilinear infill pattern of 25% was conducted to determine the highest resolution printing parameters. Each composition started under the same initial printing conditions of 25 °C under air, 20 kPa of pressure, and extrusion rate of 10 mm/s using a 30-gauge nozzle. If the bioink was not successful in extruding through the 30-gauge nozzle using the initial conditions, the pressure was increased in increments of 5 kPa until a maximum of 75 kPa was reached. If there was still no success of extrusion at 75 kPa of pressure, the nozzles were changed to a higher gauge (25-gauge, then 22-gauge). The pressure settings were returned to initial conditions and the 5 kPa incremental increase was repeated until the extrusion was successful. The final high resolution printing parameters determined the ideal nozzle gauge to be 25-gauge, with pressure continually decreasing as CNC content increased from compositions of 90/10 – 60/40 w/w respectively, and were used as the initial printing conditions for the bioink scaffolds.

4.2.5.1 Single Material Scaffolds

A basic rectangle scaffold of dimensions 35 x 7 x 1 mm was designed using Autodesk Fusion 360 AutoCAD software, with the intention of being used for tension testing during mechanical characterization. Each single material scaffold was printed using a single composition of bioink, except for the 95/5 w/w, which showed poor printing properties. The printing conditions were initially set at the highest resolution parameters, and were adjusted based on how the material extruded during printing. As previously determined, a 25-gauge nozzle was used for all bioink compositions, and pressures were set at 45, 20, 15, and 12 kPa, decreasing as CNC content increased from compositions of 90/10 – 60/40 w/w, respectively. It should be noted that the printing resolution increased as well as, with increasing CNC content, further discussed in the rheology data, *Section 4.4.1*. Each scaffold composition was printed at least three times using a grid infill pattern of 100% at 25 °C under air, and UV-cured using a Gesswein 110V, 365 nm UV

post curing chamber for 60 s following an adapted procedure from Fairbanks et al.[32] Each scaffold was stored in a container filled with 50 mL of DI water until time of mechanical testing.

4.2.5.2 Gradient Scaffolds

As with the single material scaffolds, a basic rectangle scaffold of dimensions 35 x 7 x 1 mm was used for each gradient scaffold in order to maintain uniformity during mechanical characterization. However, the rectangular scaffolds were split into different designs, with each section of the design containing a different bioink composition, shown in **Table 4.2**. The four different designs include a three-layered rectangle, a two-layered rectangle, a three-sectioned rectangle, and a two-sectioned rectangle, shown in **Figure 4.5 and 4.8**. The compositions of 90/10, 80/20, and 70/30 w/w were the three chosen based on the mechanical properties determined from tension testing of the single material scaffolds. The 95/5 w/w was unable to print and the 60/40 w/w was too brittle to test reliably.

Table 4.2 The compositions of different sections used for each gradient scaffold.

Scaffold Design	Layer/Section 1 (w/w PEGDA/CNC)	Layer/Section 2 (w/w PEGDA/CNC)	Layer/Section 3 (w/w PEGDA/CNC)
Three-Layers	90/10	80/20	70/30
Two-Layers	90/10	80/20	N/A
Three-Sections	90/10	80/20	90/10
Two-Sections	90/10	80/20	N/A

It should be noted that each of the three available print heads contained one composition of bioink as follows: print head 1 = 90/10 w/w; print head 2 = 80/20 w/w; and print head 3 = 70/30 w/w. Additionally, the BIO X printer software was not yet capable of printing with multiple print heads from an AutoCAD assembly design STL file. Therefore, since multiple print heads were used for printing the gradient scaffolds, the AutoCAD design needed to first be exported to Slic3r, and assembled into a workable multi-material scaffold capable of using three print heads. After the scaffold was reworked in Slic3r, the design was exported as a GCode file and transferred to the BIO X printer. At least 3 of each gradient scaffold was printed using the same parameters as the single material scaffolds, with a grid infill pattern of 100% at 25 °C under air. Each scaffold was then UV-cured using the previously mentioned curing technique for the single material scaffold, following an adapted procedure from Fairbanks et al. [32]. The scaffolds were subsequently stored in a container filled with 50 mL of DI water until time of mechanical testing.

4.2.5.3 Mechanical Testing and Characterization

After the printed samples had been cured, three of each composition from both single material scaffolds and gradient scaffolds, as well as three of each cast scaffolds were mechanically tested utilizing a TA Q800 Dynamic Mechanical Analyzer (DMA). Each sample was tested in tension using an isostatic force test with a force ramp rate of 3 N/min at 25 °C until either the scaffold fractured or a maximum of 18 N was reached. It should be noted that all samples remained submerged in DI water to stay hydrated until time of testing.

4.3 Results and Discussion

4.3.1 Bioink Characterization

PEGDA and CNCs were chosen as the polymer matrix and reinforcing agent, respectively, for the composite bioscaffolds due to biocompatibility, tunability, and extensive research on the materials [29-36]. PEGDA shows very low viscosity at room temperature, limiting this material to SLA bioprinting and other similar techniques. Almost all related studies have shown success with printing PEGDA scaffolds for biomedical applications using SLA, however this technique only allows for one material resin and one cell type to be printed per scaffold [18-19,29-32]. CNCs have shown the ability to vary mechanical properties of polymer composites and scaffolds based on varying content within the polymer matrix [33-34,37-40]. The addition of CNCs will therefore help to increase viscosity and stiffen the bioinks in order to limit the deformation and help to maintain their structure before photocrosslinking [41-42]. This ability to hold their shape is crucial to expanding the printability of PEGDA to extrusion bioprinting techniques, which will lead to more complex printing structures compared to SLA, such as gradient scaffolds using multiple materials and cell types. As well, the ability to use multiple printheads of an extrusion printer, each containing bioinks of varying CNC content, allows for the fabrication of gradient scaffolds with varying stiffness, and potential incorporation of multiple types of cells that can be specifically placed among the scaffold [28]. In further comparison, gradient scaffolds with regards to porosity can be obtained through SLA, while scaffolds with stiffness gradients and multiple cell types cannot.[25-28] Therefore, these bioink compositions could progress the field of extrusion bioprinting.

Drying tests and TGA were performed to determine the water content, and subsequent dry weight of PEGDA and CNC within the bioinks, shown in **Table 4.1** and **Figure 4.1**. A few trends were observed with varying CNC concentration, including higher water content and char yield

with increasing CNC content, while maintaining nearly identical degradation onsets of each component in the bioink. Polymer composites using CNCs as a reinforcing agent have been shown in literature to increase water absorption with increasing CNC content, even for hydrophobic polymer composite systems.[38,43-44] As water comes into contact with the CNC network, the hydrogen bonds between the CNCs are broken leading to increased space and swelling within the composite or bioink.[38-39,43-44] With regards to the onset of thermal degradation, the expected results agreed with the observed trends, in which each bioink component degraded within its respective range (i.e. water near 100 °C, sulfated CNCs between 260-280 °C,[45-46] and PEGDA between 350-450 °C[47-48]). It should be noted that at the 90/10 w/w composition, the bioink goes through a transitioning point from low to high viscosity and develops agglomerates of separate discrete phases within the PEGDA. It is assumed that the clumps lead to the discontinuity in weight loss during the onset of PEGDA degradation.

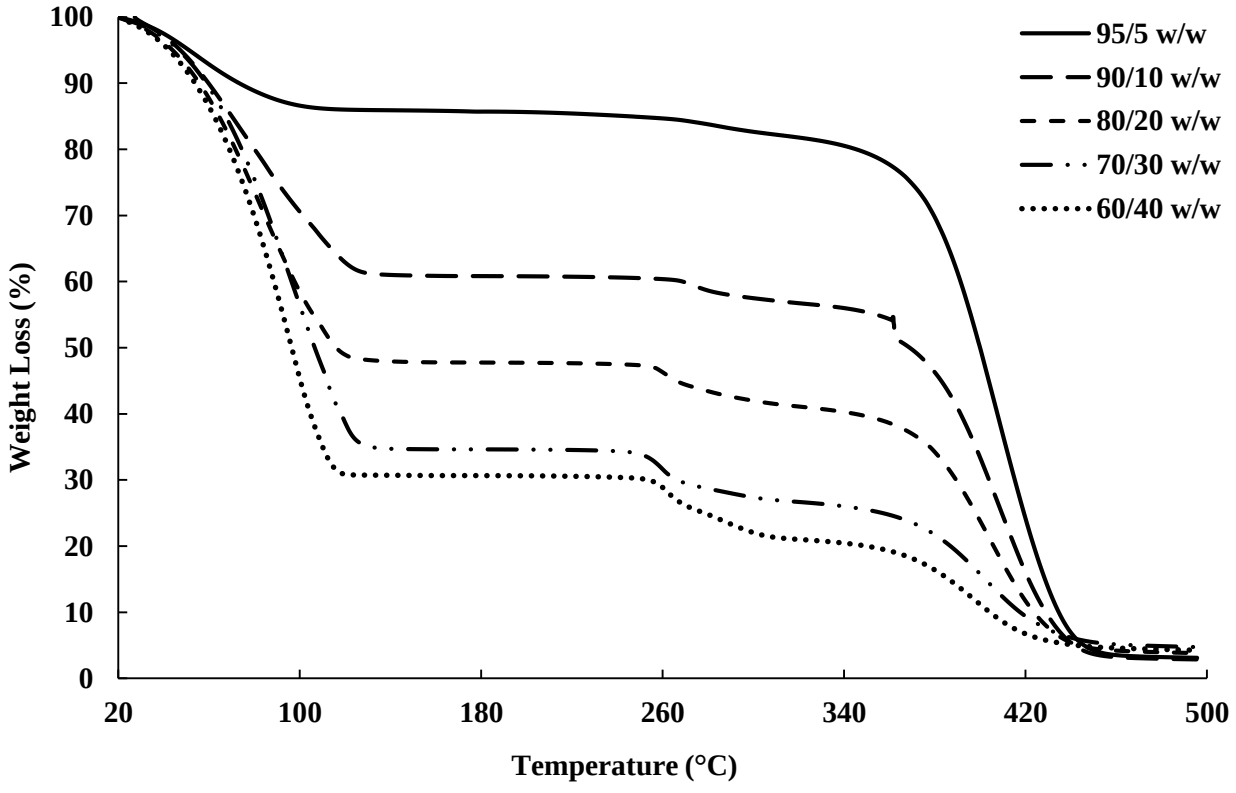

Figure 4.1 TGA plot of weight loss versus temperature showing the evaporation of water near 100 °C, followed by the CNC degradation between 260-280 °C and PEGDA degradation between 350-450 °C.[45-47]

Steady shear torsional rheometry of the bioinks revealed shear thinning behavior of the PEGDA/CNC suspensions over all measured rates. This behavior is typical of CNCs within a suspension or viscous matrix, such as a melt or a gel, in which shear thinning increases as shear rate increases due to the alignment of the CNCs in the shear direction.[49-51] **Figure 4.2** displays the viscosity as a function of the shear rate for each of the bioinks. As expected, higher CNC loading corresponds to higher viscosities, however, above 20 wt% CNC there is minimal change in steady shear behavior. The 95/5 w/w PEGDA/CNC sample presented issues due to its low viscosity, approaching the lower load limit of the transducer. **Figure 4.2** also displays the power-law model (**Eq. 1**) fits for each composition. The flow consistency index and flow behavior index are provided in **Table 4.3**. Aside from the 95/5 composition, the flow index was similar at approximately 0.11 for all samples, suggesting similar shear thinning behavior across all compositions. Furthermore, the flow consistency index reflects the increasing zero-shear viscosity of the samples as CNC content is increased. **Table 4.3** also presents the yield stress for each sample, which increase with CNC content. A higher yield stress should withstand higher load before induced flow, allowing for more layers to be deposited before photo-curing is necessary to retain the scaffold shape. While this is beneficial for printing taller scaffolds quickly, it also necessitates higher stresses on any cells that may be printed at the same time. As a result, tuning of these parameters is necessary for successful printing of both the geometry and the cell lines. Similarly, both the flow rate and the corresponding viscosity of the bioink must be carefully tuned to control road volume and to avoid pressure buildup within the printer.

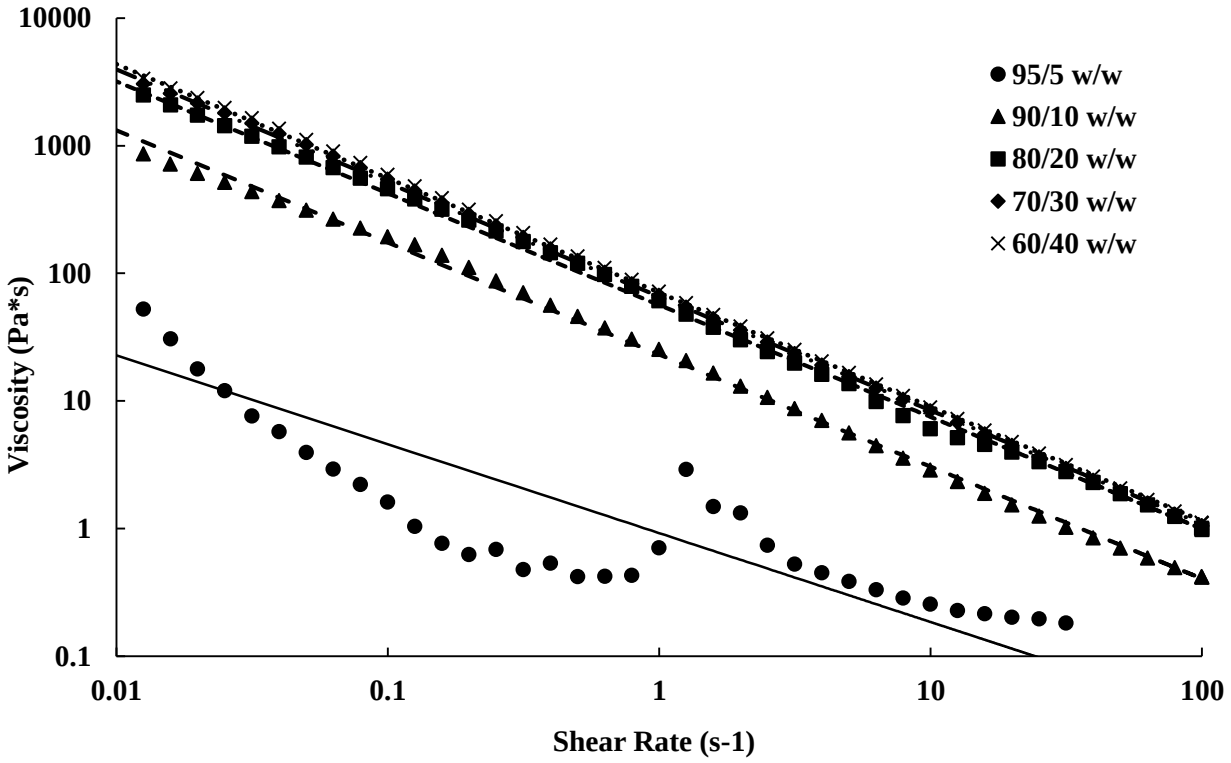

Figure 4.2 Steady shear viscosity as a function of shear rate showing shear thinning properties of each bioink over approximately four decades. Increasing viscosities are observed as CNC content increases in the bioink compositions. Data points represent actual data, and lines are power-law model fits.

Table 4.3 Yield stress and power law model parameters for each bioink composition.

Composition (w/w PEGDA/CNC)	Yield Stress (Pa)	Flow Consistency Index, K ($Pa \cdot s^n$)	Flow Behavior Index, n
95/5	0.79	0.95	0.37
90/10	37.75	23.08	0.12
80/20	40.09	56.41	0.12
70/30	57.63	65.57	0.11
60/40	60.94	70.67	0.10

4.3.2 Cast PEGDA/CNC Scaffolds

Each composition of bioink was cast into a Teflon petri dish and cured using UV light, resulting in the disc-shaped scaffolds shown in **Figure 4.3**. Drying and swelling tests revealed that the higher CNC content scaffolds (80/20, 70/30, and 60/40 w/w) start to deform and actuate when

dried, and fully recover their initial shape after subsequent swelling. The lower CNC content scaffolds (95/5 and 90/10 w/w) showed less deformation and change during drying and swelling, maintaining their disc-like shape throughout the process, however, fracture occurred during swelling from rapid expansion of the brittle cross-linked PEGDA.[52-53] It is believed that as CNC content increases, the crosslinking of the PEGDA is increasingly inhibited, leading to shorter chains and networks throughout the composite. This phenomenon induces greater strains on the longer, less mobile networks of chains when the lower CNC compositions are swelled.[54] This leads to a higher chance of fracture, unlike more elastic polymers such as polyurethane, where the swelling of the composite would result in no fractures.[38] As well, the drying and reswelling properties themselves showed novelty compared to typical CNC hydrogels found in literature.[55-57] Usual trends observe that as CNC content within the scaffolds increases, specifically above 5 wt%, the swelling properties drastically decrease and lead to further embrittlement.[55-57] The composite scaffolds in this study showed a surprisingly opposite effect, in which additional CNC content resulted in higher swelling properties and lower fracture potential upon drying and reswelling. These unique properties can be attributed to efficient dispersion of CNCs within the scaffolds and increased defects in the PEGDA crosslinking due to higher inhibition from increased CNC content, leading to additional free volume within the scaffold. The optical properties also fluctuated with varying CNC content, increasing in opaqueness as CNC content increased.[38] Although color and transparency varied between the scaffold compositions, they all demonstrated enough transparency to see lettering underneath, shown in **Figure 4.3**.

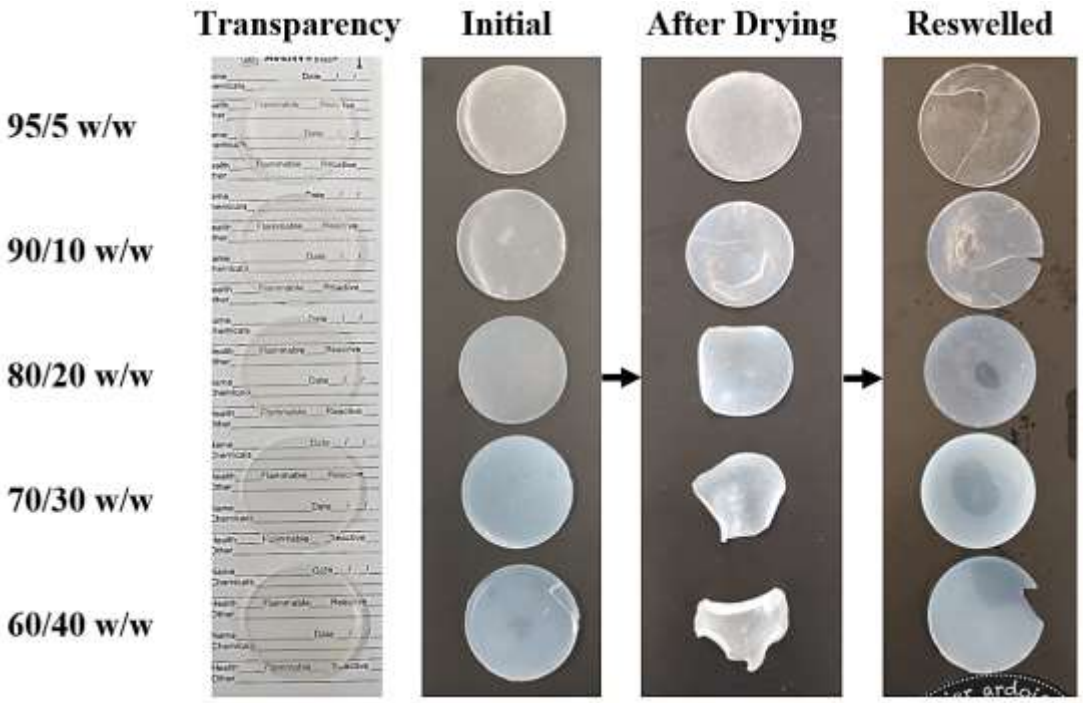

Figure 4.3 An image showing the optical properties and drying and swelling properties of each composition of cast scaffolds. The arrows show the scaffolds going from initially crosslinked to dried back to swelled. Deformation of the dried scaffold increases as CNC content increases. Opacity also increases with CNC content, however, the scaffolds still remain translucent in the swelled state (left most image).

4.3.3 Bioprinted PEGDA/CNC Scaffolds

Scaffolds of each bioink composition and gradients of bioink compositions were 3D bioprinted using a three-headed printer (CELLINK BIO X, Blacksburg, VA). Unlike the casting technique, the bioprinting technique allowed for ordered scaffolds with specific infill patterns and CNC alignment with subsequent crosslinking alignment of PEGDA. When the bioink is extruded through the print head nozzles, they experience a shear stress that aligns the CNCs in the direction of the print head movements.[58-59] The alignment of CNCs can be utilized to design complex hierarchical structures leading to directionality of mechanical properties and, when introduced, specific cell alignment.[58-60] This alignment also creates a larger barrier in one direction due to the aspect ratio of the CNCs, inhibiting the crosslinking of PEGDA in certain directions, leading to a general alignment of the crosslinked networks in the scaffolds.[61-62] This can be compared to the typical SLA technique, which exhibits random CNC orientation within the scaffold from the dispersion in the liquid polymer resin.[18-19,29] These comparisons can also be applied to cells and

other biological components within the scaffolds, in which extrusion bioprinting has the ability to align and place in specific locations.[11,18,33,60]

Each single material scaffold was printed using the parameters listed in *Section 4.3.5.1*, however the 95/5 w/w bioink was unable to print due to the low viscosity. Instead of holding its shape after printing, the low surface energy caused the bioink to adhere and wet the surface. The single material scaffolds showed a higher uniformity in its dimensions compared to both the cast and gradient scaffolds, shown in **Figure 4.4 and 4.5a**. Since the cast scaffolds were cut into strips using a razor blade, the brittleness of the crosslinked PEGDA led to rough, defected edges, while the printer was able to lay down a much smoother perimeter of bioink to hold the dimensions of the scaffolds before crosslinking.

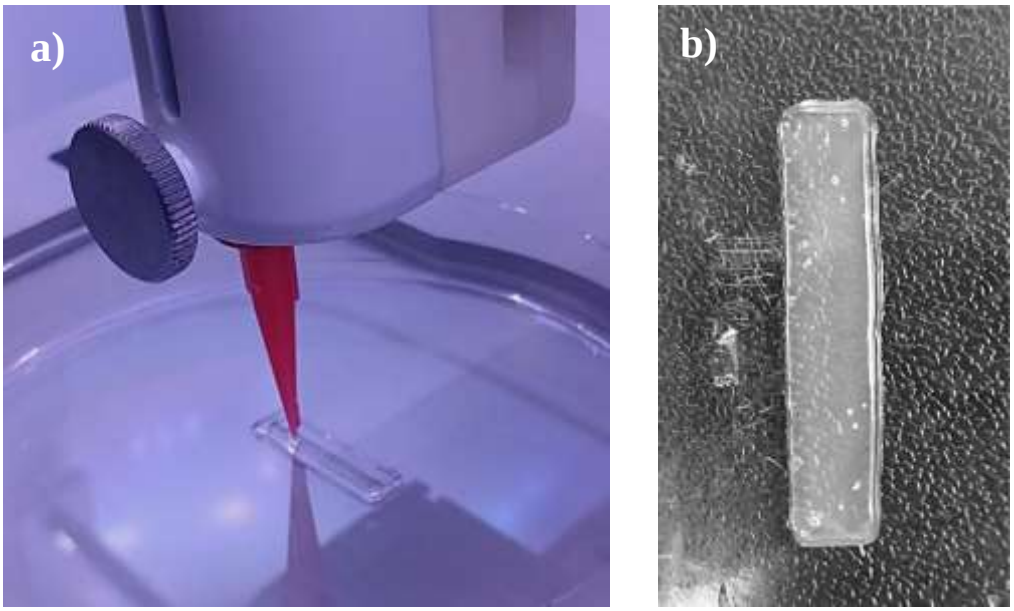

Figure 4.4 Images depicting a) **the printing process of each scaffold, laying down the perimeter and grid infill pattern, and** b) **an example of the single material scaffolds (90/10 w/w) after crosslinking via UV light. Smooth and uniform dimensions were produced from printing single material scaffolds.**

The gradient scaffolds were printed using the parameters listed in *Section 4.3.5.2*. Although the gradient scaffolds were printed using the same parameters as the single material scaffolds, they showed a decreased uniformity due to the use of multiple print heads, shown in **Figure 4.5a**. Each print head had to be calibrated identically. However, the calibration was manually performed, therefore the dimensions were not as uniform as the single material scaffolds. The layered gradient scaffolds showed higher uniformity, similar to that of the single material scaffolds, shown in **Figure 4.5b**. Although the dimensions were slightly less uniform, the gradient scaffolds showed

distinct regions in which different bioink compositions were used. Unfortunately, even with distinct regions printed, the relatively low yield stress properties of the bioinks caused the different compositions to flow slightly into one another. This creating crosslinking between the sections and layers. Additionally, the 90/10 and 80/20 w/w compositions, shown in **Figure 4.5a**, demonstrated a unique optical property, switching translucency after crosslinking.[63]

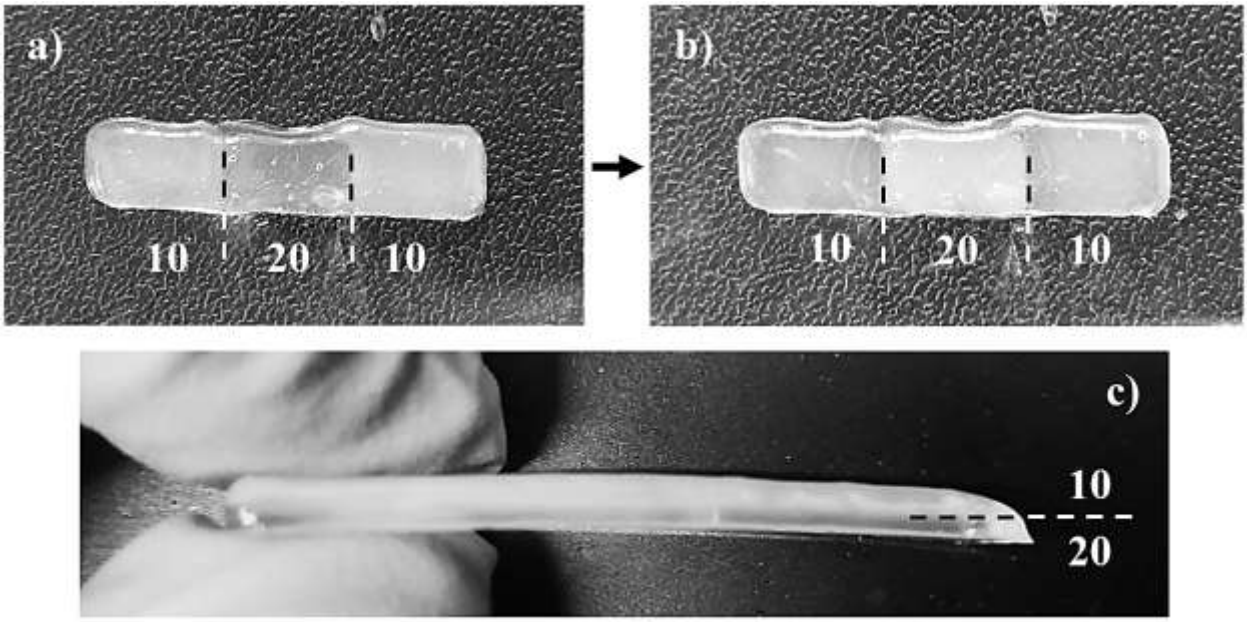

Figure 4.5 Images depicting a) **the 10/20/10 (by wt% CNC) sectioned scaffold before and** b) **after crosslinking via UV light, and** c) **the 10/20 (by wt% CNC) layered scaffold after crosslinking via UV light. The sectioned scaffold was less uniform due to small calibration errors in the print heads, and demonstrates unique optical properties, switching translucency of compositions after crosslinking. The layered scaffold stayed relatively uniform, and the multiple layers can be seen.**

4.3.4 Mechanical Testing and Characterization

Three samples of each composition of cast, single material, and gradient material scaffolds were mechanically tested and characterized using a controlled force ramp in a DMA, resulting in the mechanical properties shown in **Table 4.4**. Throughout all of the samples, a general trend was observed in which the elastic moduli and yield stresses decreased as CNC content increased. The strain at break however, showed no observable trend for the cast scaffolds, and a decreasing trend with additional CNC content for the single material scaffolds. The gradient scaffolds showed unique characteristics and trends, borrowing certain properties from each composition of bioinks used, which is typical for multi-material composites.[34,64-66]

Table 4.4 Mechanical properties of the cast, single material, and gradient scaffolds as determined by DMA.

Cast Scaffolds					
Composition	95/5 w/w	90/10 w/w	80/20 w/w	70/30 w/w	60/40 w/w
Elastic Modulus (MPa)	27.8 ± 5.8	18.3 ± 2.5	9.6 ± 0.5	1.7 ± 0.1	0.4 ± 0.1
Yield Stress (MPa)	0.7 ± 0.1	0.5 ± 0.1	0.4 ± 0.1	0.2 ± 0.1	0.1 ± 0.0
Strain at Break (%)	12.9 ± 11.3	14.2 ± 9.6	7.5 ± 3.5	14.5 ± 6.3	22.9 ± 8.9
Single Material Scaffolds					
Composition	95/5 w/w	90/10 w/w	80/20 w/w	70/30 w/w	60/40 w/w
Elastic Modulus (MPa)		16.5 ± 3.0	7.5 ± 3.3	2.7 ± 0.2	0.9 ± 0.1
Yield Stress (MPa)	N/A	0.3 ± 0.1	0.1 ± 0.1	0.1 ± 0.0	0.1 ± 0.0
Strain at Break (%)		46.7 ± 22.3	22.1 ± 4.8	15.5 ± 8.9	8.1 ± 2.3
Gradient Material Scaffolds					
Composition*	10/20/30 Layered	10/20 Layered	10/20/10 Sectioned	10/20 Sectioned	
Elastic Modulus (MPa)	11.3 ± 0.7	16.7 ± 1.3	14.7 ± 2.4	12.1 ± 2.6	
Yield Stress (MPa)	0.3 ± 0.1	0.1 ± 0.0	0.2 ± 0.0	0.1 ± 0.0	
Strain at Break (%)	40.9 ± 30.2	8.7 ± 3.4	17.6 ± 8.5	8.0 ± 3.6	

*As previously discussed in *Section 4.3.5.2*, the numbers refer to the wt% CNC in the composition

4.3.4.1 Cast Scaffolds

The DMA data acquired for the cast scaffolds during tensile testing revealed a general trend of decreasing elastic moduli and tensile yield stresses with increasing CNC content, shown in **Figure 4.6**. It should be noted that the elastic moduli were determined by the taking the slope of the linear viscoelastic region and tensile yield stresses were determined by the break in linearity from the linear viscoelastic region. Although this disagrees with most literature, in which CNCs typically increase the mechanical integrity of the composites,[34,37-40,67-68] these observations can be explained by the unique crosslinking inhibition of the CNCs in PEGDA, as well as the increased water absorption through higher degrees of hydrophilicity.[29,61-62] As the CNC content increases, the PEGDA chains have less ability to form crosslinked networks from the barrier formed by the CNCs.[61-62,69] Additionally, the hydrophilicity of CNCs caused an increased plasticization within the composites by breaking the hydrogen bonds between CNC networks.[29,35-36] Furthermore, the cast scaffolds maintained random orientation of CNCs within the PEGDA, causing the lower CNC

compositions (95/5, 90/10, and 80/20 w/w) to stay under the percolation threshold.[38] This allowed the cast scaffolds to be slightly more reinforced than their bioprinted single-material scaffold counterparts, discussed in *Section 4.4.4*. However, as the CNC content increased into the 30 wt% regime, the random orientation of the CNCs caused the scaffolds to pass the percolation threshold isotropically, resulting in defects and lower mechanical properties.[38] The strain at break showed no specific trend with increasing CNC content, however the 80/20 w/w scaffolds showed the lowest value of 7.5 ± 3.5%, while the other compositions were at minimum above 10%.

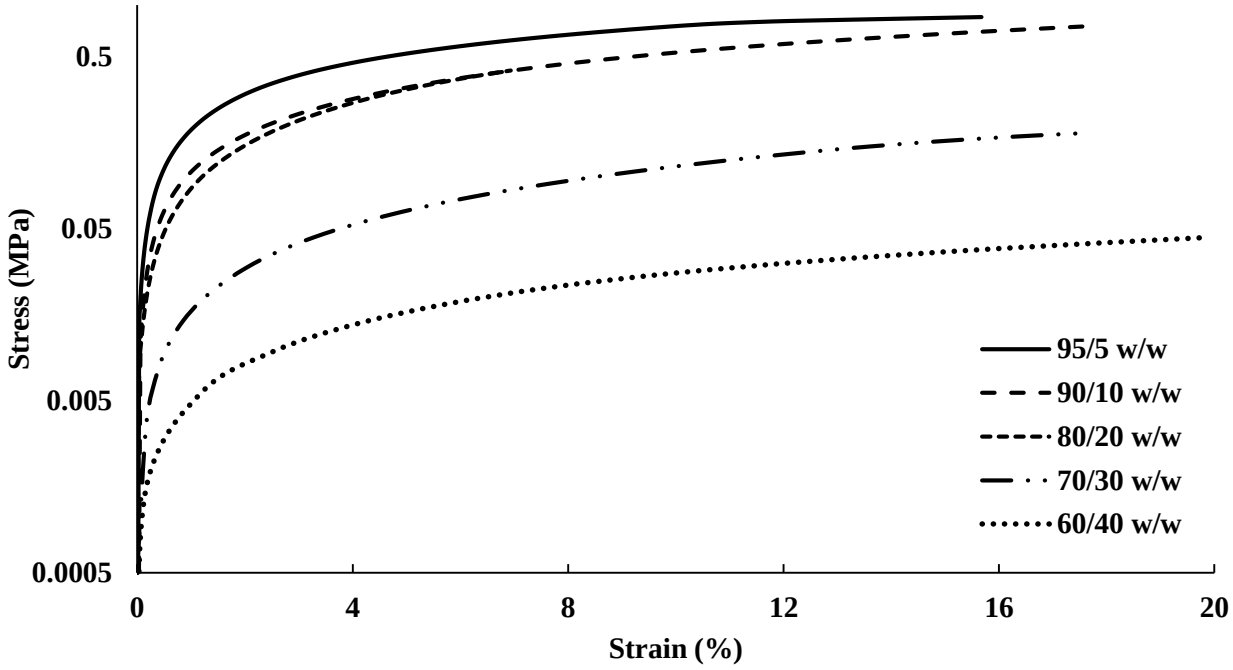

Figure 4.6 DMA stress versus strain plot of each composition of cast scaffolds showing strain until break.

4.3.4.2 Single Material Scaffolds

The DMA data obtained for the single material scaffolds revealed a similar trend to the cast scaffolds, decreasing in elastic moduli and tensile yield stresses with increasing CNC content, shown in **Figure 4.7**. Like the cast scaffolds, this trend disagrees with most literature reporting increased tensile mechanical reinforcement with increasing CNC content.[34,37-40,67-68] As previously discussed, this is believed to be caused by the increase of CNCs inhibiting the crosslinking ability of the PEGDA, with the additional plasticization via increase in water content .[35-36,61-62] However, another general trend was observed that agrees with most literature, in which the strain at break decreased with increasing CNC content.[38-40,67-68] The 90/10 w/w showed the best mechanical properties of higher reinforcement and strain at break compared to all other compositions.

Although the elastic moduli for the 90/10 and 80/20 w/w compositions were slightly below the cast scaffolds, the higher CNC content of 70/30 and 60/40 w/w compositions showed almost double the elastic moduli in comparison. Further, the 90/10, 80/20, and 70/30 w/w compositions showed higher strains at break than their cast scaffold counterparts. The tensile yield stresses of all compositions, however, maintained lower values than the cast scaffolds. These changes in mechanical properties may be caused by the alignment of the CNCs within the printed scaffolds.[58-59] As previously discussed, when the bioinks are extruded through the print head, the CNCs undergo shear stresses that align them in the direction of the nozzle and its motion.[58-59] Since a grid infill pattern was used for the single material scaffolds, printing at ± 45° angles to the perimeter, the mechanical properties followed the trends of a traditional composite material at those same angles, such as carbon fiber composites made with alternating sheet angles.[70-72] This allowed for nearly identical mechanical reinforcement properties as the cast scaffolds, however, drastically improved the strain at break for the lower CNC compositions, due to the "scissor" effect.[72-74] Moreover, since the CNCs were aligned at ± 45° angles to the tension testing clamps, the tensile yield stresses showed a decrease from the cast scaffolds due to the same "scissor" effect.[72-74] It should be noted that previous studies have shown CNC and material alignment through polarized Raman spectroscopy, when shear force is applied through either rheology, extrusion, or 3D printing.[44,51,75-76] And although polarized Raman spectroscopy was not performed in this study to show CNC alignment, based on current literature references of CNC alignment properties through shear, it can be inferred that some alignment within the structure in the direction of the printing nozzle occurred, leading to the observed mechanical properties and trends.[44,51,75-76] Since the 95/5 w/w composition had too low of a viscosity to print successfully, the properties could not be compared with the 95/5 w/w cast scaffold.

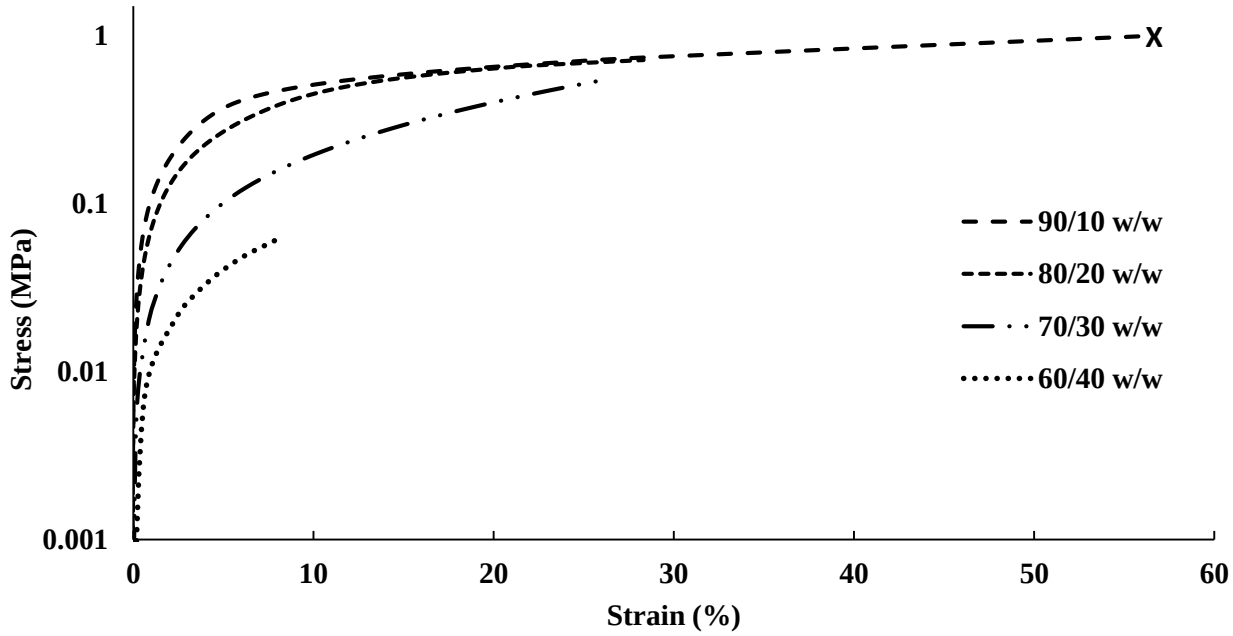

Figure 4.7 DMA stress versus strain plot of each composition of single material scaffolds showing strain until break.

4.3.4.3 Gradient Material Scaffolds

The DMA data for the gradient scaffolds did not show any specific trend with regards to CNC content increasing, however, demonstrated properties from all compositions used within the scaffolds, shown in **Figure 4.8**. The best mechanical properties were exhibited by the layered scaffolds, increasing the overall elastic moduli and tensile yield stresses when compared to the higher CNC compositions of the cast and single material scaffolds. The layered scaffolds show an ideal distribution of loads, in which the weaker compositions increased in mechanical toughness and the flexible compositions increased the elongation of the gradient composites,[34,64-66] shown in **Table 4.4**. The sectioned scaffolds showed a similar combination of characteristics from the use of multiple bioink compositions, however, the seams of the sections led to failure through separation.[77] The force applied by the DMA was perpendicular to the crosslinked seams within the sectioned scaffolds, causing failure to occur at those stress points,[77] as opposed to the layered scaffolds having equally distributed force among all of the layers.[78] It should be noted that the layers did not delaminate during tensile testing. As well, the network of CNCs maintained the same alignment effects as the single material scaffolds, lending the flexibility of the "scissor" effect to the structure, while the strength of the 90/10 w/w composition was utilized.[72-74] These scaffolds

demonstrated stiffness gradients that could be fine-tuned by using different bioinks of PEGDA/CNC ratios, while most other studies show the ability of porosity gradients.[25-28]

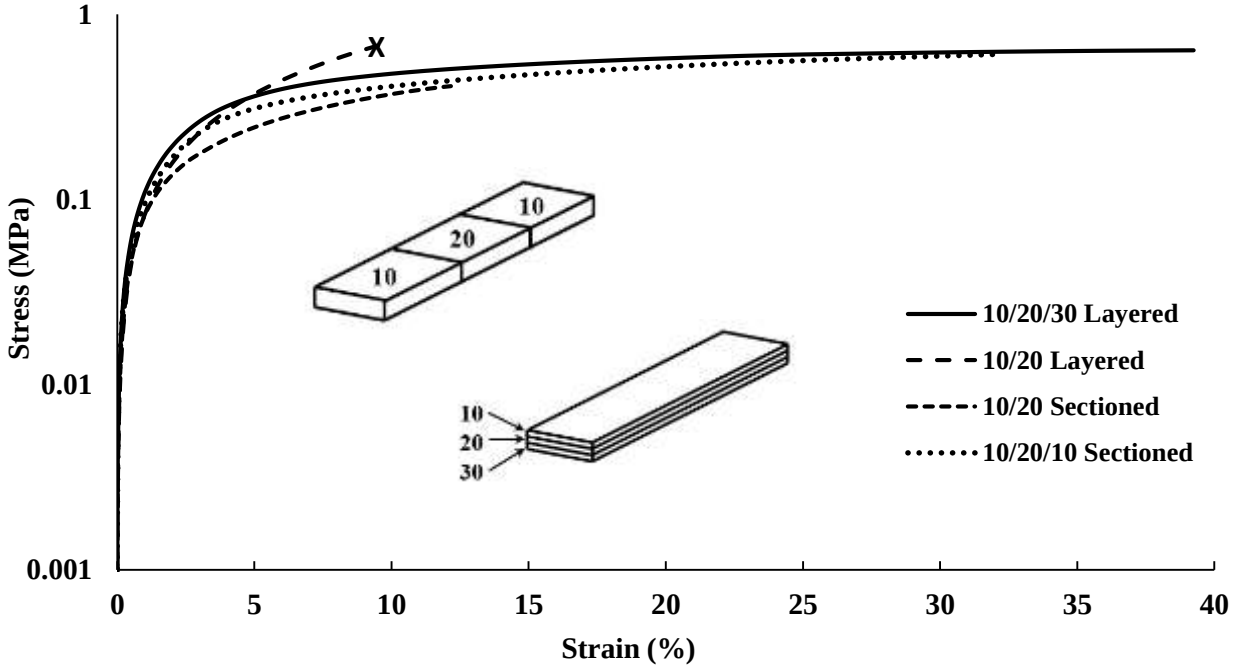

Figure 4.8 DMA stress versus strain plot of each composition of gradient scaffolds showing strain until break. Note that the scaffolds were split into sectioned and layered designs, superimposed into the graph, with each section of the design containing a different bioink composition. The compositions used for each scaffold are shown in Table 4.2**, for example, the 10/20/30 layered relating to 90/10, 80/20, and 70/30 w/w layers.**

Overall, the gradient scaffolds showed increased mechanical properties when compared to the cast and single material scaffolds of similar compositions. For example, the 10/20/30 layered gradient scaffold showed lower mechanical properties than the cast and single material 90/10 w/w compositions, however, they showed drastic improvements for both the 80/20 and 70/30 w/w compositions in all categories (elastic modulus, tensile yield stress, and strain at break). These results prove the ability to print multiple materials in a single scaffold, allowing for the tunability of the gradient scaffolds as a whole.

4.4 Conclusions

Bioprinting has advanced through many challenges and limitations in the past few decades, with research focusing on improving bioprinter technology, biomaterials, cell sources and viability, vascularization, innervation, maturation, and complex 4D functionalization. Recent advances such as novel bioinks, gradient scaffolds, and stem cell differentiation within scaffolds

have paved the way for complex 4D tissue scaffolds with improved reliability and functionality for modern biomedical applications. This study focused on expanding the bioprinting field through fabrication of PEGDA/CNC bioinks for extrusion bioprinting of single material and gradient scaffolds. The bioinks and scaffolds were thermally and mechanically characterized by TGA, rheology, and DMA. The final compositions of bioinks were determined, and a general trend of increasing water content and decreasing rheological yield stress with increasing CNC content was established. The 90/10, 80/20, 70/30, and 60/40 w/w bioinks showed high enough viscosities to print successful scaffolds, while the 95/5 w/w bioink not only demonstrated a low viscosity, but also showed slippage during rheology resulting in poor data. Unlike most CNC composites shown in literature,[35,37-39] as the CNC content increased, the scaffolds demonstrated a decrease in both elastic modulus and yield stress, while no specific trend was observed for the strain at break. The cast scaffolds showed higher mechanical properties for the 90/10 and 80/20 w/w compositions, and lower mechanical properties for the 70/30 and 60/40 w/w compositions when compared to the single material scaffolds. The gradient scaffolds showed unique mechanical properties, utilizing the benefits of each composition to increase mechanical properties of the scaffold as a whole. The bioinks and gradient scaffolds successfully demonstrated tunability of their mechanical properties by varying CNC content within the bioink composition and the compositions used in the gradient scaffolds. This work makes strides to overcome the main disadvantages of SLA printing which consist of the inability to print multiple cell types and materials in resin form, the lack of controlled directionality of materials, and the inability to place fillers, cells, and other biological components in specific locations among the scaffolds.[13,18-19,29-33] The PEGDA/CNC bioinks and scaffolds produced in this study seek to progress biomaterials and bioprinting technologies, by transitioning SLA-dominated PEGDA bioprinting to extrusion bioprinting, in order to produce more complex, functional scaffolds for tissue engineering. Extrusion bioprinting will allow for controlled directionality, cell placement, and increased complexity of materials and cell types, improving the reliability and functionality of the scaffolds for tissue engineering applications.

Chapter 5: Controlled Shape Memory Effects of Magnetic Polymer Nanocomposites via Induction Heating

5.1 Introduction

Stimuli-responsive materials, sometimes referred to as "smart materials", are those with the ability to change and adapt based on external stimuli and their surrounding environment.[1-2] Over the last few decades, functional polymeric materials have been designed and developed with this specific interest in mind, rapidly expanding their applications in scientific fields, such as nanotechnology, organic and physical chemistry, materials science, aerospace, biomedicine, tissue engineering, and regenerative medicine.[1-5] Although a multitude of characteristics can be obtained through different stimuli-responsive materials, 4-dimensional shape memory effects have been of particular interest.[4-7] These 4-dimensional effects are typically regarded as physical characteristics that can change over time. For example, the shape memory polymers (SMPs) that exhibit a time-controlled ability to change their hierarchical structure in response to external stimuli, such as chemical, electrical, thermal, light, moisture, and mechanical force, can be referred to as 4-dimensional materials.[7-11] By identifying suitable polymer architectures and functionalizing them through tailored programming, SMPs can respond to specific controlled stimuli, allowing them to be employed in a wide variety of applications.[11] Specifically, SMPs have found increasing interest in biomedical applications, such as tissue engineering, regenerative medicine, medical devices, and drug delivery, for their ability to behave similarly to the natural functions and movements of the human body.[9,11-16] When activated by stimulation, SMPs pass a thermal transition point, typically the glass transition temperature (T_g) of the polymer, which causes them to switch between an externally stressed and relaxed state.[9-11] These properties have been able to promote minimally invasive surgery, provide structural support, exert stabilizing forces, elute therapeutic agents, and biodegrade.[12-16]

Although the majority of SMPs are activated through direct contact with stimuli, such as a hot plate, chemical reaction, or electrical signals, some applications prevent direct contact resulting in a need for noncontact methods.[7-9,12-14,16-17] Common noncontact heat transfer methods include sources such as gaseous mediums, sunlight, or radiation to transition the SMPs past their activation temperature, but newer methods are being progressively researched.[17-18] Recently, increased attention has been given to SMP composites with the ability to undergo thermally activated shape

change by way of noncontact induction heating.[18-21] However, since polymeric materials do not contain electrical or magnetic properties, the addition of ferromagnetic nanoparticles embedded into SMP matrices is necessary to induce a thermal transition through induction.[17,20] Through varying ferromagnetic particle loading and strength of magnetic fields, defined movements of implants can be controlled and triggered directly, via different heating rates, final temperatures, and finely-tuned hierarchical changes.[14,17-21] This ability to finely-tune the SMP activation and movements significantly increases the potential of induction heating as a technically advanced noncontact heat transfer method.[17-18,20]

Although SMPs can mimic certain functions of natural human tissues by adapting and changing to external stimuli, they lack the hierarchical complexity and functionality mimicking the intricate ensembles of various cell types within well-defined extracellular matrices (ECM) needed for most biomedical purposes.[22-25] Hierarchical tissue structures are of significant importance to biological functions, lending abilities of protection, support, mechano-sensitivity, electro-activity, and shear stress-sensitivity through complex nanotopography.[26-29] However, this same intricacy that promotes vital biological functions, also creates a barrier in tissue engineering, due to the enormous variety of properties needed to replicate natural tissue function, growth, and recovery.[23-24,26-28] Therefore, in order to better mimic the complex architectural design of various biological tissues, hydrogel scaffolds have been exhaustively researched, making significant impacts in the biomedical field for their tunable and complex hierarchical structures, and ability to keep tissue hydrated, fight infection, and biodegrade.[30-33] Specifically, complex hydrogel fabrication from an abundance of both natural and synthetic polymeric materials, growth factors, and living cells, has been in the forefront of literature for their ability to replicate natural tissues.[30-33] And as such, have been employed in a variety of applications such as wound healing, promoting natural cell and ECM growth, and drug delivery.[23,28,34-37]

The final consideration that needs to be taken into account, is the viability of living cells within a given environment.[38-40] Very specific conditions are needed for cell survival, such as constant temperature of 37 °C, hydration, and sources of nutrients, and a hindrance of any of these conditions will result in significant decrease or complete termination of cell growth and viability.[22,27,38-41] Typically, SMPs have transition temperatures well above 37 °C, making induction heating a potential danger to cell survival, while most hydrogels lack the shape-memory

effects needed to actuate through stimuli.[17,20,30-33] Therefore, by combining the induction heating of SMPs composites with the intricate 4-dimensional structures and thermal buffering of hydrogel scaffolds, controlled hierarchical shape changes can take effect within the hydrogel without damaging cells due to excess heating and lack of hydration.

This research seeks to combine the biomedical enhancements and intricacies of hydrogel scaffolds with the ability to control hierarchical change using induction heating of an attached ferromagnetic SMP composite substrate. All polymers used are FDA-approved and biocompatible, with varying T_g and crystallinity, to show a wide range of thermal activation capabilities. Polyurethane, polyvinyl acetate, and nylon-11 were used as the SMP matrix with various iron oxide nanoparticle (Fe_3O_4 NPs) loadings, from 0 to 10 wt%, for induction heating variance. Each SMP composite was thermally characterized using thermogravimetric analysis, differential scanning calorimetry, and x-ray diffraction spectroscopy, and inductively heated using a multitude of magnetic field strengths. The hydrogel scaffolds were fabricated with varying ratios of sodium alginate (SA) to cellulose nanocrystal (CNCs) to finely-tune the mechanical properties, as determined by tension testing using a dynamic mechanical analyzer. Once all material characterizations were complete, a finalized scaffold was fabricated by crosslinking the hydrogel mixture directly onto the SMP composite substrate surface to induce mechanical interlocking between components, with the purpose of growing desired cells, based on any given application. The scaffold was then heated to produce controlled topographical shrinkage within the hydrogel, subsequently increasing internal pressure, to theoretically mechanically eject any embedded cells or components for enhancing replating techniques and tissue engineering applications. This study showed the benefits of creating a multi-functional scaffold with the ability to exhibit finely-tuned hierarchical changes through a noncontact stimulus method for a variety of potential biomedical applications, such as controlled cell proliferation and ejection, stimuli-responsive drug delivery and growth factor release, and various stem cell differentiation through manipulation of external environments.

5.2 Experimental Methods

5.2.1 Materials

Texin RxT85A, an FDA-approved, biocompatible thermoplastic polyurethane (TPU), was purchased from Covestro, with further material specifications detailed from the given reference.[56]

Polyvinyl acetate of M_w = 100,000 g/mol (PVAc), FDA-approved sodium alginate (SA) extracted from brown seaweed with M/G ratio of approximately 1.12, iron oxide nanoparticles of 50-100 nm diameter with 97% trace metals basis (Fe_3O_4 NP), calcium chloride ($CaCl_2$), N,N-Dimethylformamide (DMF), and acetone were all purchased from Sigma-Aldrich. Nylon-11 (N-11) was purchased from McMasters-CARR, with further material specifications detailed from the given reference.[43] Never-dried cellulose nanocrystals (CNCs) suspension of 11.8 wt%, 5-10 nm diameter, 150-200 nm length, and surface sulfation of 0.94 wt% sufur in sodium form, were manufactured by the US Forest Service's Cellulose Nanomaterials Pilot Plant and purchased from University of Maine Process Development Center.[44] Polymers were chosen based on varying glass transition temperatures (Tg) ranging from below room temperature (-50-(-30) °C) for TPU, roughly body temperature (35-40 °C) for PVAc, and significantly higher than room temperature (60-70 °C) for N-11. In addition, Fe_3O_4 NPs were loaded in each polymer matrix of varying concentrations from 0.0 to 10.0 wt%, detailed further in **Table A**.

5.2.2 Fabrication of pre-strained TPU composites

TPU was dissolved in DMF to create a concentrated stock solution of 100 mg/mL. Similarly, Fe_3O_4 NPs were dispersed in DMF to create a concentrated stock suspension of 50 mg/mL. The stock solutions were mixed together in the pre-determined composition ratios to form a final dry sample weight of 10.0 g. The mixed solution was then cast into a Teflon petri dish, and left on a hotplate at 80 °C until complete evaporation of the solvent (verified by TGA). The films were then repeatedly melt pressed at 148 °C to ensure uniform thickness of 500 µm and dispersion of Fe_3O_4 NPs throughout the entire film. Each film was subsequently cut into 5 cm x 1 cm ribbons for induction heating tests. It should be noted that due to the low Tg of the TPU, the samples were not able to retain any residual strain.

5.2.3 Fabrication of pre-strained PVAc composites

Following a similar initial procedure as TPU, PVAc was dissolved in acetone to create a concentrated stock solution of 100 mg/mL, and Fe_3O_4 NPs were dispersed in acetone to create a concentrated stock suspension of 50 mg/mL. The stock solutions were mixed together in the pre-determined composition ratios to form a final dry sample weight of 10.0 g. The mixed solution was then cast into a Teflon petri dish, and left on a hotplate at 60 °C until complete evaporation of the solvent (verified by TGA). The films were then melt pressed at 60 °C to a uniform thickness

of 500 µm, and cut into 2 cm x 1 cm rectangles. Each rectangle was heated to 40 °C, strained over 200% to dimensions of roughly 5 cm x 1 cm, and immediately quenched to retain the induced strain. All ribbons were stored in a refrigerator to ensure the retainment of residual strain before heating testing.

5.2.4 Fabrication of pre-strained Nylon-11 composites

Pure Nylon-11 (N-11) was melt pressed into films at 205 °C. Fe_3O_4 NPs were dispersed in Acetone at 50 mg/mL, added onto the films in pre-determined wt% compositions, and allowed to dry. The films were then melt pressed repeatedly until uniform dispersion of Fe_3O_4 NPs was achieved. A final melt press was performed on each film to a uniform thickness of 500 µm, immediately quenched, and cut into rectangles with dimensions of roughly 5 cm x 1 cm for induction heating testing. To induce residual strain for shape memory effects, each ribbon was heated until just below the melting point (~180 °C), bent in half, and immediately quenched. Following the quench, the resulting deformed ribbons were manually re-straightened at room temperature to induce cold straining within the polymer matrix.

It should be noted that at higher Fe_3O_4 NPs concentrations, agglomerations started to develop within the N-11 polymer matrix. Therefore, to obtain better dispersion of Fe_3O_4 particles, high energy ball milling of the N-11 and desired Fe_3O_4 NPs wt% prior to melt pressing should be performed. This allows for the embedment of Fe_3O_4 NPs into the N-11 matrix prior to melt pressing, subsequently limiting agglomerations of particles.

5.2.5 Fabrication of alginate and CNC hydrogel composites

SA and CNC hydrogel composites were fabricated using a solution mixture, solution casting method, and a subsequent crosslinking agent, following an adapted procedure by Kuo et al.[45] SA was dissolved in 18 MΩ deionized water (diH_2O) to create a concentrated stock solution of 100 mg/mL. As well, the 11.8 wt% never-dried CNC suspension was diluted with diH_2O to a 10 wt% (100 mg/L) concentrated stock solution. The solutions were mixed together in varying ratios of SA to CNCs, with compositions detailed in **Table B**, to create a multitude of mechanically tunable hydrogel composite scaffolds for different types of cell growth.[46-47] The samples were named for the SA and CNC content respectively, i.e. the 5 wt% SA and 2 wt% CNC composition was labeled 5A2C, with further labeling detailed in **Table B**. The combined SA and CNC mixtures were then heated and sonicated to remove any excess air bubbles, cast into roughly 2 cm diameter

Nalgene vials, and crosslinked using either a 100 mM, 500 mM, or 1M aqueous solution of $CaCl_2$, through 60 s of vortexing and 48 h of room temperature storage for complete gelation. It should be noted that only the SA molecules were chemically crosslinked, forming entrapping networks around the CNCs. Once crosslinked, the hydrogel composite scaffolds were cut into ribbons with cross-sections of 5 mm x 1 mm, and cylindrical disks with dimensions of 7 mm x 7 mm (d x h) for mechanical testing.

5.2.6 Thermogravimetric analysis (TGA) of SMP composites

TGA was performed on each polymer composite composition, **Table 5.1**, using a TA Instruments TGA Q500 thermal analyzer. Each composite film was cut into 15 mg samples, measured into a platinum TGA pan, and heated from 25 °C to 500 °C at a rate of 10 °C/min. The decomposition temperature was determined by the loss of 5 wt%, $T_{d5\%}$, after any residual moisture/solvent had been removed from the sample.

5.2.7 Differential scanning calorimetry (DSC) of SMP composites

DSC was performed on each polymer composite composition, **Table A**, using a TA Instruments DSC Q10 differential scanning calorimeter. The PVAc and N-11 composites were cut into small samples and placed into Tzero DSC pans and lids, and tested using a heat/cool/heat cycle, with heating and cooling rates of 10 °C/min from 0 °C to 250 °C. Due to the low T_g of the TPU, the heat/cool/heat cycle used the same heating and cooling rates of 10 °C/min, but was cycled from -50 °C to 250 °C using liquid nitrogen. The data was analyzed using the cooling curve and second heat curve, in order to negate any prior processing conditions.

5.2.8 X-ray powder diffraction (XRD) of SMP composites

XRD was performed on each polymer composite composition, **Table A**, using a Philips PW3040 X'Pert High Resolution X-Ray Diffractometer to quantify changes in crystallinity in the polymer nanocomposites before and after induction heating. A 2θ range from 5º to 65º provided the necessary spectra to measure both the polymer structure, as well as the principle crystalline peaks of the iron oxide nanoparticles. The XRD utilized Cu-Kα X-rays, which have a wavelength of 0.15418 nm. XRD principle peaks for the iron oxide nanoparticles were verified with the RRUFF database.[48]

5.2.9 Hydration properties and thermal buffering properties of SA and CNC hydrogels

Following 48 h of Ca^{2+} crosslinking and gelation, each hydrogel composition in **Table B** were tested for general hydration properties, including water loss during crosslinking, water absorption, and water retention, as well as thermal buffering properties using each SMP polymer matrix (TPU, PVAc, and N-11) as a substrate. Before and after 48 h crosslinking of each hydrogel composite, sample dimensions were measured and recorded to determine initial water content, followed by any shrinking and water loss that occurs during crosslinking, following a similar procedure by Kuo et al.[45] Each hydrogel composite was then submerged into 50 mL of 18 MΩ diH_2O for 24 h to determine any subsequent water absorption properties following complete crosslinking. Once swelled for 24 h, each sample was left in an uncovered Teflon petri dish on a tabletop at room temperature for 24, 48, 72, and >96 h to determine total water content and retention, measuring sample dimensions and weight at each time point.

To determine the thermal buffering properties of the hydrogel composites, each were cut into rectangular samples with identical dimensions to the SMP composite ribbons described previously. To more accurately simulate cellular and *in vivo* applicability, all samples were submerged and incubated at 37 °C for 24 h prior to testing. The rectangular hydrogel samples were then placed on top of TPU, PVAc, and N-11 composite ribbons with Fe_3O_4 NPs concentrations of 10 wt%, and placed on a pre-heated hotplate set to the respective temperature needed to induce shrinking within each substrate (TPU = >37 °C, PVAc = 40 °C, N-11 = 70 °C). The thermal conductivity from the substrate to the hydrogel, and subsequent thermal dissipation of the hydrogel, were measured using a thermal probe for 20 s of heating to determine the thermal buffering properties of the hydrogel composites.

5.2.10 SA and CNC hydrogel mechanical characterization

To determine the mechanical characteristics of the varying hydrogel compositions, **Table B**, a TA Instruments Q800 Dynamic Mechanical Analyzer (DMA) was employed for tension and compression testing. For tension, five 5 mm x 1 mm ribbons of each hydrogel composition were tested at room temperature (roughly 25 °C) using an isostatic force ramp of 1 N/min until failure occurred, or a maximum force or displacement was reached. Stress and strain were recorded for each test, and analyzed to determine tensile moduli, ultimate tensile strengths, and elongations at break. For compression, five cylindrical disks with roughly dimensions of 7 mm x 7 mm (d x h)

were tested at room temperature (roughly 25 °C) using an isostatic force ramp of 1 N/min until failure occurred, or a maximum force or displacement was reached. Stress and strain were recorded for each test, and analyzed to determine compressive (bulk) moduli. It should be noted that neither ultimate compressive strength nor deformation until failure were recorded for compression, as all of the samples were classified as incompressible hydrogels.

5.2.11 Induction heating and thermal camera imagery

All induction heating processes for this study were performed on all polymer composite compositions, **Table A**, using an Ambrell EasyHeat LI 8310, 10 kW, 150-400 kHz induction heater. The working coil used in the processes consisted of a 7-turn, square-tube copper coil with an inside diameter of 25 mm and a length of 44 mm, which, when coupled with the internal capacitor bank, resulted in a resonant frequency of 305 kHz. By varying the current passing through the coil between 600 A and 200 A, a range of magnetic field magnitudes from 110 kA/m to 30 kA/m, respectively, were generated for testing the polymers. A semi-circular, 3-D printed platform provided support for the polymer samples and ensured that they remained close to the geometric center of the working coil during heating, which coincides with the region of highest magnetic flux.

A Flir A600 series thermal camera supplied the thermal imaging for this study. For each trial, the camera was angled in a manner that allowed the full length of the polymer sample to be in focus within the coil. During heating, a selected area temperature measurement was gathered, as shown in **Figure 5.1**, which indicated the maximum temperature of the sample at a particular frame. Flir Tools+ software allowed these temperature measurements to be interpreted with respect to time. The analyzed temperature curves were then used to calculate heating rates for each trial.

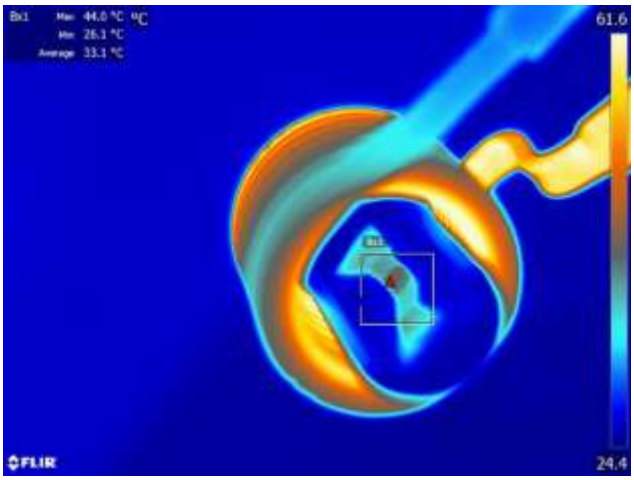

Figure 5.1 Example depiction of measurement methods for induction heating tests of SMP composites utilizing a Flir A600 series thermal camera.

In addition to temperature measurements, the length of each PVAc sample was measured both before (l_b) and after (l_a) heating to quantify the rate of shape recovery (**Eq. 1**). In the case of the N-11 samples, the angle of the sample was measured before (θ_b) and after (θ_a) heating to calculate an angular rate of shape recovery (**Eq. 2**), where Δt is the measured time.

$$Rate\ of\ Recovery\ _{PVAc} = \frac{l_b - l_a}{\Delta t} \qquad (1)$$

$$Rate\ of\ Recovery\ _{N-11} = \frac{\theta_b - \theta_a}{\Delta t} \qquad (2)$$

5.2.12 Heat transfer and dissipation through induction heating methods

In addition to utilizing the thermal camera to monitor temperature gradients throughout the SMP samples, heat dissipation into an aqueous environment was also measured. Monitoring the thermal transport from the SMPs to the surrounding water provided a reasonable methodology to simulate hydrogel thermal buffering (i.e. the heat transfer occurring between SMP substrate and the hydrogel). SMP samples (TPU, PVAc, and N-11) with the highest concentration of NPs (10 wt.%) were fully submerged in 6 mL of deionized water. The submerged SMP samples were heated via induction at the optimal magnetic field strength (determined from the thermal camera analysis), while a fiber optic thermocouple monitored the temperature of the surrounding water.

5.3 Results and Discussion

5.3.1 Fabrication of SMP composite films and optical variations

Due to the various fabrication methods of the SMP composites, slight differences occurred between the varying polymer matrices, such as Fe_3O_4 NPs dispersion uniformity and agglomeration, uniform sample size, and ability to induce residual stresses. The TPU and PVAc composites were fabricated utilizing solution casting methods, in which the Fe_3O_4 NPs were dispersed in the same solvent used for each respective polymer. This allowed for optimal dispersion of the Fe_3O_4 NPs through a mixture of similar solutions, prior to solvent evaporation and solidification of the composites. Therefore, ideal particle dispersion was maintained throughout both the TPU and PVAc matrices before, during, and after melt pressing into uniform films, including the composites with higher Fe_3O_4 NPs loading content. N-11, however, had some additional challenges, since the polymer is less soluble than TPU and PVAc in commonly used solvents. Therefore, N-11 composites were created strictly by continuous melt pressing processes, allowing the Fe_3O_4 NPs to further disperse with each repeated pressing cycle. This inability to uniformly disperse the Fe_3O_4 NPs within the polymer matrix prior to melt pressing, led to large agglomerations throughout the majority of the N-11 composites, drastically increasing with increased particle loading. These agglomerations at higher Fe_3O_4 NPs content, especially within the N-11 composites, can be visibly seen in **Figure 5.2**, alongside uniformly dispersed composites.

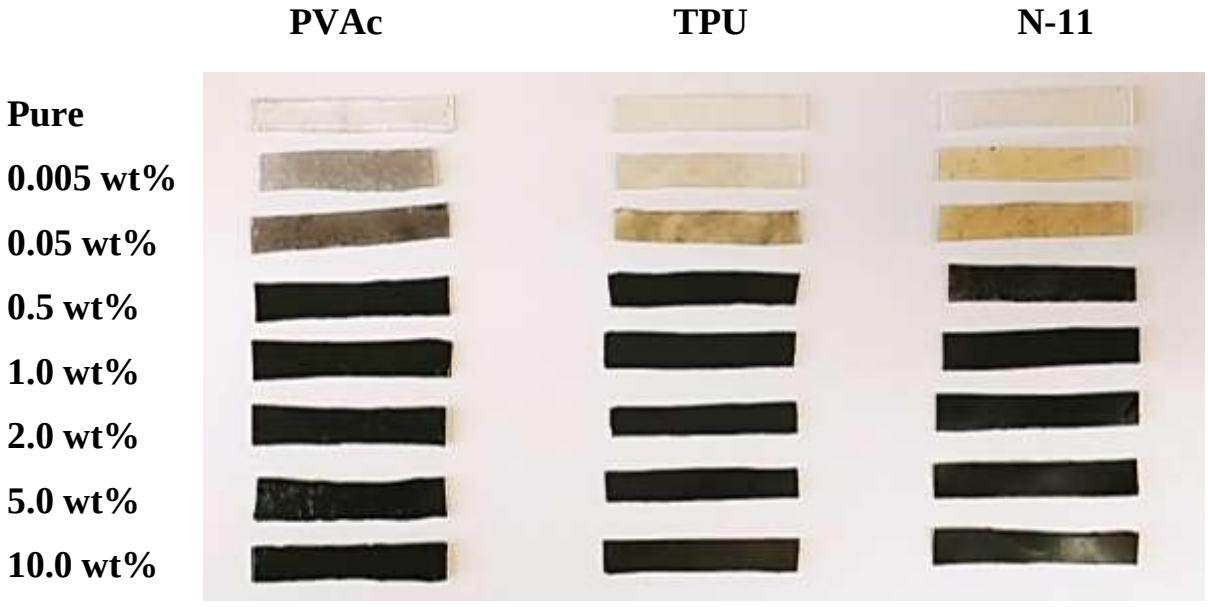

Figure 5.2 Depiction of PVAc (left), TPU (middle), and N-11 (right) SMP composite samples with varying Fe_3O_4 NPs content, comparing uniformity of particle dispersion. Initial observations reveal a slight difference in the uniformity of particle dispersion within the different polymer matrices, increasing in overall particle agglomerations from left to right, i.e. PVAc, TPU, and N-11. Once the Fe_3O_4 NPs concentration reached 1.0 wt% or above, the particles completely filled each polymer matrix, even if agglomerations existed.

Although most of the defect-causing variations within each SMP composite were a result of the differing fabrication methods, the few remaining variations were caused by the specific properties of each individual polymer matrix. One such variation is the ability to change shape through the application of induction heating, which is highly dependent on the transition temperatures of the polymer, as well as the crystallinity residing in the macrostructure.[49-50] All of the aforementioned factors, further discussed in later sections, play a significant role in whether or not a given polymer will be useful for SMP applications, and if so, which specific applications they can successfully be employed.[49-50]

5.3.2 SA and CNC hydrogel fabrication and observed variations

Unique hydrogel composites were created through crosslinking of various SA and CNC wt% ratios, in order to obtain a multitude of samples exhibiting a wide range of hydration, thermal buffering, and mechanical properties. During the fabrication process, a few distinct characteristics were observed, including shrinkage from crosslinking, variation in hydrogel opacity, and shape of the final composite. Comparable to the study performed by Kuo at al., the variations observed were all affected by the concentration of the $CaCl_2$ aqueous solution, the SA content, and the CNC content.[45] As SA and CNC content increased within the hydrogel, the shrinking decreased post-crosslinking, while an inversely proportional result occurred through increasing concentration of the $CaCl_2$ aqueous solution. As well, it was noticed that an increase in all of the previous variables caused significant increases in densification, opacity, and overall shape change within the final crosslinked hydrogels, shown in **Figure 5.3**.

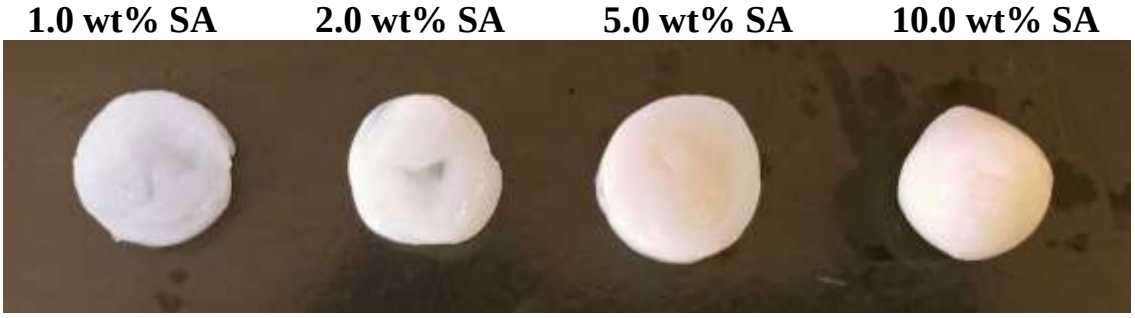

Figure 5.3 Above (top) and profile (bottom) images of fabricated SA and CNC hydrogels, with increasing SA content from left to right and a constant CNC content of 1.0 wt%. Although all hydrogel compositions showed nearly identical characteristics, the specific compositions above exemplify the differences in hydrogel shape formation from various crosslinking speeds due to increased SA content, while containing "average" CNC content.

The change in densification can be justified by the rapid crosslinking caused by the increase in available Ca^{2+} ions in the higher concentrated $CaCl_2$ solutions. The higher the availability of Ca^{2+} ion content enhances inter- and intra-molecular interactions, shortening the average distance between ionic crosslinks, and subsequently decreasing the void space left by longer crosslinking distances.[45,52] Like densification, the changes in the overall shape can be attributed to the rapid surface crosslinking of the SA and CNC mixtures, enveloping the unreacted mixture in a congealed, crosslinked coating.[45,52] Therefore, when vortexed, the centrifugal force shaped the composites into various forms while crosslinking progressed, as shown in **Figure 5.3**. Although the largest changes in hydrogel opacity seemed to vary with increased CNC content, the rapid crosslinking of higher $CaCl_2$ concentration and SA content showed slight affects as well. With increasing CNC content, the quicker crosslinking resulted in the formation of larger agglomerations and particulate sizes, further reflecting light causing significant changes to the increasing opacity.[45,53]

5.3.3 Thermal properties of SMP composites

TGA and DSC were performed on all SMP composite compositions to determine if an increasing concentration of Fe_3O_4 NPs caused any significant effects to the thermal characteristics of the polymers. Although neither TGA nor DSC results validated significant thermal changes due to variations in Fe_3O_4 NPs concentrations, TGA showed more variance in the thermal degradation onsets, than changes observed in T_g, T_c, and T_m through DSC. It should be noted that all thermal characterization data were recorded in **Table 5.1**.

Table 5.1 Thermal properties of TPU, PVAc, and Nylon-11 composites with increasing Fe_3O_4 NPs content as determined by TGA and DSC.

	wt% Fe_3O_4 in TPU 85A							
	Pure	**0.005**	**0.05**	**0.5**	**1.0**	**2.0**	**5.0**	**10.0**
T_g (°C)[1]	< 40	< 40	< 40	< 40	< 40	< 40	< 40	< 40
T_m Peak (°C)[1]	195-205	195-205	195-205	195-205	195-205	195-205	195-205	195-205
T_c Peak (°C)[1]	~90	~90	~90	~90	~90	~90	~90	~90
$T_{d5\%}$ (°C)[2]	313/400	313/402	315/407	307/397	309/405	310/406	298/405	294/404
	wt% Fe_3O_4 in PVAc*							
	Pure	**0.005**	**0.05**	**0.5**	**1.0**	**2.0**	**5.0**	**10.0**
T_g (°C)[1]	38.5	38.6	38.7	37.0	34.0	33.0	35.0	35.3
$T_{d5\%}$ (°C)[2]	315/440	312/448	314/445	312/453	312/454	313/455	313/454	314/454
	wt% Fe_3O_4 in Nylon 11							
	Pure	**0.005**	**0.05**	**0.5**	**1.0**	**2.0**	**5.0**	**10.0**
T_g (°C)[1]	46.9	47.2	46.0	46.5	45.0	44.8	44.9	44.0
T_m Peak (°C)[1]	185.1	185.5	184.6	185.0	184.5	184.6	185.0	184.7
T_c Peak (°C)[1]	159.3	158.1	158.3	158.5	159.5	159.4	160.1	160.3
$T_{d5\%}$ (°C)[2]	395	393	392	423	422	433	442	436

[1] Determined by DSC

[2] Determined by TGA

* PVAc is amorphous, therefore no melting or crystallization temperatures were observed.

For all SMP composites, it was observed that as Fe_3O_4 NPs content increased, there was a proportional increase in remaining mass after completion of TGA attributed to the non-volatilized metal residue.[54] As well as the difference in residual mass, each polymer showed slight additional

changes due to the incorporation of Fe_3O_4 NPs.[54] TPU SMP composites showed two opposing shifts with increasing Fe_3O_4 NPs content, a decrease in the initial $T_{d5\%}$ of the soft segments, followed by an increase in the secondary $T_{d5\%}$ of the hard segments, as recorded in **Table 5.1**. As heat is absorbed by the Fe_3O_4 NPs, a quicker heating flux is introduced to the urethane bonds, leading to a faster initial decomposition and formation of various radical fragments/small molecules, including isocyanates and polyol containing ester, caprolactone, or amide groups.[51,55] Simultaneously, the heat absorbed by the Fe_3O_4 NPs leads to slight heat flux variations within the resulting radical fragments/small molecules, causing an additional minute increase in the secondary $T_{d5\%}$.[55]

Similar to the TPU composites, the PVAc SMP composites showed two distinct stages of thermal degradation, an initial decomposition and volatilization of the acetate groups, followed by a secondary decomposition of the ethylene backbone.[56-57] As Fe_3O_4 NPs content was increased within the PVAc composites, no significant changes were observed within the initial $T_{d5\%}$ of the acetate groups, while an increase occurred within the secondary $T_{d5\%}$ of the ethylene backbone, as detailed in **Table 5.1**. When metal nanoparticles are added to the PVAc matrix, they act as a crosslinking catalyst at lower temperatures, leading to a higher crosslinking density within the composite prior to reaching the second stage of thermal degradation.[57-58] This phenomenon causes a shift in the secondary $T_{d5\%}$, as more energy is needed to sever the bonds of the crosslinked polymer chains.[57-58]

N-11 SMP composites showed only one stage of thermal decomposition, however, the variations observed from increased Fe_3O_4 NPs loading were greater than those previously seen in both the TPU and PVAc composites. As Fe_3O_4 NPs content increased past 0.05 wt%, the $T_{d5\%}$ of the N-11 samples exhibited an increase as well, resulting in higher thermal stability at higher loading capacities, recorded in **Table 5.1**. The observed trends can be attributed to the addition of Fe_3O_4 NPs within the N-11 matrix essentially acting as an effective physical barrier, inhibiting the release of any volatile products during thermal decomposition, which becomes more prominent as higher particle loading is employed.[59] As well, the metallic nanoparticles act as a thermal "magnet", absorbing larger amounts of the applied heat, and dissipating the energy throughout the larger Fe_3O_4 NPs agglomerations, ultimately resulting in the need for additional thermal energy to activate decomposition.[59]

It should be noted that, although TGA data is important to fully characterize the SMP composites, the main factors involved during induction heating are the thermal transition characteristics, T_g, T_c, and T_m, specifically the glass transition temperature. Therefore, the results obtained by DSC have greater relevance to the actuation predictions of the SMP composites when heated inductively.[17-18,60-61] It was determined that since negligible changes were observed during DSC, SMP composites proved optimal ability to maintain nearly identical thermal transitions to the natural polymers, regardless of the variance in Fe_3O_4 NPs content, further detailed in **Table 5.1**. This feature is highly important because similarities in thermal transitions allows for easily manageable, reliable, and repeatable induction heating methods and shape memory effects.

Thermal transition ranges of the semi-crystalline TPU composites remained relatively the same with the introduction of Fe_3O_4 NPs, regardless of loading content, comparing very well to the manufacturer's (Covestro) specified thermal properties of the TPU.[42] All compositions were shown to reside within the thermal ranges specified by Covestro, specifically T_g < -40 °C, T_c = ~90 °C, and T_m = ~200 °C.[56] Unlike the TPU composites, PVAc composites showed only a single sharp thermal transition, T_g = 35-38 °C, since it is completely amorphous and does melt or recrystallize without the aid of another component, such as a polymer blend.[62-63] The N-11 composites are semi-crystalline, showing all relative thermal transitions, T_g = 44-47 °C, T_c = ~159 °C, and T_m = ~185 °C. Although the T_m of all compositions remained nearly identical, DSC resulted in a shift in the individual sharpness of bimodal melting peaks within the composites, relating to the melting of the small and large crystals.[61,64] This phenomenon is attributed to the addition Fe_3O_4 NPs hindering crystallite growth within the N-11 matrix, therefore, decreasing overall crystal size, and subsequently shifting the intensities of the bimodal melting peaks.[65]

It should be noted that the only slight variations observed in thermal transitions, were in T_g for both PVAc and N-11 composites with the addition of Fe_3O_4 NPs. However, the decreases observed within the T_g range with increased loading were insignificant, especially with regards to the induction heating experiments. Therefore, DSC proved that each SMP composite, regardless of matrix or Fe_3O_4 NPs loading, maintained almost identical thermal transition ranges, which is crucial for both successful applicability of induction heating and inducing optimal shape memory effects.[17-18,60]

5.3.4 Crystallinity properties of SMP composites

Structure, crystallinity, and crystallization of polymer matrices and composites are all significant for shape memory properties, and subsequent success of induction heating.[60,66] Although the methods of induction heating used within this study will not cause the composites to surpass the recrystallization temperature, when the polymer is heated past the T_g, the residual strain induced prior to heating will be relieved and should produce noticeable shifts and variations in the XRD results.[60,66-67] In general, all of the composites showed a similar trend of increasing crystallinity with increasing Fe_3O_4 NPs content, due to the additional crystalline peaks of the metallic nanoparticles.[61] As well, each composite matrix also showed slight individual trends related to their specific morphological structures. However, due to slightness of change observed for the PVAc and TPU composites and lack of visual clarity when plotted, only XRD of N-11 composites were exemplified in **Figure 5.4**.

a.

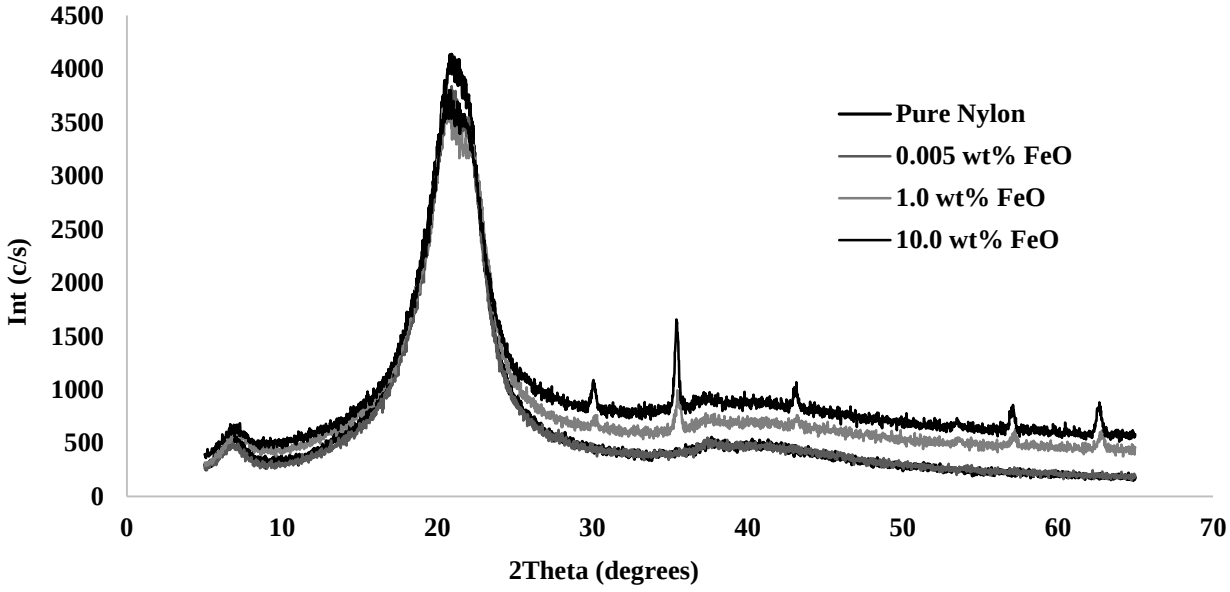

b.

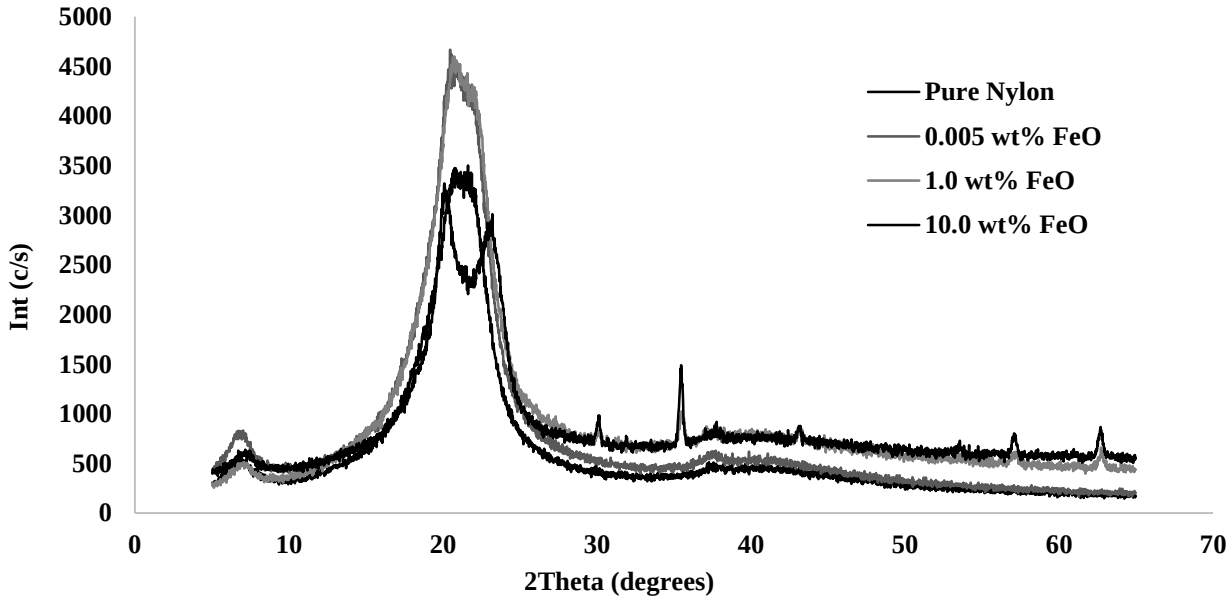

Figure 5.4 XRD crystallinity spectra of N-11 composites (pure, 0.005, 1.0, and 10.0 wt% Fe_3O_4 NPs) a) **before and** b) **after induction heating from 2 Theta of 5° to 65°, showing the amorphous and crystalline regions of the N-11, as well as crystalline structure peaks of the Fe_3O_4 NPs. It was observed that as the N-11 composites were inductively heated, enough thermal energy was absorbed to induce reorganization and crystallization shifts of the polymer chains, subsequently increasing overall % crystallinity through rapid annealing.**

As previously discussed, the T_g of the TPU SMP composites resides well below room temperature, resulting in an identical semi-crystalline structure both before and after induction heating, further revealed by XRD.[42] When given enough thermal energy to transition from a glassy state to a rubbery state, polymer chains start to reorganize into a more suitable structure and relaxed state.[68] Therefore, since the TPU composites are consistently above their T_g at room temperature, and no additional thermal transition range was surpassed, the structure of the composites remained the same throughout the entire induction heating process, regardless of Fe_3O_4 NPs content.[68-69]

XRD of the PVAc SMP composites showed negligible shifts and variations in the crystalline content and/or peak intensities as a result of induction heating. Since PVAc is a completely amorphous polymer, it does not possess the ability to manifest crystalline structures through heating, cooling, or annealing, regardless of additional filler content.[68,70] Although literature suggests PVAc composites can obtain crystallinity through various processes, including copolymerization, as an individual polymer, PVAc will always remain amorphous.[70-71] However, PVAc does exhibit a T_g above room temperature (~35-40 °C), which allows for the retaining of internal stresses from induced strains above that T_g followed by immediate quenching.[68-72]

Therefore, even with the lack of crystallization abilities, PVAc composites can prove useful in many SMP composite applications utilizing induction heating.[72]

Due to the semi-crystalline structure of N-11 and T_g well above room temperature, the N-11 SMP composites showed the greatest variations of crystalline content, peak shifts, and peak intensities, when analyzed through XRD, **Figure 5.4**. Although T_c and T_m were not reached during induction heating, the induced annealing temperatures surpassed the T_g of the N-11, allowing for the reorganization of the amorphous regions through the relief of residual stresses.[68-73] As the amorphous regions begin to move and reorganize into a lesser stressed state, the N-11 matrix starts to become more crystalline in nature causing variations in the crystalline peaks and intensities, when observed through XRD.[60-61,73] As well, XRD revealed varying crystalline 2 Theta peaks within the N-11 matrix, with the addition of Fe_3O_4 NPs. This can be attributed to the thermal history obtained during the N-11 SMP composite processing, in which a shift in the T_m bimodal peaks occurs with increasing Fe_3O_4 NPs content, due to differences in small and large crystal structures.[61] Therefore, as induction heating rates and temperatures of the N-11 SMP composites increase with larger Fe_3O_4 NPs content, the crystalline peaks start to shift lessening the gaps between the large and small crystal structures formed through sample melt processing.[61,73]

5.3.5 Hydration and thermal buffering properties of hydrogel composites

Similar to what has been observed in literature by Kuo et al., the hydrogels produced in this study showed vast differences in characteristics, such as shrinking, water absorption, water retention, thermal buffering, opacity, and mechanical stability and strength, through variation of $CaCl_2$ aqueous solution concentrations, SA content, and CNC content, shown in **Figure 5.4, Figure 5.5, Table 5.2, and Table 5.3**.[45,52-53]

Table 5.2 Dimension change after crosslinking, hydration properties (i.e. swelling, water retention), and average thermal buffering properties.

	Hydrogel shrinkage (% original size) with increasing wt% CNC				
Alginate Content (wt%)	**0**	**0.5**	**1.0**	**2.0**	**5.0**
1.0	28.0	49.0	52.0	69.0	79.0
2.0	66.0	63.0	70.0	78.0	90.0
5.0	85.0	88.0	88.0	92.0	95.0
10.0	95.0	96.0	94.0	98.0	99.0

	Total water content (%) with increasing wt% CNC				
Alginate Content (wt%)	**0**	**0.5**	**1.0**	**2.0**	**5.0**
1.0	95.18	94.75	94.97	91.44	89.19
2.0	94.76	94.30	94.76	92.38	88.23
5.0	92.53	92.17	92.01	90.78	88.56
10.0	85.12	87.91	85.61	83.66	82.81
	Water retention (%/h) with increasing wt% CNC				
Alginate Content (wt%)	**0**	**0.5**	**1.0**	**2.0**	**5.0**
1.0	-0.92	-0.95	-1.03	-1.03	-1.06
2.0	-1.01	-1.03	-1.05	-1.05	-1.04
5.0	-1.39	-1.00	-1.00	-1.02	-1.00
10.0	-0.99	-1.01	-1.03	-1.03	-1.01
	Thermal buffering (°C/s) with increasing wt% CNC				
Alginate Content (wt%)	**0**	**0.5**	**1.0**	**2.0**	**5.0**
1.0	0.040	0.040	0.047	0.047	0.063
2.0	0.040	0.043	0.047	0.050	0.063
5.0	0.043	0.047	0.050	0.057	0.080
10.0	0.043	0.047	0.047	0.053	0.083

In general, the hydration properties of the hydrogel composites decreased with increasing SA and CNC content, as well as higher $CaCl_2$ aqueous solution concentrations. As briefly mentioned, an increase in SA and CNC content resulted in less post-crosslinking shrinkage, while an increase in availability of Ca^{2+} ions resulted in higher shrinkage, shown in **Figure 5.5a**. For example, it was observed that samples 1A0C shrunk to nearly 25% of its original size, while the 10A5C samples retained nearly 99%. Furthermore, the increase of all variables caused significant increases in the densification of the crosslinked hydrogels. Both of these factors play significant roles in limiting the availability of fluid uptake and retention to a certain quantity before the hydrogel becomes oversaturated, shown in **Figure 5.5b and 5.5c**.[45,52-53] Therefore, when the hydrogel shrinks excessively due to crosslinking, the total expansive volume the hydrogel can achieve through swelling and retention of water or other aqueous solutions is negatively

affected.[74-75] Likewise, as density of crosslinking increases, less void space is available between the crosslinked sites for the water to penetrate and reside.[76-77]

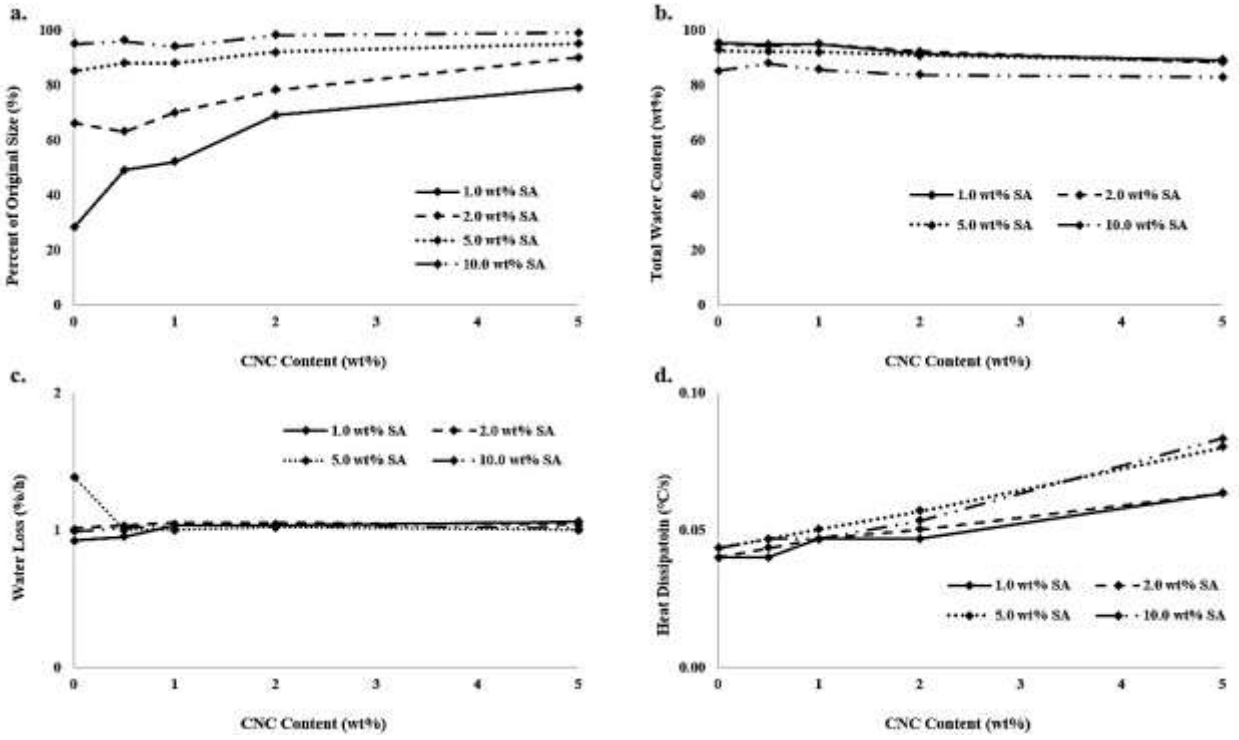

Figure 5.5 Depiction of the hydration and thermal buffering characteristics exhibited by the various SA/CNC hydrogel composite compositions, including a) **shrinkage from original dimensions due to crosslinking (%),** b) **total water content after swelling (wt%),** c) **water retention (% water loss/h), and** d) **thermal buffering during heating tests and rate of temperature fluctuation (°C/s).**

The fabricated hydrogel composites in this study agree with correlations discussed in literature, in which hydration properties can be manipulated through variation of SA content, CNC content, and availability of Ca^{2+} ions for crosslinking.[45,74-80] These factors become exceedingly important with regards to biological mimicry and preservation of living cells through varying degrees of hydration, and subsequent thermal dissipation with the introduction of heat.[75,77-81] The optimal hydration capabilities of biological tissues, and tunable scaffolds engineered to mimic those tissues, are essential for biological functionality, including maintenance of cell differentiation, proliferation, maturation, and viability, as well as dissipation of thermal energy to prevent cell apoptosis and necropsy due to excessive heat fluctuations.[40,79-87] Countless studies have been reported in literature detailing optimal conditions for cell survival, and the specific selectivity of conditions based on various cell types, with a great deal of emphasis on the state of

hydration and thermal regulation.[83-87] Cells are known to not only thrive in well-hydrated environments, but also withstand much greater variations of stress with significantly limited cell death.[83-86] Additionally, cell necropsy and apoptosis both decrease significantly when thermal fluctuations are minimal in either direction, greatly preventing thermal shock within cellular structures.[86-87] Therefore, maintaining ideal cell culture conditions within the hydrogel composites throughout the induction heating process is vital to the success of their biological functionality.

As depicted in **Figure 5.5c and 5.5d**, the hydration properties of the hydrogel composites, specifically total water content, have a direct contribution to the ability of the hydrogels to dissipate externally applied heat. Since both CNCs and SA possess higher thermal conductivity, yet lower specific heat capacity than water, each material takes less energy to heat, while simultaneously transferring that heat more quickly.[88-90] Therefore, with increasing concentrations of either CNCs or SA, the thermal insulation abilities of the hydrogels became more limited, exemplified in **Figure 5.5d and Table 5.2**. It was determined that when compared to a purely liquid medium, the hydrogels exhibit a lesser ability to dissipate thermal energy. However, since the hydrogels were characterized as having at least 82% water content within the least hydrated composition (10A5C), with upwards of 96% water content in the most hydrated (1A0C), variations between the liquid medium and hydrogel composites were proven to be minute.

5.3.6 Mechanical properties of hydrogel scaffolds

Mechanical characterization was carried out on all SA/CNC hydrogel compositions, **Table B**, utilizing a DMA for both tension and compression testing. To ensure uniformity of hydration and testing results between the hydrogel composites, all of the samples from each composition were submerged in 30 mL of diH_2O for at least 48 h to reach maximum water content, and only removed when it needed to be tested. It should be noted that only samples crosslinked with the 1.0 M $CaCl_2$ aqueous solution were used due to the higher structural stability needed for testing. The other samples experienced less robust mechanical characteristics, leading to a lack of testing ability. As well, the hydrogels were deemed incompressible, therefore, only compressive (bulk) moduli were recorded for compression testing.

As hypothesized from literature,[45,53,91] the hydrogels showed a general trend of increased overall strength and toughness with increasing SA and CNC content, while reducing elongation to failure (in tension). However, in lower SA content hydrogels, specifically the 1.0 wt%

composition, the higher CNC content led to an oversaturation of filler, subsequently causing a decrease in all mechanical properties during tension, depicted further in **Figure 5.6a, 5.6b, and 5.6c**.

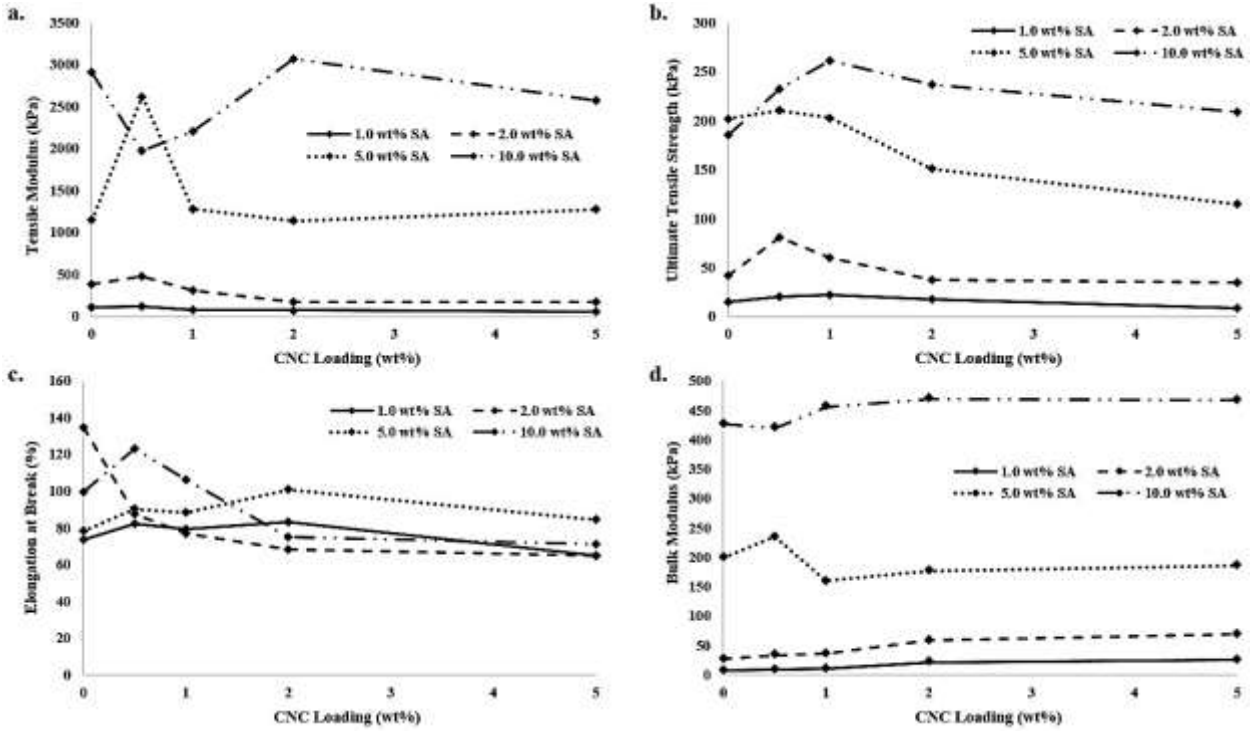

Figure 5.6 Mechanical characterization plots of a) **tensile moduli in kPa,** b) **ultimate tensile strengths (UTS) in kPa,** c) **elongations at break in % strain, and** d) **compressive (bulk) moduli in kPa, for SA/CNC hydrogel composites of increasing CNC content, as determined by DMA. It was observed throughout the majority of the hydrogels, that as the concentration of CNCs increase, both the elastic modulus and UTS increased, while the elongation at break decreased.**

This phenomenon is due to the filler network exceeding the percolation threshold.[92] When the proper filler concentration is employed, the formation of an ideal percolating network of interconnected nanoparticles occurs, which inhibit free movement of polymer chains through interfacial interactions.[91-93] However, when the filler concentration exceeds that needed to produce such a network, the nanoparticles start to agglomerate, leading to defects and stress concentrators within the composite structure.[92] This prominent mechanism for mechanical reinforcement was observed CNC content increased past a certain threshold unique to each varying SA concentration, exemplified in **Figure 5.6a, 5.6b, 5.6c, and Table 5.3**. Inversely, during compression testing, increasing CNC content led to greater compressive moduli, even within the oversaturated composites, shown in **Figure 5.6d**. This can be attributed to the greater overall strength and

stiffness of the CNCs themselves, in which the network of agglomerated CNCs begin to support the majority of the compressive load at higher concentrations.[92]

Table 5.3 Mechanical properties of the hydrogel composite scaffolds with varying alginate and CNC content as determined by DMA tension testing.

	Tensile Modulus (kPa) with increasing wt% CNC				
Alginate Content (wt%)	**0**	**0.5**	**1.0**	**2.0**	**5.0**
1.0	110.8 ± 33.5	125.2 ± 17.5	82.3 ± 25.1	75.2 ± 5.3	63.7 ± 22.4
2.0	388.5 ± 27.5	484.9 ± 6.6	313.2 ± 84.5	176.8 ± 73.6	172.3 ± 25.1
5.0	1149 ± 51.3	2621 ± 142.3	1285 ± 163.6	1140 ± 101.3	1278 ± 281.1
10.0	2907 ± 163.2	1978 ± 205.7	2208 ± 153.9	3073 ± 228.3	2576 ± 250.7
	Ultimate Tensile Strength (kPa) with increasing wt% CNC				
Alginate Content (wt%)	**0**	**0.5**	**1.0**	**2.0**	**5.0**
1.0	15.4 ± 5.0	20.8 ± 1.4	22.2 ± 7.2	18.1 ± 0.5	8.3 ± 2.5
2.0	42.4 ± 13.6	80.5 ± 17.4	60.4 ± 6.8	37.5 ± 5.1	34.6 ± 7.4
5.0	201.9 ± 22.4	210.7 ± 26.5	202.7 ± 45.9	150.9 ± 11.6	114.7 ± 9.9
10.0	185.8 ± 7.6	232.4 ± 37.4	261.2 ± 3.6	236.8 ± 8.7	208.9 ± 20.2
	Elongation at Break (%) with increasing wt% CNC				
Alginate Content (wt%)	**0**	**0.5**	**1.0**	**2.0**	**5.0**
1.0	73.8 ± 24.0	82.4 ± 8.2	79.6 ± 7.1	83.3 ± 1.7	64.8 ± 6.4
2.0	134.7 ± 9.2	87.7 ± 3.9	77.2 ± 5.5	68.5 ± 3.7	65.1 ± 14.0
5.0	78.4 ± 11.3	90.3 ± 12.1	88.5 ± 6.2	100.9 ± 9.1	84.6 ± 10.0
10.0	99.7 ± 13.3	123.1 ± 5.8	106.5 ± 8.5	75.1 ± 4.1	71.4 ± 3.1
	Compressive (Bulk) Modulus (kPa) with increasing wt% CNC				
Alginate Content (wt%)	**0**	**0.5**	**1.0**	**2.0**	**5.0**
1.0	7.1 ± 4.4	8.9 ± 0.6	10.3 ± 1.3	21.6 ± 0.9	25.3 ± 1.8
2.0	26.9 ± 8.7	33.7 ± 3.9	36.5 ± 3.5	58.5 ± 7.3	69.2 ± 3.6

5.0	199.5 ± 31.0	234.9 ± 32.9	160.2 ± 22.0	176.8 ± 23.1	185.5 ± 19.5
10.0	427.2 ± 56.1	420.3 ± 15.5	456.4 ± 50.8	469.8 ± 11.0	467.5 ± 26.1

Overall, the addition of CNCs as a reinforcement filler, along with varying SA concentrations, led to significant improvements in tunability of mechanical properties. The obtained results prove that the mechanical property ranges can be accurately tuned to suit the unique needs of various cell types and ECMs, to promote proliferation, growth, and viability, which can drastically range in moduli depending on cellular functions (i.e. 13-68 kPa for osteogenic differentiation and proliferation).[83,94-96] As well, with the vast hydrogel mechanical properties ranging from 63.7 ± 22.4 kPa to 3.1 ± 0.2 MPa for tensile moduli, 8.3 ± 2.5 kPa to 261.2 ± 3.6 kPa for UTS, 64.8 ± 6.4 % to 134.7 ± 9.2 % for elongation to failure, and 7.1 ± 4.4 kPa to 469.8 ± 11.0 kPa for compressive (bulk) moduli coupled with the aforementioned hydrational tunability, the applicability for other biomedical solutions is further increased, potentially to those such as drug delivery, stem cell differentiation, and other tissue engineering applications.[95,97] For example, researched performed by Shan et al. revealed promising skin healing characteristics in rats, such as wound closer, granulation tissue, and collagen content control, utilizing hydrogels with tunable tensile moduli ranging from 14.3 to 25.6 MPa.[97] Additionally, a study conducted by Li et al. designed hydrogel delivery systems, in which the mechanical and physiochemical properties could be finely manipulated to produce precise release profiles for various therapeutic agents, including small-molecule drugs, macromolecular drugs, and cells.[97]

5.3.7 Shape memory characterization of SMP composites

Induction heating served as the driving force behind the remote thermal activation of the SMP composites. Essentially, the dispersed NPs provided a uniform, internal thermal load that initiated the shape memory response; the iron oxide NPs, due to their relatively high magnetism, interact strongly with the magnetic field generated by the induction heater. Several factors play a role in the magnitude of thermal energy generated during induction heating,[99] with the most prominent being nanoparticle concentration and the strength of the applied magnetic field. The heating rate of each SMP composite was analyzed in terms of varying concentration (wt%) and magnetic field strength (kA/m). In addition, the shape memory response of each SMP was

observed as well, and quantified in terms of activation time (i.e. heating time elapsed until response occurs) and rate of recovery (i.e. the speed at which the material recovers its shape).

5.3.8 Induction heating of TPU SMP composites

As stated earlier, the TPU composites were analyzed solely in terms of their heating rate, since they were not able to retain any residual strain.[51-53] The heating rates of the TPU samples were gathered at NP concentrations ranging from 0 - 10 wt% and at magnetic field strengths ranging from 36.6 – 110 kA/m. **Figure 5.7** illustrates the results graphically to better visualize the observable trends. The complete dataset can be found below in **Table 5.4**.

Table 5.4 Thermal activation properties* of TPU composites with increasing Fe_3O_4 NPs content and increasing magnetic field strength, as determined by induction heating and thermal camera.

	TPU Heating Rates (°C/s) with increasing wt% Fe_3O_4 NPs							
Magnetic Field (kA/m)	**0**	**0.005**	**0.05**	**0.5**	**1.0**	**2.0**	**5.0**	**10.0**
36.63	0.01	0.01	0.03	0.56	1.09	2.45	4.79	8.86
55.0	0.07	0.07	0.10	1.06	2.04	2.94	9.14	20.50
73.7	0.09	0.13	0.16	1.47	2.59	5.09	8.19	15.20
91.3	0.14	0.14	0.16	1.46	2.31	4.95	9.03	13.11
110	0.12	0.15	0.17	1.32	2.31	4.68	8.29	21.72

*It should be noted that the TPU composites were above T_g prior to induction heating, resulting in a negligible activation. Therefore, activation time and recovery rate could not be recorded.

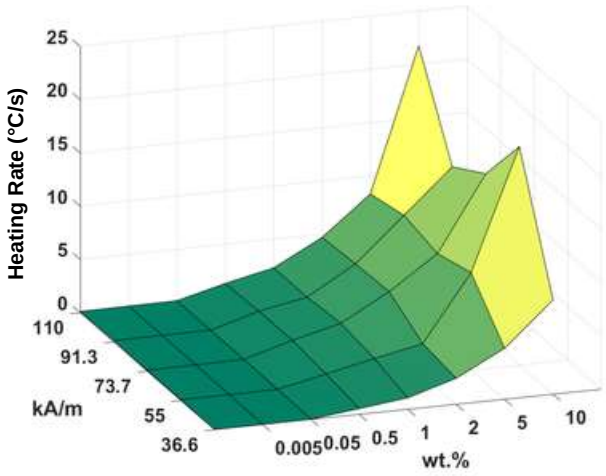

Figure 5.7 Induction heating plot showing the heating rate (°C/s) of TPU composites with respect to Fe_3O_4 NPs concentration and magnetic field strengths. It should be noted that unlike the other two polymer matrices, only a heating rate was observed and plotted, due to the T_g of TPU residing well below room temperature.[51-53]

The heating behavior of the TPU composites coincided with initial expectations. Since NP thermal output tends to maintain proportionality with magnetic field strength and NP concentration, it was unsurprising that the highest heating rate (21.7 ºC/s) was observed during the test where both of those parameters were maximum (110 kA/m and 10 wt%). In terms of concentration, the heating rate decreased exponentially as the concentration approached 0 wt%. At the lowest concentrations, it became apparent that the NP heating contribution was negligible, and the majority of the measured thermal load originated from the copper coil (i.e. heat conducted from the coil to the sample as a result of Joule heating). This conducted thermal load is largely managed by the circulating water within the coil; however, due to high amperages, the coils do get slightly warmer during testing.

5.3.9 Induction heating of PVAc and N-11 SMP composites

Similar to the TPU samples, the thermal camera analyzed the temperature gradients within the PVAc and N-11 SMP composites; however, since both of these samples were able to retain residual strain, their shape memory responses were noted as well. **Figure 5.8** provides a visual representation of their thermal response, activation time, as well as rate of recovery. Full datasets can be found below in **Tables 5.5** and **5.6**.

Table 5.5 Thermal activation properties of PVAc composites with increasing Fe_3O_4 NPs content and increasing magnetic field strength, as determined by induction heating and thermal camera.

	PVAc Heating Rates (°C/s) with increasing wt% Fe_3O_4 NPs							
Magnetic Field (kA/m)	**0**	**0.005**	**0.05**	**0.5**	**1.0**	**2.0**	**5.0**	**10.0**
36.63	0.01	0.02	0.05	0.53	1.14	1.01	1.98	5.23
55.0	0.03	0.06	0.15	0.88	1.44	1.76	2.50	11.72
73.7	0.11	0.07	0.18	1.04	1.57	4.39	2.19	12.09
91.3	0.17	0.13	0.21	1.00	1.67	3.59	6.86	21.50
110	0.16	0.12	0.23	1.56	1.82	4.49	4.45	10.42
	PVAc Activation Time (s) with increasing wt% Fe_3O_4 NPs							
Magnetic Field (kA/m)	**0**	**0.005**	**0.05**	**0.5**	**1.0**	**2.0**	**5.0**	**10.0**
36.63	N/A	N/A	N/A	54.60	37.72	17.50	11.32	4.28
55.0	N/A	N/A	N/A	39.72	22.56	8.00	7.08	1.08
73.7	N/A	N/A	N/A	17.96	20.88	5.40	13.48	1.16
91.3	N/A	N/A	170.00	25.08	21.26	5.84	3.88	1.00
110	42.92	N/A	122.12	15.12	15.52	4.32	3.80	1.32
	PVAc Rate of Recovery (cm/s) with increasing wt% Fe_3O_4 NPs							
Magnetic Field (kA/m)	**0**	**0.005**	**0.05**	**0.5**	**1.0**	**2.0**	**5.0**	**10.0**
36.63	N/A	N/A	N/A	0.03	0.06	0.01	0.38	0.25
55.0	N/A	N/A	N/A	0.02	0.02	0.36	0.22	0.42
73.7	N/A	N/A	N/A	0.08	0.02	0.37	0.16	1.00
91.3	N/A	N/A	0.02	0.03	0.02	0.22	0.51	1.37
110	0.00	N/A	0.01	0.03	0.06	0.12	0.19	1.03

Table 5.6 Thermal activation properties of Nylon-11 composites with increasing Fe_3O_4 NPs content and increasing magnetic field strength, as determined by induction heating and thermal camera.

Nylon-11 Heating Rates (°C/s) with increasing wt% Fe_3O_4 NPs

Magnetic Field (kA/m)	0	0.005	0.05	0.5	1.0	2.0	5.0	10.0
36.63	0.01	0.12	0.04	1.50	5.95	5.68	5.48	3.86
55.0	0.06	0.19	0.14	1.85	7.83	15.56	13.68	6.07
73.7	0.13	0.53	0.42	3.63	16.05	19.95	10.23	7.63
91.3	0.11	0.35	0.34	4.29	12.29	27.90	21.25	9.45
110	0.10	0.11	0.19	2.37	8.36	16.35	11.07	7.84

Nylon-11 Activation Time (s) with increasing wt% Fe_3O_4 NPs

Magnetic Field (kA/m)	0	0.005	0.05	0.5	1.0	2.0	5.0	10.0
36.63	N/A	N/A	N/A	N/A	12.32	17.76	4.22	16.36
55.0	N/A	N/A	N/A	N/A	6.16	3.08	2.16	9.28
73.7	N/A	N/A	N/A	13.64	4.04	3.32	1.28	6.08
91.3	N/A	N/A	N/A	5.96	5.52	3.16	2.08	2.48
110	N/A	N/A	N/A	16.96	6.00	2.00	2.00	7.00

Nylon-11 Rate of Recovery (deg/s) with increasing wt% Fe_3O_4 NPs

Magnetic Field (kA/m)	0	0.005	0.05	0.5	1.0	2.0	5.0	10.0
36.63	N/A	N/A	N/A	N/A	1.18	1.76	0.98	1.5
55.0	N/A	N/A	N/A	N/A	2.05	2.40	3.91	5.49
73.7	N/A	N/A	N/A	0.65	3.43	3.99	9.72	3.08
91.3	N/A	N/A	N/A	0.22	0.78	2.67	21.42	12.59
110	N/A	N/A	N/A	1.51	2.41	5.92	15.87	9.95

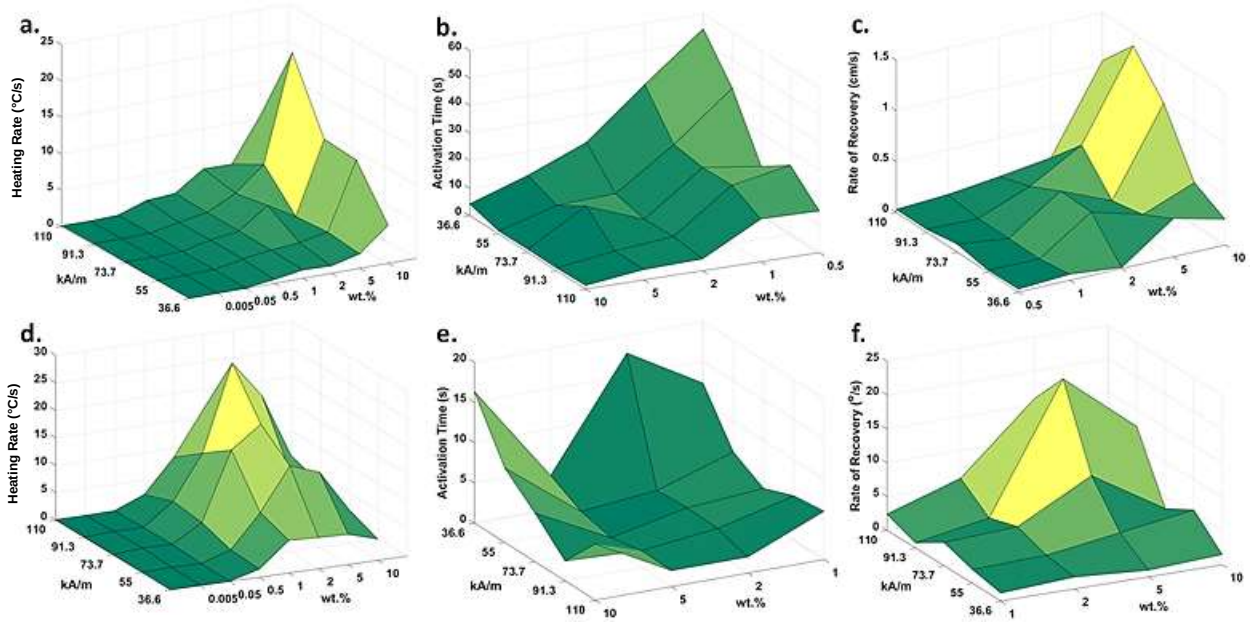

Figure 5.8 Induction heating characteristics of PVAc and N-11 samples: a) **PVAc heating rate;** b) **PVAc activation time;** c) **PVAc rate of shape recovery;** d) **N-11 heating rate;** e) **N-11 activation time;** f) **N-11 rate of shape recovery. A general trend was observed, showing an increase in heating rate and rate of recovery, and a decrease of activation time with increasing Fe_3O_4 NPs content and magnetic field strength. (Note the change in x-y scale with** b. **and** e.**)**

In terms of thermal output, the PVAc samples behaved similarly as to the TPU samples: the heating rate increased with respect to both magnetic field strength and concentration. However, the optimal magnetic field strength was recorded at 91.3 kA/m, rather than at the highest strength (110 kA/m), **Figure 5.8a**. A similar occurrence can be found with the N-11 samples, where the optimal field strength is 91.3 kA/m, yet, in terms of concentration, the highest heating rate peaked at 2 wt% rather than 10 wt%, **Figure 5.8d**. Observations such as these imply that optimal heating is a function of the polymer material properties rather than the NPs, and it could be advantageous in terms of overall process efficiency. If optimal heating occurs at lower magnetic field strengths, then the induction heater expends less energy to achieve a more favorable result. Similarly, if optimal heating occurs at a lower NP concentration, then less iron oxide is needed during fabrication, which presents a more cost-efficient option. Another key observation made during heating showcased poor dispersion within the N-11 samples, resulting in non-uniform heating (i.e. heating in discrete regions within the SMP), **Figure 5.9a**. Poor dispersion within the N-11 matrix

encouraged the formation of NP clusters, which, during heating, created these discrete regions of elevated temperature.

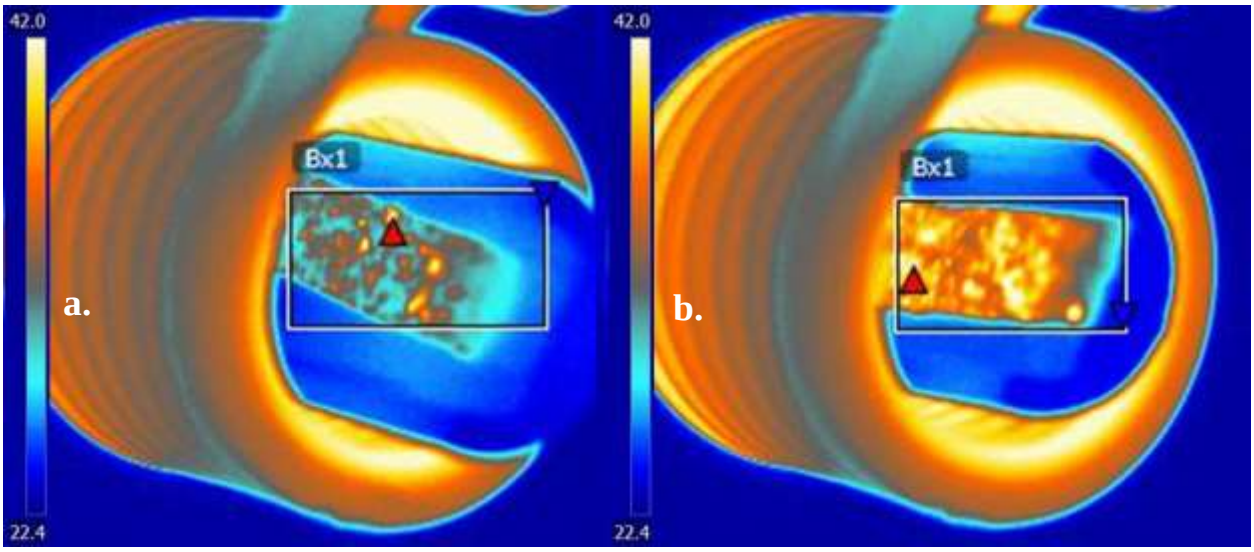

Figure 5.9 N-11 thermal gradients during induction heating: a) **2 wt% sample ~ 2 seconds into heating** b) **5 wt% sample ~2 seconds into heating.**

For both PVAc and N-11, activation times varied inversely to the measured heating rates; however, since N-11 requires a higher temperature to initiate a response, the activation times were slightly longer. The shortest activation time for PVAc (1 s) was observed at 10 wt% and 91.3 kA/m, which coincided with the highest heating rate. In the case of N-11, the lowest activation time (1.28 s) occurred at 5 wt% and 73.7 kA/m, which deviated from the highest heating rate mentioned earlier. Non-uniform heating explained this discrepancy. The thermal camera recorded the maximum temperature within the composite; however, this max temperature in N-11 occurs within one of the discrete clusters of NPs. The thermal energy must be given time to diffuse throughout the polymer, increase the average temperature, and initiate the shape memory response. In the 2 wt% sample, **Figure 5.9a**, the NP clusters created regions of higher temperature, which resulted in a high heating rate; however, due to relatively low concentration, these clusters were few in number, resulting in a slower thermal transport throughout the polymer and slower activation time (3.16 s). With the 5 wt% sample, **Figure 5.9b**, the higher concentration resulted in a much more uniform average temperature increase, which lowered the time to activation (1.28 s). Rate of recovery for both samples tended to vary inversely with activation time (proportionally to heating rate). For the PVAc samples, the highest rate of recovery (1.37 cm/s) originated in the

same sample with the lowest activation time (10 wt%, 91.3 kA/m). Since the rectangular PVAc samples were deformed in the axial direction, their shape memory response is represented as a linear speed (cm/s); however, for the N-11 samples, the represented speed is in terms of angular velocity (°/s). Similar to the activation time measurements, the fastest rate of recovery for the N-11 samples occurred at 5 wt%; however, 91.3 kA/m was indicated to be the optimal magnetic field strength. For both samples, the average speed declined with decreasing concentration and magnetic field strength. Studying activation times and recovery rates proved that while analyzing the polymers in terms of max heating rate can prove to be beneficial, observing the shape memory response can provide a more holistic view of the remote activation brought upon by induction heating.

It should be further noted that although shape recovery ratios and shape fixation ratios were not determined within this study, according to previous SMP composites studies by Behl et al., Mohr et al., and Lendlein et al., in which upwards of 10 wt% magnetic nanoparticles were employed, if the specific thermal transition temperatures of the polymer matrix are achieved, the ratios will act independently from the particle content.[11,14,17] In addition, the success shown by the SMP composites to hold and recover their shape through each Fe3O4 NP loading content, suggests that the nanoparticle loading does not play a significant role on the shape recovery ratio and shape fixation ratio.

5.3.10 Heat dissipation during induction heating

An important parameter to consider when adhering hydrogels to the SMP composites is the role of thermal buffering. Essentially how the temperature of the hydrogels will increase during the shape recovery process. A simple experiment quantified this change in temperature by submerging SMP samples in a 6 mL deionized aqueous suspension and observing the rise in local temperature with a thermocouple, **Figure 5.10**.

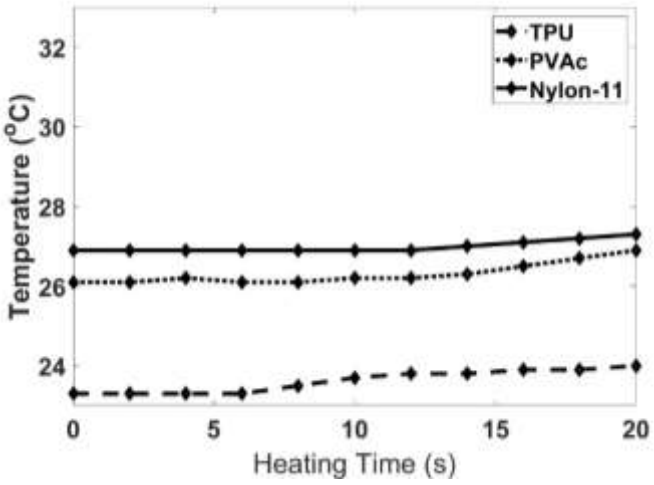

Figure 5.10 Time plot depicting temperature increase for water suspension containing 10 wt% Fe_3O_4 NP SMP samples heated at 91.3 kA/m, as determined by thermal/IR camera. It can be observed that the thermal dissipation of SMP composites into a liquid medium during induction heating was relatively negligible within the time required to induce any shape memory effects.

The temperature plots indicated very promising results. Within the 20 second measurement period, the change in temperature of the surrounding water did not exceed 2 ℃. Surprisingly, even when completely submerged in water, a shape recovery response was observed for both the PVAc and N-11 samples. While this is not necessarily a direct comparison with the actual hydrogel composites, the test indicated that the SMP substrate could quickly undergo a shape memory response remotely via induction with limited thermal transport into the hydrogel. Limiting this thermal transport is necessary to maintain cell viability, which reiterates the novelty of these SMP substrates.[86-87]

5.4 Conclusions

Shape-memory materials, specifically shape-memory polymers (SMP), have received a substantial increase in research interest due to the vast array of applications for which they can be employed. Typically, SMPs are activated through direct contact of stimuli, however, higher degrees of control and applicability are being discovered for SMPs that can be activated through indirect methods of simulations. One of the most prominent methods of indirect stimulation is through induction heating, in which strong magnetic fields are used to energize magnetic nanoparticles embedded within polymer matrices to induce a thermal shape change. This study sought to utilize this method of indirect stimulation to concisely control shape-memory effects

among a variety of different SMP composites comprised of magnetite nanoparticles (Fe_3O_4 NPs) dispersed in three commonly employed biocompatible polymers, TPU, PVAc, and N-11. Once fabricated, each SMP composite was successfully characterized through a series of thermal, morphological, and induction heating tests, resulting in promising shape-memory activation that could be rapidly triggered and controlled through manipulation of Fe_3O_4 NPs content and magnetic field strengths. As well, a multitude of tunable biocompatible SA and CNC hydrogel composites were fabricated and analyzed through mechanical, hydrational, and thermal experimentation to determine the potential biological functionality. A large variance of hydrational and mechanical properties were observed within the span of hydrogel composites, ultimately deeming them capable of supporting a wide variety of cellular structures through mimicry of specific extracellular matrix necessities, as well as providing a great deal of thermal shock buffering.

Although separately these functional materials possess interesting characteristics, when combined to produce a multi-composite scaffold, similar to the study performed by De France et al., the resulting highly unique properties allow for greater applicability through a range of scientific fields.[37] Specifically noted, is the ability to control hierarchical topographical changes within the hydrogel composites through activation of the SMP composite substrate shape-memory effects, without inducing thermal shock in seeded biological components. This unique capability lends itself to significant compatibility for biological functionality, including the ability to maintain cellular differentiation, proliferation, growth, and maturation through both thermal and physical manipulation of their environments. Along with the potential cell culture aspects, these multi-composite scaffolds could create a segue into new and improved biological applications, including controlled drug delivery, tuned ejection of biological components, and *in vivo* manipulation of biomaterial implants.

Chapter 6: Mechanically and Directionally Tunable Gelatin and Cellulose Nanocrystal/Nanofibril Composite Hydrogel Scaffolds for Multi-Functional Scar Tissue Prevention

6.1 Introduction

The human body is one of the most advanced and intricate biological systems in the world, comprising of complex ensembles of living cells and tissues responsible for all of the vital functions needed to support life.[1-3] In particular, as the largest organ of the body, human skin exemplifies the necessity for unification of biological complexity, from the multitude of biological components working in ensemble to the specific orientation and structuring of individual cells and fibers.[4-6] Skin is constructed of both epithelial and connective tissues, including nearly ageless dermal collagens, elastic fibers, proteoglycans, and hyaluronic acid, to create very particular chemical and mechanical properties.[4-8] The cohesive contributions of these two tissues are of vital importance to sustaining the intricate molecular composition and protective structure of the skin.[4-8] Therefore, when faced with injuries, including burns, lacerations, chronic ulcers, disease, and impact hemorrhaging, a range of defects can occur within the natural composition and structuration of the skin.[9-11] Following an injury, an immediate biological response is initiated, typically involving hemostasis, inflammation, formation of granulation tissue, re-epithelialization, and matrix remodeling, in order to recover and heal the damaged skin tissues.[11-13] Although effective, this natural method of wound healing leads to the formation of undesired scar tissue.[14] Comprised of the same collagen as the original tissue, yet due to overexpression and crosslinking of collagen fiber networks, scar tissue lacks elasticity through formation of fiber entanglements, subsequently compromising the natural integrity of the biological tissue.[13-15]

Since skin comprises of nearly 5-6% of the entire body's mass and fully encases all internal systems, retaining its natural protective barrier through the treatment of scar tissue is vital to its biological functions.[6,11-15] In the United States alone, millions of people are afflicted by significant scar tissue formation annually, leading to an estimated $12 billion scar treatment market.[14] In addition to the high number of cases and medical costs, due to media-defined "beauty", individuals with deforming scars tend to suffer from social stigma ridicule and psychological trauma, as well as the long-term physical dysfunction.[14,17] As such, research interest to enhance natural wound healing and scar tissue reduction through a variety of medical and tissue engineering techniques

has drastically risen, especially given the low quantity and efficacy of organ transplantation and regenerative medicine techniques following severe injuries.[14-16] The most common techniques for minor injuries and scarring are cosmetic treatments employed by dermatologists and plastic surgeons, including chemical peels, filler injections, laser treatment, radiotherapy, topical silicone, steroids, plastic surgery, and vitamins, however, nearly all of these treatment options fail to prevent or completely eradicate scar tissue.[14,17-18] Instead, they only involve rehabilitating previously formed scar tissue to reduce size, shape, and noticeability, while attempting to increase elasticity and mechanical integrity.[14,17,19]

In the case of severe injuries, such as third degree burns and full-thickness tears or lacerations of the tissue, natural wound healing will not always suffice, leading to infections, maiming, amputation, and potentially death.[9-11] Therefore, in an effort to further increase the rate of wound healing and mitigate the potential complications above, a multitude of tissue engineering and regenerative medicine techniques have been researched to enhance hydration and complex cell growth, while reducing infections through antimicrobial properties.[20-25] For example, a review by Yu et al. explores the enormous clinical significance of skin tissue engineering techniques for supporting the regeneration of the native cellular and physiological functions of skin.[20] Similarly, hybrid biomaterials comprised of biocompatible matrices housing cellular cultures have been heavily researched, in order to enhance integration of foreign scaffolds, while enhancing the prevention of water loss via evaporation and signaling for wound closure.[21-22] Other reviews performed by Khan et al. and Tay et al. exemplify the necessity for complex structuration of three-dimensional nano-engineered biomaterial scaffolds to promote cell growth and morphogenesis of new tissues through interactions with human cells.[23-24] Yet, many of these still face major scientific and clinical challenges, especially when it comes to completely healing the skin injury, while simultaneously maintaining the native structuration and cellular composition.[21-22,24] For example, a particular study recently performed by Shan et al. shows significantly improved wound healing through gelatin and sodium alginate hybrid scaffolds, however, the major challenge of subsequent scar tissue formation remains, leading to incomplete total wound healing capabilities.[25] Therefore, it is imperative for future regenerative techniques to possess not only the same rate of wound healing potential, but also the structuration, integration, and aftermath of tissue regeneration for optimal retainment of native physiological functions of the skin.[26-30] A plethora of recent literature

reviews and perspectives, such as those by Jones et al., Mir et al., and Kargozar et al., discuss critical criteria for the success of future tissue engineering and regeneration techniques, including three-dimensional nanostructuration utilizing both biomimetic materials and embedded biological components, cohesive biomaterial and tissue interactions and integration, and *in situ* tissue repair initiated in the host tissue.[26,29-30]

The ability of current techniques to meet the discussed critical criteria, specifically those for skin tissue engineering and regeneration, is still lacking in practical application.[27-29] As well, nearly all of these techniques tend to focus on decreasing the overall time of wound healing and affliction, yet somewhat neglect the complete quality of the healed tissue and ability to mitigate scar tissue formation.[25-26,29] Therefore, in order to combat these challenge, this research seeks to enhance the overall quality of regenerated tissue through three simultaneously working components: 1) supplying an enhanced ECM environment for cell growth and viability; 2) inhibition of scar tissue formation due to overexpression of collagen fiber growth in sporadic orientation; and 3) generating alignment and structuration of new cells and tissues that most closely mimic native tissues to prevent fiber entanglements that lack elasticity and relaxation abilities. Highly tunable, multicomponent hydrogel composites, comprised of microbiological gelatin and cellulose nanocrystals (CNC) and nanofibrils (CNF) were fabricated through solution casting and bioprinting techniques in an attempt to form complex structures with controlled alignment resembling natural skin tissues. In addition, through manipulation of hydrogel compositions, mechanical properties, filler orientation, biodegradation rate, and scaffold nanostructuration, this research investigated increased adaptability for multiple skin injuries and scar tissue prevention. The hydrogel scaffolds were characterized for swelling capabilities, gelatin degradation, glutaraldehyde release, mechanical properties, and filler alignment, via swelling and drying tests, UV spectroscopy, dynamic mechanical analysis, and polarized light microscopy (PLM). Following scaffold fabrication, characterization, and optimization, *in vivo* animal studies were theorized on how the significance of controlled alignment and structuration of complex hydrogel scaffolds would affect inhibition of random tissue orientation during the natural healing processes, reducing undesired scar tissue formation.[25,31-32]

6.2 Experimental Methods

6.2.1 Materials

Type A microbiological gelatin (300 g Bloom) from porcine skin, 50 wt% glutaraldehyde (GTA) aqueous solution, molecular biology BioUltra glycine, 1X BioPerformance certified phosphate buffer saline (PBS) packets, BioReagent urea powder, and ACS Reagent copper(II) sulfate pentahydrate were all purchased from Sigma-Aldrich. Bicinchoninic acid solution (BCA Reagent A) was purchased from G-Biosciences. The BCA solution, copper(II) sulfate pentahydrate, and PBS were used to create a typical BCA protein assay kit. Never-dried commercial sulfated cellulose nanocrystals (CNCs) in an 11.8 wt% aqueous suspension were purchased from the University of Maine Nanocellulose Facility. The CNCs were extracted from a wood source and characterized with average dimensions of 150-200 nm in length and 5-20 nm in width, sulfur content of 0.94 wt%, and surface charge density of 330 ± 15 mmol/kg cellulose. TEMPO-oxidized cellulose nanofibrils (CNFs) in a 1.0 wt% aqueous suspension were purchased from the US Department of Agriculture Forest Products Laboratory. The CNFs were extracted from a wood source and characterized with average dimensions of up to several hundred microns in length and nominal width of 50 nm, and a sodium carboxylate salt content of 1.4×10^{-3} mmol/kg cellulose.

6.2.2 Fabrication and characterization of gelatin and CNC/CNF composite hydrogels

Crosslinked gelatin samples of varying concentrations and crosslinking densities were fabricated from an adapted procedure established by Bigi et al.[33] Microbiological gelatin was taken as received and added to deionized water (diH_2O) in a concentration of 40 wt% (400mg/mL), to create a stock solution for all subsequent hydrogel fabrication. The 40 wt% gelatin stock solution and a beaker of diH_2O were set on a hotplate at 40 °C to restrict the gelatin from congealing before crosslinking. From the stock solution, 10 mL samples were created by diluting with additional heated diH_2O to the desired concentrations of 2, 5, 10, 15, and 20 wt% gelatin. While in liquid form, GTA was added to the samples in varying ratios ranging from 0.1 to 2.0 wt% to ensure uniform crosslinking throughout the entire gelatin sample. The final solution was cast into a 5 cm Teflon petri dish, and left for 24 h before testing to allow for full crosslinking throughout the hydrogel sample, as previously determined by Bigi et al.[33] After a full 24 h, each sample was removed from the petri dish and washed thoroughly with a 1M urea aqueous solution and

additional diH_2O to terminate and remove any remaining unreacted aldehyde groups of the GTA. Each hydrogel composition was subsequently stored in a closed environment to ensure retainment of moisture until testing. The hydrogels were named by composition of gelatin and GTA crosslinker content, e.g. 10 wt% gelatin and 0.5 wt% GTA was labeled 10G0.5X, with further compositions and naming noted in **Table C** for easier reference throughout the manuscript.

Following preliminary characterization of the gelatin hydrogels above, shown in **Table 6.1 and 6.2**, CNCs and CNFs were introduced into the 5, 10, 15, and 20 wt% gelatin hydrogels to determine their effect as a reinforcing agent and ability to manipulate mechanical properties. It should be noted that the 2 wt% gelatin hydrogel was omitted from further studies due to poor performance and lack of mechanical stability. The 11.8 wt% CNC aqueous suspension was diluted with additional diH_2O to create a 10 wt% stock solution for easier measurements. CNCs and CNFs were introduced into the hydrogels with compositions of 0.5, 1.0, 2.0, and 5.0 wt% CNCs, and 0.1, 0.2, and 0.5 wt% CNFs. Samples were produced by taking the required volume from the stock gelatin solution and either stock CNC or CNF suspensions to total a volume of 10 mL with the pre-determined compositions, further detailed in **Table D**. Following mixtures, CNC and CNF shear alignment was obtained through established 3D bioprinting techniques prior to crosslinking, and verified utilizing polarized light microscopy (PLM).[34-36] PLM was performed on all composite compositions using a Leica DM750 P microscope equipped with cross-polarized filters, following a protocol established by Hausmann et al.[35]

As stated above, the hydrogels were named by the composition of gelatin, GTA, and either CNC or CNF content, e.g. 10 wt% gelatin, 0.5 wt% GTA, and 2 wt% CNC was labeled 10G0.5X2CNC, with further compositions and naming noted in **Table D** for easier reference throughout the manuscript. It should be noted that the 20 wt% gelatin hydrogels were too viscous, pre-crosslinking, to add greater than 2 wt% CNC and 0.2 wt% CNF and still form stable, uniform hydrogels.

6.2.2.1 Swelling tests

Swelling tests were performed utilizing a drying and swelling method, similar to Bigi et al. and Ofner et al., to determine water uptake of each hydrogel composition.[33,37] Each composition of crosslinked gelatin films were cut into three samples with dimensions measuring 1x1x0.5 mm^3 and weighed. Following the initial measurement, all samples were air-dried for at least 24 h under

a movable ventilation hood. After drying, each sample was reweighed and submerged in 20 mL of 0.01 M PBS at 37 °C to swell for 72 h. Following swelling, each sample was removed from the PBS, surface dried with a Kimwipe EX-L to remove excess liquid, and reweighed to determine final swelled mass. All sample measurements were normalized to the dry mass to ensure accurate measurements from any variations in sample size or weight. The amount of absorbed water was then determined using the equation below, **Eq. 1 and Eq. 2**, and reported as swelling percent and recovery percent in **Table 6.1**. To determine the effects of CNC and CNF addition on the swelling and recovery of the hydrogels, sample composition of 15G0.5X was chosen and reinforced with all CNC and CNF compositions. The effects of CNCs and CNFs on the swelling and recovery abilities of the hydrogels were recorded further in **Table 6.2**.

$$Swelling\ \% = \frac{(W_S - W_D)}{W_D} \times 100 \qquad \textbf{Eq. 1}$$

$$Recovery\ \% = \frac{(W_S - W_D)}{(W_i - W_D)} \times 100 \qquad \textbf{Eq. 2}$$

W_S = Final weight after 72 h of swelling, W_D = Dry weight after 24 h of drying, W_i = Initial weight of hydrogels immediately after crosslinking.

6.2.2.2 Gelatin degradation and GTA release profiles

Hydrogel scaffold degradation studies were performed on all gelatin compositions with varying GTA crosslinker content to determine the release profile of both gelatin and GTA *in vitro*, reported in **Table 6.3 and 6.4**.

Gelatin degradation studies were performed following an establish procedure by Bigi et al. to determine the degradation/leaching of gelatin within the crosslinked hydrogels.[33] Before each degradation study, the samples were thoroughly and repeatedly washed with diH_2O. The degradation of gelatin was evaluated by immersing 50 mg of each gelatin film composition into 5 mL of PBS and stored at 37 °C for 24 h, 2 d, 4 d, 1 w, 2 w, and 4 w, exchanging the 5 mL of PBS release buffer each time. The gelatin content within the release buffer was determined using a BCA protein colorimetric assay. A 200 µL fraction of the collected release buffer was added to 2 mL of an assay solution comprising of 4 wt% copper (II) sulphate pentahydrate solution and BCA reagent A in a 1:50 v/v final ratio, respectively. The final volume of each sample was brought up to 5 mL using additional PBS, and subsequently cooled to room temperature. The absorbance of each final solution was measured at 562 nm using an Agilent Cary 60 UV-Vis spectrophotometer, and

compared to a calibration curve formulated from blank protein assays to determine concentrations of gelatin degradation from each composition. The obtained degradation results were recorded in **Table 6.3**.

GTA release studies were performed following an established procedure by Bigi et al. to ensure the removal of all the GTA as a potential toxin to the body.[33] Before each release study, the samples were thoroughly and repeatedly washed with diH_2O. The release of GTA was evaluated by immersing 50 mg of each gelatin film composition into 3 mL of PBS and stored at 37 °C for 24 h, 1 w, 2 w, and 4 w, exchanging the 3 mL of PBS release buffer each time. The collected release buffer was then added to 7 mL of 0.1 M glycine solution, and further stored at 37 °C for 24 h, or until a stable coloring was reached. The absorbance of each final solution was measured at 436 nm using an Agilent Cary 60 UV-Vis spectrophotometer, and compared to a calibration curve formulated from blank solutions of varying GTA to determine concentrations of GTA release from the samples. The obtained release concentrations were recorded in **Table 6.4**.

6.2.2.3 Mechanical tests and characterization

Both compression and tension tests were used for mechanical characterization, performed with a TA Q800 dynamic mechanical analyzer (DMA), due to the soft mechanical properties of the hydrogels. Preliminary compression tests were conducted on each gelatin hydrogel composition, refer to **Table C**, to determine initial bulk mechanical properties. Each hydrogel was cut into five 27 mm diameter samples, and tested using a non-constrained, controlled isostatic force ramp of 3 N/min at 27 °C, until sample failure was achieved or DMA was maxed out in force and/or displacement. Tension tests were conducted on each hydrogel composite composition, refer to **Table D**, to determine the tensile properties, including elastic modulus, ultimate tensile strength, and elongation at failure. Each hydrogel composite was cut into five ribbons with cross-sections of 5 x 1 mm^2 samples, and tested using a controlled isostatic force ramp of 1 N/min at 27 °C, until sample failure was achieved or DMA was maxed out in force and/or displacement. All data was recorded at a rate of 0.5 s/pt, and analyzed using TA universal analysis.

It should be noted that a DMA was used instead of a typical Instron universal testing machine, in order to determine more accurate viscoelastic properties of the hydrogels, since there is no lag time between sample displacement and the force needed to maintain the rate of displacement.[36-37] The controlled force ramp allows for the viscous and elastic portions of the

material to take equal effect, rather than displacement ramp, which allows the viscous component to take a greater effect on the material properties.[38-39]

6.3 Results and Discussion

6.3.1 Characterization of composite hydrogel scaffolds

A multitude of composite hydrogel scaffolds were fabricated using solution casting and established 3D bioprinting techniques,[34-36,40] and characterized following similar procedures by Bigi et al., Ofner et al., and Yin et al.[33,37,41] Through manipulation of the gelatin, CNC/CNF, and GTA components, each unique scaffold composition was able to show distinct variation in hydration, biodegradation, and mechanical properties. It should be noted that during fabrication, the CNCs and CNFs were not chemically crosslinked, but rather formed a percolating network that became entrapped by the crosslinked gelatin proteins.[42]

6.3.1.1 Swelling behavior

Swelling tests were performed to determine the hydration and water retention abilities of the hydrogel scaffolds. In addition, recovery tests were performed to determine the ability of the hydrogel scaffolds to return to their original water content after being completely dried. The results concluded that after 72 h of swelling, each scaffold composition was able to swell well beyond its dried state, however, not enough to reconstitute its original water content, detailed in **Table 6.1**.

Table 6.1 Preliminary swelling and recovery data of varying crosslinked gelatin hydrogels after 72 h of submersion in PBS. All values were normalized to the respective sample's dried weight.

Swelling % after 72 h of Submersion

Gelatin Content (wt%)	Glutaraldehyde Content (wt%)			
	0.1	**0.5**	**1.0**	**2.0**
2.0	411	628	N/A	N/A
5.0	422	307	410	368
10.0	747	298	266	318
15.0	637	355	250	252
20.0	619	553	333	N/A

Recovery % after 72 h of Submersion

Gelatin Content (wt%)	Glutaraldehyde Content (wt%)			
	0.1	**0.5**	**1.0**	**2.0**

2.0	11.4	15.4	N/A	N/A
5.0	21.8	16.6	23.0	24.6
10.0	89.2	36.2	33.6	45.7
15.0	137.3	77.7	57.7	59.8
20.0	193.9	167.6	106.0	N/A

As gelatin content increased and GTA content decreased, swelling equilibrium drastically increased from 250% up to 750% due to excess space within a less-dense crosslinked gelatin network and larger pore sizes,[25] further discussed in the *Section 6.4.1.2*. In addition, hydrogel scaffolds produced with CNCs and CNFs caused no significant change in swelling and hydration properties, shown in **Table 6.2**.

Table 6.2 Preliminary drying, swelling, and recovery data of 15G0.5X hydrogels with CNCs and CNFs.

	CNC Content (wt%)				
	0.0	**0.5**	**1.0**	**2.0**	**5.0**
Swelling %	331 ± 11	247 ± 15	254 ± 17	198 ± 4	244 ± 14
Recovery %	52 ± 3	37 ± 2	41 ± 2	34 ± 1	53 ± 1
	CNF Content (wt%)				
	0.1	**0.2**	**0.5**	**1.0**	
Swelling %	314 ± 54	296 ± 19	236 ± 2	364 ± 60	
Recovery %	55 ± 7	54 ± 2	44 ± 1	71 ± 10	

Proper hydration of wounds is crucial to the regeneration and protection of new tissues, through mimicry of the native tissue's highly-saturated ECM.[44-46] Therefore, the promising swelling behaviors exhibited by the hydrogel scaffolds are crucial features for improving skin regeneration capabilities, specifically, maintaining wound moisture balance, protecting against foreign bodies, positively influencing diffusion of nutrients, and enhancing absorption of exudates.[25,43-45]

6.3.1.2 Degradation profile and release of gelatin and GTA

Preliminary gelatin biodegradation and GTA release studies for *in vivo* testing were simulated through an 8-week incubation process of the hydrogel scaffolds in a PBS media. The release profiles of gelatin and GTA were established and detailed in **Table 6.3 and 6.4**, with measurements recorded after 24 h, 2 d, 4 d, 1 w, 2 w, 4 w, and 8 w. Based on gelatin content and crosslinking density, degradation rates were successfully manipulated over an 8-week incubation period, showing initial to complete degradation between 2 days and 8 weeks. Although quantitative release profiles were not established, qualitative results in **Table 6.3** show biodegradation over the necessary time period of typical wound healing in rats (~21-28 days).[25,43-45]

Table 6.3 Qualitative gelatin release profile over an 8-week span, where X = **no visible degradation,** + = **beginning of noticeable degradation, and** 100% = **fully-degraded samples.**

	Cumulative Gelatin Release Over Time (wt%)						
Hydrogel Composition	**24 h**	**2 d**	**4 d**	**1 w**	**2 w**	**4 w**	**8 w**
5G0.1X	X	X	+	+	100%	100%	100%
5G0.5X	X	X	X	X	+	100%	100%
5G1X	X	X	X	X	100%	100%	100%
10G0.1X	X	X	X	+	100%	100%	100%
10G0.5X	X	X	X	X	X	+	100%
10G1X	X	X	X	X	X	X	X
15G0.1X	X	X	X	+	100%	100%	100%
15G0.5X	X	X	X	X	+	100%	100%
15G1X	X	X	X	X	X	X	+
20G0.1X	X	+	+	100%	100%	100%	100%
20G0.5X	X	X	X	+	100%	100%	100%
20G1X	X	X	X	+	+	100%	100%

Higher GTA content intrinsically increases the crosslinking density within the hydrogel scaffolds by reducing the amount of non-crosslinked amide bonds along the gelatin backbone.[46-47] However, an opposite effect is observed with increasing gelatin content, in which excess non-crosslinked gelatin pockets reside within the hydrogel. Both of these factors can be finely-tuned to manipulate crosslinking density within the scaffolds, causing variable biodegradation properties through changes in water molecule penetration.[47] As more water is allowed to penetrate the crosslinked network, higher degrees of swelling occurs, leading to faster hydrolysis of the amide bonds and overall biodegradation.[46-47] For example, the low amount of crosslinking and excess gelatin within the 20G0.1X scaffold allows for a large amount of water molecules to penetrate the hydrogel, disrupting the bonds between the non-crosslinked gelatin peptides through hydrolysis.[46-47] It should be noted that gelation hydrogels undergo enzymatic degradation *in vivo*, as well as hydrolysis, which would further increase the biodegradation rates when compared to the recorded values in **Table 6.3**.[47]

As well as biodegradation studies, the release of GTA during degradation was also observed since its presence can induce cytotoxic effects within living tissue.[48] In the case of humans, the National Institute of Health (NIH) regulations state that active GTA content needs to be less than 2 ppm when in contact with living tissue to show no cytotoxic effects.[49] Since GTA release was no longer detected after the first 24 hours, content was determined over the first 24 hours. The majority of the scaffolds showed promising results for GTA release content, with only a few scaffolds, 5G0.5X, 5G1X, and 10G1X, showing quantities greater than 2 ppm, detailed in **Table 6.4**.

Table 6.4 Glutaraldehyde release. Less than 2 ppm is considered okay by NIH regulations.

	GTA Release Over 24 h (ppm)		
Gelatin Content (wt%)	**0.1 wt% GTA**	**0.5 wt% GTA**	**1.0 wt% GTA**
5.0	1.62 ± 0.14	4.59 ± 0.29	6.66 ± 0.20
10.0	0.81 ± 0.43	0.37 ± 0.06	2.25 ± 0.14
15.0	0.23 ± 0.10	0.63 ± 0.20	1.14 ± 0.05
20.0	0.47 ± 0.02	0.77 ± 0.10	0.12 ± 0.08

These results are not only promising for precise biodegradation tunability, but also for potential drug delivery and sustained release applications, including tissue regeneration, various chronic wound healing, and cancer cell targeting, among others.[46-47,50-52] As the scaffold degrades, it provides the wound with a natural source of hydrolyzed collagen and moisture as a starting material for new ECM generation and tissue growth.[46-47,51] In addition, the remaining CNC and CNF networks act as a hierarchical structure for promoting proliferation and natural alignment of new cell and tissue growth through enhanced cellular and protein adsorption, while lending mechanical support and stability.[26,52-53]

6.3.1.3 Mechanical characterization

Dynamic mechanical analysis was performed on each hydrogel composition, listed in **Table C and D**, to determine the variability and tunability of tensile and compressive mechanical properties with varying crosslinking densities and addition of CNCs and CNFs. Preliminary compression data obtained was crucial for determining the effects of varying gelatin and GTA content, and subsequently crosslinking density on bulk material properties. The results showed insightful variations to the bulk moduli of the scaffolds, as well as the structural integrity of the hydrogel scaffolds prior to the addition of CNCs and CNFs. As shown in **Figure 6.1 and Table 6.5**, hydrogel mechanical properties vary significantly due to both gelatin and GTA content, with bulk moduli ranging from 1.6 ± 0.5 kPa for 2G1X to 162.4 ± 6.0 kPa for 15G2X. Higher GTA content led to enhanced mechanical strength, however, induced brittle fractures within the hydrogels from increased crosslinking densities.[37,54-55] Similarly, higher gelatin content also led to enhanced mechanical strength, yet contrastingly more viscous properties from increased swelling and loosely bonded gelatin.[33,37,54-55]

Table 6.5 Preliminary mechanical data for gelatin hydrogels (bulk/compressive moduli in kPa).

Gelatin Content (wt%)	Glutaraldehyde Content (wt%)			
	0.1	**0.5**	**1.0**	**2.0**
2.0	3.6 ± 0.9	2.0 ± 0.4	1.6 ± 0.5	N/A
5.0	3.8 ± 0.8	2.2 ± 0.1	4.2 ± 1.6	5.0 ± 0.7
10.0	9.7 ± 0.8	37.1 ± 8.8	50.7 ± 2.0	44.3 ± 1.5
15.0	49.2 ± 4.8	80.6 ± 6.4	118.4 ± 6.4	162.4 ± 6.0
20.0	68.1 ± 8.2	95.4 ± 10.5	134.5 ± 12.2	N/A

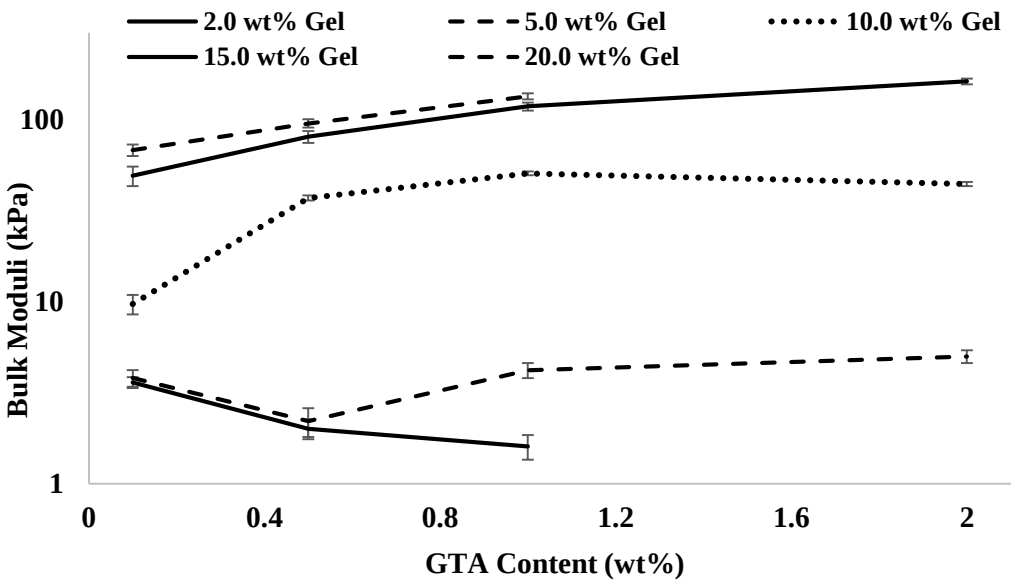

Figure 6.1 Preliminary compression tests of crosslinked gelatin hydrogels of varying gelatin and GTA content as determined by DMA. A general trend showed an increase in bulk moduli as both gelatin and GTA content increased, with the exception of the 2.0 wt% gelatin scaffolds, which showed a decrease due to the lack of structural stability.

In order to further finely-tune the mechanical strength and durability of the hydrogel scaffolds, CNCs and CNFs were added in varying concentrations to form interconnecting networks throughout the crosslinked gelatin networks.[56] With an increasing addition of CNCs and CNFs, mechanical characterization revealed a general increase in both tensile moduli and ultimate tensile strength, while causing distinctive variability in the amount of tolerated strain before failure, detailed in **Table 6.6 and 6.7**.

Table 6.6 Mechanical properties of CNC composite hydrogels, including tensile moduli, UTS, and elongation at failure.

Tensile Moduli (kPa)

Ideal Gelatin Compositions	CNC Content (wt%)				
	0.0	**0.5**	**1.0**	**2.0**	**5.0**
5G0.1X	17.1 ± 6.0	17.3 ± 7.2	10.9 ± 1.1	26.6 ± 3.6	85.4 ± 5.1
5G0.5X	28.5 ± 5.6	12.4 ± 3.8	5.8 ± 0.9	18.0 ± 7.4	68.4 ± 14.5

5G1X	22.8 ± 4.9	10.7 ± 1.4	12.7 ± 4.3	19.5 ± 1.7	49.3 ± 13.5
10G0.1X	44.5 ± 7.9	39.3 ± 2.9	48.2 ± 3.8	56.6 ± 5.9	101.7 ± 12.6
10G0.5X	63.8 ± 1.5	74.6 ± 2.9	52.1 ± 4.7	75.6 ± 14.6	218.5 ± 13.0
10G1X	48.0 ± 2.2	64.2 ± 10.1	87.8 ± 5.7	95.2 ± 20.5	221.8 ± 23.7
15G0.1X	71.2 ± 6.3	83.4 ± 14.2	91.6 ± 26.9	112.0 ± 12.9	159.4 ± 13.9
15G0.5X	84.8 ± 6.6	85.1 ± 13.6	78.9 ± 2.7	118.3 ± 17.1	204.2 ± 3.7
15G1X	121.7 ± 9.2	129.3 ± 18.6	171.3 ± 16.8	154.1 ± 25.7	250.9 ± 24.5
20G0.1X	99.8 ± 5.9	120.5 ± 7.0	96.2 ± 2.0	146.9 ± 12.1	N/A
20G0.5X	116.9 ± 9.6	117.1 ± 14.8	111.5 ± 3.7	165.1 ± 2.1	N/A
20G1X	144.4 ± 3.6	198.2 ± 8.3	273.7 ± 53.5	235.8 ± 16.3	N/A

Ultimate Tensile Strength (kPa)

Ideal Gelatin Compositions	**CNC Content (wt%)**				
	0.0	**0.5**	**1.0**	**2.0**	**5.0**
5G0.1X	7.2 ± 0.7	9.8 ± 2.0	12.5 ± 0.6	17.6 ± 6.5	27.5 ± 0.5
5G0.5X	5.9 ± 1.1	4.3 ± 0.3	5.9 ± 0.4	7.7 ± 1.4	8.7 ± 1.6
5G1X	3.8 ± 0.3	2.2 ± 0.3	3.1 ± 0.9	8.0 ± 0.9	13.2 ± 2.5
10G0.1X	30.3 ± 8.5	42.1 ± 7.4	59.7 ± 0.6	64.4 ± 3.4	53.3 ± 5.6
10G0.5X	15.9 ± 0.8	22.1 ± 3.6	28.1 ± 1.4	48.9 ± 10.7	91.1 ± 6.8
10G1X	14.6 ± 0.8	13.8 ± 1.5	23.5 ± 3.8	32.0 ± 2.3	104.4 ± 3.0
15G0.1X	65.8 ± 6.9	97.7 ± 8.9	119.9 ± 4.0	136.0 ± 15.5	124.9 ± 3.5
15G0.5X	24.3 ± 1.1	49.8 ± 3.6	56.9 ± 11.4	98.3 ± 13.7	144.4 ± 12.4
15G1X	41.5 ± 0.6	49.5 ± 15.2	34.1 ± 7.7	45.0 ± 3.4	40.1 ± 2.9
20G0.1X	82.6 ± 17.7	153.2 ± 12.1	116.2 ± 2.6	120.3 ± 7.1	N/A
20G0.5X	51.0 ± 7.8	55.3 ± 16.5	76.5 ± 12.5	111.5 ± 9.4	N/A
20G1X	25.8 ± 3.3	58.5 ± 10.2	73.4 ± 12.0	113.1 ± 6.6	N/A

Elongation at Failure (% Strain)

	CNC Content (wt%)

Ideal Gelatin Compositions	0.0	0.5	1.0	2.0	5.0
5G0.1X	129.5 ± 6.5	104.3 ± 8.1	121.8 ± 24.4	70.0 ± 14.9	120.2 ± 0.8
5G0.5X	90.0 ± 21.2	128.3 ± 7.7	127.1 ± 31.5	77.3 ± 9.7	55.9 ± 7.2
5G1X	74.7 ± 16.5	62.7 ± 10.9	65.1 ± 15.7	74.9 ± 1.0	57.3 ± 16.3
10G0.1X	127.7 ± 14.3	186.3 ± 14.5	347.9 ± 37.1	324.3 ± 23.5	160.0 ± 57.6
10G0.5X	97.8 ± 12.3	90.4 ± 8.2	104.9 ± 12.0	96.9 ± 27.1	120.9 ± 3.1
10G1X	44.7 ± 13.2	51.6 ± 3.6	73.7 ± 7.9	76.0 ± 8.7	115.9 ± 33.0
15G0.1X	422.7 ± 29.5	431.9 ± 9.2	426.2 ± 10.9	428.2 ± 16.1	414.8 ± 9.9
15G0.5X	66.1 ± 6.3	148.3 ± 5.1	116.5 ± 15.0	171.2 ± 89.2	374.0 ± 27.9
15G1X	84.2 ± 14.2	81.8 ± 25.2	54.2 ± 12.1	74.9 ± 7.0	50.7 ± 6.9
20G0.1X	322.1 ± 56.0	389.4 ± 6.0	420.9 ± 10.3	467.8 ± 4.9	N/A
20G0.5X	124.7 ± 18.2	118.5 ± 44.7	192.3 ± 60.4	274.9 ± 42.0	N/A
20G1X	34.4 ± 5.0	60.1 ± 13.5	97.1 ± 31.8	186.5 ± 19.7	N/A

Table 6.7 Mechanical properties of CNF composite hydrogels, including tensile moduli, UTS, and elongation at failure.

Tensile Moduli (kPa)

Ideal Gelatin Compositions	CNF Content (wt%)			
	0.0	**0.1**	**0.2**	**0.5**
5G0.1X	17.1 ± 6.0	27.5 ± 9.6	25.7 ± 4.1	44.9 ± 4.7
5G0.5X	28.5 ± 5.6	17.2 ± 0.2	28.3 ± 7.1	22.9 ± 1.6
5G1X	22.8 ± 4.9	11.6 ± 0.7	14.9 ± 0.9	25.6 ± 1.4
10G0.1X	44.5 ± 7.9	34.0 ± 11.5	52.3 ± 8.4	53.5 ± 3.4
10G0.5X	63.8 ± 1.5	55.1 ± 9.9	59.1 ± 9.9	79.5 ± 12.0
10G1X	48.0 ± 2.2	55.1 ± 7.9	50.5 ± 10.6	61.3 ± 14.2
15G0.1X	71.2 ± 6.3	78.0 ± 5.9	92.1 ± 3.9	101.5 ± 4.0
15G0.5X	84.8 ± 6.6	126.0 ± 22.1	90.8 ± 0.9	96.2 ± 2.1
15G1X	121.7 ± 9.2	130.8 ± 23.6	146.8 ± 42.1	207.9 ± 4.5

20G0.1X	99.8 ± 5.9	109.5 ± 17.4	125.5 ± 6.9	N/A
20G0.5X	116.9 ± 9.6	125.1 ± 8.4	148.1 ± 17.1	N/A
20G1X	144.4 ± 3.6	222.2 ± 45.6	316.1 ± 54.5	N/A

Ultimate Tensile Strength (kPa)

Ideal Gelatin Compositions	**CNF Content (wt%)**			
	0.0	**0.1**	**0.2**	**0.5**
5G0.1X	7.2 ± 0.7	11.5 ± 0.9	17.5 ± 0.3	17.4 ± 1.8
5G0.5X	5.9 ± 1.1	6.0 ± 1.0	9.9 ± 0.9	12.7 ± 0.2
5G1X	3.8 ± 0.3	6.3 ± 0.6	5.6 ± 0.5	8.1 ± 0.4
10G0.1X	30.3 ± 8.5	49.9 ± 7.2	58.0 ± 7.2	39.4 ± 1.0
10G0.5X	15.9 ± 0.8	23.1 ± 1.3	24.8 ± 4.3	53.1 ± 2.6
10G1X	14.6 ± 0.8	21.7 ± 2.1	31.9 ± 4.0	20.3 ± 0.9
15G0.1X	65.8 ± 6.9	95.4 ± 15.9	115.4 ± 8.5	131.1 ± 6.5
15G0.5X	24.3 ± 1.1	78.6 ± 0.7	41.3 ± 4.3	77.0 ± 4.7
15G1X	41.5 ± 0.6	40.9 ± 3.4	52.5 ± 3.7	59.3 ± 5.7
20G0.1X	82.6 ± 17.7	116.8 ± 20.7	139.3 ± 11.7	N/A
20G0.5X	51.0 ± 7.8	47.5 ± 4.0	91.4 ± 9.5	N/A
20G1X	25.8 ± 3.3	61.8 ± 12.8	88.5 ± 18.0	N/A

Elongation at Failure (% Strain)

Ideal Gelatin Compositions	**CNF Content (wt%)**			
	0.0	**0.1**	**0.2**	**0.5**
5G0.1X	129.5 ± 6.5	168.9 ± 16.3	221.7 ± 19.4	85.8 ± 9.2
5G0.5X	90.0 ± 21.2	85.9 ± 11.0	123.6 ± 30.9	119.1 ± 9.7
5G1X	74.7 ± 16.5	131.2 ± 7.9	141.2 ± 46.5	63.6 ± 1.7
10G0.1X	127.7 ± 14.3	328.3 ± 9.1	390.3 ± 3.9	185.9 ± 2.8
10G0.5X	97.8 ± 12.3	89.5 ± 6.2	80.0 ± 12.0	125.1 ± 3.4
10G1X	44.7 ± 13.2	84.1 ± 2.6	125.5 ± 18.4	108.1 ± 13.1

15G0.1X	422.7 ± 29.5	360.1 ± 12.8	393.0 ± 15.9	343.6 ± 11.0
15G0.5X	66.1 ± 6.3	205.6 ± 0.9	103.1 ± 2.1	254.0 ± 38.9
15G1X	84.2 ± 14.2	101.2 ± 7.4	195.6 ± 10.3	92.8 ± 11.7
20G0.1X	322.1 ± 56.0	351.3 ± 19.3	423.8 ± 19.3	N/A
20G0.5X	124.7 ± 18.2	90.7 ± 20.1	174.5 ± 37.4	N/A
20G1X	34.4 ± 5.0	68.3 ± 13.5	94.5 ± 31.8	N/A

With lower concentrations of CNCs and CNFs, combined with higher non-crosslinked gelatin molecules, there was a lack of a percolating network between the CNCs and CNFs, while promoting a denser network of gelatin molecules interactions.[40,56] This phenomenon not only led to an increase in reinforced properties through gelatin-filler interactions, but also lower plastic deformation and higher elongation until failure through maintained gelatin-gelatin interactions.[40] Contrastingly, as filler content rose to high enough levels within lower gelatin content hydrogels, the networks of CNCs and CNFs exceeded the percolation threshold, leading to increased brittleness from defects caused by agglomerations of filler-filler interactions.[57] Following similar trends found in literature with regards to reinforced hydrogels, **Figure 6.2** shows the tensile moduli variations with varying CNC and CNF content, generally increasing with increased filler content.[40,56]

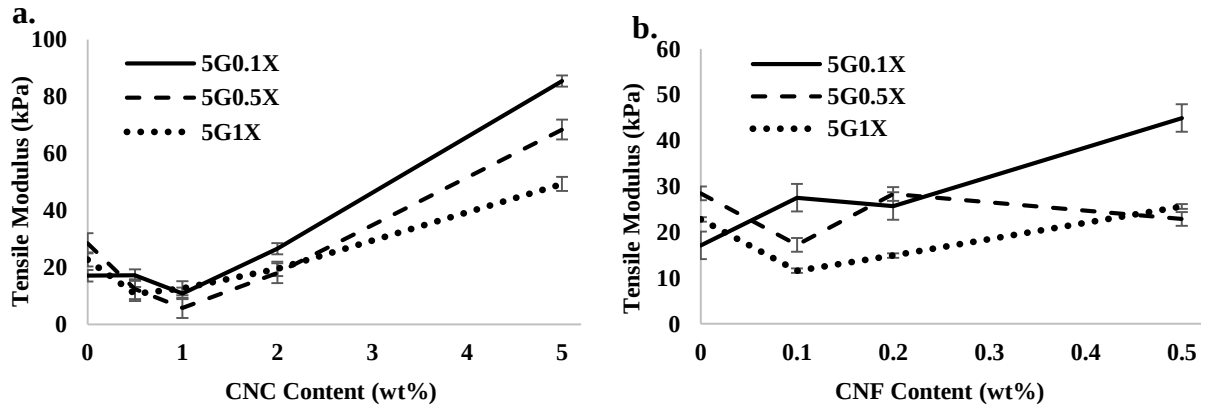

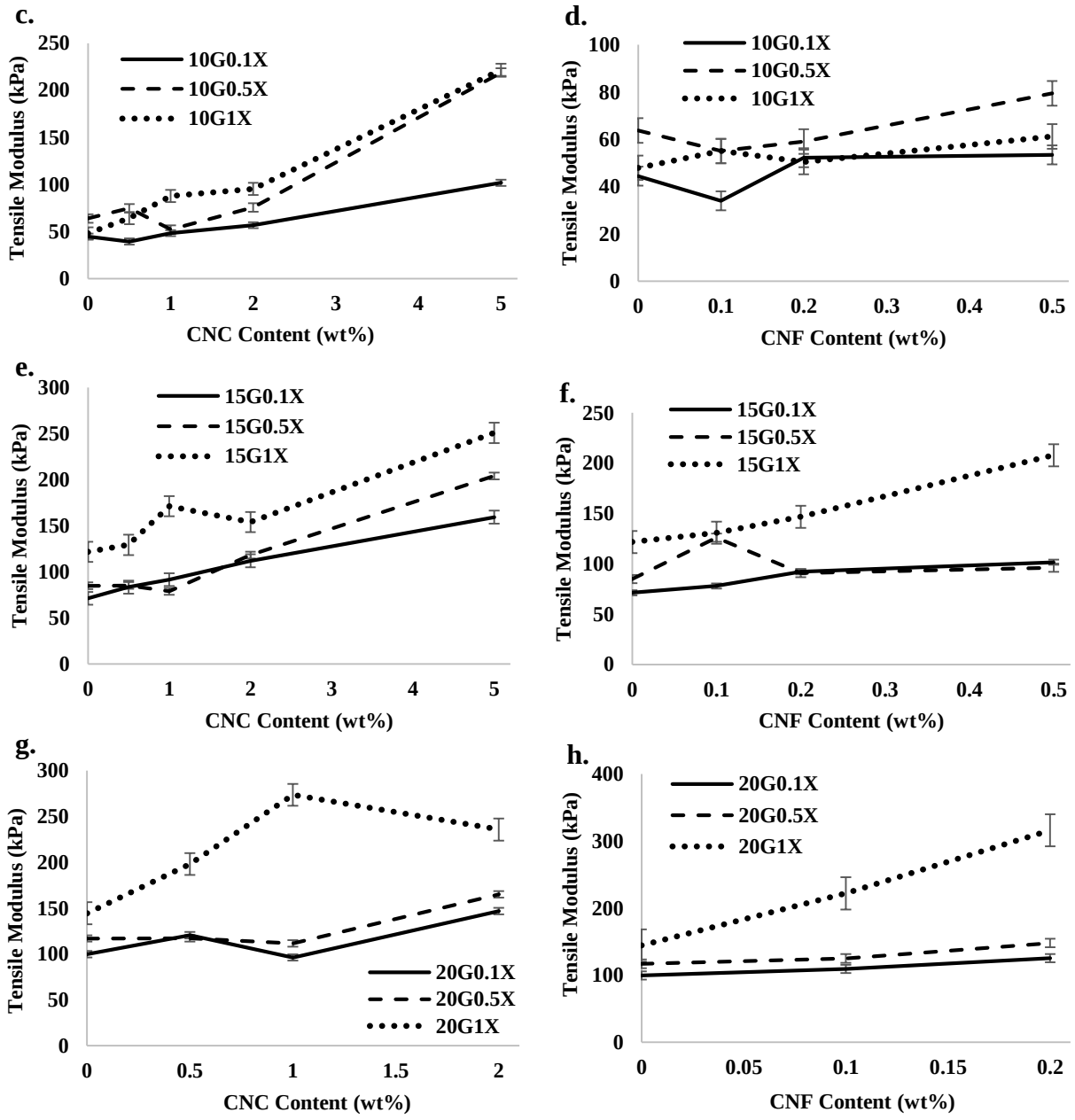

Figure 6.2 Plots of observed tensile moduli for 5.0, 10.0, 15.0, and 20.0 wt% gelatin scaffolds with varying CNC content and CNF content, as determined by DMA. In plotted order: a) **5.0 wt% gelatin with CNCs,** b) **5.0 wt% gelatin with CNFs,** c) **10.0 wt% gelatin with CNCs,** d) **10.0 wt% gelatin with CNFs,** e) **15.0 wt% gelatin with CNCs,** f) **15.0 wt% gelatin with CNFs,** g) **20.0 wt% gelatin with CNCs,** h) **20.0 wt% gelatin with CNFs. A general trend showed an increase in tensile moduli with increasing CNC and CNF content for all compositions.**

Through variations in gelatin, GTA crosslinker, CNC, and CNF content, mechanical properties could be successfully fine-tuned, with tensile moduli ranging between 5.8 ± 0.9 kPa for 5G0.5X1CNC to 316.1 ± 54.5 kPa for 20G1X0.2CNF, ultimate tensile strength ranging between

2.2 ± 0.3 kPa for 5G1X0.5CNC to 153.2 ± 12.1 kPa for 20G0.1X0.5CNC, and elongation until break ranging between 34.4 ± 5.0 % for 20G1X to 467.8 ± 4.9 % for 20G0.1X2CNC, further recorded in **Table 6.6 and 6.7**. The ability to manipulate mechanical properties is vital to wound healing and tissue engineering applications, specifically with regards to mimicking the natural ECM of native tissues and lending structural support to newly developing tissues.[58-61] Previous literature studies have not only shown the wound healing benefits of matching natural ECM as closely as possible, but also how detrimental it can be the further strayed from biomimetic design.[59,61] For example, a particular study by Chen et al. shows the difference between low, medium, and high stiffness hydrogel scaffolds with comparison to open wound healing on rats.[59] As the induced wounds healed, the medium stiffness hydrogel, which most closely resembled the modulus of skin, produced new tissue growth and wound contraction approximately 50% faster than the control and 25% faster than the low and high stiffness hydrogels. In addition, after Day 5 of healing, the medium stiffness group showed over 200% increase of positive cell growth compared to all other groups tested.[59] This study, among others, demonstrates the necessity for maximum mechanical property manipulation of hydrogel scaffolds to induce the greatest wound healing effect based on ECM and native tissue mimicry.[58-61]

6.3.1.4 Shear alignment of CNCs and CNFs

Polarized light microscopy (PLM) was performed on the cast and 3D printed hydrogel scaffolds to determine alignment of CNCs and CNFs through shear forces produced by the 3D printer, similar to studies by Hausmann et al. and Siqueira et al.[35-36] PLM revealed that CNCs and CNFs can be successfully aligned through shear forces introduced during extrusion bioprinting. Although no quantitative results were measured, the alignment comparison between the cast and 3D printed hydrogel scaffolds could be assessed through qualitative visual assessment.

6.4 Conclusions

Although a multitude of techniques have been researched to enhance the rate of wound healing, each method lacks the ability to promote “complete” tissue regeneration. While faster wound healing is beneficial, the subsequently produced scar tissue consisting of fibrous collagen I and II overgrowth and entanglements, still poses substantial challenges. This buildup of unsightly scar tissue leads to both physical and mental dysfunctionalities, including reduction of hydration, innervation, thermal regulation, elasticity, and barrier properties, as well as causing anguish to

those suffering from disfiguring scars and the social stigma of "beauty". The research performed in this study not only focused on the rate at which the wounds healed, but also the quality of regenerated tissue and its biomimicry to the native tissues. In order to accomplish this goal, a few objectives were set in place: 1) fabrication of mechanically and directionally tunable scaffolds utilizing CNCs and CNFs embedded in a gelatin matrix; 2) characterization of the hydrogel composite scaffolds through mechanical, hydration, and biodegradation analyses; and 3) proposing the utilization and benefits for *in vivo* animal studies, while inferring potential benefits from reviews of current literature. Tunable gelatin-based, CNC and CNF biodegradable hydrogel composites with controlled nanostructuration, were successfully produced in order to promote better biomimicry of regenerated tissue and improve the overall healing quality of wounds. Initial characterizations consisting of swelling potential, hydration retention, biodegradation rate, and GTA release, were performed on crosslinked gelatin scaffolds without any nanofillers to determine the ability to maintain a hydrated environment for optimal wound healing, while simultaneously producing a natural source of hydrolyzed collagen for new ECM generation through biodegradation. It was observed that depending on the degree of crosslinking, hydration equilibrium within the hydrogels change drastically between 250 and 750 wt% diH_2O, as well as tunable biodegradation rates from 2 days to 8 weeks. Additionally, negligible GTA release was detected, falling within the acceptable limit established by the NIH for cytotoxicity. Following initial characterization, CNCs and CNFs were introduced into the hydrogel matrix to create mechanically reinforced and nanostructurally aligned composite scaffolds. Through variation of CNC and CNF content, tensile modulus was tuned between 5.8 ± 0.9 kPa and 316.1 ± 54.5 kPa, while maintaining high elasticity of over 400 % strain. Along with mechanical tunability, 3D extrusion printing techniques allowed for the controlled orientation of CNC and CNF networks throughout the hydrogel matrices to better represent the natural structuration found in skin ECM and tissues.

Although *in vivo* testing was out of the scope of this study due to time constraints, these aligned nanofiller networks have been shown in literature to promote better wound healing and quality of regenerated tissue through guided cell proliferation and tissue growth.[53] However, the overall results proved successful in fabricating a novel hydrogel composite with oriented nanofillers for controlled nanostructuration and mechanical tunability. As such, this concept of

skin ECM biomimicry through hierarchical 3D constructs, has the potential to pose significant benefits for both biomedical and tissue engineering designs, along with clinical applicability for improving native tissue growth during wound healing, while reducing the amount of fibrous scar tissue formed.

Chapter 7: Conclusion and Outlook

7.1 Conclusions

Tissue engineering and regenerative medicine is progressing at a rapid rate, as new materials and techniques are continuously improving, while biological impairments are becoming more problematic.[1] Through enhanced knowledge of human biology, biomaterials processing, structuration, and characterization, and internal interactions, advancements can be achieved through intensive research.[2] Recent advances such as novel bioinks, gradient scaffolds, and cellular embedment within scaffolds have paved the way for complex 4D tissue scaffolds with improved reliability and functionality for modern biomedical applications.[1-2] This dissertation sought to provide novel methods and approaches for extraction and utilization of CNMs and MNPs to enhance PNCs for biomedical applications through various independent research investigations. Specifically, the abilities to finely tune nanostructuration and mechanical robustness through addition of CNMs, as well as induce controlled shape-memory effects through addition of MNPs, show great promise.[3-4]

The novel extraction and isolation method of p-CNCs from spent coffee grounds in Chapter 3, shows the potential for a new agricultural waste product to be recycled and reused in substantial materials research applications. Through intensive bleaching, purification, and phosphoric acid hydrolysis processes, p-CNCs were successfully isolated from spent coffee grounds. Through chemical and physical characterization techniques previously established by Foster et al.,[5] the morphology, thermal stability, surface charge density, dispersibility, and reinforcing capabilities of the isolated p-CNCs, were evaluated and characteristics compared to those in literature, as well as those commercially produced. A few crucial characteristics revealed were an aspect ratio of 12 ± 3, an apparent crystallinity of 74.2%, and a high phosphate content and surface charge density of 25.8 ± 9.6 mmol/kg cellulose and 48.4 ± 6.2 mmol/kg cellulose, respectively. Specifically, the ability to offer mechanical reinforcement in a PU matrix by a factor of 2 shows promise for the viability of these isolated p-CNCs for industrial uses. Finally, although the yields were found to be minimal due to the lack of cellulose within the raw material, the abundance of spent coffee grounds disposed around the world annually lend well to the viability of this process to be scaled to levels of commercial production.

Subsequently, Chapters 4-6 defines multi-step methods of the utilization of CNMs and MNPs into unique biomaterial PNCs, which were successfully fabricated for specific biomedical applications. Described in Chapter 4 is the first PNC biomedical application, in which a 3D bioprinting method for fabricating tunable CNC and PEGDA scaffolds with mechanical property gradients was established. One major challenge that bioprinting AM technology currently faces is the inability to accurately fabricate multi-compositional scaffolds. Due to the low viscosities of most biomaterial resins, specifically PEGDA, multi-step procedures are typically required for multiple material resins and cell types, being used almost exclusively in SLA.[6] With the goal of expanding the bioprinting field, viscous bioinks comprised of PEGDA/CNC compositions ranging between 90/10 to 60/40 w/w were created to produce single and multi-composition scaffolds of varying and gradient mechanical properties through multi-nozzle extrusion, as opposed to SLA. Both solution cast and 3D bioprinted scaffolds were compared for their mechanical characteristics, showing tunable ranges from 0.4 ± 0.1 to 27.8 ± 5.8 MPa for elastic modulus, 0.1 ± 0.0 to 0.7 ± 0.1 MPa for yield stress, and 7.5 ± 3.5 to 46.7 ± 22.3 % for strain at failure. Additionally, complex gradient scaffolds of multiple compositions were successfully fabricated, demonstrating the unique ability to utilize the benefits of each incorporated composition to increase overall mechanical integrity. Through the success of this work, progress towards transitioning from SLA-dominated PEGDA bioprinting to extrusion bioprinting is achieved, opening further potential for more complex and functional scaffolds, including those with controlled directionality, cell placements and variety, and multi-material components.

In a following independent study, Chapter 5 pursued the challenge of creating a 2.5D and 4D hydrogel construct with the ability to change topographically through indirect stimulation of an attached substrate. This chapter explored a different attribute of PNCs, in which MNPs were incorporated into three polymer matrices (TPU, PVAc, and N-11) to control shape memory effects through induction heating using various Fe_3O_4 NP loading capacities and magnetic field strengths. Initial characterization of the substrates consisted of induction heating tests and thermal camera imaging to determine the thermal absorption and dissipation abilities, rate of shape change, and initial recovery response of each PNC. Observations revealed that the PVAc and N-11 composite substrates reacted well to induction heating, specifically at Fe_3O_4 NP concentrations between 5.0 wt% and 10.0 wt% for PVAc and 2.0 wt% and 5.0 wt% for N-11, and magnetic field strengths

above 73.7 kA/m. Contrastingly, the TPU composite substrates showed no shape recovery during induction heating, as the T_g was well below room temperature, therefore could not hold any residual strain. Thermal dissipation experiments indicated very promising results for all PNC substrates, in which the maximum heating conditions produced less than a 2 °C change in the surrounding water after a 20 s measurement period. Additionally, SA and CNC hydrogels of various compositions were fabricated and analyzed for tunable mechanical, hydration, and thermal buffering properties. Characterization of the hydrogels established mechanical tunability from 63.7 ± 22.4 kPa to 3.1 ± 0.2 MPa for tensile modulus, a minimum water content and retention of 82 wt%, and average thermal buffering properties of 0.052 ± 0.011 °C/s. The mechanical tunability, hydration properties, thermal dissipation, and thermal buffering characterization showed great potential for the combined hydrogel and PNC substrates to support a multitude of cellular structures, while providing a large degree of protection from thermal shock. With the success of this study, in combination with the brief works published in literature,[7] hydrogel constructs with improved hierarchical structuration can be used and manipulated indirectly to produce vast topographical and morphological changes. This could significantly improve the biomedical and regenerative medicine fields through enhanced control of drug delivery, embedded cell and biological component release, stem cell replating, biosensing, and interfacial interactions, to list a few.

Chapter 6 followed similar methods to Chapter 4 to produce mechanically and directionally tunable scaffolds utilizing CNCs and CNFs in a gelatin matrix for wound healing applications. Typical biomaterials and tissue engineering scaffolds focus on the rate of wound healing rather than the quality of the regenerated tissue. As such, a few significant discoveries have already been made, producing biomaterial scaffolds that promote wounds to heal at a more rapid pace compared to the natural healing process.[1-2,8] However, the quality of regenerated scar tissue is lesser than that of native tissue, comprising of an overexpression and entanglement of fibrous collagen I and II.[8] This chapter focused on fabricating a tunable gelatin-based biodegradable hydrogel composite with controlled nanostructuration, in order to promote better biomimicry of regenerated tissue and improve the overall healing quality of wounds, as opposed to focusing on the rate of healing. Initial hydrogel characterization consisted of swelling potential, hydration properties, biodegradation rate, and GTA release to determine the ability to maintain a hydrated environment for optimal

wound healing, while simultaneously producing a natural source of hydrolyzed collagen for new ECM generation through biodegradation. Depending on the degree of crosslinking, the hydrogels showed remarkable swelling properties reaching equilibrium between 250 and 750 wt% diH_2O, as well as tunable biodegradation rates from 2 days to 8 weeks with negligible GTA release. Following gelatin hydrogel characterization, CNCs and CNFs were introduced into the hydrogel matrix to create mechanically reinforced and nanostructurally aligned composite scaffolds. Through variation of CNC and CNF content, tensile modulus was tuned between 5.8 ± 0.9 kPa and 316.1 ± 54.5 kPa, while maintaining high levels of elasticity over 400 % strain. Along with mechanical tunability, 3D extrusion printing techniques allowed for the controlled orientation of CNC and CNF networks throughout the hydrogel matrices to better represent the natural structuration found in skin ECM and tissues. Although not specifically tested, aligned nanofiller networks have been shown to promote better wound healing and quality of regenerated tissue through guided cell proliferation and tissue growth, similar to results described by Espinosa et al.[9] The overall results proved successful in creating a novel mechanically reinforced hydrogel composite with oriented CNCs and CNFs for controlled nanostructuration. By utilizing this concept of tissue mimicry through hierarchical 3D constructs, regeneration of tissue closer to that of native tissue was improved in rodent models, while significantly reducing the amount of fibrous scar tissue formed. Additionally, significant clinical implications can be drawn from this research, in which further study and progression could have vastly beneficial effects in the biomedical field for wound healing and other tissue engineering applications.

7.2 Outlook and Future Work

Through the described works performed in this dissertation, the complexity and relationships of biomaterial PNC compositions, structuration, and applications, gain an increased depth in the biomedical field and respective literature. This is shown through publication validation of the works in Chapters 3, 4, and 5, U.S. patent of the work in Chapter 5, as well as clinical trials and future publication of Chapter 6. However, the added support of these studies to literature are still in the infantile stages, as significantly more research is required to pursue clinical implementation, specifically with regards to the biological components and further cell and tissue engineering studies.

Although the discovered method of extrusion bioprinting was only applied to PEGDA scaffolds using CNCs as the nanofiller to increase viscosity, this same concept can be extrapolated to other biomaterial resins, in which SLA is the dominating AM technique. Through increasing viscosities of biomaterial resins utilizing specific bioinert NPs, multi-nozzle extrusion bioprinting can be further adapted to other PNC hydrogel systems to improve ECM replication, gradient physical and chemical properties, and various cell type embedment, while mitigating the need for multiple processing stages. In order to continue the progression of this novel 3D printing method towards large scale implementation, research incorporating a variety of NPs and biomaterial resins should be performed to better justify the breadth and universal application of this technique. Additionally, embedded cells, growth factors, and other biological components should be incorporated to determine efficacy of printable tissue engineering scaffolds for *in vitro* and *in vivo* applications.

Expanding on this established method, extrusion bioprinting can be used to develop innovative constructs with 2.5D and 4D hierarchical nanostructuration within hydrogel scaffolds, as discussed in Chapters 4 and 6. Furthermore, it allows for integration of specifically calculated topographical changes through controlled orientation of nanofiller networks (i.e. uniaxial, biaxial, and isotropic), as well as finely-tuned mechanical and hydration properties. Extensive hydrogel composite characterization showed the successful ability to manipulate a multitude of properties to better mimic the natural properties of the tissues being regenerated, however, materials characterization on its own is not enough to prove efficacy for wound healing potential *in vivo*. Consequently, cell cultures and animal studies will need to be performed to determine *in vitro* and *in vivo* benefits through guided cell growth and mechanical, biodegradable, hydration, and nanostructure tunability. Following *in vitro* and *in vivo* studies, histology and pathology of regenerated cells and tissues through H&E and M-G staining can be observed to determine efficacy of scar tissue reduction/prevention for future clinical implementation.

Lastly, the use of MNPs to produce magnetic capabilities and shape memory effects in electrically resistant polymer matrices are being continuously researched as an indirect stimuli-responsive promoter. As a new up-and-coming technology for SMP manipulation, induction heating utilizing MNPs has vast potential in a wide breadth of technical fields, in which indirect shape memory activation is required with minimal secondary responses. The results in Chapter 5

show the capabilities of PNCs embedded with MNPs to undergo hierarchical shape memory changes through thermal transitions brought about by absorption of magnetic energy within the polymer matrix. Additionally, the ability to induce shape memory effects with negligible thermal dissipation, allows for the incorporation and viability of living cells without the potential damage from thermal shock. Therefore, progression of this technique with the use of living cells could benefit the biomedical field in a variety of ways, including drug delivery, stem cell replating, hyperthermia, tissue engineering, theranostics, and site specific magnetic targeting and imaging. However, more research is needed to prove viability for clinical implementation, such as cellular cultures with mechanical ejection, embedded growth factor release, and potential controlled drug delivery release profiles.

Overall, the works in this dissertation have shown innovative approaches to combat a few crucial challenges in the biomedical and biomaterial fields, while lending greater depth and understanding to the current literature. However, looking to the future, each study will need to be further researched with a larger variety of NPs, polymer matrices, cellular studies, and *in vitro* and *in vivo* testing to justify the continuation into clinical applications. Furthermore, potential collaborations with industrial and clinical partners should be investigated to provide significant progression of these works.

References

R.1

1. Zaferani, S. H., 1 - Introduction of polymer-based nanocomposites. In *Polymer-based Nanocomposites for Energy and Environmental Applications*, Jawaid, M.; Khan, M. M., Eds. Woodhead Publishing: 2018; pp 1-25, https://doi.org/10.1016/B978-0-08-102262-7.00001-5.
2. Karak, N., Chapter 1 - Fundamentals of Nanomaterials and Polymer Nanocomposites. In *Nanomaterials and Polymer Nanocomposites*, Karak, N., Ed. Elsevier: 2019; pp 1-45, https://doi.org/10.1016/B978-0-12-814615-6.00001-1.
3. Passador, F. R.; Ruvolo-Filho, A.; Pessan, L. A., 7 - Nanocomposites of Polymer Matrices and Lamellar Clays. In *Nanostructures*, Da Róz, A. L.; Ferreira, M.; de Lima Leite, F.; Oliveira, O. N., Eds. William Andrew Publishing: 2017; pp 187-207, https://doi.org/10.1016/B978-0-323-49782-4.00007-3.
4. Mansor, M. R.; Akop, M. Z., 9 - Polymer nanocomposites smart materials for energy applications. In *Polymer Nanocomposite-Based Smart Materials*, Bouhfid, R.; Qaiss, A. e. K.; Jawaid, M., Eds. Woodhead Publishing: 2020; pp 157-176, https://doi.org/10.1016/B978-0-08-103013-4.00009-1.
5. Chen, Q.; Gong, S.; Moll, J.; Zhao, D.; Kumar, S. K.; Colby, R. H., Mechanical Reinforcement of Polymer Nanocomposites from Percolation of a Nanoparticle Network. *ACS Macro Letters* **2015,** *4* (4), 398-402, 10.1021/acsmacrolett.5b00002.
6. Papageorgiou, D. G.; Li, Z.; Liu, M.; Kinloch, I. A.; Young, R. J., Mechanisms of mechanical reinforcement by graphene and carbon nanotubes in polymer nanocomposites. *Nanoscale* **2020,** *12* (4), 2228-2267, 10.1039/C9NR06952F.
7. Frost, B. A.; Sutliff, B. P.; Thayer, P.; Bortner, M. J.; Foster, E. J., Gradient Poly(ethylene glycol) Diacrylate and Cellulose Nanocrystals Tissue Engineering Composite Scaffolds via Extrusion Bioprinting. *Frontiers in Bioengineering and Biotechnology* **2019,** *7* (280), 10.3389/fbioe.2019.00280.
8. Du, F.; Scogna, R. C.; Zhou, W.; Brand, S.; Fischer, J. E.; Winey, K. I., Nanotube Networks in Polymer Nanocomposites: Rheology and Electrical Conductivity. *Macromolecules* **2004,** *37* (24), 9048-9055, 10.1021/ma049164g.
9. Seidel, G. D.; Lagoudas, D. C., A Micromechanics Model for the Electrical Conductivity of Nanotube-Polymer Nanocomposites. *Journal of Composite Materials* **2009,** *43* (9), 917-941, 10.1177/0021998308105124.
10. Chow, W. S.; Ishak, Z. A. M., Smart polymer nanocomposites: A review. *Express Polymer Letters* **2020,** *14* (5), 416-435, http://dx.doi.org/10.3144/expresspolymlett.2020.35.
11. Joseph, J. P.; Singh, A.; Pal, A., Molecular Design Approaches to Self-healing Materials from Polymer and its Nanocomposites. In *Smart Polymer Nanocomposites: Energy Harvesting, Self-Healing and Shape Memory Applications*, Ponnamma, D.; Sadasivuni, K.

K.; Cabibihan, J.-J.; Al-Maadeed, M. A.-A., Eds. Springer International Publishing: Cham, 2017; pp 181-218, 10.1007/978-3-319-50424-7_7.
12. Ni, Q.-Q.; Zhang, C.-s.; Fu, Y.; Dai, G.; Kimura, T., Shape memory effect and mechanical properties of carbon nanotube/shape memory polymer nanocomposites. *Composite Structures* **2007,** *81* (2), 176-184, https://doi.org/10.1016/j.compstruct.2006.08.017.
13. Patel, N. P.; Miller, A. C.; Spontak, R. J., Highly CO2-Permeable and Selective Polymer Nanocomposite Membranes. *Advanced Materials* **2003,** *15* (9), 729-733, https://doi.org/10.1002/adma.200304712.
14. Rao, H.; Zhang, Z.; Tian, Y., Preparation and high oxygen-enriching properties of cross-linking polydimethylsiloxane/SiO2 nanocomposite membranes for air purification. *AIChE Journal* **2013,** *59* (2), 650-655, https://doi.org/10.1002/aic.13860.
15. Pandey, N.; Shukla, S. K.; Singh, N. B., Water purification by polymer nanocomposites: an overview. *Nanocomposites* **2017,** *3* (2), 47-66, 10.1080/20550324.2017.1329983.
16. Khaydarov, R. A.; Khaydarov, R. R.; Gapurova, O., Water purification from metal ions using carbon nanoparticle-conjugated polymer nanocomposites. *Water Research* **2010,** *44* (6), 1927-1933, https://doi.org/10.1016/j.watres.2009.11.041.
17. Hussain, F.; Hojjati, M.; Okamoto, M.; Gorga, R. E., Review article: Polymer-matrix Nanocomposites, Processing, Manufacturing, and Application: An Overview. *Journal of Composite Materials* **2006,** *40* (17), 1511-1575, 10.1177/0021998306067321.
18. Fischer, H., Polymer nanocomposites: from fundamental research to specific applications. *Materials Science and Engineering: C* **2003,** *23* (6), 763-772, https://doi.org/10.1016/j.msec.2003.09.148.
19. Mohammed, N.; Grishkewich, N.; Tam, K. C., Cellulose nanomaterials: promising sustainable nanomaterials for application in water/wastewater treatment processes. *Environmental Science: Nano* **2018,** *5* (3), 623-658, 10.1039/C7EN01029J.
20. Gul, S.; Khan, S. B.; Rehman, I. U.; Khan, M. A.; Khan, M. I., A Comprehensive Review of Magnetic Nanomaterials Modern Day Theranostics. *Frontiers in Materials* **2019,** *6* (179), 10.3389/fmats.2019.00179.
21. Hon, D. N. S., Cellulose: a random walk along its historical path. *Cellulose* **1994,** *1* (1), 1-25, 10.1007/BF00818796.
22. Holtzapple, M. T., CELLULOSE. In *Encyclopedia of Food Sciences and Nutrition (Second Edition)*, Caballero, B., Ed. Academic Press: Oxford, 2003; pp 998-1007.
23. O'Sullivan, A. C., Cellulose: the structure slowly unravels. *Cellulose* **1997,** *4* (3), 173-207, 10.1023/A:1018431705579.
24. Klemm, D.; Heublein, B.; Fink, H.-P.; Bohn, A., Cellulose: Fascinating Biopolymer and Sustainable Raw Material. *Angewandte Chemie International Edition* **2005,** *44* (22), 3358-3393, https://doi.org/10.1002/anie.200460587.

25. Michelin, M.; Gomes, D. G.; Romaní, A.; Polizeli, M. d. L. T. M.; Teixeira, J. A., Nanocellulose Production: Exploring the Enzymatic Route and Residues of Pulp and Paper Industry. *Molecules* **2020,** *25* (15), 3411.
26. Bai, F.-W.; Yang, S.; Ho, N. W. Y., 3.05 - Fuel Ethanol Production From Lignocellulosic Biomass. In *Comprehensive Biotechnology (Third Edition)*, Moo-Young, M., Ed. Pergamon: Oxford, 2019; pp 49-65, https://doi.org/10.1016/B978-0-444-64046-8.00150-6.
27. Saxena, I. M.; Brown, R. M., Biosynthesis of Cellulose. In *Progress in Biotechnology*, Morohoshi, N.; Komamine, A., Eds. Elsevier: 2001; Vol. 18, pp 69-76, https://doi.org/10.1016/S0921-0423(01)80057-5.
28. Alberts, B.; Johnson, A.; Lewis, J. et al. The Plant Cell Wall. In *Molecular Biology of the Cell (Fourth Edition)*. Garland Science: New York, 2002.
29. Brigham, C., Chapter 3.22 - Biopolymers: Biodegradable Alternatives to Traditional Plastics. In *Green Chemistry*, Török, B.; Dransfield, T., Eds. Elsevier: 2018; pp 753-770, https://doi.org/10.1016/B978-0-12-809270-5.00027-3.
30. Havstad, M. R., Chapter 5 - Biodegradable plastics. In *Plastic Waste and Recycling*, Letcher, T. M., Ed. Academic Press: 2020; pp 97-129, https://doi.org/10.1016/B978-0-12-817880-5.00005-0.
31. Lavanya, D.; Dixit, M.; Raavi, P. K.; Krishna, V. In *SOURCES OF CELLULOSE AND THEIR APPLICATIONS - A REVIEW*, 2011.
32. Seddiqi, H.; Oliaei, E.; Honarkar, H.; Jin, J.; Geonzon, L. C.; Bacabac, R. G.; Klein-Nulend, J., Cellulose and its derivatives: towards biomedical applications. *Cellulose* **2021,** *28* (4), 1893-1931, 10.1007/s10570-020-03674-w.
33. Kögel-Knabner, I.; Amelung, W., 12.7 - Dynamics, Chemistry, and Preservation of Organic Matter in Soils. In *Treatise on Geochemistry (Second Edition)*, Holland, H. D.; Turekian, K. K., Eds. Elsevier: Oxford, 2014; pp 157-215, https://doi.org/10.1016/B978-0-08-095975-7.01012-3.
34. Misra, M.; Vivekanandhan, S.; Mohanty, A. K.; Denault, J., 4.10 - Nanotechnologies for Agricultural Bioproducts. In *Comprehensive Biotechnology (Third Edition)*, Moo-Young, M., Ed. Pergamon: Oxford, 2011; pp 119-127, https://doi.org/10.1016/B978-0-444-64046-8.00217-2.
35. Boufi, S., 6 - Agricultural crop residue as a source for the production of cellulose nanofibrils. In *Cellulose-Reinforced Nanofibre Composites*, Jawaid, M.; Boufi, S.; H.P.S, A. K., Eds. Woodhead Publishing: 2017; pp 129-152, https://doi.org/10.1016/B978-0-08-100957-4.00006-1.
36. Sundarraj, A. A.; Ranganathan, T. V., A review on cellulose and its utilization from agro-industrial waste. *Drug Invention Today* **2018**, 89-94.
37. Kamel, R.; El-Wakil, N. A.; Dufresne, A.; Elkasabgy, N. A., Nanocellulose: From an agricultural waste to a valuable pharmaceutical ingredient. *International Journal of*

Biological Macromolecules **2020,** *163*, 1579-1590, https://doi.org/10.1016/j.ijbiomac.2020.07.242.
38. de Souza, A. G.; Barbosa, R. F. S.; Rosa, D. S., Nanocellulose from Industrial and Agricultural Waste for Further Use in PLA Composites. *Journal of Polymers and the Environment* **2020,** *28* (7), 1851-1868, 10.1007/s10924-020-01731-w.
39. Iguchi, M.; Yamanaka, S.; Budhiono, A., Bacterial cellulose—a masterpiece of nature's arts. *Journal of Materials Science* **2000,** *35* (2), 261-270, 10.1023/A:1004775229149.
40. Esa, F.; Tasirin, S. M.; Rahman, N. A., Overview of Bacterial Cellulose Production and Application. *Agriculture and Agricultural Science Procedia* **2014,** *2*, 113-119, https://doi.org/10.1016/j.aaspro.2014.11.017.
41. Azeredo, H. M. C.; Barud, H.; Farinas, C. S.; Vasconcellos, V. M.; Claro, A. M., Bacterial Cellulose as a Raw Material for Food and Food Packaging Applications. *Frontiers in Sustainable Food Systems* **2019,** *3* (7), 10.3389/fsufs.2019.00007.
42. Arévalo Gallegos, A. M.; Carrera, S. H.; Parra, R.; Keshavarz, T.; Iqbal, H. M. N., Bacterial cellulose: A sustainable source to develop value-added products - A review. *BioRes* **2016**, *11*(2), 5641-5655.
43. Dunlop, M. J.; Acharya, B.; Bissessur, R., Isolation of nanocrystalline cellulose from tunicates. *Journal of Environmental Chemical Engineering* **2018,** *6* (4), 4408-4412, https://doi.org/10.1016/j.jece.2018.06.056.
44. Dunlop, M. J.; Clemons, C.; Reiner, R.; Sabo, R.; Agarwal, U. P.; Bissessur, R.; Sojoudiasli, H.; Carreau, P. J.; Acharya, B., Towards the scalable isolation of cellulose nanocrystals from tunicates. *Scientific Reports* **2020,** *10* (1), 19090, 10.1038/s41598-020-76144-9.
45. Phanthong, P.; Reubroycharoen, P.; Hao, X.; Xu, G.; Abudula, A.; Guan, G., Nanocellulose: Extraction and application. *Carbon Resources Conversion* **2018,** *1* (1), 32-43, https://doi.org/10.1016/j.crcon.2018.05.004.
46. Zhang, P. P.; Tong, D. S.; Lin, C. X.; Yang, H. M.; Zhong, Z. K.; Yu, W. H.; Wang, H.; Zhou, C. H., Effects of acid treatments on bamboo cellulose nanocrystals. *Asia-Pacific Journal of Chemical Engineering* **2014,** *9* (5), 686-695, https://doi.org/10.1002/apj.1812.
47. Kusmono; Listyanda, R. F.; Wildan, M. W.; Ilman, M. N., Preparation and characterization of cellulose nanocrystal extracted from ramie fibers by sulfuric acid hydrolysis. *Heliyon* **2020,** *6* (11), e05486, https://doi.org/10.1016/j.heliyon.2020.e05486.
48. Xie, H.; Du, H.; Yang, X.; Si, C., Recent Strategies in Preparation of Cellulose Nanocrystals and Cellulose Nanofibrils Derived from Raw Cellulose Materials. *International Journal of Polymer Science* **2018,** *2018*, 7923068, 10.1155/2018/7923068.
49. Frost, B.-A.; Foster, E.-J., Isolation of Thermally Stable Cellulose Nanocrystals from Spent Coffee Grounds via Phosphoric Acid Hydrolysis. *Journal of Renewable Materials* **2020,** *8* (2), 187-203.

50. Piras, C. C.; Fernández-Prieto, S.; De Borggraeve, W. M., Ball milling: a green technology for the preparation and functionalisation of nanocellulose derivatives. *Nanoscale Advances* **2019,** *1* (3), 937-947, 10.1039/C8NA00238J.
51. Phanthong, P.; Karnjanakom, S.; Reubroycharoen, P.; Hao, X.; Abudula, A.; Guan, G., A facile one-step way for extraction of nanocellulose with high yield by ball milling with ionic liquid. *Cellulose* **2017,** *24* (5), 2083-2093, 10.1007/s10570-017-1238-5.
52. Tang, L.; Huang, B.; Lu, Q.; Wang, S.; Ou, W.; Lin, W.; Chen, X., Ultrasonication-assisted manufacture of cellulose nanocrystals esterified with acetic acid. *Bioresource Technology* **2013,** *127*, 100-105, https://doi.org/10.1016/j.biortech.2012.09.133.
53. Sasaki, M.; Kabyemela, B.; Malaluan, R.; Hirose, S.; Takeda, N.; Adschiri, T.; Arai, K., Cellulose hydrolysis in subcritical and supercritical water. *The Journal of Supercritical Fluids* **1998,** *13* (1), 261-268, https://doi.org/10.1016/S0896-8446(98)00060-6.
54. Novo, L. P.; Bras, J.; García, A.; Belgacem, N.; Curvelo, A. A. d. S., A study of the production of cellulose nanocrystals through subcritical water hydrolysis. *Industrial Crops and Products* **2016,** *93*, 88-95, https://doi.org/10.1016/j.indcrop.2016.01.012.
55. Martínez-Abad, A.; Giummarella, N.; Lawoko, M.; Vilaplana, F., Differences in extractability under subcritical water reveal interconnected hemicellulose and lignin recalcitrance in birch hardwoods. *Green Chemistry* **2018,** *20* (11), 2534-2546, 10.1039/C8GC00385H.
56. Zhang, R.-Y.; Liu, H.-M.; Hou, J.; Yao, Y.-G.; Ma, Y.-X.; Wang, X.-D., Cellulose fibers extracted from sesame hull using subcritical water as a pretreatment. *Arabian Journal of Chemistry* **2021,** *14* (6), 103178, https://doi.org/10.1016/j.arabjc.2021.103178.
57. Pereira, B.; Arantes, V., Production of cellulose nanocrystals integrated into a biochemical sugar platform process via enzymatic hydrolysis at high solid loading. *Industrial Crops and Products* **2020,** *152*, 112377, https://doi.org/10.1016/j.indcrop.2020.112377.
58. Rovera, C.; Ghaani, M.; Santo, N.; Trabattoni, S.; Olsson, R. T.; Romano, D.; Farris, S., Enzymatic Hydrolysis in the Green Production of Bacterial Cellulose Nanocrystals. *ACS Sustainable Chemistry & Engineering* **2018,** *6* (6), 7725-7734, 10.1021/acssuschemeng.8b00600.
59. Ehmann, H. M. A.; Mohan, T.; Koshanskaya, M.; Scheicher, S.; Breitwieser, D.; Ribitsch, V.; Stana-Kleinschek, K.; Spirk, S., Design of anticoagulant surfaces based on cellulose nanocrystals. *Chemical Communications* **2014,** *50* (86), 13070-13072, 10.1039/C4CC05254D.
60. Fraschini, C.; Chauve, G.; Bouchard, J., TEMPO-mediated surface oxidation of cellulose nanocrystals (CNCs). *Cellulose* **2017,** *24* (7), 2775-2790, 10.1007/s10570-017-1319-5.
61. Dhuiège, B.; Pecastaings, G.; Sèbe, G., Sustainable Approach for the Direct Functionalization of Cellulose Nanocrystals Dispersed in Water by Transesterification of Vinyl Acetate. *ACS Sustainable Chemistry & Engineering* **2019,** *7* (1), 187-196, 10.1021/acssuschemeng.8b02833.

62. Leszczyńska, A.; Radzik, P.; Szefer, E.; Mičušík, M.; Omastová, M.; Pielichowski, K., Surface Modification of Cellulose Nanocrystals with Succinic Anhydride. *Polymers (Basel)* **2019,** *11* (5), 866, 10.3390/polym11050866.
63. Eyley, S.; Thielemans, W., Surface modification of cellulose nanocrystals. *Nanoscale* **2014,** *6* (14), 7764-7779, 10.1039/C4NR01756K.
64. Tang, J.; Sisler, J.; Grishkewich, N.; Tam, K. C., Functionalization of cellulose nanocrystals for advanced applications. *Journal of Colloid and Interface Science* **2017,** *494*, 397-409, https://doi.org/10.1016/j.jcis.2017.01.077.
65. Foster, E. J.; Moon, R. J.; Agarwal, U. P.; Bortner, M. J.; Bras, J.; Camarero-Espinosa, S.; Chan, K. J. et al. Current characterization methods for cellulose nanomaterials. *Chemical Society Reviews* **2018,** *47* (8), 2609-2679, 10.1039/C6CS00895J.
66. George, J.; Sabapathi, S. N., Cellulose nanocrystals: synthesis, functional properties, and applications. *Nanotechnol Sci Appl* **2015,** *8*, 45-54, 10.2147/NSA.S64386.
67. Moon, R.; Beck, S.; Rudie, A. In *Cellulose Nanocrystals-A material with Unique Properties and Many Potential Applications*, 2013.
68. Trache, D.; Tarchoun, A. F.; Derradji, M.; Hamidon, T. S.; Masruchin, N.; Brosse, N.; Hussin, M. H., Nanocellulose: From Fundamentals to Advanced Applications. *Frontiers in Chemistry* **2020,** *8* (392), 10.3389/fchem.2020.00392.
69. Nagarajan, K. J.; Ramanujam, N. R.; Sanjay, M. R.; Siengchin, S.; Surya Rajan, B.; Sathick Basha, K.; Madhu, P.; Raghav, G. R., A comprehensive review on cellulose nanocrystals and cellulose nanofibers: Pretreatment, preparation, and characterization. *Polymer Composites* **2021,** *42* (4), 1588-1630, https://doi.org/10.1002/pc.25929.
70. Yao, J.; Huang, H.; Mao, L.; Li, Z.; Zhu, H.; Liu, Y., Structural and optical properties of cellulose nanocrystals isolated from the fruit shell of Camellia oleifera Abel. *Fibers and Polymers* **2017,** *18* (11), 2118-2124, 10.1007/s12221-017-7489-9.
71. Habibi, Y.; Lucia, L. A.; Rojas, O. J., Cellulose Nanocrystals: Chemistry, Self-Assembly, and Applications. *Chemical Reviews* **2010,** *110* (6), 3479-3500, 10.1021/cr900339w.
72. Calvino, C.; Macke, N.; Kato, R.; Rowan, S. J., Development, processing and applications of bio-sourced cellulose nanocrystal composites. *Progress in Polymer Science* **2020,** *103*, 101221, https://doi.org/10.1016/j.progpolymsci.2020.101221.
73. Rahimi, S. K.; Otaigbe, J. U., 4 - Green hybrid composites from cellulose nanocrystal. In *Hybrid Polymer Composite Materials*, Thakur, V. K.; Thakur, M. K.; Gupta, R. K., Eds. Woodhead Publishing: 2017; pp 65-99, https://doi.org/10.1016/B978-0-08-100791-4.00004-5.
74. Kim, J.-H.; Shim, B. S.; Kim, H. S.; Lee, Y.-J.; Min, S.-K.; Jang, D.; Abas, Z.; Kim, J., Review of nanocellulose for sustainable future materials. *International Journal of Precision Engineering and Manufacturing-Green Technology* **2015,** *2* (2), 197-213, 10.1007/s40684-015-0024-9.

75. Meesorn, W.; Shirole, A.; Vanhecke, D.; de Espinosa, L. M.; Weder, C., A Simple and Versatile Strategy To Improve the Mechanical Properties of Polymer Nanocomposites with Cellulose Nanocrystals. *Macromolecules* **2017,** *50* (6), 2364-2374, 10.1021/acs.macromol.6b02629.
76. Miao, C.; Hamad, W. Y., Critical insights into the reinforcement potential of cellulose nanocrystals in polymer nanocomposites. *Current Opinion in Solid State and Materials Science* **2019,** *23* (4), 100761, https://doi.org/10.1016/j.cossms.2019.06.005.
77. Karkhanis, S. S.; Stark, N. M.; Sabo, R. C.; Matuana, L. M., Water vapor and oxygen barrier properties of extrusion-blown poly(lactic acid)/cellulose nanocrystals nanocomposite films. *Composites Part A: Applied Science and Manufacturing* **2018,** *114*, 204-211, https://doi.org/10.1016/j.compositesa.2018.08.025.
78. Chakrabarty, A.; Teramoto, Y., Recent Advances in Nanocellulose Composites with Polymers: A Guide for Choosing Partners and How to Incorporate Them. *Polymers (Basel)* **2018,** *10* (5), 517.
79. Khan, A.; Khan, R. A.; Salmieri, S.; Le Tien, C.; Riedl, B.; Bouchard, J.; Chauve, G.; Tan, V.; Kamal, M. R.; Lacroix, M., Mechanical and barrier properties of nanocrystalline cellulose reinforced chitosan based nanocomposite films. *Carbohydrate Polymers* **2012,** *90* (4), 1601-1608, https://doi.org/10.1016/j.carbpol.2012.07.037.
80. Gopakumar, D. A.; Arumughan, V.; Pasquini, D.; Leu, S.-Y.; H.P.S, A. K.; Thomas, S., Chapter 3 - Nanocellulose-Based Membranes for Water Purification. In *Nanoscale Materials in Water Purification*, Thomas, S.; Pasquini, D.; Leu, S.-Y.; Gopakumar, D. A., Eds. Elsevier: 2019; pp 59-85, https://doi.org/10.1016/B978-0-12-813926-4.00004-5.
81. Lasrado, D.; Ahankari, S.; Kar, K., Nanocellulose-based polymer composites for energy applications—A review. *Journal of Applied Polymer Science* **2020,** *137* (27), 48959, https://doi.org/10.1002/app.48959.
82. Wang, X.; Yao, C.; Wang, F.; Li, Z., Cellulose-Based Nanomaterials for Energy Applications. *Small* **2017,** *13* (42), 10.1002/smll.201702240, 10.1002/smll.201702240.
83. Panchal, P.; Ogunsona, E.; Mekonnen, T., Trends in Advanced Functional Material Applications of Nanocellulose. *Processes* **2019,** *7* (1), 10.
84. Farnia, F.; Fan, W.; Dory, Y.; Zhao, Y., Making Nanocomposites of Hydrophilic and Hydrophobic Polymers Using Gas-Responsive Cellulose Nanocrystals. *Macromolecular Rapid Communications* **2019,** *40* (12), 1900114, https://doi.org/10.1002/marc.201900114.
85. Camarero-Espinosa, S.; Rothen-Rutishauser, B.; Weder, C.; Foster, E. J., Directed cell growth in multi-zonal scaffolds for cartilage tissue engineering. *Biomaterials* **2016,** *74*, 42-52, https://doi.org/10.1016/j.biomaterials.2015.09.033.
86. Hickey, R. J.; Pelling, A. E., Cellulose Biomaterials for Tissue Engineering. *Frontiers in Bioengineering and Biotechnology* **2019,** *7* (45), 10.3389/fbioe.2019.00045.
87. Pajorova, J.; Skogberg, A.; Hadraba, D.; Broz, A.; Travnickova, M.; Zikmundova, M.; Honkanen, M.; Hannula, M.; Lahtinen, P.; Tomkova, M.; Bacakova, L.; Kallio, P.,

Cellulose Mesh with Charged Nanocellulose Coatings as a Promising Carrier of Skin and Stem Cells for Regenerative Applications. *Biomacromolecules* **2020,** *21* (12), 4857-4870, 10.1021/acs.biomac.0c01097.

88. Akbarzadeh, A.; Samiei, M.; Davaran, S., Magnetic nanoparticles: preparation, physical properties, and applications in biomedicine. *Nanoscale Research Letters* **2012,** *7* (1), 144, 10.1186/1556-276X-7-144.
89. Duguet, E.; Vasseur, S.; Mornet, S.; Devoisselle, J.-M., Magnetic nanoparticles and their applications in medicine. *Nanomedicine* **2006,** *1* (2), 157-168, 10.2217/17435889.1.2.157.
90. Mørup, S.; Hansen, M. F.; Frandsen, C., 1.14 - Magnetic Nanoparticles. In *Comprehensive Nanoscience and Technology*, Andrews, D. L.; Scholes, G. D.; Wiederrecht, G. P., Eds. Academic Press: Amsterdam, 2011; pp 437-491, https://doi.org/10.1016/B978-0-12-374396-1.00036-2.
91. Seyfoori, A.; Koshkaki, M. R.; Majidzadeh-A, K., 26 - Nanohybrid Stimuli-Responsive Microgels: A New Approach in Cancer Therapy. In *Nanoarchitectonics for Smart Delivery and Drug Targeting*, Holban, A. M.; Grumezescu, A. M., Eds. William Andrew Publishing: 2016; pp 715-742, https://doi.org/10.1016/B978-0-323-47347-7.00026-4.
92. Mohr, R.; Kratz, K.; Weigel, T.; Lucka-Gabor, M.; Moneke, M.; Lendlein, A., Initiation of shape-memory effect by inductive heating of magnetic nanoparticles in thermoplastic polymers. *Proceedings of the National Academy of Sciences of the United States of America* **2006,** *103* (10), 3540-3545, 10.1073/pnas.0600079103.
93. Bayerl, T.; Duhovic, M.; Mitschang, P.; Bhattacharyya, D., The heating of polymer composites by electromagnetic induction – A review. *Composites Part A: Applied Science and Manufacturing* **2014,** *57*, 27-40, https://doi.org/10.1016/j.compositesa.2013.10.024.
94. Theato, P.; Sumerlin, B. S.; O'Reilly, R. K.; Epps, I. I. I. T. H., Stimuli responsive materials. *Chemical Society Reviews* **2013,** *42* (17), 7055-7056, 10.1039/C3CS90057F.
95. Stuart, M. A. C.; Huck, W. T. S.; Genzer, J.; Müller, M.; Ober, C.; Stamm, M.; Sukhorukov, G. B.; Szleifer, I.; Tsukruk, V. V.; Urban, M.; Winnik, F.; Zauscher, S.; Luzinov, I.; Minko, S., Emerging applications of stimuli-responsive polymer materials. *Nature Materials* **2010,** *9* (2), 101-113, 10.1038/nmat2614.
96. Roy, D.; Cambre, J. N.; Sumerlin, B. S., Future perspectives and recent advances in stimuli-responsive materials. *Progress in Polymer Science* **2010,** *35* (1), 278-301, https://doi.org/10.1016/j.progpolymsci.2009.10.008.
97. Bayerl, T.; Schledjewski, R.; Mitschang, P., Induction Heating of Thermoplastic Materials by Particulate Heating Promoters. *Polymers and Polymer Composites* **2012,** *20*, 333 - 342.
98. Yerushalmi, R.; Scherz, A.; van der Boom, M. E.; Kraatz, H.-B., Stimuli responsive materials: new avenues toward smart organic devices. *Journal of Materials Chemistry* **2005,** *15* (42), 4480-4487, 10.1039/B505212B.

99. Small, I. V. W.; Singhal, P.; Wilson, T. S.; Maitland, D. J., Biomedical applications of thermally activated shape memory polymers. *Journal of Materials Chemistry* **2010,** *20* (17), 3356-3366, 10.1039/B923717H.
100. Amalraj, A.; Gopi, S.; Thomas, S.; Haponiuk, J. T., Cellulose Nanomaterials in Biomedical, Food, and Nutraceutical Applications: A Review. *Macromolecular Symposia* **2018,** *380* (1), 1800115, https://doi.org/10.1002/masy.201800115.
101. Lin, N.; Dufresne, A., Nanocellulose in biomedicine: Current status and future prospect. *European Polymer Journal* **2014,** *59*, 302-325, https://doi.org/10.1016/j.eurpolymj.2014.07.025.
102. Dumanli, A. G., Nanocellulose and its Composites for Biomedical Applications. *Current medicinal chemistry* **2017,** *24* (5), 512-528, 10.2174/0929867323666161014124008.
103. WANG, J.; ZHU, Y.; DU, J., BACTERIAL CELLULOSE: A NATURAL NANOMATERIAL FOR BIOMEDICAL APPLICATIONS. *Journal of Mechanics in Medicine and Biology* **2011,** *11* (02), 285-306, 10.1142/s0219519411004058.
104. Murizan, N. I. S.; Mustafa, N. S.; Ngadiman, N. H. A.; Mohd Yusof, N.; Idris, A., Review on Nanocrystalline Cellulose in Bone Tissue Engineering Applications. *Polymers (Basel)* **2020,** *12* (12), 10.3390/polym12122818.
105. Dutta, S. D.; Patel, D. K.; Lim, K.-T., Functional cellulose-based hydrogels as extracellular matrices for tissue engineering. *Journal of Biological Engineering* **2019,** *13* (1), 55, 10.1186/s13036-019-0177-0.
106. Ferreira, F. V.; Otoni, C. G.; De France, K. J.; Barud, H. S.; Lona, L. M. F.; Cranston, E. D.; Rojas, O. J., Porous nanocellulose gels and foams: Breakthrough status in the development of scaffolds for tissue engineering. *Materials Today* **2020,** *37*, 126-141, https://doi.org/10.1016/j.mattod.2020.03.003.
107. Joseph, B.; K, S. V.; Sabu, C.; Kalarikkal, N.; Thomas, S., Cellulose nanocomposites: Fabrication and biomedical applications. *Journal of Bioresources and Bioproducts* **2020,** *5* (4), 223-237, https://doi.org/10.1016/j.jobab.2020.10.001.
108. Cardoso, V. F.; Francesko, A.; Ribeiro, C.; Bañobre-López, M.; Martins, P.; Lanceros-Mendez, S., Advances in Magnetic Nanoparticles for Biomedical Applications. *Advanced healthcare materials* **2018,** *7* (5), 10.1002/adhm.201700845.
109. Anderson, S. D.; Gwenin, V. V.; Gwenin, C. D., Magnetic Functionalized Nanoparticles for Biomedical, Drug Delivery and Imaging Applications. *Nanoscale Research Letters* **2019,** *14* (1), 188, 10.1186/s11671-019-3019-6.
110. Guleria, A.; Priyatharchini, K.; Kumar, D., Chapter 12 - Biomedical Applications of Magnetic Nanomaterials. In *Applications of Nanomaterials*, Mohan Bhagyaraj, S.; Oluwafemi, O. S.; Kalarikkal, N.; Thomas, S., Eds. Woodhead Publishing: 2018; pp 345-389, https://doi.org/10.1016/B978-0-08-101971-9.00013-2.

111. Tran, N.; Webster, T. J., Magnetic nanoparticles: biomedical applications and challenges. *Journal of Materials Chemistry* **2010,** *20* (40), 8760-8767, 10.1039/C0JM00994F.
112. McNamara, K.; Tofail, S. A. M., Nanoparticles in biomedical applications. *Advances in Physics: X* **2017,** *2* (1), 54-88, 10.1080/23746149.2016.1254570.

R.2

1. Yu, J. R.; Navarro, J.; Coburn, J. C.; Mahadik, B.; Molnar, J.; Holmes IV, J. H.; Nam, A. J.; Fisher, J. P., Current and Future Perspectives on Skin Tissue Engineering: Key Features of Biomedical Research, Translational Assessment, and Clinical Application. *Advanced Healthcare Materials* **2019,** *8* (5), 1801471, 10.1002/adhm.201801471.
2. Khan, F.; Tanaka, M., Designing Smart Biomaterials for Tissue Engineering. *Int J Mol Sci* **2017,** *19* (1), 10.3390/ijms19010017.
3. Tay, C. Y.; Irvine, S. A.; Boey, F. Y. C.; Tan, L. P.; Venkatraman, S., Micro-/Nano-engineered Cellular Responses for Soft Tissue Engineering and Biomedical Applications. *Small* **2011,** *7* (10), 1361-1378, 10.1002/smll.201100046.
4. Murphy, S. V.; Atala, A., 3D bioprinting of tissues and organs. *Nature Biotechnology* **2014,** *32*, 773, https://doi.org/10.1038/nbt.2958.
5. De France, K. J.; Babi, M.; Vapaavuori, J.; Hoare, T.; Moran-Mirabal, J.; Cranston, E. D., 2.5D Hierarchical Structuring of Nanocomposite Hydrogel Films Containing Cellulose Nanocrystals. *ACS Applied Materials & Interfaces* **2019,** *11* (6), 6325-6335, 10.1021/acsami.8b16232.
6. Camarero Espinosa, S.; Kuhnt, T.; Foster, E. J.; Weder, C., Isolation of Thermally Stable Cellulose Nanocrystals by Phosphoric Acid Hydrolysis. *Biomacromolecules* **2013**, *14* (4), 1223-1230.
7. Foster, E. J.; Moon, R. J.; Agarwal, U. P.; Bortner, M. J.; Bras, J. et al., Current characterization methods for cellulose nanomaterials. *Chemical Society Reviews* **2018,** *47* (8), 2609-2679.
8. Shan, Y.; Li, C.; Wu, Y.; Li, Q.; Liao, J., Hybrid cellulose nanocrystal/alginate/gelatin scaffold with improved mechanical properties and guided wound healing. *RSC Advances* **2019,** *9* (40), 22966-22979, 10.1039/C9RA04026A.

R.3

1. Hon, D.N.S. (1994). Cellulose: a random walk along its historical path. *Cellulose*, *1*, 1-25.
2. Holtzapple, M. T. (2003). CELLULOSE. In *Encyclopedia of Food Sciences and Nutrition (Second Edition)*, Caballero, B., Ed. Academic Press: Oxford; pp 998-1007.
3. O'Sullivan, A. C. (1997). Cellulose: the structure slowly unravels. *Cellulose, 4(3),* 173-207.

4. Klemm, D., Heublein, B., Fink, H.-P., Bohn, A. (2005). Cellulose: Fascinating Biopolymer and Sustainable Raw Material. *Angewandte Chemie-International Edition, 44(22),* 3358-3393.
5. George, J., Sabapathi, S. N. (2015). Cellulose nanocrystals: synthesis, functional properties, and applications. *Nanotechnology, Science and Applications, 8*, 45-54.
6. Habibi, Y., Lucia, L. A., Rojas, O. J. (2010). Cellulose Nanocrystals: Chemistry, Self-Assembly, and Applications. *Chemical Reviews, 110(6),* 3479-3500.
7. Xing, L., Gu, J., Zhang, W., Tu, D., Hu, C. (2018). Cellulose I and II nanocrystals produced by sulfuric acid hydrolysis of Tetra pak cellulose I. *Carbohydrate Polymers, 192*, 184-192.
8. Camarero Espinosa, S., Kuhnt, T., Foster, E. J., Weder, C. (2013). Isolation of Thermally Stable Cellulose Nanocrystals by Phosphoric Acid Hydrolysis. *Biomacromolecules, 14(4),* 1223-1230.
9. Foster, E. J.; Moon, R. J.; Agarwal, U. P.; Bortner, M. J.; Bras, J. et al. (2018). Current characterization methods for cellulose nanomaterials. *Chemical Society Reviews, 47(8),* 2609-2679.
10. Moon, R.J., Martini, A., Nairn, J., Simonsen, J., Youngblood, J. (2011). Cellulose nanomaterials review: structure, properties, and nanocomposites. *Chemical Society Reviews, 40,* 3941-3994.
11. Dufresne, A. (2012). *Nanocellulose: from Nature to High Performance Tailored Materials*. De Gruyter, Berlin; Boston.
12. Dufresne, A. (2013). Nanocellulose: a new ageless bionanomaterial. *Materials Today, 16(6),* 220-227.
13. Inc., F.M. (2019). *The Global Market for Nanocellulose to 2030*. Technology Report 60.
14. Nicharat, A., Foster, E.J., Weder, C. (2017). Thermally-activated shape memory behavior of melt-mixed polyurethane and upscalable phosphorylated- cellulose nanocrystal nanocomposites. *Journal of Applied Polymer Science, 134*, 45033.
15. Natterodt, J.C., Sapkota, J., Foster, E.J., Weder, C. (2017). Polymer Nanocomposites with Cellulose Nanocrystals Featuring Adaptive Surface Groups. *Biomacromolecules, 18(2),* 517–525.
16. Sapkota, J., Natterodt, J., Shirole, A., Foster, E.J., Weder, C. (2016). Fabrication and Properties of Polyethylene / Cellulose Nanocrystal Composites. *Macromolecular Materials and Engineering, 302*, 1600300.
17. Mendez, J., Annamalai, P.K., Eichhorn, S.J., Rusli, R., Rowan, S.J. et al. (2011). Bioinspired Mechanically Adaptive Polymer Nanocomposites with Water-Activated Shape-Memory Effect. *Macromolecules*, *44(17),* 6827-6835.
18. Smyth, M., Fournier, C., Driemeier, C., Picart, C., Foster, E.J. et al. (2017). Tunable Structural and Mechanical Properties in liquid of Cellulose Nanofiber Substrates for Stem Cell Culture. *Biomacromolecules, 18(7),* 2034–2044.

19. Smyth, M., M'Bengue, M-.S., Terrien, M., Picart, C., Bras, J. et al. (2018). The effect of hydration on the material and mechanical properties of cellulose nanocrystal-alginate composites. *Carbohydrate Polymers, 179*, 186-195.
20. DiLoreto, E., Haque, E., Berman, A., Moon, R.J., Kalaitzidou, K. (2019). Freeze dried cellulose nanocrystal reinforced unsaturated polyester composites: challenges and potential. *Cellulose, 26(7),* 4391-4403.
21. Frost, B. A., Foster, E. J. (2019). Replication of annulus fibrosus through fabrication and characterization of polyurethane and cellulose nanocrystal composite scaffolds. *Nanocomposites, 5(1),* 13-27.
22. Venkantramen, P., Gohn, A.M., Rhoades, A.M., Foster, E.J. (2019). Developing high performance PA 11/cellulose nanocomposites for industrial-scale melt processing. *Composites Part B-Engineering, 174*, 106988.
23. Tran, A., Hamad, W.Y., MacLachlan, M.J. (2018). Fabrication of Cellulose Nanocrystal Films through Differential Evaporation for Patterned Coatings. *ACS Applied Nano Materials, 17*, 3098-3104.
24. Giese, M., Spengler, M. (2019). Cellulose nanocrystals in nanoarchitectonics – towards photonic functional materials. *Molecular Systems Design & Engineering, 4*, 29-48.
25. Tingaut, P., Zimmermann, T., Sebe, G. (2012). Cellulose nanocrystals and microfibrillated cellulose as building blocks for the design of hierarchical functional materials. *Journal of Materials Chemistry, 22*, 20105-20111.
26. Kuhnt, T., Herrman, A., Foster, E.J., Weder, C. (2015). Functionalized cellulose nanocrystals as nanocarriers for sustained fragrance release. *Polymer Chemistry, 6*, 6553 - 6562.
27. Schyrr, B., Pasche, S., Voirin, G., Weder, C., Simon, Y.C. et al. (2014). Biosensors based on porous cellulose nanocrystal – poly(vinyl alcohol) as scaffolds. *ACS Applied Materials & Interfaces, 6(15),* 12674–12683.
28. Potter, K.A., Jorfi, M., Householder, K.T., Foster, E.J., Weder, C. et al. (2014). Curcumin-releasing mechanically-adaptive intracortical implants improve the proximal neuronal density and blood-brain barrier stability. *Acta Biomaterialia, 10(5),* 2209–2222.
29. Jorfi, M., Roberts, M.N., Foster, E.J., Weder, C. (2013). Mechanically-Adaptive Bio-Nanocomposites for Biomedical Applications. *ACS Applied Materials & Interfaces, 5(4),* 1517–1526.
30. Alexandrescu, L., Syverud, K., Nicosia, A. Santachiara, G., Fabrizi, A. et al. (2016). Airborne Nanoparticles Filtration by Means of Cellulose Nanofibril Based Materials. *Journal of Biomaterials & Nanobiotechnology, 7*, 29-36.
31. Mussatto, S. I., Machado, E. M. S., Martins, S., Teixeira, J. A. (2011). Production, Composition, and Application of Coffee and Its Industrial Residues. *Food & Bioprocess Technology, 4(5),* 661.

32. Mussatto, S. I., Carneiro, L. M., Silva, J. P. A., Roberto, I. C., Teixeira, J. A. (2011). A study on chemical constituents and sugars extraction from spent coffee grounds. *Carbohydrate Polymers, 83(2),* 368-374.
33. Woodward, J., Evans, B. (2019). *Utilization of biocatalysts in cellulose waste minimization*.
34. Nagendran, R. (2011). Chapter 24 - Agricultural Waste and Pollution. In *Waste*, Letcher, T. M., Vallero, D. A. Eds. Academic Press: Boston; pp 341-355.
35. Wang, Y. (2010). Fiber and Textile Waste Utilization. *Waste & Biomass Valorization, 1(1),* 135-143.
36. Silvério, H. A., Flauzino Neto, W. P., Dantas, N. O., Pasquini, D. (2013). Extraction and characterization of cellulose nanocrystals from corncob for application as reinforcing agent in nanocomposites. *Industrial Crops & Products, 44,* 427-436.
37. Mendes, C. A. d. C., Ferreira, N. M. S., Furtado, C. R. G., de Sousa, A. M. F. (2015). Isolation and characterization of nanocrystalline cellulose from corn husk. *Materials Letters, 148,* 26-29.
38. Johar, N., Ahmad, I., Dufresne, A. (2012). Extraction, preparation and characterization of cellulose fibres and nanocrystals from rice husk. *Industrial Crops & Products, 37(1),* 93-99.
39. Thambiraj, S., Shankaran, D.R. (2017) Preparation and physicochemical characterization of cellulose nanocrystals from industrial waste cotton. *Applied Surface Science, 412,* 405-416.
40. Lam, N. T., Chollakup, R., Smitthipong, W., Nimchua, T., Sukyai, P. (2017). Characterization of Cellulose Nanocrystals Extracted from Sugarcane Bagasse for Potential Biomedical Materials. *Sugar Tech, 19(5),* 539-552.
41. Collazo-Bigliardi, S., Ortega-Toro, R., Chiralt Boix, A. (2018). Isolation and characterisation of microcrystalline cellulose and cellulose nanocrystals from coffee husk and comparative study with rice husk. *Carbohydrate Polymers, 191,* 205-215.
42. Alghooneh, A., Mohammad Amini, A., Behrouzian, F., Razavi, S. M. A. (2017). Characterisation of cellulose from coffee silverskin. *International Journal of Food Properties, 20(11),* 2830-2843.
43. Marett, J., Aning, A., Foster, E. J. (2017). The isolation of cellulose nanocrystals from pistachio shells via acid hydrolysis. *Industrial Crops & Products, 109,* 869-874.
44. Camarero-Espinosa, S., Rothern-Rutishauser, B., Weder, C., Foster, E.J. (2016). Directed cell growth in multi-zonal scaffolds for cartilage tissue engineering. *Biomaterials, 74,* 42-52.
45. Lokker, B. (2013). Coffee Roasts from Light to Dark. https://www.coffeecrossroads.com/coffee-101/coffee-roasts-from-light-to-dark.

46. Ballesteros, L. F., Teixeira, J. A., Mussatto, S. I. (2014). Chemical, Functional, and Structural Properties of Spent Coffee Grounds and Coffee Silverskin. *Food & Bioprocess Technology, 7(12),* 3493-3503.
47. Mueller, S., Weder, C., Foster, E. J. (2014). Isolation of cellulose nanocrystals from pseudostems of banana plants. *RSC Advances, 4(2),* 907-915.
48. Zhang, J., Wang, Y., Zhang, L., Zhang, R., Liu, G. et al. (2014). Understanding changes in cellulose crystalline structure of lignocellulosic biomass during ionic liquid pretreatment by XRD. *Bioresource Technology, 151,* 402-405.
49. Vanderfleet, O. M., Osorio, D. A., Cranston, E. D. (2018). Optimization of cellulose nanocrystal length and surface charge density through phosphoric acid hydrolysis. *Philosophical Transactions of the Royal Society A-Mathematical Physical and Engineering Sciences, 376(2112),* 20170041.
50. Reid, M.S., Villalobos, M., Cranston, E.D. (2017). Benchmarking Cellulose Nanocrystals: From the Laboratory to Industrial Production. *Langmuir, 33(7),* 1583-1598.
51. Zhao, H., Kwak, J. H., Conrad Zhang, Z., Brown, H. M., Arey, B. W. et al. (2007). Studying cellulose fiber structure by SEM, XRD, NMR and acid hydrolysis. *Carbohydrate Polymers, 68(2),* 235-241.
52. Zhou, Y.M. (2012). Effect of nanocellulose isolation techniques on the formation of reinforced poly(vinyl alcohol) nanocomposite films. *Express Polymer Letters, 6,* 794-804.
53. Aguayo, M. G., Fernández Pérez, A., Reyes, G., Oviedo, C., Gacitua, W. et al. (2018). Isolation and Characterization of Cellulose Nanocrystals from Rejected Fibers Originated in the Kraft Pulping Process. *Polymers, 10,* 1145.
54. Noguchi, Y., Homma, I., Matsubara, Y. (2017). Complete nanofibrillation of cellulose prepared by phosphorylation. *Cellulose, 24(3),* 1295-1305.
55. Cheng, G., Zhou, M., Wei, Y.-J., Cheng, F., Zhu, P.-X. (2019). Comparison of mechanical reinforcement effects of cellulose nanocrystal, cellulose nanofiber, and microfibrillated cellulose in starch composites. *Polymer Composites, 40(S1),* E365-E372.
56. Jain, R. K., Lal, K., Bhatnagar, H. L. (1985). Thermal degradation of cellulose and its phosphorylated products in air and nitrogen. *Journal of Applied Polymer Science, 30(3),* 897-914.
57. Kumar, A., Negi, Y. S., Choudhary, V., Bhardwaj, N. K. (2014). Characterization of Cellulose Nanocrystals Produced by Acid-Hydrolysis from Sugarcane Bagasse as Agro-Waste. *Journal of Materials Physics and Chemistry, 2(1),* 1-8.
58. Das, K., Ray, D., Bandyopadhyay, N. R., Sengupta, S. (2010). Study of the Properties of Microcrystalline Cellulose Particles from Different Renewable Resources by XRD, FTIR, Nanoindentation, TGA and SEM. *Journal of Polymers and the Environment, 18(3),* 355-363.

59. Jia, C., Bian, H., Gao, T., Jiang, F., Kierzewski, I. M. et al. (2017). Thermally Stable Cellulose Nanocrystals Toward High-Performance 2D and 3D Nanostructures. *ACS Applied Materials & Interfaces, 9(34),* 28922-28929.
60. Viet, D., Beck-Candanedo, S., Gray, D.G. (2007). Dispersion of cellulose nanocrystals in polar organic solvents. *Cellulose, 14*, 109-113.
61. Araki, J., Wada, M., Kuga, S., Okano, T. (2000). Birefringent Glassy Phase of a Cellulose Microcrystal Suspension. *Langmuir, 16(6),* 2413-2415.
62. Urena-Benavides, E.E., Ao, G., Davis, V.A., Kitchens, C.L. (2011). Rheology and Phase Behavior of Lyotropic Cellulose Nanocrystal Suspensions. *Macromolecules, 44(22)*, 8990-8998.
63. Bondeson, D., Mathew, A., Oksman, K. (2006). Optimization of the isolation of nanocrystals from microcrystalline cellulose by acid hydrolysis. *Cellulose, 13,* 171-180.
64. Shanmugarajah, B., Kiew, P.L., Chew, I.M.L., Choong, T.S.Y., Tan, K.W. (2015). Isolation of NanoCrystalline Cellulose (NCC) from Palm Oil Empty Fruit Bunch (EFB): Preliminary Result on FTIR and DLS Analysis. *Chemical Engineering Transactions*, *45*, 1705-1710.
65. Bras, J., Viet, D., Bruzzese, C., Dufresne, A. (2011). Correlation between stiffness of sheets prepared from cellulose whiskers and nanoparticles dimensons. *Carbohydrate Polymers, 84(1),* 211-215.
66. Wik, V.M., Aranguren, M.I., Mosiewicki, M.A. (2011). Castor oil-based polyurethanes containing cellulose nanocrystals. *Polymer Engineering and Science, 51(7),* 1389-1396.
67. Liu, D., Zhong, T., Chang, P.R., Li, K., Wu, Q. (2010). Starch composites reinforced by bamboo cellulosic crystals. *Bioresource Technology, 101*, 2529-2536.
68. Ulbrich, R.R., Wadud, S.E.B. (2019) Dynamic Mechanical Analyzer DMA 2980. http://www.tainstruments.com/pdf/literature/newdma.pdf.
69. Menard, K.P. (2008). *Dynamic Mechanical Analysis: A Practical Introduction, 2nd Edition.* Location: CRC Press.
70. Shrestha, S., Montes, F., Schueneman, G.T., Snyder, J.F., Youngblood, J.P. (2018). Effects of aspect ratio and crystal orientation of cellulose nanocrystals on properties of poly(vinyl alcohol) composite fibers. *Composites Science and Technology, 167*, 482-488.

R.4

1. Gebhardt, A., Understanding Additive Manufacturing. In *Understanding Additive Manufacturing*, Gebhardt, A., Ed. Hanser: 2011; pp I-IX, https://doi.org/10.3139/9783446431621.fm.
2. Bandyopadhyay, A.; Bose, S., *Additive Manufacturing*. CRC Press: 2015.
3. Guo, N.; Leu, M. C., Additive manufacturing: technology, applications and research needs. *Frontiers of Mechanical Engineering* **2013,** *8* (3), 215-243, https://doi.org/10.1007/s11465-013-0248-8.

4. Gibson, I.; Rosen, D.; Stucker, B., Vat Photopolymerization Processes. In *Additive Manufacturing Technologies: 3D Printing, Rapid Prototyping, and Direct Digital Manufacturing*, Springer New York: New York, NY, 2015; pp 63-268, https://doi.org/10.1007/978-1-4939-2113-3_4.
5. Ngo, T. D.; Kashani, A.; Imbalzano, G.; Nguyen, K. T. Q.; Hui, D., Additive manufacturing (3D printing): A review of materials, methods, applications and challenges. *Composites Part B: Engineering* **2018,** *143*, 172-196, https://doi.org/10.1016/j.compositesb.2018.02.012.
6. Tofail, S. A. M.; Koumoulos, E. P.; Bandyopadhyay, A.; Bose, S.; O'Donoghue, L.; Charitidis, C., Additive manufacturing: scientific and technological challenges, market uptake and opportunities. *Materials Today* **2018,** *21* (1), 22-37, https://doi.org/10.1016/j.mattod.2017.07.001.
7. Wang, X.; Jiang, M.; Zhou, Z.; Gou, J.; Hui, D., 3D printing of polymer matrix composites: A review and prospective. *Composites Part B: Engineering* **2017,** *110*, 442-458, https://doi.org/10.1016/j.compositesb.2016.11.034.
8. Quan, Z.; Wu, A.; Keefe, M.; Qin, X.; Yu, J.; Suhr, J.; Byun, J.-H.; Kim, B.-S.; Chou, T.-W., Additive manufacturing of multi-directional preforms for composites: opportunities and challenges. *Materials Today* **2015,** *18* (9), 503-512, https://doi.org/10.1016/j.mattod.2015.05.001.
9. Tuomi, J.; Paloheimo, K.-S.; Vehviläinen, J.; Björkstrand, R.; Salmi, M.; Huotilainen, E.; Kontio, R.; Rouse, S.; Gibson, I.; Mäkitie, A. A., A Novel Classification and Online Platform for Planning and Documentation of Medical Applications of Additive Manufacturing. *Surgical Innovation* **2014,** *21* (6), 553-559, https://doi.org/10.1177/1553350614524838.
10. Mironov, V.; Reis, D. N.; Derby, B., Review: Bioprinting: A Beginning. *Tissue Engineering* **2006,** *12* (4), 631-634, https://doi.org/10.1089/ten.2006.12.631.
11. Murphy, S. V.; Atala, A., 3D bioprinting of tissues and organs. *Nature Biotechnology* **2014,** *32*, 773, https://doi.org/10.1038/nbt.2958.
12. Tasoglu, S.; Demirci, U., Bioprinting for stem cell research. *Trends in Biotechnology* **2013,** *31* (1), 10-19, https://doi.org/10.1016/j.tibtech.2012.10.005.
13. Bishop, E. S.; Mostafa, S.; Pakvasa, M.; Luu, H. H.; Lee, M. J.; Wolf, J. M.; Ameer, G. A.; He, T.-C.; Reid, R. R., 3-D bioprinting technologies in tissue engineering and regenerative medicine: Current and future trends. *Genes Dis* **2017,** *4* (4), 185-195, https://doi.org/10.1016/j.gendis.2017.10.002.
14. Zhang, B.; Luo, Y.; Ma, L.; Gao, L.; Li, Y.; Xue, Q.; Yang, H.; Cui, Z., 3D bioprinting: an emerging technology full of opportunities and challenges. *Bio-Design and Manufacturing* **2018,** *1* (1), 2-13, https://doi.org/10.1007/s42242-018-0004-3.
15. Guillotin, B.; Souquet, A.; Catros, S.; Duocastella, M.; Pippenger, B.; Bellance, S.; Bareille, R.; Rémy, M.; Bordenave, L.; Amédée, J.; Guillemot, F., Laser assisted

bioprinting of engineered tissue with high cell density and microscale organization. *Biomaterials* **2010,** *31* (28), 7250-7256, https://doi.org/10.1016/j.biomaterials.2010.05.055.
16. Iwanaga, S.; Arai, K.; Nakamura, M., Chapter 4 - Inkjet Bioprinting. In *Essentials of 3D Biofabrication and Translation*, Atala, A.; Yoo, J. J., Eds. Academic Press: Boston, 2015; pp 61-79, https://doi.org/10.1016/B978-0-12-800972-7.00004-9.
17. Pati, F.; Jang, J.; Lee, J. W.; Cho, D.-W., Chapter 7 - Extrusion Bioprinting. In *Essentials of 3D Biofabrication and Translation*, Atala, A.; Yoo, J. J., Eds. Academic Press: Boston, 2015; pp 123-152, https://doi.org/10.1016/B978-0-12-800972-7.00007-4.
18. Jiang, T.; Munguia-Lopez, J. G.; Flores-Torres, S.; Kort-Mascort, J.; Kinsella, J. M., Extrusion bioprinting of soft materials: An emerging technique for biological model fabrication. *Applied Physics Reviews* **2019,** *6* (1), 011310, https://doi.org/10.1063/1.5059393.
19. Raman, R.; Bashir, R., Chapter 6 - Stereolithographic 3D Bioprinting for Biomedical Applications. In *Essentials of 3D Biofabrication and Translation*, Atala, A.; Yoo, J. J., Eds. Academic Press: Boston, 2015; pp 89-121, https://doi.org/10.1016/B978-0-12-800972-7.00006-2.
20. Ozbolat, I. T.; Yu, Y., Bioprinting Toward Organ Fabrication: Challenges and Future Trends. *IEEE Transactions on Biomedical Engineering* **2013,** *60* (3), 691-699, https://doi.org/10.1109/TBME.2013.2243912.
21. Irvine, S. A.; Venkatraman, S. S., Bioprinting and Differentiation of Stem Cells. *Molecules* **2016,** *21* (9), 1188, https://doi.org/10.3390/molecules21091188.
22. Hwang, N. S.; Varghese, S.; Elisseeff, J., Controlled differentiation of stem cells. *Adv Drug Deliv Rev* **2008,** *60* (2), 199-214, https://doi.org/10.1016/j.addr.2007.08.036.
23. Moore, C. A.; Shah, N. N.; Smith, C. P.; Rameshwar, P., 3D Bioprinting and Stem Cells. In *Somatic Stem Cells: Methods and Protocols*, Singh, S. R.; Rameshwar, P., Eds. Springer New York: New York, NY, 2018; pp 93-103, https://doi.org/10.1007/978-1-4939-8697-2_7.
24. Chamberlain, G.; Fox, J.; Ashton, B.; Middleton, J., Concise Review: Mesenchymal Stem Cells: Their Phenotype, Differentiation Capacity, Immunological Features, and Potential for Homing. *STEM CELLS* **2007,** *25* (11), 2739-2749, https://doi.org/10.1634/stemcells.2007-0197.
25. Bracaglia, L. G.; Smith, B. T.; Watson, E.; Arumugasaamy, N.; Mikos, A. G.; Fisher, J. P., 3D printing for the design and fabrication of polymer-based gradient scaffolds. *Acta Biomaterialia* **2017,** *56*, 3-13, https://doi.org/10.1016/j.actbio.2017.03.030.
26. An, J.; Teoh, J. E. M.; Suntornnond, R.; Chua, C. K., Design and 3D Printing of Scaffolds and Tissues. *Engineering* **2015,** *1* (2), 261-268, https://doi.org/10.15302/J-ENG-2015061.
27. Woodfield, T. B. F.; Blitterswijk, C. A. V.; Wijn, J. D.; Sims, T. J.; Hollander, A. P.; Riesle, J., Polymer Scaffolds Fabricated with Pore-Size Gradients as a Model for Studying the

Zonal Organization within Tissue-Engineered Cartilage Constructs. *Tissue Engineering* **2005,** *11* (9-10), 1297-1311, https://doi.org/10.1089/ten.2005.11.1297.

28. Bittner, S. M.; Smith, B. T.; Diaz-Gomez, L.; Hudgins, C. D.; Melchiorri, A. J.; Scott, D. W.; Fisher, J. P.; Mikos, A. G., Fabrication and mechanical characterization of 3D printed vertical uniform and gradient scaffolds for bone and osteochondral tissue engineering. *Acta Biomaterialia* **2019,** *90*, 37-48, https://doi.org/10.1016/j.actbio.2019.03.041.
29. Palaganas, N. B.; Mangadlao, J. D.; de Leon, A. C. C.; Palaganas, J. O.; Pangilinan, K. D.; Lee, Y. J.; Advincula, R. C., 3D Printing of Photocurable Cellulose Nanocrystal Composite for Fabrication of Complex Architectures via Stereolithography. *ACS Applied Materials & Interfaces* **2017,** *9* (39), 34314-34324, https://doi.org/10.1021/acsami.7b09223.
30. Jiang, Z.; Shaha, R.; Jiang, K.; McBride, R.; Frick, C.; Oakey, J., Composite Hydrogels with Controlled Degradation in 3D Printed Scaffolds. *IEEE Transactions on NanoBioscience* **2019,** *18* (2), 261-264, https://doi.org/10.1109/TNB.2019.2905510.
31. Jaramillo, L.; Briceno, I.; Duran, C. Odontogenic cell culture in PEGDA hydrogel scaffolds for use in tooth regeneration protocols. *Acta. Odontol. Latinoam.* **2012**, *25*(3), 243-254.
32. Fairbanks, B. D.; Schwartz, M. P.; Bowman, C. N.; Anseth, K. S., Photoinitiated polymerization of PEG-diacrylate with lithium phenyl-2,4,6-trimethylbenzoylphosphinate: polymerization rate and cytocompatibility. *Biomaterials* **2009,** *30* (35), 6702-6707, https://doi.org/10.1016/j.biomaterials.2009.08.055.
33. Tang, A.; Li, J.; Li, J.; Zhao, S.; Liu, W.; Liu, T.; Wang, J.; Liu, Y., Nanocellulose/PEGDA aerogel scaffolds with tunable modulus prepared by stereolithography for three-dimensional cell culture. *Journal of Biomaterials Science, Polymer Edition* **2019,** *30* (10), 797-814, https://doi.org/10.1080/09205063.2019.1602904.
34. Camarero-Espinosa, S.; Rothen-Rutishauser, B.; Foster, E. J.; Weder, C., Articular cartilage: from formation to tissue engineering. *Biomaterials Science* **2016,** *4* (5), 734-767, https://doi.org/10.1039/C6BM00068A.
35. Kumar, A.; Negi, Y. S.; Choudhary, V.; Bhardwaj, N. K., Microstructural and mechanical properties of porous biocomposite scaffolds based on polyvinyl alcohol, nano-hydroxyapatite and cellulose nanocrystals. *Cellulose* **2014,** *21* (5), 3409-3426, https://doi.org/10.1007/s10570-014-0339-7.
36. Dugan, J. M.; Gough, J. E.; Eichhorn, S. J., Bacterial cellulose scaffolds and cellulose nanowhiskers for tissue engineering. *Nanomedicine* **2013,** *8* (2), 287-298, https://doi.org/10.2217/nnm.12.211.
37. Smyth, M.; Fournier, C.; Driemeier, C.; Picart, C.; Foster, E.J.; Bras, J. Tunable Structural and Mechanical Properties in liquid of Cellulose Nanofiber Substrates for Stem Cell Culture. *Biomacromolecules* **2017** *18* (7), 2034–2044. https://doi.org/10.1021/acs.biomac.7b00209.

38. Frost, B. A.; Foster, E. J., Replication of annulus fibrosus through fabrication and characterization of polyurethane and cellulose nanocrystal composite scaffolds. *Nanocomposites* **2019,** *5* (1), 13-27. https://doi.org/10.1080/20550324.2019.1585651.
39. Sapkota, J.; Natterodt, J.; Shirole, A.; Foster, E.J.; Weder, C. Fabrication and Properties of Polyethylene / Cellulose Nanocrystal Composites. *Macromol Mater Eng.* **2016**, *302*, 1600300. https://doi.org/10.1002/mame.201600300.
40. Jorfi, M.; Roberts, M.N.; Foster, E.J.; Weder, C. Mechanically-Adaptive Bio-Nanocomposites for Biomedical Applications. *ACS Appl Mater Inter* **2013,** *5* (4)**,** 1517–1526. https://doi.org/ 10.1021/am303160j.
41. Zhou, C.; Wu, Q.; Yue, Y.; Zhang, Q., Application of rod-shaped cellulose nanocrystals in polyacrylamide hydrogels. *Journal of Colloid and Interface Science* **2011,** *353* (1), 116-123, https://doi.org/10.1016/j.jcis.2010.09.035.
42. Ben Azouz, K.; Ramires, E. C.; Van den Fonteyne, W.; El Kissi, N.; Dufresne, A., Simple Method for the Melt Extrusion of a Cellulose Nanocrystal Reinforced Hydrophobic Polymer. *ACS Macro Letters* **2012,** *1* (1), 236-240, https://doi.org/10.1021/mz2001737.
43. Smyth, M.; M'Bengue, M-.S.; Terrien, M.; Picart, C.; Bras, J.; Foster, E.J. The effect of hydration on the material and mechanical properties of cellulose nanocrystal-alginate composites. *Carbohyd Polym* **2018**, *179*, 186-195. https://doi.org/10.1016/j.carbpol.2017.09.002.
44. Mendez, J.; Annamalai, P.K.; Eichhorn, S.J.; Rusli, R.; Rowan, S.J.; Foster, E.J.; Weder, C. Bioinspired Mechanically Adaptive Polymer Nanocomposites with Water-Activated Shape-Memory Effect. *Macromolecules* **2011,** *44* (17), 6827-6835. https://doi.org/10.1021/ma201502k.
45. Reid, M.S.; Villalobos, M.; Cranston, E.D. Benchmarking Cellulose Nanocrystals: From the Laboratory to Industrial Production. *Langmuir* **2017**, *33* (7), 1583-1598. https://doi.org/10.1021/acs.langmuir.6b03765.
46. Camarero Espinosa, S.; Kuhnt, T.; Foster, E. J.; Weder, C., Isolation of Thermally Stable Cellulose Nanocrystals by Phosphoric Acid Hydrolysis. *Biomacromolecules* **2013,** *14* (4), 1223-1230, https://doi.org/10.1021/bm400219u.
47. Ronca, A.; D'Amora, U.; Raucci, M.; Lin, H.; Fan, Y.; Zhang, X.; Ambrosio, L., *A Combined Approach of Double Network Hydrogel and Nanocomposites Based on Hyaluronic Acid and Poly(ethylene glycol) Diacrylate Blend*. 2018; Vol. 11, p 2454, https://doi.org/10.3390/ma11122454.
48. Kurdikar, D. L.; Peppas, N. A., The volume shrinkage, thermal and sorption behaviour of polydiacrylates. *Polymer* **1995,** *36* (11), 2249-2255, https://doi.org/10.1016/0032-3861(95)95304-J.
49. Shafiei-Sabet, S.; Hamad, W. Y.; Hatzikiriakos, S. G., Rheology of Nanocrystalline Cellulose Aqueous Suspensions. *Langmuir* **2012,** *28* (49), 17124-17133, https://doi.org/10.1021/la303380v.

50. Khabibullin, A.; Alizadehgiashi, M.; Khuu, N.; Prince, E.; Tebbe, M.; Kumacheva, E., Injectable Shear-Thinning Fluorescent Hydrogel Formed by Cellulose Nanocrystals and Graphene Quantum Dots. *Langmuir* **2017,** *33* (43), 12344-12350, https://doi.org/10.1021/acs.langmuir.7b02906.
51. Fallon, J. J.; Kolb, B. Q.; Herwig, C. J.; Foster, E. J.; Bortner, M. J., Mechanically adaptive thermoplastic polyurethane/cellulose nanocrystal composites: Process-driven structure–property relationships. *Journal of Applied Polymer Science* **2019,** *136* (4), 46992, https://doi.org/10.1002/app.46992.
52. Khandaker, M.; Orock, A.; Tarantini, S.; White, J.; Yasar, O., Biomechanical Performances of Networked Polyethylene Glycol Diacrylate: Effect of Photoinitiator Concentration, Temperature, and Incubation Time. *International Journal of Biomaterials* **2016,** *2016*, 8, https://doi.org/10.1155/2016/3208312.
53. Zhu, W.; George, J. K.; Sorger, V. J.; Grace Zhang, L., 3D printing scaffold coupled with low level light therapy for neural tissue regeneration. *Biofabrication* **2017,** *9* (2), 025002, https://doi.org/10.1088/1758-5090/aa6999.
54. Castro, D.; Ingram, P.; Kodzius, R.; Conchouso, D.; Yoon, E.; Foulds, I. G. In *Characterization of solid UV cross-linked PEGDA for biological applications*, 2013 IEEE 26th International Conference on Micro Electro Mechanical Systems (MEMS), 20-24 Jan. 2013; 2013; pp 457-460.
55. Yin, O. S.; Ahmad, I.; Amin, M. C. I. M., Synthesis of chemical cross-linked gelatin hydrogel reinforced with cellulose nanocrystals (CNC). *AIP Conference Proceedings* **2014,** *1614* (1), 375-380, https://doi.org/10.1063/1.4895226.
56. Jayaramudu, T.; Ko, H-.U.; Kim, H.C.; Kim, J.W.; Kim, J. Swelling Behavior of Polyacrylamide-Cellulose Nanocrystal Hydrogels: Swelling Kinetics, Temperature, and pH Effects. *Materials* **2019**, *12*, 2080, https://doi.org/10.3390/ma12132080.
57. Li, B.; Zhang, Y.; Wu, C.; Guo, B.; Luo, Z., Fabrication of mechanically tough and self-recoverable nanocomposite hydrogels from polyacrylamide grafted cellulose nanocrystal and poly(acrylic acid). *Carbohydrate Polymers* **2018,** *198*, 1-8, https://doi.org/10.1016/j.carbpol.2018.06.047.
58. Siqueira, G.; Kokkinis, D.; Libanori, R.; Hausmann, M. K.; Gladman, A. S.; Neels, A.; Tingaut, P.; Zimmermann, T.; Lewis, J. A.; Studart, A. R., Cellulose Nanocrystal Inks for 3D Printing of Textured Cellular Architectures. *Advanced Functional Materials* **2017,** *27* (12), https://doi.org/1604619, 10.1002/adfm.201604619.
59. Walther, A.; Timonen, J. V. I.; Díez, I.; Laukkanen, A.; Ikkala, O., Multifunctional High-Performance Biofibers Based on Wet-Extrusion of Renewable Native Cellulose Nanofibrils. *Advanced Materials* **2011,** *23* (26), 2924-2928, https://doi.org/10.1002/adma.201100580.

60. Bourget, J.-M.; A, F.; Germain, L.; Guillemette, M.; Veres, T., Alignment of Cells and Extracellular Matrix Within Tissue- Engineered Substitutes. 2013, https://doi.org/10.5772/54142.
61. Lin, H.; Kai, T.; Freeman, B. D.; Kalakkunnath, S.; Kalika, D. S., The Effect of Cross-Linking on Gas Permeability in Cross-Linked Poly(Ethylene Glycol Diacrylate). *Macromolecules* **2005,** *38* (20), 8381-8393, https://doi.org/10.1021/ma0510136.
62. Kashima, M.; Cao, H.; Liu, H.; Meng, Q.; Wang, D.; Li, F.; Yang, H., Effects of the chain length of crosslinking agents on the electro-optical properties of polymer-dispersed liquid crystal films. *Liquid Crystals* **2010,** *37* (3), 339-343, https://doi.org/10.1080/02678290903568495.
63. Liu, H.; Liu, D.; Yao, F.; Wu, Q., Fabrication and properties of transparent polymethylmethacrylate/cellulose nanocrystals composites. *Bioresource Technology* **2010,** *101* (14), 5685-5692, https://doi.org/10.1016/j.biortech.2010.02.045.
64. Gay, D., *Composite materials: design and applications*. Third edition. ed.; CRC Press, Taylor & Francis: Boca Raton, 2015; p xxiii, 611 pages.
65. Jones, R. M., *Mechanics of composite materials*. 2nd ed.; Taylor & Francis: Philadelphia, PA, 1999; p xvi, 519 p.
66. Gao, B.; Yang, Q.; Zhao, X.; Jin, G.; Ma, Y.; Xu, F., 4D Bioprinting for Biomedical Applications. *Trends in Biotechnology* **2016,** *34* (9), 746-756, https://doi.org/10.1016/j.tibtech.2016.03.004.
67. Kargarzadeh, H.; Sheltami, R.M.; Ahmad, I.; Abdullah, I.; Dufresne, A. Cellulose nanocrystal: A promising toughening agent for unsaturated polyester nanocomposites. *Polymer* **2015**, *56*, 346-357. https://doi.org/10.1016/j.polymer.2014.11.054.
68. Xu, S.; Girouard, N.; Schueneman, G.; Shofner, M.L.; Meredith, J.C. Mechanical and thermal properties of waterborne epoxy composites containing cellulose nanocrystals. *Polymer* **2013**, *54*(24), 6589-6598. https://doi.org/10.1016/j.polymer.2013.10.011.
69. Khan, A.; Khan, R. A.; Salmieri, S.; Le Tien, C.; Riedl, B.; Bouchard, J.; Chauve, G.; Tan, V.; Kamal, M. R.; Lacroix, M., Mechanical and barrier properties of nanocrystalline cellulose reinforced chitosan based nanocomposite films. *Carbohydrate Polymers* **2012,** *90* (4), 1601-1608, https://doi.org/10.1016/j.carbpol.2012.07.037.
70. Lee, K. J.; Cheng, H. Z.; Jou, W. S.; Chen, G. J.; Liang, C. W., The influence of carbon fiber orientation on the mechanical and tribological behavior of carbon fiber/LCP composites. *Materials Chemistry and Physics* **2007,** *102* (2), 187-194, https://doi.org/10.1016/j.matchemphys.2006.12.002.
71. Nak-Ho, S.; Suh, N. P., Effect of fiber orientation on friction and wear of fiber reinforced polymeric composites. *Wear* **1979,** *53* (1), 129-141, https://doi.org/10.1016/0043-1648(79)90224-2.

72. Pereira, A. B.; de Morais, A. B., Mode I interlaminar fracture of carbon/epoxy multidirectional laminates. *Composites Science and Technology* **2004,** *64* (13), 2261-2270, https://doi.org/10.1016/j.compscitech.2004.03.001.
73. Snell, M. B., Strength and elastic response of symmetric angle-ply cfrp. *Composites* **1978,** *9* (3), 167-176, https://doi.org/10.1016/0010-4361(78)90342-7.
74. Botelho, E. C.; Pardini, L. C.; Rezende, M. C., Evaluation of hygrothermal effects on the shear properties of Carall composites. *Materials Science and Engineering: A* **2007,** *452-453*, 292-301, https://doi.org/10.1016/j.msea.2006.10.127.
75. Hausmann, M. K.; Rühs, P. A.; Siqueira, G.; Läuger, J.; Libanori, R.; Zimmermann, T.; Studart, A. R., Dynamics of Cellulose Nanocrystal Alignment during 3D Printing. *ACS Nano* **2018,** *12* (7), 6926-6937, https://doi.org/10.1021/acsnano.8b02366.
76. Reising, A.B.; Moon, R.J.; Youngblood, J.P. Effect of particle alignment on mechanical properties of neat cellulose nanocrystal films. *Journal of Science & Technology for Forest Products and Processes*, 2012, *2* (6), 32-41.
77. Schumacher, J.; Bomas, H.; Zoch, H. W., Failure Behaviour of Advanced Seam Structures for CFRP- Aluminium Connections. *Procedia Materials Science* **2013,** *2*, 227-233, https://doi.org/10.1016/j.mspro.2013.02.028.
78. Kelly, A.; Zweben, C. H., *Comprehensive composite materials*. Elsevier: Amsterdam; New York, 2000.

R.5

1. Urban, M. W., *Handbook of Stimuli-Responsive Materials*. Wiley: 2011.
2. Li, Q., *Intelligent Stimuli-Responsive Materials: From Well-Defined Nanostructures to Applications*. Wiley: 2013.
3. Theato, P.; Sumerlin, B. S.; O'Reilly, R. K.; Epps, I. I. I. T. H., Stimuli responsive materials. *Chemical Society Reviews* **2013,** *42* (17), 7055-7056, 10.1039/C3CS90057F.
4. Yerushalmi, R.; Scherz, A.; van der Boom, M. E.; Kraatz, H.-B., Stimuli responsive materials: new avenues toward smart organic devices. *Journal of Materials Chemistry* **2005,** *15* (42), 4480-4487, 10.1039/B505212B.
5. Liu, Y.; Du, H.; Liu, L.; Leng, J., Shape memory polymers and their composites in aerospace applications: a review. *Smart Materials and Structures* **2014,** *23* (2), 023001, 10.1088/0964-1726/23/2/023001.
6. Roy, D.; Cambre, J. N.; Sumerlin, B. S., Future perspectives and recent advances in stimuli-responsive materials. *Progress in Polymer Science* **2010,** *35* (1), 278-301, https://doi.org/10.1016/j.progpolymsci.2009.10.008.
7. Stuart, M. A. C.; Huck, W. T. S.; Genzer, J.; Müller, M.; Ober, C.; Stamm, M.; Sukhorukov, G. B.; Szleifer, I.; Tsukruk, V. V.; Urban, M.; Winnik, F.; Zauscher, S.; Luzinov, I.; Minko, S., Emerging applications of stimuli-responsive polymer materials. *Nature Materials* **2010,** *9* (2), 101-113, 10.1038/nmat2614.

8. Safranski, D. L., Chapter One - Introduction to Shape-Memory Polymers. In *Shape-Memory Polymer Device Design*, Safranski, D. L.; Griffis, J. C., Eds. William Andrew Publishing: 2017; pp 1-22, https://doi.org/10.1016/B978-0-323-37797-3.00001-4.
9. Leng, J.; Lan, X.; Liu, Y.; Du, S., Shape-memory polymers and their composites: Stimulus methods and applications. *Progress in Materials Science* **2011,** *56* (7), 1077-1135, https://doi.org/10.1016/j.pmatsci.2011.03.001.
10. Hu, J.; Zhu, Y.; Huang, H.; Lu, J., Recent advances in shape–memory polymers: Structure, mechanism, functionality, modeling and applications. *Progress in Polymer Science* **2012,** *37* (12), 1720-1763, https://doi.org/10.1016/j.progpolymsci.2012.06.001.
11. Behl, M.; Lendlein, A., Shape-memory polymers. *Materials Today* **2007,** *10* (4), 20-28, https://doi.org/10.1016/S1369-7021(07)70047-0.
12. Lendlein, A.; Langer, R., Biodegradable, Elastic Shape-Memory Polymers for Potential Biomedical Applications. *Science* **2002,** *296* (5573), 1673, 10.1126/science.1066102.
13. Small, I. V. W.; Singhal, P.; Wilson, T. S.; Maitland, D. J., Biomedical applications of thermally activated shape memory polymers. *Journal of Materials Chemistry* **2010,** *20* (17), 3356-3366, 10.1039/B923717H.
14. Lendlein, A.; Behl, M.; Hiebl, B.; Wischke, C., Shape-memory polymers as a technology platform for biomedical applications. *Expert Review of Medical Devices* **2010,** *7* (3), 357-379, 10.1586/erd.10.8.
15. Gall, K.; Yakacki, C. M.; Liu, Y.; Shandas, R.; Willett, N.; Anseth, K. S., Thermomechanics of the shape memory effect in polymers for biomedical applications. *Journal of Biomedical Materials Research Part A* **2005,** *73A* (3), 339-348, 10.1002/jbm.a.30296.
16. Yakacki, C. M.; Gall, K., Shape-Memory Polymers for Biomedical Applications. In *Shape-Memory Polymers*, Lendlein, A., Ed. Springer Berlin Heidelberg: Berlin, Heidelberg, 2010; pp 147-175, 10.1007/12_2009_23.
17. Mohr, R.; Kratz, K.; Weigel, T.; Lucka-Gabor, M.; Moneke, M.; Lendlein, A., Initiation of shape-memory effect by inductive heating of magnetic nanoparticles in thermoplastic polymers. *Proc Natl Acad Sci U S A* **2006,** *103* (10), 3540-3545, 10.1073/pnas.0600079103.
18. Bayerl, T.; Duhovic, M.; Mitschang, P.; Bhattacharyya, D., The heating of polymer composites by electromagnetic induction – A review. *Composites Part A: Applied Science and Manufacturing* **2014,** *57*, 27-40, https://doi.org/10.1016/j.compositesa.2013.10.024.
19. Vattathurvalappil, S. H.; Haq, M., Thermomechanical characterization of Nano-Fe3O4 reinforced thermoplastic adhesives and single lap-joints. *Composites Part B: Engineering* **2019,** *175*, 107162, https://doi.org/10.1016/j.compositesb.2019.107162.
20. Bayerl, T.; Schledjewski, R.; Mitschang, P., Induction Heating of Thermoplastic Materials by Particulate Heating Promoters. *Polymers and Polymer Composites* **2012,** *20*, 333-342, 10.1177/096739111202000401.

21. Rudolf, R.; Mitschang, P.; Neitzel, M., Induction heating of continuous carbon-fibre-reinforced thermoplastics. *Composites Part A: Applied Science and Manufacturing* **2000,** *31* (11), 1191-1202, https://doi.org/10.1016/S1359-835X(00)00094-4.
22. Kim, H. N.; Jiao, A.; Hwang, N. S.; Kim, M. S.; Kang, D. H.; Kim, D.-H.; Suh, K.-Y., Nanotopography-guided tissue engineering and regenerative medicine. *Advanced Drug Delivery Reviews* **2013,** *65* (4), 536-558, https://doi.org/10.1016/j.addr.2012.07.014.
23. Alcocer-Cuarón, C.; Rivera, A. L.; Castaño, V. M., Hierarchical structure of biological systems: a bioengineering approach. *Bioengineered* **2014,** *5* (2), 73-79, 10.4161/bioe.26570.
24. Fratzl, P.; Weinkamer, R., Nature's hierarchical materials. *Progress in Materials Science* **2007,** *52* (8), 1263-1334, https://doi.org/10.1016/j.pmatsci.2007.06.001.
25. Bar-On, B.; Wagner, H. D., Structural motifs and elastic properties of hierarchical biological tissues – A review. *Journal of Structural Biology* **2013,** *183* (2), 149-164, https://doi.org/10.1016/j.jsb.2013.05.012.
26. Paris, O.; Zizak, I.; Lichtenegger, H.; Roschger, P.; Klaushofer, K.; Fratzl, P., Analysis of the hierarchical structure of biological tissues by scanning X-ray scattering using a micro-beam. *Cell Mol Biol (Noisy-le-grand)* **2000,** *46* (5), 993-1004.
27. Derényi, I.; Szöllősi, G. J., Hierarchical tissue organization as a general mechanism to limit the accumulation of somatic mutations. *Nature Communications* **2017,** *8* (1), 14545, 10.1038/ncomms14545.
28. Katz, J. L.; Misra, A.; Spencer, P.; Wang, Y.; Bumrerraj, S.; Nomura, T.; Eppell, S. J.; Tabib-Azar, M., Multiscale mechanics of hierarchical structure/property relationships in calcified tissues and tissue/material interfaces. *Materials Science and Engineering: C* **2007,** *27* (3), 450-468, https://doi.org/10.1016/j.msec.2006.05.055.
29. Liu, Y.; Luo, D.; Wang, T., Hierarchical Structures of Bone and Bioinspired Bone Tissue Engineering. *Small* **2016,** *12* (34), 4611-4632, 10.1002/smll.201600626.
30. Zhao, Z.; Fang, R.; Rong, Q.; Liu, M., Bioinspired Nanocomposite Hydrogels with Highly Ordered Structures. *Advanced Materials* **2017,** *29* (45), 1703045, 10.1002/adma.201703045.
31. Markstedt, K.; Mantas, A.; Tournier, I.; Martínez Ávila, H.; Hägg, D.; Gatenholm, P., 3D Bioprinting Human Chondrocytes with Nanocellulose–Alginate Bioink for Cartilage Tissue Engineering Applications. *Biomacromolecules* **2015,** *16* (5), 1489-1496, 10.1021/acs.biomac.5b00188.
32. Jones, J. R.; Lee, P. D.; Hench, L. L., Hierarchical porous materials for tissue engineering. *Philosophical Transactions of the Royal Society A: Mathematical, Physical and Engineering Sciences* **2006,** *364* (1838), 263-281, doi:10.1098/rsta.2005.1689.
33. Hongji, W.; Jinyang, L.; Gregory, F. P.; Qi, F.; Minhua, L.; Jingxuan, C.; Hua, D.; Xiaodong, C., Hierarchical patterning via dynamic sacrificial printing of stimuli-responsive hydrogels. *Biofabrication* **2020**.

34. Caló, E.; Khutoryanskiy, V. V., Biomedical applications of hydrogels: A review of patents and commercial products. *European Polymer Journal* **2015,** *65*, 252-267, https://doi.org/10.1016/j.eurpolymj.2014.11.024.
35. Hoffman, A. S., Hydrogels for biomedical applications. *Advanced Drug Delivery Reviews* **2012,** *64*, 18-23, https://doi.org/10.1016/j.addr.2012.09.010.
36. Chai, Q.; Jiao, Y.; Yu, X., Hydrogels for Biomedical Applications: Their Characteristics and the Mechanisms behind Them. *Gels* **2017,** *3* (1), 6, 10.3390/gels3010006.
37. De France, K. J.; Babi, M.; Vapaavuori, J.; Hoare, T.; Moran-Mirabal, J.; Cranston, E. D., 2.5D Hierarchical Structuring of Nanocomposite Hydrogel Films Containing Cellulose Nanocrystals. *ACS Applied Materials & Interfaces* **2019,** *11* (6), 6325-6335, 10.1021/acsami.8b16232.
38. Fang, I. J.; Trewyn, B. G., Chapter three - Application of Mesoporous Silica Nanoparticles in Intracellular Delivery of Molecules and Proteins. In *Methods in Enzymology*, Düzgüneş, N., Ed. Academic Press: 2012; Vol. 508, pp 41-59, https://doi.org/10.1016/B978-0-12-391860-4.00003-3.
39. Lee, F.; Iliescu, C.; Yu, F.; Yu, H., Chapter 3 - Constrained spheroids/organoids in perfusion culture. In *Methods in Cell Biology*, Doh, J.; Fletcher, D.; Piel, M., Eds. Academic Press: 2018; Vol. 146, pp 43-65, https://doi.org/10.1016/bs.mcb.2018.05.003.
40. Uysal, O.; Sevimli, T.; Sevimli, M.; Gunes, S.; Eker Sariboyaci, A., Chapter 17 - Cell and Tissue Culture: The Base of Biotechnology. In *Omics Technologies and Bio-Engineering*, Barh, D.; Azevedo, V., Eds. Academic Press: 2018; pp 391-429, https://doi.org/10.1016/B978-0-12-804659-3.00017-8.
41. Vander Heiden, M. G.; Plas, D. R.; Rathmell, J. C.; Fox, C. J.; Harris, M. H.; Thompson, C. B., Growth factors can influence cell growth and survival through effects on glucose metabolism. *Mol Cell Biol* **2001,** *21* (17), 5899-5912, 10.1128/mcb.21.17.5899-5912.2001.
42. Product Center Thermoplastic Polyurethanes [Internet]. Covestro; 2015 [cited 2020 April 15]. Available from: https://www.tpu.covestro.com/en/Products/Texin/ProductList/201403080434/Texin-RxT85A.aspx.
43. McMASTER-CARR – Nylon [Internet]. McMasters-CARR; 2019 [cited 2020 April 16]. Available from: https://www.mcmaster.com/nylon.
44. The Process Development Center – Nanocellulose Data Sheets [Internet]. The University of Maine; 2019 [cited 2020 March 20]. Available from: https://umaine.edu/pdc/nanocellulose/nanocellulose-spec-sheets-and-safety-data-sheets/
45. Kuo, C. K.; Ma, P. X., Ionically crosslinked alginate hydrogels as scaffolds for tissue engineering: Part 1. Structure, gelation rate and mechanical properties. *Biomaterials* **2001**, *22* (6), 511-521, https://doi.org/10.1016/S0142-9612(00)00201-5.
46. Irvine, S. A.; Venkatraman, S. S., Bioprinting and Differentiation of Stem Cells. *Molecules* **2016,** *21* (9), 1188, https://doi.org/10.3390/molecules21091188.

47. Hwang, N. S.; Varghese, S.; Elisseeff, J., Controlled differentiation of stem cells. *Adv Drug Deliv Rev* **2008,** *60* (2), 199-214, https://doi.org/10.1016/j.addr.2007.08.036.
48. Lafuente, B.; Downs, R. T.; Yang, H.; Stone, N., 2015, "The power of databases: the RRUFF project," Highlights in Mineralogical Crystallography, W. De Gruyter, Berlin, Germany, pp. 1-30.
49. Lamberti, G.; Peters, G. W. M.; Titomanlio, G., Crystallinity and Linear Rheological Properties of Polymers. *Int Polym Proc* **2007**, *22* (3), 303-310, https://doi.org/10.3139/217.2006.
50. Zheng, Y. R.; Tee, H. T.; Wei, Y.; Wu, X. L.; Mezger, M. et al., Morphology and Thermal Properties of Precision Polymers: The Crystallization of Butyl Branched Polyethylene and Polyphosphoesters. *Macromolecules* **2016**, *49* (4), 1321-1330, https://doi.org/ 10.1021/acs.macromol.5b02581.
51. Lei, W.; Fang, C.; Zhou, X.; Cheng, Y.; Yang, R.; Liu, D., Morphology and thermal properties of polyurethane elastomer based on representative structural chain extenders. *Thermochim Acta* **2017**, *653*, 116-125, https://doi.org/10.1016/j.tca.2017.04.008.
52. Russo, R.; Malinconico, M.; Santagata, G., Effect of Cross-Linking with Calcium Ions on the Physical Properties of Alginate Films. *Biomacromolecules* **2007**, *8* (10), 3193-3197, https://doi.org/10.1021/bm700565h.
53. Abdollahi, M.; Alboofetileh, M.; Behrooz, R.; Rezaei, M.; Miraki, R., Reducing water sensitivity of alginate bio-nanocomposite film using cellulose nanoparticles. *Int J Biol Macromol* **2013**, *54*, 166-173, https://doi.org/10.1016/j.ijbiomac.2012.12.016.
54. Shekhar, S.; Prasad, V.; Subramanyam, S. V., Structural and electrical properties of composites of polymer-iron carbide nanoparticles embedded in carbon. *Mater Sci Eng B* **2006**, *133* (1-3), 108-112, https://doi.org/10.1016/j.mseb.2006.06.010.
55. Zain, N. M.; Roslin, E. N.; Ahmad, S., Preliminary study on bio-based polyurethane adhesive/aluminum laminated composites for automotive applications. *Int J Adhes Adhes* **2016**, *71*, 1-9, https://doi.org/10.1016/j.ijadhadh.2016.08.001.
56. Holland, B. J.; Hay, J. N., The thermal degradation of poly(vinyl acetate) measured by thermal analysis-Fourier transform infrared spectroscopy. *Polymer* **2002**, *43* (8), 2207-2211, https://doi.org/10.1016/S0032-3861(02)00038-1.
57. Galikova, A.; Pola, J., Highly sensitive TGA diagnosis of thermal behavior of laser-deposited materials. *Thermochim Acta* **2008**, *473* (1-2), 54-60, https://doi.org/10.1016/j.tca.2008.04.014.
58. Chakraborty, M.; Mukherjee, D. C.; Mandal, B. M., Interpenetrating polymer network composites of polypyrrole and poly(vinyl acetate). *Synthetic Met* **1999**, *98* (3), 193-200, https://doi.org/10.1016/S0379-6779(98)00184-2.
59. Roy, S.; Tang, X. Z.; Das, T.; Zhang, L.; Li, Y. et al., Enhanced Molecular Level Dispersion and Interface Bonding at Low Loading of Modified Graphene Oxide to

Fabricate Super Nylon 12 Composites. *ACS Appl Mater Inter* **2015**, *7* (5), 3142-3151, https://doi.org/ 10.1021/am5074408.
60. Nagahama, K.; Ueda, Y.; Ouchi, T.; Ohya, Y., Biodegradable Shape-Memory Polymers Exhibiting Sharp Thermal Transitions and Controlled Drug Release. *Biomacromolecules* **2009**, *10* (7), 1789-1794, https://doi.org/10.1021/bm9002078.
61. Boudenne, A.; Ibos, L.; Fois, M.; Gehin, E.; Majeste, J. C., Thermophysical properties of polypropylene/aluminum composites. *J Polym Sci B Polym Phys* **2004**, *42*, 722-732, https://doi.org/10.1002/polb.10713.
62. Baskaran, R.; Selvasekarapandian, S.; Kuwata, N; Kawamura, J.; Hattori, T., Conductivity and thermal studies of blend polymer electrolytes based on PVAc-PMMA. *Solid State Ionics* **2006**, *177* (26-32), 2679-2682, https://doi.org/10.1016/j.ssi.2006.04.013.
63. Chen, X.; An, L.; Li, L.; Yin, J.; Sun, Z., Mixing Enthalpy and Phase Behavior of PEO/PVAc Blends. *Macromolecules* **1999**, *32* (18), 5905-5910, https://doi.org/10.1021/ma981889v.
64. Zhang, Q.; Mo, Z.; Liu, S.; Zhang, H., Influence of Annealing on Structure of Nylon-11. *Macromolecules* **2000**, *33* (16), 5999-6005, https://doi.org/10.1021/ma000298d.
65. Ogunsona, E. O.; Misra, M.; Mohanty, A. K., Influence of epoxidized natural rubber on the phase structure and toughening behavior of biocarbon reinforced nylon 6 biocomposites. *RSC Adv* **2017**, *7* (15), 8727-8739, https://doi.org/10.1039/C6RA27177D.
66. Gall, K.; Dunn, M. L.; Liu, Y., Internal stress storage in shape memory polymer nanocomposites. *Appl Phys Lett* **2004**, *85* (2), 290-292, https://doi.org/10.1063/1.1769087.
67. Yuan, H. C.; Ma, Z., High-speed strained-single-crystal-silicon thin-film transistors on flexible polymers. *J Appl Phys* **2006**, *100* (1), 013708, https://doi.org/10.1063/1.2214301.
68. Li, Y.; You, J., Micro-phase separation and crystallization behavior of amorphous oriented PLLA/PVAc blends during heat treatment under strain. *Polymer* **2011**, *52* (13), 2964-2969, https://doi.org/10.1016/j.polymer.2011.05.003.
69. Xu, X.; Fan, P.; Ren, J.; Cheng, Y.; Ren, J.; Zhao, J.; Song, R., Self-healing thermoplastic polyurethane (TPU)/polycaprolactone (PCL)/multi-wall carbon nanotubes (MWCNTs) blend as shape-memory composites. *Compos Sci Technol* **2018**, *168*, 255-262, https://doi.org/10.1016/j.compscitech.2018.10.003.
70. Ding, N.; Shentu, B.; Pan, P.; Shan, G.; Bao, Y.; Weng, Z., Synthesis and Crystallization of Poly(vinyl acetate)-*g*-Poly($_L$-lactide) Graft Copolymer with Controllable Graft Density. *Ind Eng Chem Res* **2013**, *52* (36), 12897-12905, https://doi.org/10.1021/ie401958m.
71. Abdelghany, A. M.; Meikhail, M. S.; Asker, N., Synthesis and structural-biological correlation of PVC/PVAc polymer blends. *J Mater Res Technol* **2019**, *8* (5), 3908-3916, https://doi.org/10.1016/j.jmrt.2019.06.053.
72. Sabzi, M.; Babaahmadi, M.; Samadi, N.; Mahdavinia, G. R.; Keramati, M.; Nikfarjam, N., Graphene network enabled high speed electrical actuation of shape memory

nanocomposite based on poly(vinyl acetate). *Polym Int* **2016**, *66* (5), 665-671, https://doi.org/10.1002/pi.5303.
73. Nair, S. S.; Ramesh, C.; Tashiro, K., Crystalline Phases in Nylon-11: Studies Using HTWAXS and HTFTIR. *Macromolecules* **2006**, *39* (8), 2841-2848, https://doi.org/10.1021/ma052597e.
74. Espinosa, E.; Filgueira, D.; Rodríguez, A.; Chinga-Carrasco, G., Nanocellulose-Based Inks-Effect of Alginate Content on the Water Absorption of 3D Printed Constructs. *Bioengineering (Basel)* **2019,** *6* (3), 65, https://doi.org/10.3390/bioengineering6030065.
75. Shivakumara, L. R.; Demappa, T., Synthesis and Swelling Behavior of Sodium Alginate/Poly(vinyl alcohol) Hydrogels. *Turk J Pharm Sci* **2019,** *16* (3), 252-260, https://doi.org/10.4274/tjps.galenos.2018.92408.
76. Serrano-Aroca, Á.; Ruiz-Pividal, J.-F.; Llorens-Gámez, M., Enhancement of water diffusion and compression performance of crosslinked alginate films with a minuscule amount of graphene oxide. *Sci Rep* **2017,** *7* (1), 11684-11684, https://doi.org/10.1038/s41598-017-10260-x.
77. Jang, J.; Seol, Y.-J.; Kim, H. J.; Kundu, J.; Kim, S. W.; Cho, D.-W., Effects of alginate hydrogel cross-linking density on mechanical and biological behaviors for tissue engineering. *J Mech Behav Biomed* **2014,** *37*, 69-77, https://doi.org/10.1016/j.jmbbm.2014.05.004.
78. Huang, M.-H.; Yang, M.-C., Swelling and biocompatibility of sodium alginate/poly(γ-glutamic acid) hydrogels. *Polym Advan Technol* **2010,** *21* (8), 561-567, https://doi.org/10.1002/pat.1466.
79. Lee, K. Y.; Mooney, D. J., Alginate: properties and biomedical applications. *Prog Polym Sci* **2012,** *37* (1), 106-126, https://doi.org/10.1016/j.progpolymsci.2011.06.003.
80. Cui, X. F.; Zheng, W. J.; Zou, W.; Liu, X. Y.; Yang, H.; Yan, J.; Gao, Y., Water-retaining, tough and self-healing hydrogels and their uses as fire-resistant materials. *Polym Chem-UK* **2019,** *10* (37), 5151-5158, https://doi.org/10.1039/C9PY01015G.
81. Li, Y.; Huang, G.; Zhang, X.; Li, B.; Chen, Y.; Lu, T.; Lu, T. J.; Xu, F., Magnetic Hydrogels and Their Potential Biomedical Applications. *Adv Funct Mater* **2013,** *23* (6), 660-672, https://doi.org/10.1002/adfm.201201708.
82. Bidarra, S. J.; Barrias, C. C.; Granja, P. L., Injectable alginate hydrogels for cell delivery in tissue engineering. *Acta Biomater* **2014**, *10* (4), 1646-1662, https://doi.org/10.1016/j.actbio.2013.12.006.
83. Hwang, N. S.; Varghese, S.; Elisseeff, J., Controlled differentiation of stem cells. *Adv Drug Deliv Rev* **2008,** *60* (2), 199-214, https://doi.org/10.1016/j.addr.2007.08.036.
84. Chamberlain, G.; Fox, J.; Ashton, B.; Middleton, J., Concise Review: Mesenchymal Stem Cells: Their Phenotype, Differentiation Capacity, Immunological Features, and Potential

for Homing. *STEM CELLS* **2007,** *25* (11), 2739-2749, https://doi.org/10.1634/stemcells.2007-0197.
85. Schliess, F.; Häussinger, D., The cellular hydration state: a critical determinant for cell death and survival. *Biological chemistry* **2002,** *383* (3-4), 577-83, https://doi.org/10.1515/bc.2002.059.
86. Takagi, M.; Ueda, K., Comparison of the optimal culture conditions for cell growth and tissue plasminogen activator production by human embryo lung cells on microcarriers. *Applied Microbiology and Biotechnology* **1994,** *41* (5), 565-570, https://doi.org/10.1007/BF00178490.
87. Gao, C.-q.; Zhao, Y.-l.; Li, H.-c.; Sui, W.-g.; Yan, H.-c.; Wang, X.-q., Heat stress inhibits proliferation, promotes growth, and induces apoptosis in cultured Lantang swine skeletal muscle satellite cells. *J Zhejiang Univ Sci B* **2015,** *16* (6), 549-559, https://doi.org/10.1631/jzus.B1400339.
88. Razali, S. A.; Sidik, N. A. C.; Koten, H., Cellulose Nanocrystals: A Brief Review on Properties and General Applications. *J Adv Res Des* **2019**, *60* (1), 1-15.
89. Diaz, J. A.; Ye, Z.; Wu, X.; Moore, A. L.; Moon, R. J.; Martini, A.; Boday, D. J.; Youngblood, J. P., Thermal Conductivity in Nanostructured Films: From Single Cellulose Nanocrystals to Bulk Films. *Biomacromolecules* **2014,** *15* (11), 4096-4101, https://doi.org/10.1021/bm501131a.
90. Akinshilo, A. T.; Olofinkua, J. O.; Olaye, O., Flow and Heat Transfer Analysis of the Sodium Alginate Conveying Copper Nanoparticles between Two Parallel Plates. *J Appl Comp Mech* **2017,** *3* (4), 258-266, https://doi.org/10.22055/jacm.2017.21514.1105.
91. Smyth, M.; M'Bengue, M.-S.; Terrien, M.; Picart, C.; Bras, J.; Foster, E. J., The effect of hydration on the material and mechanical properties of cellulose nanocrystal-alginate composites. *Carbohyd Polym* **2018,** *179*, 186-195, https://doi.org/10.1016/j.carbpol.2017.09.002.
92. Rashtchian, M.; Hivechi, A.; Bahrami, S. H.; Milan, P. B.; Simorgh, S., Fabricating alginate/poly(caprolactone) nanofibers with enhanced bio-mechanical properties via cellulose nanocrystal incorporation. *Carbohyd Polym* **2020,** *233*, 115873, https://doi.org/10.1016/j.carbpol.2020.115873.
93. Xu, X.; Liu, F.; Jiang, L.; Zhu, J. Y.; Haagenson, D.; Wiesenborn, D. P., Cellulose Nanocrystals vs. Cellulose Nanofibrils: A Comparative Study on Their Microstructures and Effects as Polymer Reinforcing Agents. *ACS Appl Mater Inter* **2013,** *5* (8), 2999-3009, https://doi.org/10.1021/am302624t.
94. Sun, M.; Chi, G.; Li, P.; Lv, S.; Xu, J.; Xu, Z.; Xia, Y.; Tan, Y.; Xu, J.; Li, L.; Li, Y., Effects of Matrix Stiffness on the Morphology, Adhesion, Proliferation and Osteogenic Differentiation of Mesenchymal Stem Cells. *Int J Med Sci* **2018,** *15* (3), 257-268, https://doi.org/10.7150/ijms.21620.

95. Shan, Y.; Li, C.; Wu, Y.; Li, Q.; Liao, J., Hybrid cellulose nanocrystal/alginate/gelatin scaffold with improved mechanical properties and guided wound healing. *RSC Adv* **2019,** *9* (40), 22966-22979, https://doi.org/10.1039/C9RA04026A.
96. Sun, M.; Chi, G.; Li, P.; Lv, S.; Xu, J.; Xu, Z.; Xia, Y.; Tan, Y.; Xu, J.; Li, L.; Li, Y., Effects of Matrix Stiffness on the Morphology, Adhesion, Proliferation and Osteogenic Differentiation of Mesenchymal Stem Cells. *Int J Med Sci* **2018,** *15* (3), 257-268, https://doi.org/10.7150/ijms.21620.
97. Li, J.; Mooney, D. J., Designing hydrogels for controlled drug delivery. *Nat Rev Mater* **2016,** *1* (12), 16071, https://doi.org/10.1038/natrevmats.2016.71.
98. Dennis, C. L.; Ivkov, R., Physics of heat generation using magnetic nanoparticles for hyperthermia. *Int J Hyperther* **2013,** *29* (8), 715-729, https://doi.org/10.3109/02656736.2013.836758.

R.6

1. Betts, J.G.; Young, K.A.; Wise, J.A.; Johnson, E.; Poe, B. et al. Anatomy and Physiology. OpenStax, Ed. Rice University: Houston, Texas, 2013.
2. Wakim, S.; Grewal, M., *Human Biology*, Online Textbook: Retrieved 26 March, 2020. https://bio.libretexts.org/Bookshelves/Human_Biology/Book%3A_Human_Biology_(Wakim_and_Grewal).
3. SEER Training Modules, *Cells, Tissues, & Membranes*. U. S. National Institutes of Health, National Cancer Institute. 26 March, 2020. https://training.seer.cancer.gov/anatomy/cells_tissues_membranes/tissues/.
4. Morrow, A.; Lechler, T., Studying cell biology in the skin. *Mol Biol Cell* **2015,** *26* (23), 4183-4186, 10.1091/mbc.E15-04-0246.
5. Guimarães, J.M., Human skin biology and the search for the truth. *J Biol Med* **2019**, *3*(1), 053-054, DOI: 10.17352/jbm.000016.
6. Graham, H. K.; Eckersley, A.; Ozols, M.; Mellody, K. T.; Sherratt, M. J., Human Skin: Composition, Structure and Visualisation Methods. In *Skin Biophysics: From Experimental Characterisation to Advanced Modelling*, Limbert, G., Ed. Springer International Publishing: Cham, 2019; pp 1-18, 10.1007/978-3-030-13279-8_1.
7. A&P: A Learning Initiative. *Epithelial Tissue*. Anatomy & Physiology. Retrieved 26 March, 2020. https://anatomyandphysiologyi.com/epithelial-tissue/.
8. Chapter 32 - Connective Tissues. In *Cell Biology (Third Edition)*, Pollard, T. D.; Earnshaw, W. C.; Lippincott-Schwartz, J.; Johnson, G. T., Eds. Elsevier: 2017; pp 555-570, https://doi.org/10.1016/B978-0-323-34126-4.00032-3.
9. Kyriopoulos, E. J.; Kyriakopoulos, A.; Karonidis, A.; Gravvanis, A.; Gamatsi, I.; Tsironis, C.; Tsoutsos, D., Burn injuries and soft tissue traumas complicated by mucormycosis infection: a report of six cases and review of the literature. *Ann Burns Fire Disasters* **2015,** *28* (4), 280-287.

10. Tscherne, H.; Telger, T. C.; Gotzen, L., *Fractures with Soft Tissue Injuries*. Springer Berlin Heidelberg: 2012.
11. Rognoni, E.; Watt, F. M., Skin Cell Heterogeneity in Development, Wound Healing, and Cancer. *Trends in Cell Biology* **2018,** *28* (9), 709-722, 10.1016/j.tcb.2018.05.002.
12. Williamson, D.; Harding, K., Wound healing. *Medicine* **2004,** *32* (12), 4-7, https://doi.org/10.1383/medc.32.12.4.55399.
13. Kirwan, H.; Pignataro, R., Chapter 2 - The Skin and Wound Healing. In *Pathology and Intervention in Musculoskeletal Rehabilitation (Second Edition)*, Magee, D. J.; Zachazewski, J. E.; Quillen, W. S.; Manske, R. C., Eds. W.B. Saunders: 2016; pp 25-62, https://doi.org/10.1016/B978-0-323-31072-7.00002-6.
14. Marshall, C. D.; Hu, M. S.; Leavitt, T.; Barnes, L. A.; Lorenz, H. P.; Longaker, M. T., Cutaneous Scarring: Basic Science, Current Treatments, and Future Directions. *Adv Wound Care (New Rochelle)* **2018,** *7* (2), 29-45, 10.1089/wound.2016.0696.
15. Krafts, K. P., Tissue repair: The hidden drama. *Organogenesis* **2010,** *6* (4), 225-233, 10.4161/org.6.4.12555.
16. Olson, J. L.; Atala, A.; Yoo, J. J., Tissue engineering: current strategies and future directions. *Chonnam Med J* **2011,** *47* (1), 1-13, 10.4068/cmj.2011.47.1.1.
17. Chowdhury, M. M. U., Dermatological pharmacology: topical agents. *Medicine* **2004,** *32* (12), 16-17, https://doi.org/10.1383/medc.32.12.16.55398.
18. Dorai, A. A., Wound care with traditional, complementary and alternative medicine. *Indian J Plast Surg* **2012,** *45* (2), 418-424, 10.4103/0970-0358.101331.
19. Cantu, R.; Steffe, J. A., Chapter 2 - Soft Tissue Healing Considerations After Surgery. In *Rehabilitation for the Postsurgical Orthopedic Patient (Third Edition)*, Maxey, L.; Magnusson, J., Eds. Mosby: St. Louis (MO), 2013; pp 15-25, https://doi.org/10.1016/B978-0-323-07747-7.00002-2.
20. Yu, J. R.; Navarro, J.; Coburn, J. C.; Mahadik, B.; Molnar, J.; Holmes IV, J. H.; Nam, A. J.; Fisher, J. P., Current and Future Perspectives on Skin Tissue Engineering: Key Features of Biomedical Research, Translational Assessment, and Clinical Application. *Advanced Healthcare Materials* **2019,** *8* (5), 1801471, 10.1002/adhm.201801471.
21. Greenwood, J. E., Chapter 10 - Hybrid Biomaterials for Skin Tissue Engineering. In *Skin Tissue Engineering and Regenerative Medicine*, Albanna, M. Z.; Holmes Iv, J. H., Eds. Academic Press: Boston, 2016; pp 185-210, https://doi.org/10.1016/B978-0-12-801654-1.00010-3.
22. Downes, S.; Mishra, A. A., 7 - Tissue-biomaterial interactions. In *Advanced Wound Repair Therapies*, Farrar, D., Ed. Woodhead Publishing: 2011; pp 174-185, https://doi.org/10.1533/9780857093301.2.174.
23. Khan, F.; Tanaka, M., Designing Smart Biomaterials for Tissue Engineering. *Int J Mol Sci* **2017,** *19* (1), 10.3390/ijms19010017.

24. Tay, C. Y.; Irvine, S. A.; Boey, F. Y. C.; Tan, L. P.; Venkatraman, S., Micro-/Nano-engineered Cellular Responses for Soft Tissue Engineering and Biomedical Applications. *Small* **2011,** *7* (10), 1361-1378, 10.1002/smll.201100046.
25. Shan, Y.; Li, C.; Wu, Y.; Li, Q.; Liao, J., Hybrid cellulose nanocrystal/alginate/gelatin scaffold with improved mechanical properties and guided wound healing. *RSC Advances* **2019,** *9* (40), 22966-22979, 10.1039/C9RA04026A.
26. Jones, J. R.; Hench, L. L., Biomedical materials for new millennium: perspective on the future. *Materials Science and Technology* **2001,** *17* (8), 891-900, 10.1179/026708301101510762.
27. Hutmacher, D. W., Scaffold design and fabrication technologies for engineering tissues — state of the art and future perspectives. *Journal of Biomaterials Science, Polymer Edition* **2001,** *12* (1), 107-124, 10.1163/156856201744489.
28. Atiqah, A.; Ansari, M. N. M., Chapter 6 - Nanostructure–Polymer Composites for Soft-Tissue Engineering. In *Nanostructured Polymer Composites for Biomedical Applications*, Swain, S. K.; Jawaid, M., Eds. Elsevier: 2019; pp 105-115, https://doi.org/10.1016/B978-0-12-816771-7.00006-5.
29. Mir, T.A.; Nakamura, M.; Iwanaga, S.; et al., Biofabrication offers future hope for tackling various obstacles and challenges in tissue engineering and regenerative medicine: A Perspective. *Int J Bioprint* **2019**; *5*(1): 153. http://dx.doi.org/10.18063/ijb.v5i1.153.
30. Kargozar, S.; Ramakrishna, S.; Mozafari, M., Chemistry of biomaterials: future prospects. *Current Opinion in Biomedical Engineering* **2019,** *10*, 181-190, https://doi.org/10.1016/j.cobme.2019.07.003.
31. Petersen, H.; Tavakoli, F.; Kruber, S.; Münscher, A.; Gliese, A.; Hansen, N.-O.; Uschold, S.; Eggert, D.; Robertson, W. D.; Gosau, T.; Sehner, S.; Kwiatkowski, M.; Schlüter, H.; Schumacher, U.; Knecht, R.; Miller, R. J. D., Comparative study of wound healing in rat skin following incision with a novel picosecond infrared laser (PIRL) and different surgical modalities. *Lasers Surg Med* **2016,** *48* (4), 385-391, 10.1002/lsm.22498.
32. Kim, M.; Kim, S. W.; Kim, H.; Hwang, C. W.; Man Choi, J.; Kang, H. W., Development of a reproducible in vivo laser-induced scar model for wound healing study and management. *Biomed Opt Express* **2019,** *10* (4), 1965-1977, 10.1364/BOE.10.001965.
33. Bigi, A.; Cojazzi, G.; Panzavolta, S.; Rubini, K.; Roveri, N., Mechanical and thermal properties of gelatin films at different degrees of glutaraldehyde crosslinking. *Biomaterials* **2001,** *22* (8), 763-768, https://doi.org/10.1016/S0142-9612(00)00236-2.
34. Frost, B. A.; Sutliff, B. P.; Thayer, P.; Bortner, M. J.; Foster, E. J., Gradient Poly(ethylene glycol) Diacrylate and Cellulose Nanocrystals Tissue Engineering Composite Scaffolds via Extrusion Bioprinting. *Frontiers in Bioengineering and Biotechnology* **2019,** *7* (280), 10.3389/fbioe.2019.00280.

35. Hausmann, M. K.; Rühs, P. A.; Siqueira, G.; Läuger, J.; Libanori, R.; Zimmermann, T.; Studart, A. R., Dynamics of Cellulose Nanocrystal Alignment during 3D Printing. *ACS Nano* **2018,** *12* (7), 6926-6937, 10.1021/acsnano.8b02366.
36. Siqueira, G.; Kokkinis, D.; Libanori, R.; Hausmann, M. K.; Gladman, A. S.; Neels, A.; Tingaut, P.; Zimmermann, T.; Lewis, J. A.; Studart, A. R., Cellulose Nanocrystal Inks for 3D Printing of Textured Cellular Architectures. *Advanced Functional Materials* **2017,** *27* (12), 1604619, https://doi.org/10.1002/adfm.201604619.
37. Ofner, I. I. I. C. M.; Bubnis, W. A., Chemical and Swelling Evaluations of Amino Group Crosslinking in Gelatin and Modified Gelatin Matrices. *Pharmaceutical Research* **1996,** *13* (12), 1821-1827, 10.1023/A:1016029023910.
38. Vemuri, S., A Screening Technique to Study the Mechanical Strength of Gelatin Formulations. *Drug Development and Industrial Pharmacy* **2000,** *26* (10), 1115-1120, 10.1081/DDC-100100277.
39. Lamberson, L. E., *Dynamic Behavior of Materials, Volume 1: Proceedings of the 2019 Annual Conference on Experimental and Applied Mechanics*. Springer International Publishing: 2019.
40. Jiang, Y.; Xv, X.; Liu, D.; Yang, Z.; Zhang, Q.; Shi, H.; Zhao, G.; Zhou, J., Preparation of Cellulose Nanofiber-reinforced Gelatin Hydrogel and Optimization for 3D Printing Applications. *2018* **2018,** *13* (3), 16.
41. Yin, O. S.; Ahmad, I.; Amin, M. C. I. M., Synthesis of chemical cross-linked gelatin hydrogel reinforced with cellulose nanocrystals (CNC). *AIP Conference Proceedings* **2014,** *1614* (1), 375-380, 10.1063/1.4895226.
42. De France, K. J.; Hoare, T.; Cranston, E. D., Review of Hydrogels and Aerogels Containing Nanocellulose. *Chemistry of Materials* **2017,** *29* (11), 4609-4631, 10.1021/acs.chemmater.7b00531.
43. Junker, J. P. E.; Kamel, R. A.; Caterson, E. J.; Eriksson, E., Clinical Impact Upon Wound Healing and Inflammation in Moist, Wet, and Dry Environments. *Adv Wound Care (New Rochelle)* **2013,** *2* (7), 348-356, 10.1089/wound.2012.0412.
44. Okan, D.; Woo, K.; Ayello, E. A.; Sibbald, G., The Role of Moisture Balance in Wound Healing. *Advances in Skin & Wound Care* **2007,** *20* (1).
45. Stoica, A. E.; Chircov, C.; Grumezescu, A. M., Hydrogel Dressings for the Treatment of Burn Wounds: An Up-To-Date Overview. *Materials (Basel)* **2020,** *13* (12), 2853, 10.3390/ma13122853.
46. Tondera, C.; Hauser, S.; Krüger-Genge, A.; Jung, F.; Neffe, A. T.; Lendlein, A.; Klopfleisch, R.; Steinbach, J.; Neuber, C.; Pietzsch, J., Gelatin-based Hydrogel Degradation and Tissue Interaction in vivo: Insights from Multimodal Preclinical Imaging in Immunocompetent Nude Mice. *Theranostics* **2016,** *6* (12), 2114-2128, 10.7150/thno.16614.

47. Bakravi, A.; Ahamadian, Y.; Hashemi, H.; Namazi, H., Synthesis of gelatin-based biodegradable hydrogel nanocomposite and their application as drug delivery agent. *Advances in Polymer Technology* **2018,** *37* (7), 2625-2635, https://doi.org/10.1002/adv.21938.
48. Lai, J.-Y., Biocompatibility of chemically cross-linked gelatin hydrogels for ophthalmic use. *Journal of Materials Science: Materials in Medicine* **2010,** *21* (6), 1899-1911, 10.1007/s10856-010-4035-3.
49. Takigawa, T.; Endo, Y., Effects of glutaraldehyde exposure on human health. *Journal of occupational health* **2006,** *48* (2), 75-87, 10.1539/joh.48.75.
50. Yamamoto, M.; Ikada, Y.; Tabata, Y., Controlled release of growth factors based on biodegradation of gelatin hydrogel. *Journal of biomaterials science. Polymer edition* **2001,** *12* (1), 77-88, 10.1163/156856201744461.
51. Gaspar-Pintiliescu, A.; Stanciuc, A.-M.; Craciunescu, O., Natural composite dressings based on collagen, gelatin and plant bioactive compounds for wound healing: A review. *International Journal of Biological Macromolecules* **2019,** *138*, 854-865, https://doi.org/10.1016/j.ijbiomac.2019.07.155.
52. Grishkewich, N.; Mohammed, N.; Tang, J.; Tam, K. C., Recent advances in the application of cellulose nanocrystals. *Current Opinion in Colloid & Interface Science* **2017,** *29*, 32-45, https://doi.org/10.1016/j.cocis.2017.01.005.
53. Camarero-Espinosa, S.; Rothen-Rutishauser, B.; Weder, C.; Foster, E. J., Directed cell growth in multi-zonal scaffolds for cartilage tissue engineering. *Biomaterials* **2016,** *74*, 42-52, https://doi.org/10.1016/j.biomaterials.2015.09.033.
54. Pan, T.; Song, W.; Cao, X.; Wang, Y., 3D Bioplotting of Gelatin/Alginate Scaffolds for Tissue Engineering: Influence of Crosslinking Degree and Pore Architecture on Physicochemical Properties. *Journal of Materials Science & Technology* **2016,** *32* (9), 889-900, https://doi.org/10.1016/j.jmst.2016.01.007.
55. Yang, Y.; Ritchie, A. C.; Everitt, N. M., Comparison of glutaraldehyde and procyanidin cross-linked scaffolds for soft tissue engineering. *Materials Science and Engineering: C* **2017,** *80*, 263-273, https://doi.org/10.1016/j.msec.2017.05.141.
56. Ooi, S. Y.; Ahmad, I.; Amin, M. C. I. M., Cellulose nanocrystals extracted from rice husks as a reinforcing material in gelatin hydrogels for use in controlled drug delivery systems. *Industrial Crops and Products* **2016,** *93*, 227-234, https://doi.org/10.1016/j.indcrop.2015.11.082.
57. Cao, Y.; Zavattieri, P.; Youngblood, J.; Moon, R.; Weiss, J., The relationship between cellulose nanocrystal dispersion and strength. *Construction and Building Materials* **2016,** *119*, 71-79, https://doi.org/10.1016/j.conbuildmat.2016.03.077.
58. Yin, F.; Lin, L.; Zhan, S., Preparation and properties of cellulose nanocrystals, gelatin, hyaluronic acid composite hydrogel as wound dressing. *Journal of Biomaterials Science, Polymer Edition* **2019,** *30* (3), 190-201, 10.1080/09205063.2018.1558933.

59. Chen, S.; Shi, J.; Xu, X.; Ding, J.; Zhong, W.; Zhang, L.; Xing, M.; Zhang, L., Study of stiffness effects of poly(amidoamine)–poly(n-isopropyl acrylamide) hydrogel on wound healing. *Colloids and Surfaces B: Biointerfaces* **2016,** *140*, 574-582, https://doi.org/10.1016/j.colsurfb.2015.08.041.
60. Smithmyer, M. E.; Sawicki, L. A.; Kloxin, A. M., Hydrogel scaffolds as in vitro models to study fibroblast activation in wound healing and disease. *Biomaterials Science* **2014,** *2* (5), 634-650, 10.1039/C3BM60319A.
61. Wang, L.-S.; Du, C.; Toh, W. S.; Wan, A. C. A.; Gao, S. J.; Kurisawa, M., Modulation of chondrocyte functions and stiffness-dependent cartilage repair using an injectable enzymatically crosslinked hydrogel with tunable mechanical properties. *Biomaterials* **2014,** *35* (7), 2207-2217, https://doi.org/10.1016/j.biomaterials.2013.11.070.
62. He, X.; Xiao, Q.; Lu, C.; Wang, Y.; Zhang, X.; Zhao, J.; Zhang, W.; Zhang, X.; Deng, Y., Uniaxially Aligned Electrospun All-Cellulose Nanocomposite Nanofibers Reinforced with Cellulose Nanocrystals: Scaffold for Tissue Engineering. *Biomacromolecules* **2014,** *15* (2), 618-627, 10.1021/bm401656a.
63. Du, H.; Liu, W.; Zhang, M.; Si, C.; Zhang, X.; Li, B., Cellulose nanocrystals and cellulose nanofibrils based hydrogels for biomedical applications. *Carbohydrate Polymers* **2019,** *209*, 130-144, https://doi.org/10.1016/j.carbpol.2019.01.020.

R.7

1. Khan, F.; Tanaka, M., Designing Smart Biomaterials for Tissue Engineering. *Int J Mol Sci* **2017,** *19* (1), 10.3390/ijms19010017.
2. Tay, C. Y.; Irvine, S. A.; Boey, F. Y. C.; Tan, L. P.; Venkatraman, S., Micro-/Nano-engineered Cellular Responses for Soft Tissue Engineering and Biomedical Applications. *Small* **2011,** *7* (10), 1361-1378, 10.1002/smll.201100046.
3. Mohammed, N.; Grishkewich, N.; Tam, K. C., Cellulose nanomaterials: promising sustainable nanomaterials for application in water/wastewater treatment processes. *Environmental Science: Nano* **2018,** *5* (3), 623-658, 10.1039/C7EN01029J.
4. 2. Gul, S.; Khan, S. B.; Rehman, I. U.; Khan, M. A.; Khan, M. I., A Comprehensive Review of Magnetic Nanomaterials Modern Day Theranostics. *Frontiers in Materials* **2019,** *6* (179), 10.3389/fmats.2019.00179.
5. Foster, E. J.; Moon, R. J.; Agarwal, U. P.; Bortner, M. J.; Bras, J. et al., Current characterization methods for cellulose nanomaterials. *Chemical Society Reviews* **2018,** *47* (8), 2609-2679.
6. Raman, R.; Bashir, R., Chapter 6 - Stereolithographic 3D Bioprinting for Biomedical Applications. In *Essentials of 3D Biofabrication and Translation*, Atala, A.; Yoo, J. J., Eds. Academic Press: Boston, 2015; pp 89-121, https://doi.org/10.1016/B978-0-12-800972-7.00006-2.

7. De France, K. J.; Babi, M.; Vapaavuori, J.; Hoare, T.; Moran-Mirabal, J.; Cranston, E. D., 2.5D Hierarchical Structuring of Nanocomposite Hydrogel Films Containing Cellulose Nanocrystals. *ACS Applied Materials & Interfaces* **2019,** *11* (6), 6325-6335, 10.1021/acsami.8b16232.
8. Shan, Y.; Li, C.; Wu, Y.; Li, Q.; Liao, J., Hybrid cellulose nanocrystal/alginate/gelatin scaffold with improved mechanical properties and guided wound healing. *RSC Advances* **2019,** *9* (40), 22966-22979, 10.1039/C9RA04026A.
9. Camarero-Espinosa, S.; Rothen-Rutishauser, B.; Weder, C.; Foster, E. J., Directed cell growth in multi-zonal scaffolds for cartilage tissue engineering. *Biomaterials* **2016,** *74*, 42-52, https://doi.org/10.1016/j.biomaterials.2015.09.033.

Appendices

A.1 Induction Heating Sample Composition Labeling

Table A Compositions and labeling of all fabricated composites for TPU, PVAc, and Nylon-11, embedded with Fe_3O_4 NPs.

Polymer Matrix	Fe_3O_4 NP Composition (wt%)							
	Pure	**0.005**	**0.05**	**0.5**	**1.0**	**2.0**	**5.0**	**10.0**
RxT85A TPU	TPU	0.005TPU	0.05TPU	0.5TPU	1TPU	2TPU	5TPU	10TPU
PVAc	PVAc	0.005PVAc	0.05PVAc	0.5PVAc	1PVAc	2PVAc	5PVAc	10PVAc
Nylon-11	N11	0.005N11	0.05N11	0.5N11	1N11	2N11	5N11	10N11

Table B Compositions and labeling of all fabricated hydrogel composite scaffolds with varying alginate and CNC content.

	CNC Content (wt%)				
Alginate Content (wt%)	**0**	**0.5**	**1.0**	**2.0**	**5.0**
1.0	1A0C	1A0.5C	1A1C	1A2C	1A5C
2.0	2A0C	2A0.5C	2A1C	2A2C	2A5C
5.0	5A0C	5A0.5C	5A1C	5A2C	5A5C
10.0	10A0C	10A0.5C	10A1C	10A2C	10A5C

A.2 Gelatin and CNC/CNF Hydrogel Composition Labeling

Table C Varying compositions of gelatin hydrogels crosslinked with glutaraldehyde content, and subsequent sample naming of each.

Gelatin Content (wt%)	Glutaraldehyde Content (wt%)			
	0.1	**0.5**	**1.0**	**2.0**
2.0	2G0.1X	2G0.5X	2G1X	2G2X
5.0	5G0.1X	5G0.5X	5G1X	5G2X
10.0	10G0.1X	10G0.5X	10G1X	10G2X
15.0	15G0.1X	15G0.5X	15G1X	15G2X
20.0	20G0.1X	20G0.5X	20G1X	20G2X

Table D Compositions of workable crosslinked gelatin hydrogels with varying CNC/CNF content, and subsequent sample naming of each.

Ideal Gelatin Hydrogels	CNC Content (wt%)			
	0.5	**1.0**	**2.0**	**5.0**
5G0.1X	5G0.1X0.5CNC	5G0.1X1CNC	5G0.1X2CNC	5G0.1X5CNC
5G0.5X	5G0.5X0.5CNC	5G0.5X1CNC	5G0.5X2CNC	5G0.5X5CNC
5G1X	5G1X0.5CNC	5G1X1CNC	5G1X2CNC	5G1X5CNC
10G0.1X	10G0.1X0.5CNC	10G0.1X1CNC	10G0.1X2CNC	10G0.1X5CNC
10G0.5X	10G0.5X0.5CNC	10G0.5X1CNC	10G0.5X2CNC	10G0.5X5CNC
10G1X	10G1X0.5CNC	10G1X1CNC	10G1X2CNC	10G1X5CNC
15G0.1X	15G0.1X0.5CNC	15G0.1X1CNC	15G0.1X2CNC	15G0.1X5CNC
15G0.5X	15G0.5X0.5CNC	15G0.5X1CNC	15G0.5X2CNC	15G0.5X5CNC
15G1X	15G1X0.5CNC	15G1X1CNC	15G1X2CNC	15G1X5CNC
20G0.1X	20G0.1X0.5CNC	20G0.1X1CNC	20G0.1X2CNC	N/A
20G0.5X	20G0.5X0.5CNC	20G0.5X1CNC	20G0.5X2CNC	N/A
20G1X	20G1X0.5CNC	20G1X1CNC	20G1X2CNC	N/A
Ideal Gelatin Hydrogels	**CNF Content (wt%)**			
	0.1	**0.2**		**0.5**

5G0.1X	5G0.1X0.1CNF	5G0.1X0.2CNF	5G0.1X0.5CNF
5G0.5X	5G0.5X0.1CNF	5G0.5X0.2CNF	5G0.5X0.5CNF
5G1X	5G1X0.1CNF	5G1X0.2CNF	5G1X0.5CNF
10G0.1X	10G0.1X0.1CNF	10G0.1X0.2CNF	10G0.1X0.5CNF
10G0.5X	10G0.5X0.1CNF	10G0.5X0.2CNF	10G0.5X0.5CNF
10G1X	10G1X0.1CNF	10G1X0.2CNF	10G1X0.5CNF
15G0.1X	15G0.1X0.1CNF	15G0.1X0.2CNF	15G0.1X0.5CNF
15G0.5X	15G0.5X0.1CNF	15G0.5X0.2CNF	15G0.5X0.5CNF
15G1X	15G1X0.1CNF	15G1X0.2CNF	15G1X0.5CNF
20G0.1X	20G0.1X0.1CNF	20G0.1X0.2CNF	N/A
20G0.5X	20G0.5X0.1CNF	20G0.5X0.2CNF	N/A
20G1X	20G1X0.1CNF	20G1X0.2CNF	N/A

Note: Workable gelatin hydrogel compositions were determined by ranges of mechanical properties.